X–rays from Irregular Dwarf Galaxies: The Connection between Coronal Gas and High Energetic Stellar Events

Dissertation
zur
Erlangung des Doktorgrades (Dr. rer. nat.)
der
Mathematisch–Naturwissenschaftlichen Fakultät
der
Rheinischen Friedrich–Wilhelms–Universität
Bonn

vorgelegt von
Michael Kappes
aus Köln

Bonn, März 2005

Angefertigt mit Genehmigung
der Mathematisch–Naturwissenschaftlichen Fakultät
der Rheinischen Friedrich–Wilhelms–Universität Bonn

1. Referent: Priv. Doz. Dr. habil. Jürgen Kerp
2. Referent: Prof. Dr. Ulrich Klein

Tag der Promotion: 22.Juni 2005

Contents

1 Abstract **1**

2 Introduction **3**

2.1 Irregular Dwarf Galaxies 3

3 X–ray Astronomy **7**

3.1 X–ray Telescopes 7

3.1.1 XMM–Newton: Technical Specifications 8

3.2 Radiation Processes in the X–ray Regime 15

3.2.1 Thermal Radiation 16

3.2.2 Non–Thermal Radiation 17

3.3 Cosmic X–ray Sources 19

4 Data Analysis **25**

4.1 Data Products and Data Processing 25

4.2 Background Flares 27

4.3 Vignetting 30

4.3.1 Calculating Exposure Maps 31

4.4 Energy Bands and Hardness Ratios 34

4.5 Source Detection and Source Free Images 38

4.6 Spectral Extraction 39

4.6.1 Statistics 40

5 The Dwarf Galaxy Sample **43**

5.1 Results 43

5.1.1 Holmberg I 43

5.1.2 IC 2574 62

5.1.3 Sextans A 77

5.1.4 Holmberg II 84

5.1.5 NGC 1569 . . . 103
5.1.6 NGC 4214 . . . 124
5.1.7 NGC 4449 . . . 142
5.1.8 NGC 5253 . . . 156
5.2 An important Note on the Milky Way X–ray emission . . . 170
5.3 X–ray Point Source Content of the whole Sample . . . 174

6 Point Source Correlations and the Standard Model 177
6.1 Point Source Correlations . . . 177
6.1.1 Star Formation Rate . . . 181
6.1.2 X–ray Luminosity Function . . . 182
6.1.3 Spatial Distribution of X–ray Point Sources . . . 185
6.2 The Standard Model . . . 186

7 Summary and Future Prospects 191
7.1 The Standard model . . . 191
7.2 X–ray Point Sources . . . 194
7.3 Future Prospects . . . 196

8 Acknowledgements 199

9 Lebenslauf 201

References 203

List of Figures 211

List of Tables 217

1 Abstract

Radio observations of irregular dwarf galaxies (dIrr) in the 21 cm-line emission reveal morphological features in their interstellar medium (ISM) which are known as shells, bubbles or holes. The origin of these shells is still a matter of debate. A commonly used explanation for these shells is the creation by energetic stellar events, such as stellar winds or even supernovae. These stellar events produce hot gas (typically T$\approx 10^6$ K) which expands into the ISM, forming a shell filled with hot gas (coronal gas). The coronal gas can either break out of the neutral gas disk or it is confined by the swept up material, depending on the energetic input, the scale height of the disk and the gravitational potential well of the galaxy. I will refer to this scenario as the "standard model".

The first part of this thesis at hand will test this model using observations in the X–ray regime performed with the XMM–Newton and CHANDRA telescopes. For this aim a new data reduction method is introduced for the XMM–Newton data. The issues of data filtering and correction of the vignetting effect are the crucial steps in this method. A new software tool provides filtered light curves on an user adjustable significance threshold. Although the outer field of view beyond $20\farcm0$ from the optical axis are still not matching the observations the enhanced exposure maps, making use of the in–flight performance of XMM–Newton, are more reliable than the ones provided by the XMM–Newton software.

The standard model is evaluated on a sample of eight nearby dIrrs. The sample comprises the galaxies Holmberg I, IC 2574, Sextans A, Holmberg II, NGC 1569, NGC 4214, NGC 4449 and NGC 5253 which are concerned to be members of the local volume. The analysis of the diffuse soft X–ray emission shows that the standard model probably applies for a small number of individual shells in the neutral gas (e.g. the prominent shell in the northwest of IC 2574). However, the majority of shells is not filled with coronal gas. On the other hand there is evidence for coronal gas in the disk/halo interface of five galaxies in the sample. X–ray spectra are taken from these gas phases which give estimates for the temperatures, cooling times and sound speeds. The temperatures are in agreement with the framework of the standard model. Based on the cooling times and sound speeds an estimation is given whether or not the gas can be vented into the halo of the galaxies. This is supported by an investigation concerning the escape temperature (Martin, 1999). These findings support the results from the cooling time and sound speed estimations. According to the standard model the majority of the coronal gas phases can escape the corresponding galaxy. Accordingly, the standard model is far from being ruled out but it surely provides not the only process to create shells in the neutral gas of a galaxy.

In addition, Holmberg I is taken as an example of how to account for the foreground emission produced by the Milky Way. The soft X–ray background (SXRB) model by Pradas (2004); Pradas et al. (2003); Kappes et al. (2003) is evaluated. It turns out that

the model can be fitted to a background field of Holmberg I. This model is applied to the diffuse X–ray emission of the galaxy and the derived parameters of the coronal gas are thus in better agreement with the findings of Ott et al. (2001); Vorobyov et al. (2004). Whether or not the SXRB model is included in the investigation, the results do not change qualitatively.

The second part of the thesis concerns the X–ray point source population of the dIrrs. The point source detection is improved in contrast to the frequently used automated search algorithms in the sense that more faint point sources can be identified. In the present work the point sources are identified by eye after the processed images are smoothed in order to have a good estimation of the background variation and a higher signal–to–noise. Only sources exceeding a 4-σ background noise are considered as detections.

The X–ray luminosity functions (XLF) for all galaxies are derived from the point source fluxes. In contrast to previous work the XLFs now are much better constrained because of the higher number of detected point sources. Together with the star formation rate (SFR) different correlations are investigated. The HI mass correlates with the SFR in the cases where the XLF is unbroken. The galaxies with a broken XLF exhibit star bursts and hence a non–uniform star formation history. It is shown that the correlation between the number of HMXB and the SFR is best for a luminosity limited sample of HMXB. This is tested against a different sample of late–type galaxies, studied by Grimm et al. (2003). It turns out that the correlation in both samples is qualitatively real but for the dIrr sample the slope is flatter which is attributed to the different calculation of the SFR.

Finally, the spacial distribution of X–ray point sources in the dIrr sample suggests that the larger dIrrs ($r > 4\,\mathrm{kpc}$) show their most luminous sources in the center while the smaller galaxies show a constant luminosity of X–ray point sources for all galactocentric distances. The results concerning the XLF, SFR and spacial distribution suggests a non–universal formation process for these dIrr galaxies.

2 Introduction

The universe shows agglomerations of matter on very different scales. The largest structures known are the so–called superclusters which are extended over several hundred megaparsec. These huge superclusters consist of clusters of galaxies which are assumed to be gravitationally bound. Cluster of galaxies, or galaxy groups, consist of a mixture of different galaxy types.

A typical example of a galaxy cluster is shown in Fig.1, the Virgo cluster with the central galaxy M 87. The central galaxy is a giant elliptical surrounded by galaxies of different sizes and morphologies. The formation of these clusters and galaxies and how they evolve is still a matter of debate.

Basically, the large structures form by merging of small structures. In a galaxy cluster for example, one would expect that the smallest galaxies are more numerous than large evolved galaxies. This is indeed observed and thus the smallest galaxies are assumed to be the "building blocks" of the universe.

The present thesis examines a special type of "building block" the so–called *irregular dwarf galaxies*, abbreviated frequently as "dIrr". Their spatial distribution and dynamic, as discussed below, is a first hint for the structure formation outlined before. Here, the dIrrs will be analyzed with respect to their X–ray emission, which will highlight the energetic processes in the halos of these galaxies, as well as the evolved stellar population of dIrrs. See also Charles & Seward (1995) for a nice description of galaxy clusters in the context of X–ray astronomy.

2.1 Irregular Dwarf Galaxies

Dwarf galaxies in general are the most numerous objects in the (local) universe. The family of dwarf galaxies range from ultra compact dwarf galaxies (UCD), dwarf elliptical galaxies (dE), dwarf spheroidal galaxies (dSph) to dwarf irregular galaxies (dIrr) (see the review article by Mateo, 1998). All these objects are in general of low surface brightness. At least in the local group seems to be a morphology–position relationship: dIrrs are found more in the low density outskirts while the dEs and dSphs are located preferentially in the high density center of the local group (Pasetto et al., 2003). This implies that dIrrs are stripped while propagating through the group and hence they become dSphs. This is likely due to ram–pressure stripping as reported by Lee et al. (2003); Grebel et al. (2003). In that picture dwarf galaxies are thought to be the "building blocks" of massive galaxies.

In 1979, Heiles (1979, 1984) discovered hole–like structures in the neutral gas phase of our Galaxy. Similar structures were reported in other galaxies like M 31 (Brinks & Bajaja, 1986) or Holmberg II (Puche et al., 1992). Today these structures are well

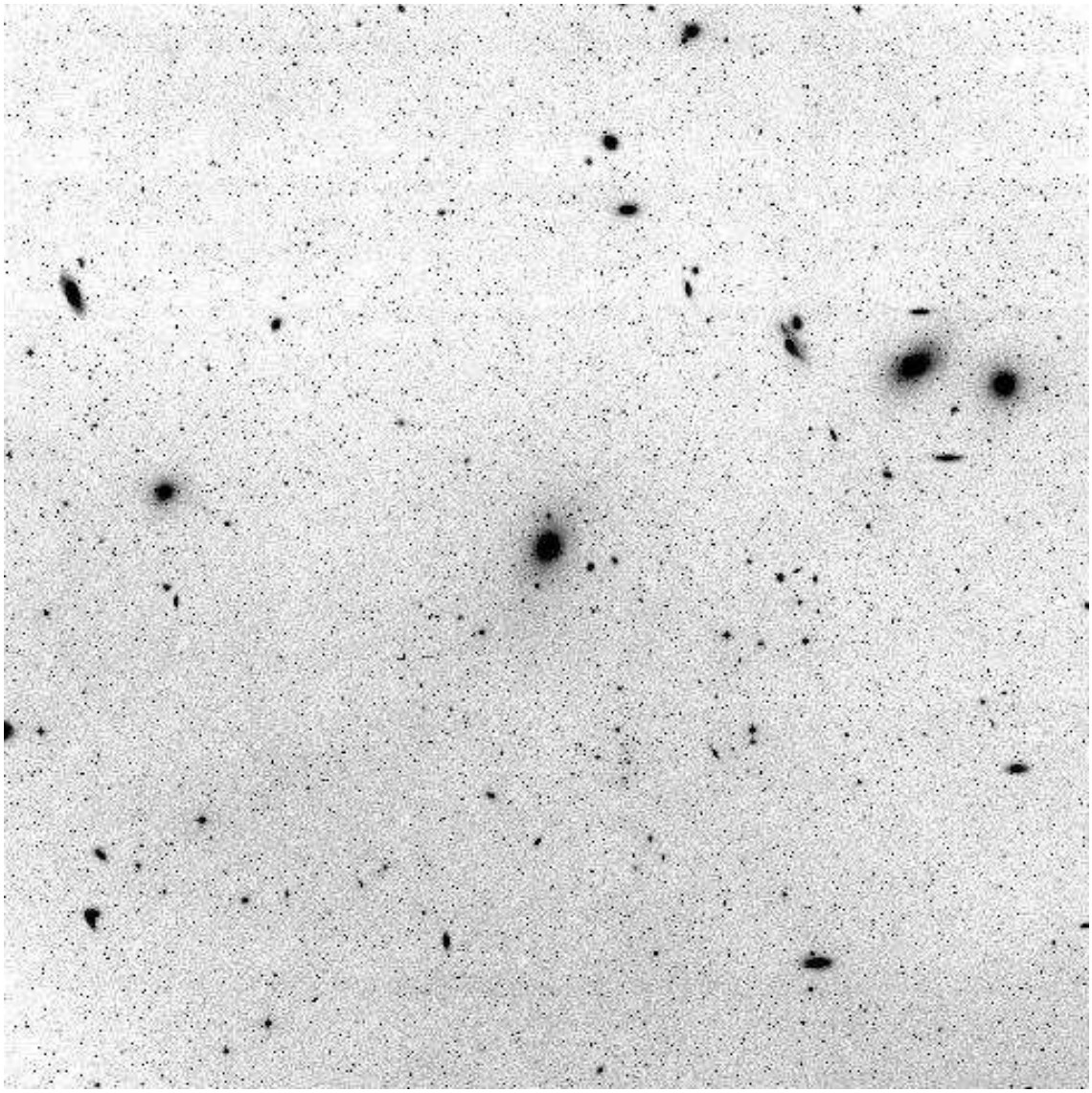

Fig. 1: *The DSS image of the Virgo galaxy cluster shows a mixture of different member galaxy morphologies. The central galaxy M 87 is a giant elliptical galaxy. Different galaxy morphologies can be identified and also different sizes.*

known in galaxies and they are frequently referred to as shells, rings, loops, holes, bubbles or cavities. It turned out that the analysis of these structures has advantages when they occur in dwarf galaxies: The dwarf galaxies have a shallow gravitational potential well and hence the shells, once formed, can grow to large sizes. Since the dwarfs are slow rotating and exhibit neither shear nor density waves, the shells are not deformed or destructed by the galactic rotation. Therefore they are expected to live longer than in grand design spirals (see e.g. Walter & Brinks, 1999; Ott et al., 2001, and references therein).

The origin of these shells, frequently cited as the "standard model", is thought to be due to stellar activity such as stellar winds or supernova explosions in e.g. an OB association. As pointed out by Walter & Brinks (1999) the potential caveats of this standard model are the following: a substantial fraction of F and A stars are expected to be found within the shells, however these could not be found in observations (see Radice et al., 1995; Rhode et al., 1999). A way out was the idea by Efremov et al. (1998) that gamma–ray bursts may form the shells. As they pointed out, the empty shells could be gamma–ray burst remnants and the old stellar population is then hard to detect. Another caveat is the energetic input provided by stellar winds and supernovae. Occasionally this input may be too low for forming large shells. Here, the way out was proposed by Tenorio-Tagle et al. (1987). They claimed that the infall of HI clouds can produce shell–like structures in the ISM of galaxies. The observational evidence was given by van der Hulst & Sancisi (1988).

Up to now a lot of shells are found also in the dwarf irregular galaxies of the local group (e.g. Puche et al., 1992; Staveley-Smith et al., 1997; Kim et al., 1998; Walter et al., 1998; Walter & Brinks, 1999). Within the framework of the standard model coronal gas emitting X–rays is expected to show up in the halo of dIrrs (Martin, 2003). Latest *CHANDRA* observations of nearby starburst dwarf galaxies like NGC 1569 (Martin et al., 2002) or the moderately active NGC 3077 (Ott et al., 2003) show that galactic winds are important to deduce a comprehensive picture of IGM[1] metal enrichment and the evolution of the universe as a whole.

Diffuse soft X-ray emission in dIrr galaxies is expected and indeed detected. The ROSAT mission was successful in detecting several nearby dwarf galaxies in the X–ray regime (e.g. della Ceca et al., 1997; Hensler et al., 1998; Kerp et al., 2002). In the case of our closest neighbor galaxy, the Large Magellanic Cloud, ROSAT revealed huge structures which are filled with hot X–ray emitting gas as well as the corresponding energetic stellar population (Chu & Mac Low, 1990; Bomans et al., 1994; Chu et al., 1995; Blondiau et al., 1997). This is an impressive demonstration for the potential of X-ray observations of dIrr galaxies in general and is a major motivation to study other nearby galaxies in greater detail. In this thesis the standard model is tested for the dIrrs Holmberg I, IC 2574 and Sextans A, with additional archival X–ray data of Holmberg II, NGC 1569, NGC 4214, NGC 4449 and NGC 5253.

[1] intergalactic medium

During the analysis of these three galaxies a further issue emerged. It turned out that the number of X–ray point sources may be correlated with the star formation rate (SFR) of the host galaxy. This connection was proposed by Grimm et al. (2003) for distant galaxies showing X–ray luminosities exceeding a luminosity $L_x = 2 \times 10^{38}$ erg s^{-1}.

Hence, this connection is analyzed for the dIrrs of the sample in this thesis. Since in the first three galaxies (Holmberg I, Sextans A and IC 2574) only one source exceeding the luminosity limit was found, I increased the number of galaxies (taking CHANDRA and XMM–Newton data from the archives) to have better statistics. It turned out that a statistical approach for X–ray point sources in dIrrs and their spacial distribution was not performed yet.

In particular, the X–ray point sources of each galaxy are investigated with respect to their deprojected distance from the galactic center versus the number of point sources per square kiloparsec. Also the source flux versus radius is investigated. Converting the fluxes to luminosities results in the X–ray luminosity function. Together with the SFR, all these figures are analyzed in order to see whether a universal star formation process is working in these galaxies or not.

The thesis is organized as follows: After a short introduction to X–ray astronomy, the properties of the XMM–Newton satellite are discussed and a brief description of radiation processes in the X–ray regime is given (Chapter 3). The general data analysis of XMM–Newton data is presented in Chapter 4 together with the caveats of the standard data reduction pipeline. Chapter 5 explains the results of the dIrr investigation for each galaxy separately. The correlation of the data output of Chapter 5 is finally presented in Chapter 6 together with an interpretation of the findings with respect to the standard model. The thesis closes with a summary in Chapter 7.

3 X–ray Astronomy

3.1 X–ray Telescopes

X–ray photons can be divided into several general energy ranges or bands. In this thesis photons with an energy of about $0.2 - 1.0$ keV are referred to as *soft X–rays* whereas photons with a higher energy than 1.0 keV are called *hard X–rays*. This categorization is somewhat arbitrary and hence the limit of 1.0 keV for the soft regime and also the upper limit for the hard part of the X–ray spectrum is not sharp.

The main obstacle to overcome in X–ray astronomy is the absorption of photons by the earth atmosphere (see Fig.2). This absorption depends on the photon energy ($\sigma \propto E^{-8/3}$ where σ is the cross section of the photoelectric absorption process). Photons at 30 keV are already observable above 35 km altitude whereas photons at 3 keV can only be observed in > 80 km altitude. For the soft energy regime (< 1 keV) the minimum altitude is about 200 km (Charles & Seward, 1995).

The first carrier devices which were capable to elevate the X–ray detectors to sufficient altitudes were balloons and rockets like the V2–rocket (Charles & Seward, 1995). With these, the first X–ray source was observed: our Sun. However, the detectors used in that experiment had a low sensitivity and were not able to detect any extrasolar X–ray source. Improvement in both detector technology and launchers allowed the observation of the first extrasolar X–ray source, namely Sco X–1 (Gursky et al., 1966). The detector sensitivity was improved by a factor of 10^5 and Riccardo Giacconi and his group measured an X–ray flux of ≈ 100 photons cm^{-2} s^{-1} coming from Sco X–1. Since then, astronomers discovered more and more X–ray sources like the crab nebula (Tau X–1) and eventually launched the first satellite UHURU which performed the first all–sky survey in X–rays (Charles & Seward, 1995).

The next cornerstone in X–ray astronomy was the detection of the first extra galactic object in 1965: M 87 (e.g. Friedman & Byram, 1967). Further quasars (e.g. Ku et al., 1980), active galactic nuclei (AGN) (e.g. Dopita, 1997) and galaxy clusters (e.g. Kellogg et al., 1973) were identified in the X–ray regime. Moreover, a soft and diffuse X–ray background was discovered by Bowyer et al. (1968) often referred to as the *soft X–ray background* (SXRB).

Many imaging X–ray telescopes have been placed in the orbit since then. In order to derive an image of the observed sky area, the ability to determine the location of an X–ray photon in two dimensions is a major goal. Such detectors were the *Imaging Proportional Counter* and the *microchannel plate detector*. The EINSTEIN satellite (see Giacconi et al., 1979) was the first X–ray telescope with imaging capabilities. In 1990, the famous European ROSAT mission (see Trümper, 1982) provided the most sensitive all–sky survey to date(!) with a factor of 1000 higher sensitivity than UHURU. Subsequently, more sensitive detectors including CCD spectrometers and CCD imaging

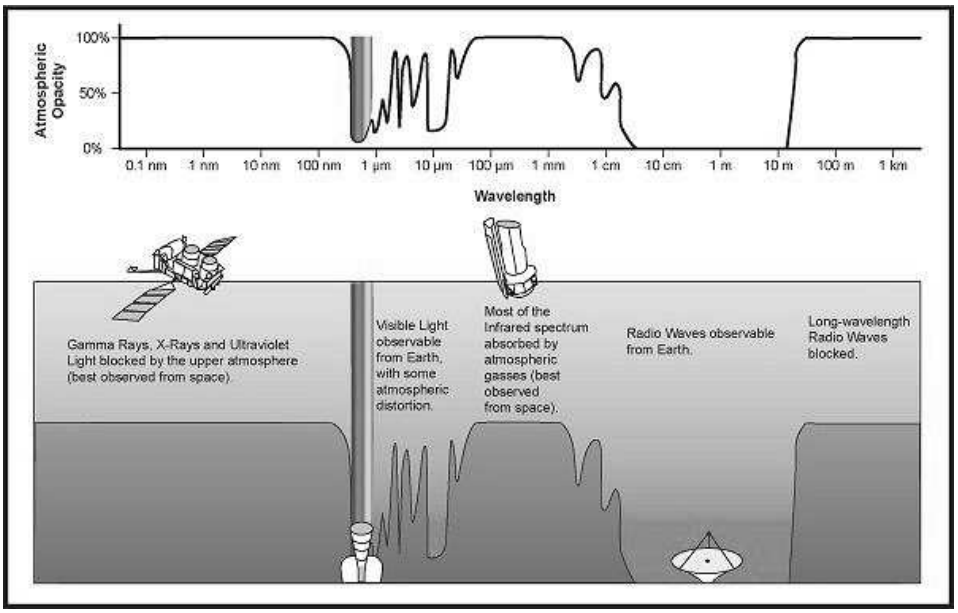

Fig. 2: *Opacity of the earth atmosphere. Unlike the visible and radio bands the X–ray band (on the left side marked by the satellite symbol) is strongly absorbed. Therefore, the X–ray telescope has to be elevated above the atmosphere, i.e. in the earth orbit. In former times, balloons and rockets were the first telescope carriers. [Image taken from Infrared Processing and Analysis Center & the SIRTF Science Center www page]*

devices have been employed. For a more detailed history of X–ray astronomy I encourage the reader to visit the WWW pages of NASA High Energy Astrophysics Science Archive Research Center[2] (HEASARC) at Goddard Space Flight Center.

Nowadays, astronomers have access to two advanced X–ray telescopes, CHANDRA (NASA) and XMM–Newton (ESA). The former provides the highest angular resolution available ($0.5''$) while the latter has the largest collecting area. This makes the XMM–Newton satellite the most effective telescope for soft diffuse X–rays. Both telescopes provide high end CCD–detectors for imaging and spectroscopy. The thesis presented here is based on data obtained with the XMM–Newton satellite while CHANDRA data is only used if higher angular resolution is needed. Therefore, the next section provides a deeper description of the technical aspects of ESA XMM–Newton (for differences to CHANDRA see Tab.1).

3.1.1 XMM–Newton: Technical Specifications

Launched by an Ariane 5 rocket in 1999 XMM–Newton orbits the earth in a highly excentric orbit with an apogee of ≈ 115000 km and an perigee of ≈ 6000 km. Besides a small UV–telescope, the satellite carries 5 detectors for observing X–rays.

[2] http://heasarc.gsfc.nasa.gov/

The XMM–Newton telescope in fact consists of three distinct co–aligned imaging telescopes with a focal length of 7.5 m. The overall assembly is sketched in Fig.3 where the three mirror units for the three different telescopes are on the left and the focal instruments on the right. The three instruments can be operated simultaneously. Each of the mirror units consist of 58 concentric nested Wolter–type–I mirrors. The *effective* area depends on the photon energy and moreover on the off–axis angle under which the photon enters the mirror assembly. The collecting area of all mirrors is about $4300\,\mathrm{cm}^2$ at 1.5 keV and $1800\,\mathrm{cm}^2$ at 8 keV. In other words a photon entering on–axis "sees" the whole mirror area while an off–axis photon only "sees" the projected mirror area. For the energy dependence it turns out that a low energy photon experiences a larger mirror area than a high energy photon (chromatic mapping). The critical angle under which total reflection of the photons can be achieved is $\theta_c \propto \lambda \cdot \sqrt{Z} = E^{-1} \cdot \sqrt{Z}$ where Z is the atomic number of the mirror material and E the energy of the incident photon. The effective area of the mirrors itself is displayed in Fig. 4.

Two of the mirror units (the upper two in Fig.3) contain the so–called Reflection Grating Assemblies (RGA) and in combination with the dedicated focal cameras they constitute the two Reflection Grating Spectrometers (RGS). The RGSs provide high spectral resolution X–ray spectroscopy ($E/\Delta E$ from $200-800$) over the energy range $0.35-2.5\,\mathrm{keV}$ ($5-35$ Å) unsurpassed by any X–ray detector in orbit. The RGAs intercept about 50% of the X–rays passing through the mirrors. The reflected X–rays are directed onto linear arrays of 9 CCD chips (384×1024 pixels each, backside illuminated) forming the focal cameras. Spherical abberation contaminating the detector images is minimized by the chosen geometry. The light diffracted by the gratings enters the camera which takes a picture of the spectrum. This appears as an 1–dimensional image across the width of the detectors. This spectrum reflects the physical processes which are at work in the source, e.g. line emission, continuum emission. However, in the thesis at hand the RGS is not used.

The most important instruments for the investigation presented here are the imaging devices namely the EPIC–MOS and EPIC–*pn* cameras. These cameras are designed to encompass the full energy range of the mirrors from $0.1-15\,\mathrm{keV}$. In addition to the imaging capabilities they also provide energy resolution at 6.5 keV of $E/\Delta E \approx 50$. The angular resolution of the CCDs itself is sufficient to resolve the mirror performance of $6.0''$ FWHM[3] for the EPIC–*pn* and $5.0''$ for the EPIC–MOS (according to $15.0''$ and $14.0''$ HEW[4]). The values of the HEW represent the size of the PSF[5] of the telescope which itself can be approximated by a King profile. According to the Nyquist sample theorem the PSF is fully sampled by the pixel size of the EPIC–MOS ($40\,\mu$m, $1.0''$ on the sky). For the EPIC–*pn* the core of the PSF is slightly undersampled (pixelsize of $150\,\mu$m, $4.1''$ on the sky). Both camera types provide a wide range in different data collection modes. For example one can use a so–called PrimeFullWindow mode to

[3]Full Width Half Maximum
[4]Half Energy Width
[5]Point Spread Function

Tab. 1: *Comparison of characteristic values for different X–ray telescope missions. [Taken from XMM–Newton User's handbook]*

Mission	Mirror PSF FWHM[″]	Mirror PSF HEW[″]	E range [keV]	A_e at 1 keV [cm^2]	Orbital target visibility [hr]
XMM–Newton	6	15	0.15 - 15	4650	40
Chandra	0.2	0.5	0.1 -10	800	50
ROSAT	3.5	7	0.1 - 2.4	400	1.3
ASCA	73	174	0.5 - 10	350	0.9

have the maximum FOV[6] or one can use only the inner CCD which has a smaller FOV but the data can be read out faster, which is interesting for rapidly variable sources. Different filters (Thin, Medium and Thick) can be moved into the light path to dilute long wavelength optical and UV radiation to avoid the detection of unrelated emission.

Each of the two EPIC–MOS cameras consists of 7 single CCDs with 600×600 pixels. They are arranged as displayed in Fig.5. The position of the chips in the vertical direction samples the curved shape of the focal surface providing a large FOV ($30\overset{\prime}{.}0$). There is also an overlap of the individual CCD chips but the rims of these are scientifically unusable areas which in fact are associated with apparent gaps in the images. This small drawback is corrected by the fact that the two EPIC–MOS cameras are rotated by 90° with respect to each other. In practice, as the reader will see later in Sec. 4, the gaps are still an issue to deal with. The EPIC–*pn* camera is made of a single silicon wafer carrying the 12 individual CCD chips. The geometric layout is shown in Fig. 6. In contrast to the EPIC–MOS chips the EPIC–*pn* chips are illuminated from the backside which leads to a different quantum efficiency (QE). In practice, the energy band width of the EPIC–MOS instruments is limited by the QE towards high energies while the EPIC–*pn* instrument reaches up to ≈ 15 keV. This is clear from Fig. 7: The EPIC–MOS camera QE drops down steeply above ≈ 3.5 keV while the EPIC–*pn* cameras are still operating up to energies of about 10 keV with an QE of 90 %.

Combining all three cameras and different filters for the optical photon rejection, the effective area of the complete X–ray telescope is displayed in Fig. 8. Here, the response function of the detectors are incorporated as well. Finally, in Tab. 1 the XMM–Newton key specifications are listed together with other X–ray missions for comparison.

[6] Field Of View

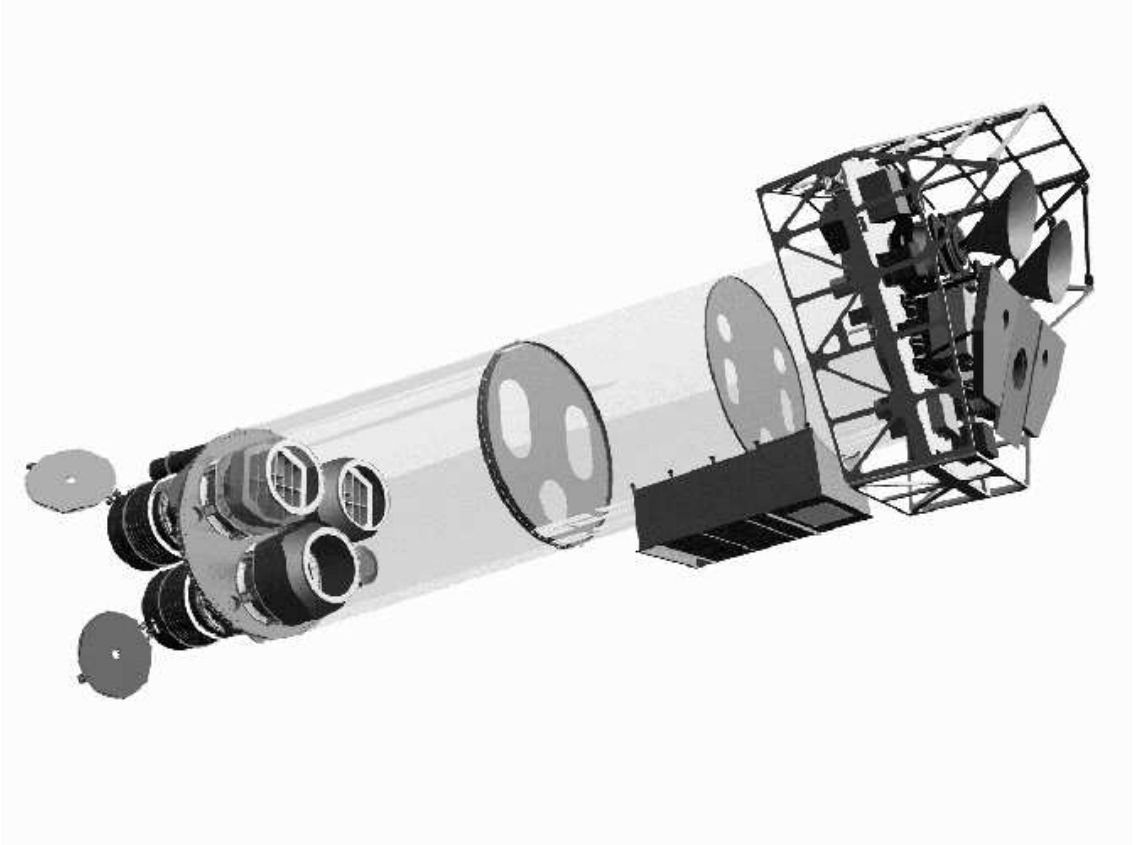

Fig. 3: *Sketch of the principal layout of the XMM–Newton satellite payload. The mirror assembly with the three mirrors are visible on the lower left. Two of them are equipped with the reflection gratings for spectroscopic purposes. The third is the entrance window for the EPIC–*pn *camera. On the right hand side the focal plane instruments (EPIC–MOS with the horn shaped radiators and EPIC–*pn*with the central plate radiator) are mounted as well as the reflection grade spectrometers with their radiators left and right of the EPIC–*pn *radiator. The optical monitor is obscured by the EPIC–*pn *mirror unit. [Image taken from XMM–Newton User's handbook]*

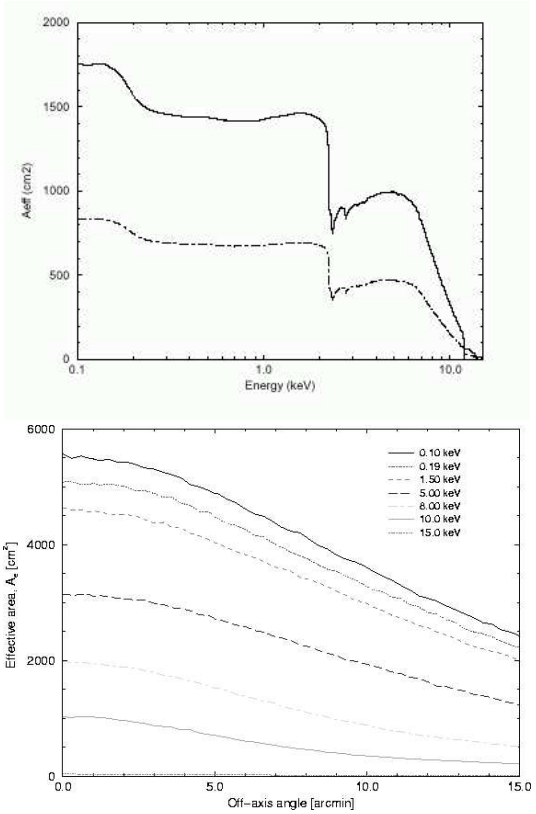

Fig. 4: **Upper Panel:** *The mirrors were tested in the* PANTER *X–ray test facility at Max–Planck–Institut für extraterrestrische Physik (MPE) Garching. This plot shows the effective area of a full aperture illuminated mirror depending on the photon energy. The "test radiation" is an X–ray line radiation between* 0.28 *and* 10 *keV, using a ROSAT PSPC as focal plane detector. The sharp drop off at* ≈ 2 *keV is due to the coating of the mirrors (Au M–edge). The figure shows the on–axis effective area of one XMM–Newton mirror without (solid line) and with (dot–dashed line) the reflection grating in the light path, while the* **lower Panel** *displays the change of the effective area with increasing off–axis angle for different photon energies as given in the upper right corner. Note that the effective area in the lower panel is the sum of all three mirrors. [Image taken from XMM–Newton User's handbook]*

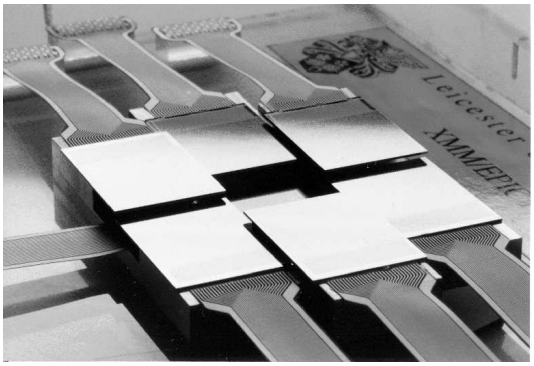

Fig. 5: *The CCD array of the EPIC–MOS camera. Note that the vertical offset of the chips is exaggerated. The central chip indeed is offset by a few millimeters with respect to the outer ones, matching onto the slightly bended focal surface of the telescope. [Image taken from HEASARC www page]*

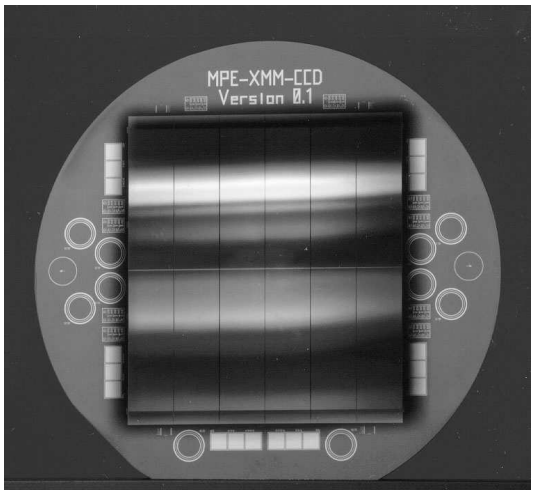

Fig. 6: *The 12 CCD chips of the EPIC–*pn *camera are produced onto a single silicon waver. Since there is a cross shaped gap in the very center of the chip array which might interfere observations of sources on–axis, the whole unit is shifted slightly with respect to the optical axis of the X–ray telescope. This makes sure that more than 90 % of the source energy is collected by the EPIC–*pn *camera when it is observed on–axis. [Image taken from HEASARC www page]*

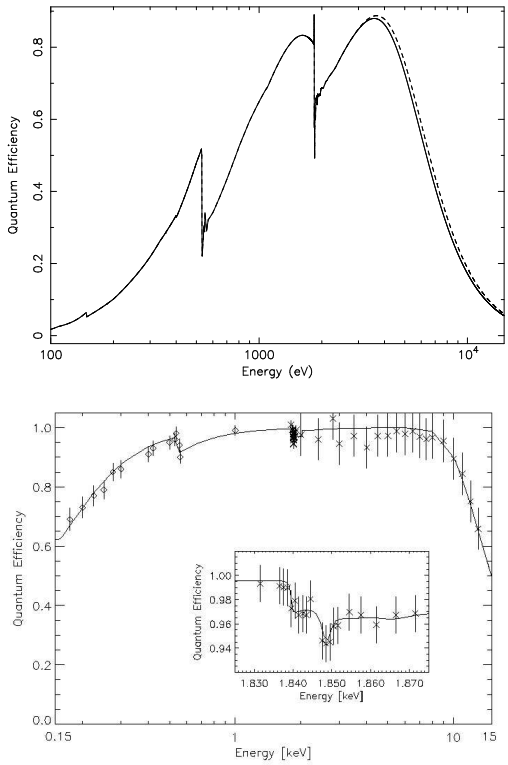

Fig. 7: **Upper panel:** *The quantum efficiency of the EPIC–MOS cameras (MOS1 solid, MOS2 dashed line) as a function of photon energy drops steeply for photons exceeding* 3.5 *keV. This drop off limits the energy band width towards higher energies in the EPIC–MOS case. Compare these curves to the* **lower panel***: Here, the quantum efficiency for the EPIC–*pn *camera versus photon energy is shown. Even for the high energy regime (*$\approx$ 10 *keV) the photons are detected with an efficiency of about* 90 *%. [Image taken from XMM–Newton User's handbook]*

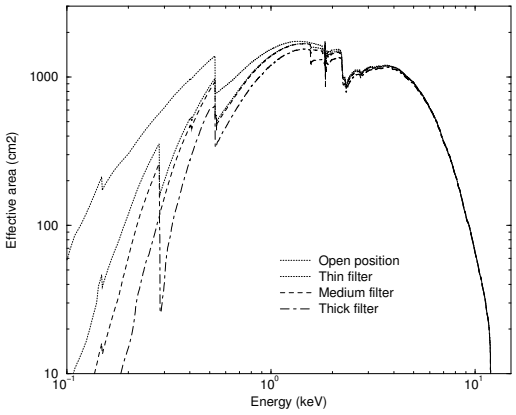

Fig. 8: *Combined effective area for all three imaging telescopes with different filters. The curve uses the detector quantum efficiency as shown in Fig. 7. [Image taken from XMM–Newton User's handbook]*

3.2 Radiation Processes in the X–ray Regime

Back in the year 1895 Wilhelm Conrad Röntgen was the first who worked on a radiation which was able to penetrate certain materials. At that time, Röntgen and others investigated cathode rays in glass tubes. It was known that the cathode rays were unable to penetrate the glass tube. However, Röntgen identified a fluorescence of barium platinocyanide coated paper plates when placed in front of a running glass tube. He was sure that the fluorescence could not be produced by the cathode rays but by another new kind of radiation he called "X–rays". The term X–rays was used to indicate that the nature of these rays was still unknown at these times. From subsequent experiments it turned out that the X–rays show up whenever cathode rays hit another material. Later, Max von Laue showed that these X–rays are of the same nature than electromagnetic waves such as light but with a higher frequency and thus, higher energy.

From that time on, X–rays were used especially in the medical setting (diagnostics) and later on also in other industrial environments (product inspection systems). Later some astronomers were curious to find out whether X–rays can be generated in a natural way. Since the energy of an X–ray photon is higher than the energy of an optical photon (a factor of $\approx 10^3$) the generation process must be connected to high energies and so, only a few astronomers believed in the possibility of natural generated X–rays.

Nowadays, X–rays from natural sources (i.e. astronomical sources) are well known and still a matter of science. Here, the reader will be introduced to the different generation processes and properties of X–rays. Astronomical X–ray sources can be divided up into two distinct major classes: thermal and non–thermal sources. The physical nature of these will be discussed in the following two sections.

3.2.1 Thermal Radiation

Basically, the emission of (electromagnetic) radiation can originate from accelerated charged particles. If the spectrum of this radiation is only dependent on the temperature, we call it "thermal radiation". The prototype of this thermal radiation is a so–called "black body". A black body is a perfect absorber for radiation. Moreover, in thermal equilibrium the black body radiates with a characteristic spectrum, known as the Planck–spectrum, which only depends on the temperature of the black body. To be more precise: the frequency at the maximum flux is directly proportional to the black body temperature. This spectrum cannot be explained in classical terms but with quantum mechanics. In Fig. 9 the black body spectrum is shown in dependence of the temperature.

The so–called (non–relativistic) bremsstrahlung is a thermal radiation process if it takes place in a plasma. Here, thermal electrons following a Maxwell–Boltzmann velocity distribution are decelerated in the (static) Coulomb–field of an ion for example. After the deceleration the electron leaves the ion (free–free radiation) with a lower velocity and the difference kinetic energy is transformed into radiation. Since the velocity of the electrons depends on the plasma temperature this process is also a thermal one. The bremsstrahlung generates a continuous spectrum with a characteristic shape and an energy cut–off (wavelength minimum) which is associated with the maximum kinetic energy of the electrons. Additionally, lines from K–shell electrons are superimposed on the continuum as shown in Fig. 10. Here, a mixture of radiative processes leads to the observed spectrum. If the temperature is sufficiently high enough ($T > 5 \times 10^6$ K) the line radiation is suppressed and the "plasma component", i.e. the bremsstrahlung is dominant. If the plasma is optically thin selfabsorption is negligible; if the plasma is optically thick it radiates with a brightness of a black body at the plasma temperature. Note, that bremsstrahlung generated in an *X–ray tube* is not strictly thermal; the accelerated electrons do not have a Maxwellian velocity distribution and especially the decelerating material is not a gas but a solid body having less degrees of freedom. This leads to a slightly different spectrum and therefore this type of bremsstrahlung is a borderline case between thermal and non–thermal.

A further thermal process in plasmas is radiative recombination. Here, an ion captures a free electron from the plasma and binds it with subsequent radiation of photons. Both continuum and spectral lines can be produced in such a recombination as the electron passes from the continuum levels into the (upper) bound levels of the ion (free–bound radiation) and then cascades down to form a ground state ion. This process can appear in a slightly different fashion: the continuum level electron can be bound without the need for radiation. In fact, the electron releases its energy to excite a low state electron which in turn emits X–rays when it decays. This process is frequently called dielectronic recombination. Further, an excited ion can emit two photons simultaneously if the transition is highly forbidden (two–photon continuum). Finally, a continuum electron can excite an inner shell electron at high energies and then the excited electron

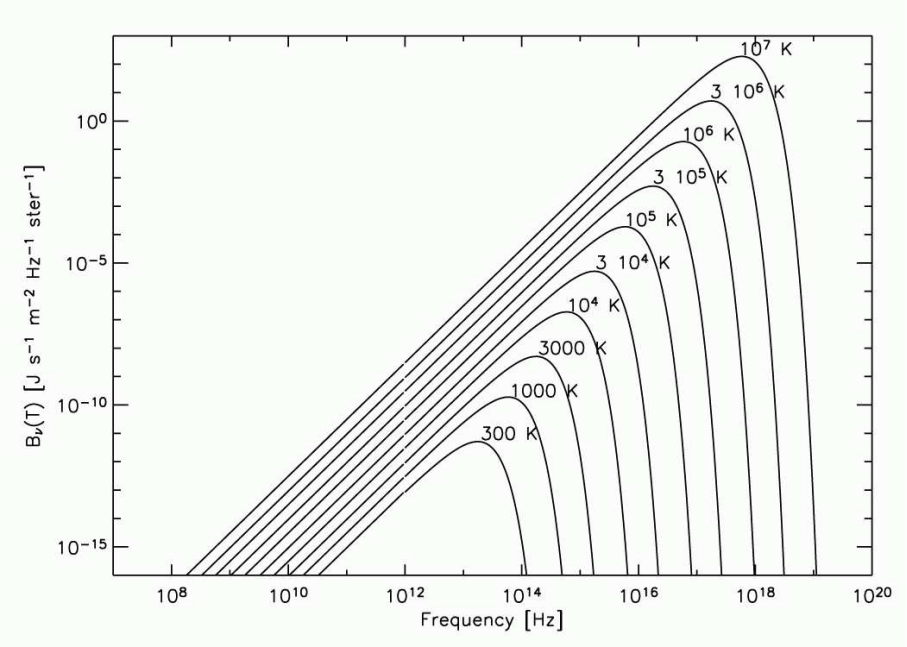

Fig. 9: *The black body spectrum versus wavelength for different temperatures. It is important to note that the spectrum only depends on the temperature alone. [Image taken from the www pages of the New Jersey Institute of Technology]*

decays by a non–radiative Auger–process where an electron is released. This process is called Excitation–Autoionization.

There is a caveat about the radiative recombination to state: The process itself clearly acts to remove energy from the plasma since the thermal electrons are captured. Therefore, it acts as a cooling mechanism. However, recombination removes the low–energy electrons from the plasma and so would increase the kinetic energy per remaining electron. This in turn appears as a heating mechanism. The effects on the thermal structure of the plasma are hence not straight forward. For further details of the radiative recombination see Jacobs et al. (1977).

3.2.2 Non–Thermal Radiation

Compared to the thermal radiative processes, the non–thermal radiation is not dependent on temperature as a characteristic parameter. As already mentioned above bremsstrahlung when generated in a solid body is on the step to a non–thermal process.

But even bremsstrahlung from a hot plasma can be non–thermal in the case that the gas is relativistic ($kT >> mc^2$). In the non–relativistic case the radiation is produced by electron–ion interactions while in the relativistic case electron–electron interactions become important (Alexanian, 1968).

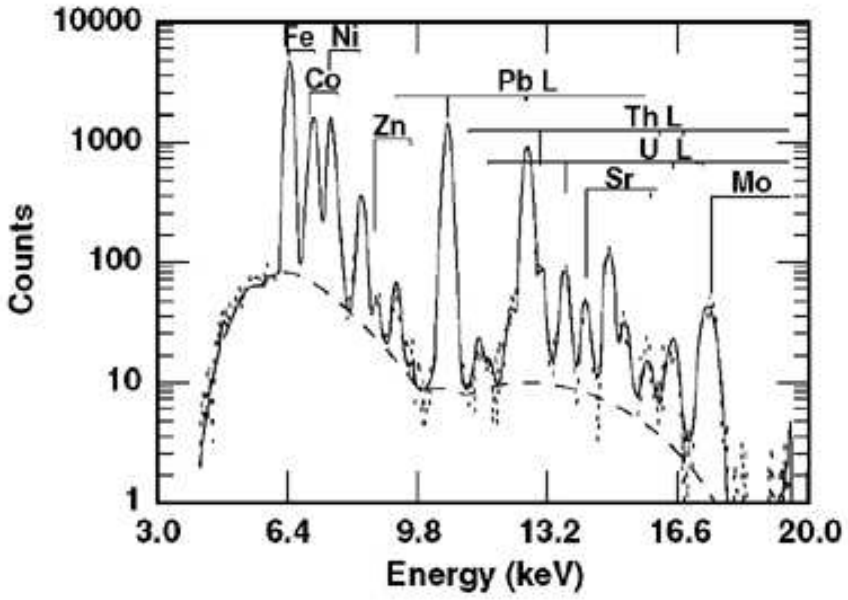

Fig. 10: *The X–ray spectrum consists of a continuous bremsstrahlung spectrum (dashed line) with a characteristic shape, cut–off energy and superimposed lines which originate basically from K–shell electrons. With increasing electron energy (i.e. increasing temperature in a plasma) the continuum moves to the right. [Image taken from the www pages of the Lawrence Livermore National Laboratory]*

When (relativistic) electrons move in a magnetic field they spiral around the magnetic field lines and therefore are accelerated. The resulting radiation is called "synchrotron radiation". The radiated intensity is proportional to the energy E of the electrons ($I \propto E^{-\gamma}$) where γ is the spectral index. The frequency of the photons is proportional to the magnetic field strength. Spectral profiles of synchrotron radiation can be described by a simple power–law.

The last major non–thermal process of X–ray generation is the so–called "inverse Compton scattering". Here, a low–energy photon gains energy from a scattering process with high–energy electrons. The low–energy photon may stem from the cosmic microwave background for example. The resulting spectral profile again can be described as a power–law like in the synchrotron case.

3.3 Cosmic X–ray Sources

After the short introduction to radiative processes some examples are given for individual sources. In practice the different processes are not isolated but occur often in combination.

- Supernova remnants:

  These high–energetic stellar events typically release energies of about 10^{51} erg. The expansion velocity of the stellar envelope is of the order $10000 - 15000\,\mathrm{km\,s^{-1}}$ and this heats the envelope as well as the surrounding medium to temperatures well above 10^6 K. The expansion of the supernova may sweep up the surrounding ISM and thus form a shell or bubble in the ISM. This is implied by the standard model which accounts for the swiss–cheese appearance of the neutral ISM of galaxies. Here, at least three processes take place: thermal emission from the hot gas of the expanding debris, synchrotron radiation from the relativistic electrons accelerated during the early stages of the supernova and also black body radiation from the remaining object (e.g. a neutron star with a surface temperature of $> 10^6$ K). The dominant process may change with the time evolution of the supernova.

- Stellar coronae:

  A star like our Sun has a surface temperature of ≈ 6000 K. This temperature is not sufficient to generate X–rays. But even the earliest observations disclosed the Sun as a bright X–ray source. Today, it appears to be clear that the X–rays originate from the corona, which is heated by magnetic recombinations of the solar or (more general) stellar magnetic field. The spectrum is dominated by hot plasma emission with superimposed lines.

- Early–type stars:

  O–stars are the most luminous ($L \approx 10^5 \times L_\odot$) and most massive stars ($M > 25\,M_\odot$) in the beginning. The typical surface temperature is of the order 40000 K and they radiate in the ultraviolet regime. However, a small fraction of the total luminosity is emitted in the soft X–ray regime. The underlying process is not well understood but it is thought that the star heatens its surroundings by hot stellar winds coupled with mass losses. Then the hot gas cools by emitting soft X–rays.

- Galactic emission:

  Apart from that galaxies are observed in X–ray due to their stellar content, they also show X–ray emission extending far beyond the stellar body. This so–called X–ray halo is hot gas ($\log(T[K]) = 6.2$ for the Milky Way) which is confined by the galactic potential and hence by the dark matter halo of the galaxy. The generation process for X–rays is nevertheless thermal bremsstrahlung and/or line emission. The emission spectrum of a hot plasma can be observed with X–ray telescopes. The data reduction provides several parameters of the X–ray emitting hot gas such as temperature and emission measure from which other parameters can be calculated such as electron density, pressure, mass, thermal energy and the cooling time. The most commonly used equations to derive these quantities are provided by e.g. Summers et al. (2004). The equations will be given in chapter 5 when the diffuse emission of dIrrs is analyzed.

- X–ray binaries:

  These objects are close binaries where the X–ray emitting object is a white dwarf, neutron star or a black hole. Both stellar components interact and exchange material. The classification turns out to be at least two fold, depending on the donator source. If it is a high–mass early–type star, the object is called high–mass X–ray binary (HMXB). More specific, the compact object is affected by a strong stellar wind provided by an early–type star. In the optical only the early–type star is visible. The driving energy for emitting X–rays is gravity and therefore the main process is bremsstrahlung. Compared to the HMXB the Low–mass X–ray binaries (LMXB) have an evolved late–type star which filles its Roche–lobe. Material is transferred via the inner Lagrangian point to the compact object. Roughly, the generation of X–rays is similar to the HMXB types. Figure 11 shows a rough sketch of the two types of X–ray binary systems. Due to the rotation of the compact object around the high–mass or low–mass star, the X–ray binaries show variable light curves. Partial, as well as total eclipses are recognized in the light curves. Hence, the systems must be close binaries. Since these object have accretion disks and also magnetic fields, the generation process for X–rays is highly complex. The physics of accretion disks is still a matter of debate. For example the accretion disk rotates very fast around the neutron star. If the rotational velocity is so high that the centrifugal forces exceed the gravitational drag towards the neutron star, the X–ray source turns off. The X–ray

luminosity at which this happens depends on the rotation period of the compact object; the faster it rotates the higher the luminosity. Also the accretion disk can obscure the compact object. The observer then only sees scattered X–rays from the extended corona around the disk. The impact region of the accreted stream onto the disk edge gives rise to modulation of the observed X–rays. Also the mass–losing star can eclipse the coronal region of the disk. Accretion of hydrogen onto the neutron star surface can lead to a hydrogen surface layer which produces helium by thermonuclear burning (see also the cataclysmic variable stars below). Eventually the helium reaches a critical point and it starts to fusing into carbon. This process is unstable which leads to a thermonuclear flash which is observable in the X–ray regime. Finally, the accretion might be stopped by the magnetic field of the neutron star. The magnetic barrier, however, will break down when enough material is accreted. The material can propagate towards the neutron star surface and the energy is released in an X–ray burst. The process starts again when the material has passed through the magnetic barrier. These object are called *Rapid burster*. For detailed information consult the works of Bondi & Hoyle (1944); Pringle & Rees (1972). LMXB and HMXB are not easy to distinguish in only X–ray observations although the luminosity is a first hint for the source. HMXB can reach higher luminosities because the stellar wind, which is virtual absent in the LMXB case, boosts the radiation of X–rays additionally. Having said this, it is always a good choice to have additional data in other wavelength than X–rays, to distinguish both binary systems. This distinction will be more clear when the dIrr galaxies will be discussed in Chapter 5.

- Cataclysmic variable stars:

  These kind of stars are also known as novae or dwarf novae indicating that they are significantly fainter than X–ray binaries although they are similar to each other. These objects show prominent outbursts due to thermonuclear burning on the surface of a white dwarf. The white dwarf itself is feeded by a companion which implies the system to be a binary one. Since the compact object is not a black hole or neutron star like in a LMXB the mass transfer is not so efficient. This leads to a shallow burning of the accreted material producing soft X–ray emission at the impact region on the white dwarf.

- Active galactic nuclei:

  AGN or quasars are located in the very center of galaxies. The term outlines a number of objects namely Seyfert galaxies (type I and II), BL Lac objects, blazars, quasi stellar objects and quasars. It turned out that these objects are just different appearances of the same object. All these objects are thought to have an accretion disk or torus around the “central machine”. The powering central source is a supermassive black hole. This unified model of AGN was an idea which was improved by Scheuer (1974); Antonucci & Miller (1985); Barthel

(1989) and many others. The different manifestations are due to the inclination angle under which the source is seen by an observer (Fig. 12), different accretion rates and also different magnetic fields of the AGN. Since they are all accreting sources the X–rays stem from the heated disk. However, the bremsstrahlung–spectrum is modificated in a complex way depending on the surroundings of the central black hole. A very detailed discussion can be found in Dopita (1997).

- Clusters of galaxies:

  Galaxy clusters are the most vast coherent structures in the universe known so far. The gravitational well created by this large amount of matter is often filled with hot gas at temperatures of tens of million of degrees. This optically thin plasma phase was discovert in 1971 by X–ray astronomers. The mass of this gas phase is at least equal to the mass of the "optical" matter. This implies an additionally hidden mass to confine the visible mass in the gravitational potential. X–ray observations of the diffuse gas component can help to shed light on the distribution of the "missing mass". Since the hot gas is a thermal plasma the spectrum again is a thermal bremsstrahlung–spectrum.

- Diffuse X–ray background:

  Besides the large variety of point sources and plasma agglomerations in space there exists a source radiating in the soft X–ray regime called the soft X–ray background (SXRB). The received opinion is that the SXRB is of cosmic origin since the observed emission is uniformly distributed on the whole sky. With very high exposure times it is possible to resolve this background into discreet sources, mainly AGN and quasars. Since the generation process is accretion the spectrum of the SXRB can be well approximated by a power–law with $\Gamma \approx 1.5$ (Hasinger et al., 2001).

The previous remarks show that three different kinds of sources can occur: thermal plasma sources, power–law sources and black body sources. But how can an observer decide which components are actually visible in the measured spectrum of an X–ray source? The answer to this question will be given in the next chapter where we discuss the data analysis of an XMM–Newton data set in detail.

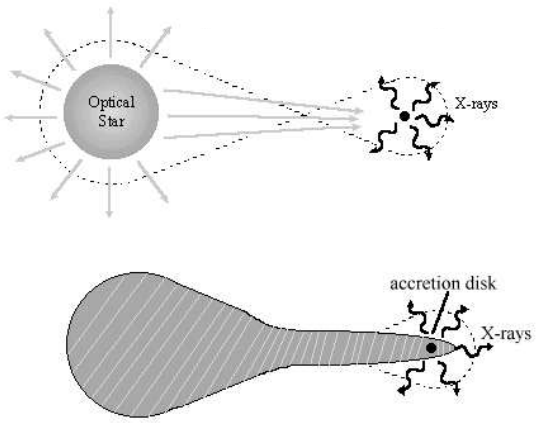

Fig. 11: *Two sketches of X–ray binaries. The* **upper** *shows the scenario for a HMXB where the donator star imposes a strong wind on the compact object. In the* **lower** *image the donator star has filled its Roche–lobe providing material to the compact object via the inner Lagrangian point. In both cases, charged particles are accelerated in the gravitational field and hence radiate X–rays. [Image taken from www pages of Cornell University]*

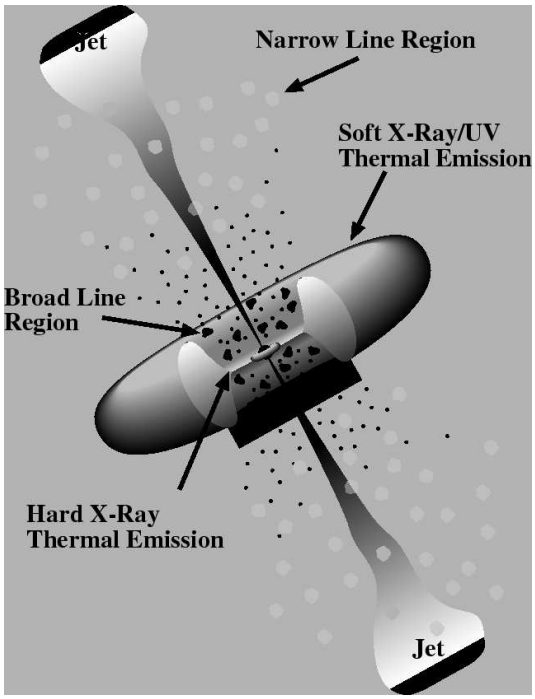

Fig. 12: *Schematic of the AGN unified theory. Depending on the inclination angle an AGN appears as different objects: The broad line region corresponds to Seyfert* I *galaxies, the narrow line region to Seyfert* II*. Looking right into the jet the object appears as a blazar. [Image taken from www pages of Department of Astronomy and Physics, Saint Mary's University]*

4 Data Analysis

In this chapter the standard data reduction and its caveats are discussed. Starting from the data obtained from the XMM–Newton Science Operations Center (SOC), the separate steps of data preparation and filtering are described. Although the SOC maintains a special purpose software package for the data analysis — the science analysis software (SAS in version 5.3.3) — one should consider additional software packages for critical steps in the reduction pipeline. The so–called FTOOLS provided by NASA HEASARC is an excellent package to create, examine, or modify the contents of FITS[7] files. Also MIRIAD and the KARMA–package are used to filter and display the data and images.

4.1 Data Products and Data Processing

Basically, the SOC offers two different data sets: the observational data file (ODF) and the pipeline products (PP). The former is the raw uncalibrated data while the latter is a preprocessed data set including calibrated photon event lists, source catalogs, and also images. For a rough overview over the data obtained, the PP data is useful whereas it is more convenient and also advisable to make use of the ODF data. For that purpose the SOC maintains a calibration data base which is updated continuously.

The raw EPIC ODF contain *event lists* for all CCD chips (frames) separately. These event lists are the central data sets which contain all the information of the detected X–ray photons that is the frame number, the X and Y pixel coordinates of the photons, and the photon energy measured in each pixel. These event lists are complemented by the so–called *auxiliary file* which provides information about the arrival time of a photon at a specific (X,Y) coordinate in a specific frame. In order to correct the raw data from the instrumental response one needs the calibration data files. These provide information about filter transmission curves, bad pixel location, detector efficiencies (vs. energy), matrices converting from CCD coordinates to sky coordinates, information about the PSF, conversion factors to calculate energy from the digitized signal, and house keeping parameters.

With the dedicated SAS tasks (`emchain` and `epchain`) the ODF data of the EPIC–MOS and EPIC–*pn* instruments is calibrated. Here, the single frames are combined to the full FOV of the instruments, the sky coordinates are computed from the calibration data base as well as the energy conversion in order to receive the “true” photon energy. Moreover, bad pixels are blanked.

To put this in a more formal way, the instrumental effects introduced by the telescope response are described by the following expression:

[7] Flexible Image Transport System

$$I(x,y,E) = R(x,y,E) \otimes O(x,y,E) \tag{1}$$

Here, I denotes the brightness distribution in the image while O describes the brightness distribution of the observed object. This then is folded by the instrumental response $R(x,y,E)$ which is:

$$R(x,y,E) = A_{\mathrm{eff}}(x,y,E) \cdot PSF(x,y,E) \cdot QE(E) \cdot FT(E) \cdot V(\theta(x,y),E) \tag{2}$$

The point spread function (PSF) and the effective area (A_{eff}) of the telescope which both depend on the position on the detector and the energy of the incident photon influence the image quality mainly. The quantum efficiency (QE), filter transmission (FT) and the vignetting (V) are also included in the instrumental response function R(x,y,E). Since the observer is also interested in the spectral properties of a source, there has to be a relation between the counts measured by the energy channels of the instrument and the actual spectrum. This relation is:

$$C(I) = \int_0^\infty S(E) \cdot RMF(C,E) \cdot \mathrm{d}E \tag{3}$$

where C are the measured counts, S is the source spectrum and RMF is the instrumental redistribution matrix including filter transmission, quantum efficiency, the PSF, and effective area influence as described in Eqn. 1 (Gondoin et al., 2000). It is to note, that the RMF does not exactly match the photon energies to the appropriate channel. This is due to the fact that the electrons read out by the CCD node loose some charge due to states in the lattice (called "traps") into which electrons can permeate from the conduction band. Therefore the detected energy becomes lower and also broader. This then produces a dependency in gain and energy resolution and differences in the quantum efficiency. All this depends on the photon input energy. This effect is known as charge transfer inefficiency (CTI) (Ferrando et al., 2003). For further details on the calibration I refer the reader to Lumb et al. (2002, 2003).

The raw data is also contaminated by instrumental backgrounds such as unrejected cosmic rays, fluorescence lines (mainly Al K @ 1.4 keV for EPIC–MOS and Cu K @ 8 keV for EPIC–*pn*) and electronic noise (see also Read & Ponman, 2003; Marty et al., 2003). Most of these effects (especially the electronic noise) are negligible since they occur below energies of 0.3 keV (which is the lowest energy used in the data analyzes) or they vanish within the broad energy bands used later.

After the calibration tasks have been run the user holds three calibrated event lists, one for each EPIC instrument. From now, the variety of data can be extracted from these event lists. As an example the spacial information of the event lists is displayed in

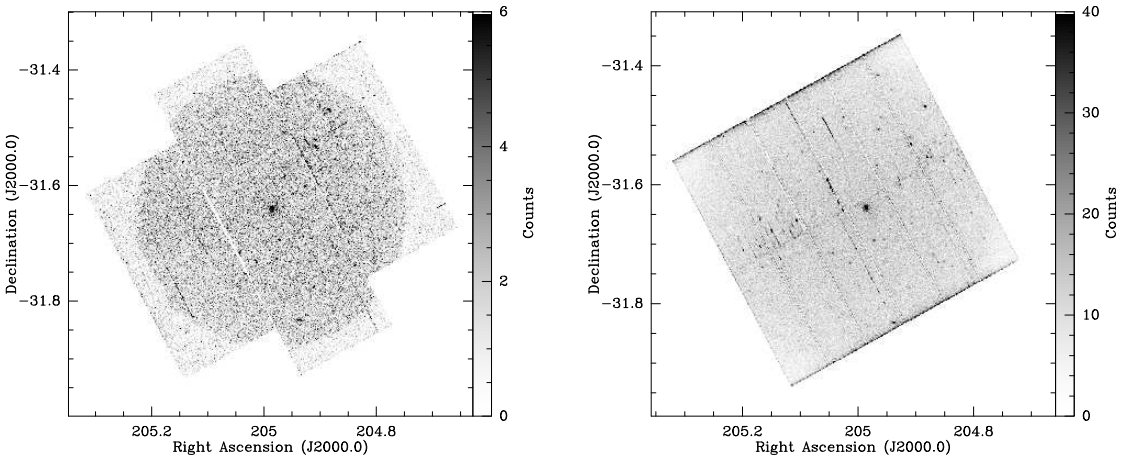

Fig. 13: *EPIC–MOS (***left***) and EPIC–*pn *(***right***) maps right after the calibration files were applied to the event lists. Especially the EPIC–MOS image shows the illuminated FOV and the surrounding detector area which is affected by the particle background. Since the event lists are raw data (no filtering was applied yet) the maps are noisy and show features which are not related to X–ray emission (e.g. the linear feature at* $\alpha = 205.^{\circ}15, \delta = -31.^{\circ}78$ *for the EPIC–MOS and the bright CCD edges in the EPIC–*pn*). The displayed energy band amounts to* $0.1 - 15.0$ *keV. Note that the EPIC–*pn *has a higher count rate due to the higher sensitivity as displayed in Fig. 7. The images show the NGC 5253 data set.*

Fig. 13. The maps show the observed photons in the full energy window provided by the XMM–Newton ranging from $0.1 - 15.0$ keV. These images are still "raw" images because they are still affected by unrelated emission and also vignetting, which is the gradual increase of noise towards the rim of the FOV. These issues will be discussed in the next sections.

4.2 Background Flares

From the event lists not only images can be extracted but also light curves. These can be splited in different energy bands[8]. Figure 14 shows the light curves for different energy bands as extracted from the EPIC–MOS1 event list encompassing the complete detector area. At first glance the light curves have different count rates for the different energy bands which reflects the spectral properties of the recorded counts. Even so, the counts do not only relate to X–ray emission but also to a flaring background which is specifically visible in the first quarter of the exposure time. After that the count rate drops to a more or less constant value which stays for the remaining observation time.

The origin of the flaring background is frequently addressed to solar activity. Depending on the spacecraft position in the highly excentrical orbit the flaring background

[8]The concept of X–ray photon energy bands will be discussed later.

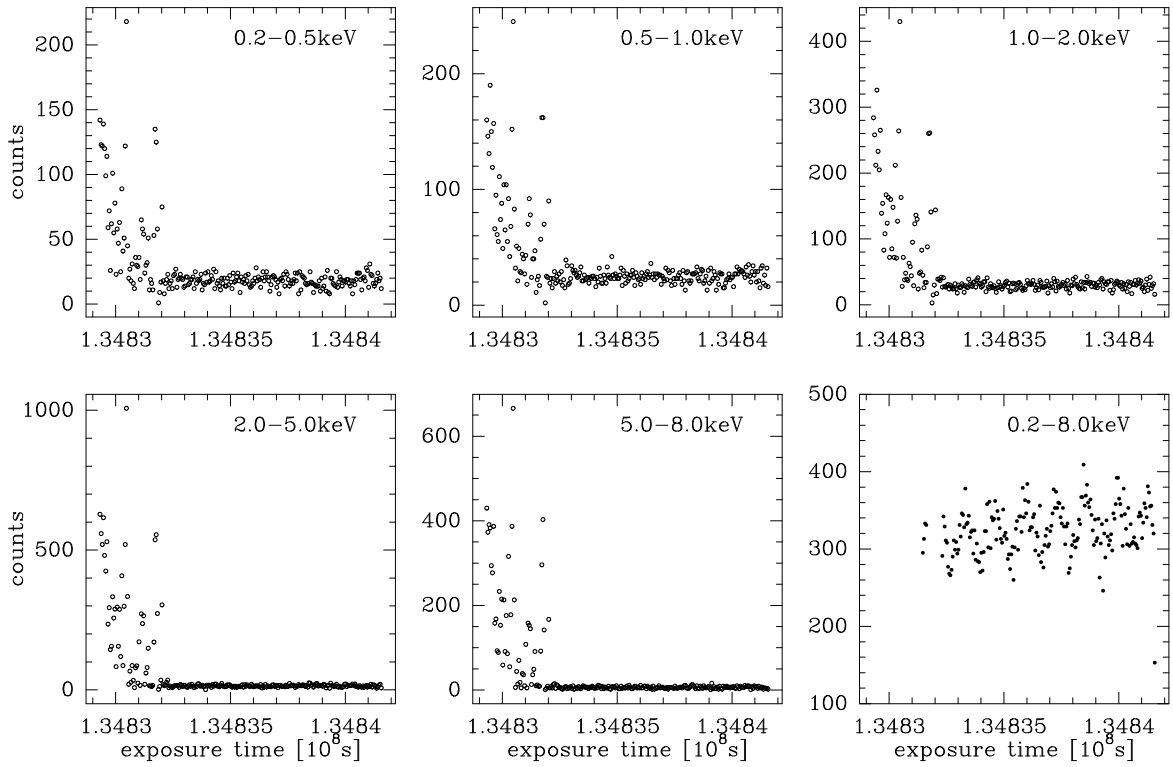

Fig. 14: *Light curves for different energy bands as denoted in each panel except the last panel which shows the filtered light curve for the full energy band. The peaks and spikes in the unfiltered light curve correspond to background flares which have to be rejected. The time bin size is 50 s. Data are taken from the observation shown in Fig.13.*

varies. When the spacecraft propagates through clouds of charged particles the flaring background is high as in the light curves shown. Unfortunately it is neither possible to predict the appearance of the flares nor the spectral shape can be determined. Therefore, the subtraction of a flare model is not feasible. On that account it is convenient to blank all counts which are above a certain threshold.

For that purpose, an iteratively acting algorithm for flare–filtering was implemented in the C programming language (Kernighan & Ritchie, 1988). Here, the idea is to estimate the mean count rate of the "real" X–ray emission and reject all excess events. In order to avoid any rejection of intrinsic intensity variation of bright point sources, the flare–filtering is evaluated only on CCDs which are free from bright sources. This procedure is valid since the particles are not vignetted (see Sec 4.3) and so only represent a constant off–set intensity across the FOV and hence all CCD chips. Certainly, the final filter is applied to all the data. Marty et al. (2003) gives an overview over the flare filters being used in the literature. However, none of this is designed to act automatically with reliable results in contrast to the filter presented here.

First of all, the mean μ_1 of the light curves in the specific energy band is calculated across the total exposure time available. After that, the user defines a σ-level above which the events are flagged at first (typically 1.5σ). The flagged events are excluded while the next new mean μ_2 is calculated. Here, $\mu_1 > \mu_2$ in all cases. The events exceeding the new adapted σ-level are flagged as well. The iteration stops when $\mu_1 - \mu_2 < \sqrt{\mu_2}$, i.e. the difference of two successive means is smaller than the statistical uncertainty of the data.

With the flagged and unflagged events the light curve is decomposed into good time intervals (GTI) and also bad time intervals (BTI). Since the light curves can be much more contaminated than the one in Fig. 14 it is of importance to keep as much of the data as possible. This can be achieved when the flagged events are reincluded if the flare duration is less than a certain time (default 5 minutes). On the other hand, unflagged events are flagged when the non-flare duration between two flares is shorter than a certain time (default 50 seconds).

Read & Ponman (2003) and also Lumb et al. (2002) suggested that the flares have hard spectra. However, from Fig.14 it is clear that the flares show up also in in the soft bands (see also the hardness ratios of the proton flares in Pradas, 2004). The filter procedure shown here filters all bands which is more reliable than the procedure used by others.

After the flares are flagged and rejected, new event lists are generated with the "real" events and for each energy band separately. The final filtered light curve for the whole energy band is displayed in the bottom right of Fig. 14. The residual oscillations of the light curve are due to a bright point source in the FOV. With the flare filtering the first obstacle in the data reduction has been smoothed out.

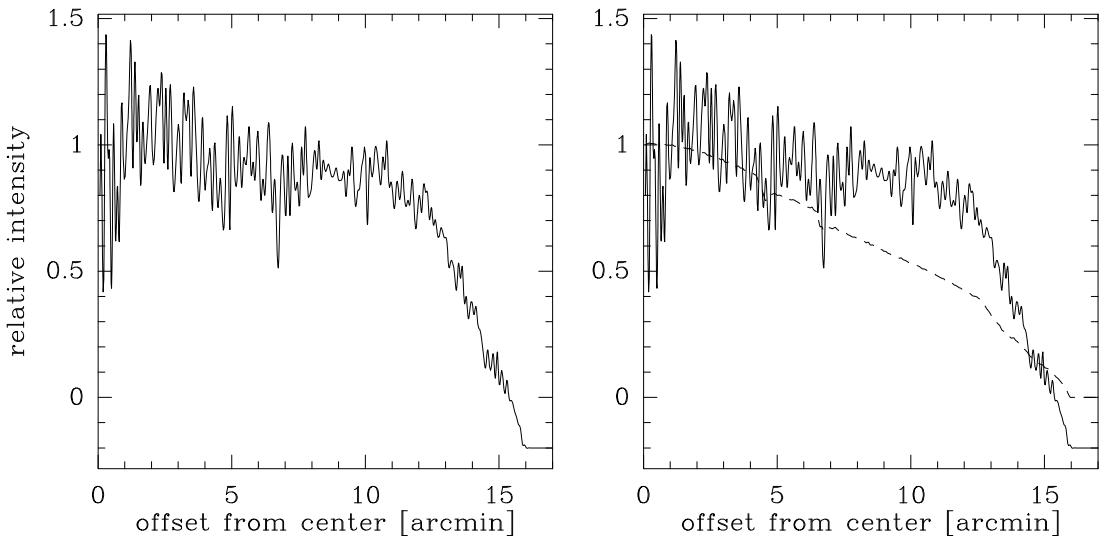

Fig. 15: **Left:** *The azimuthal integrated intensity versus radius from the Lockman hole data (EPIC–MOS) (Hasinger et al., 2001). The central intensity is normalized and the peaks correspond to point sources within the FOV. Towards the detector rim the intensity drops due to the increasing off–axis angle and hence, the sensitivity decreases. This vignetting effect has to be corrected.*
Right: *Here, the dashed line shows the radial profile of the SAS exposure map (see text) which ought to correct for the vignetting. However, the profile is inconsistent with the observational data. For off–axis angles exceeding* $5\farcm0$ *the exposure map overestimates the vignetting. The displayed energy range in both view graphs is 0.2-0.5 keV, the uncertainties in the data are less than 0.1.*

4.3 Vignetting

Having the flare–filtered event lists, a further important systematic effect has to be accounted for. As stated in Sec. 3.1.1 the effective area of the mirror assembly is changing with photon energy and off–axis angle. This leads to a gradual decrease of sensitivity towards the rim of the FOV. This behavior is demonstrated in the left panel of Fig. 15 which shows an azimuthal integrated radial plot of the EPIC–MOS1 camera observing the Lockman hole (Hasinger et al., 2001).

Normally, the dedicated software can correct the vignetting effect with a so–called *exposure map*. This is an image which compensates the intensity drop off. The correction (often referred to as "exposure correction") itself is just a simple division of the observed image by the exposure map yielding a count rate image. Of course, the exposure map has to be calculated for each energy band individually since the vignetting is energy dependent. Unfortunately, the exposure maps calculated by the SAS software are inconsistent with the observational data as displayed in the right panel of Fig. 15. For off–axis angles exceeding $\approx 5\farcm0$ the SAS–exposure map overestimates the vignetting which gets even worse towards higher off–axis angles. Since the SAS exposure map

Tab. 2: *Exposure times of the deep observations obtained for the calculation of exposure maps before and after flare filtering. All observations were performed with the Medium filter in PrimeFullWindow mode except the last (Thin1 filter).*

Observation	Total exposure [s]	Net exposure [s]
Lockman Hole	84019	46940
Lockman Hole	64819	51576
APM 08279+5255	102868	61670
Lockman Hole	49799	33090
LBQS 2212-1759	110018	91179

is unusable, new exposure maps matching the observations have to be generated. The tasks and details for the exposure map calculation are the same as for the "normal" data reduction which will be described later on. Therefore, a *brief* description of the method to obtain improved exposure maps follows.

4.3.1 Calculating Exposure Maps

From the observers point of view it is desired to derive exposure maps on the basis of the XMM–Newton in–flight performance. Therefore, deep observations from the XMM–Newton Science Archive were obtained (> 280 ks net exposure time, Tab. 2). Combining the deep field data is very sufficient to sample the full FOV and moreover it minimizes the spurious influence of point sources. In the following the data reduction steps which I use to correct for the vignetting are explained.

After the deep fields are calibrated, images for the various energy bands are calculated. Included in the SAS are tasks for point source detection which are applied to every single image. The point sources then are excluded from the images. This can be achieved with the dedicated SAS–task `esplinemap` which simply cuts out the point sources. The resulting image is called *cheese image* since it looks like a swiss cheese. Having this, the next step is to refill the holes with photon noise. This means that the hole area has to be filled randomly with artificial photon counts which meet the following constraints: I) the counts per pixel in the hole area has to be the same than the counts per pixel in the surrounding area, II) the density of the artificial counts has to be comparable to the surrounding as well. This avoids any discontinuities between the observed and the artificially added photons. Since the SAS provides no task for this procedure, the `dmfilth`–task of the software package *CIAO*[9] for the *CHANDRA* X–ray telescope is utilized. Choosing an appropriate background region the task

[9]Chandra Interactive Analysis of Observations

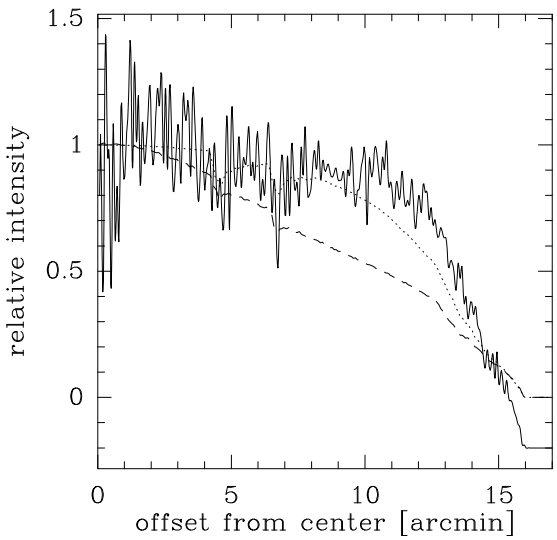

Fig. 16: *Final comparison of the SAS exposure map profile (dashed) with the improved exposure map (dotted) to the observation. The improvement is clearly visible to off–axis angles up to* 10.′0*. For angles exceeding* 10.′0 *the improved exposure map still underestimates the correction due to the polynomial fit. Hence, the noise will be increased when the observation is actually corrected. The displayed energy range is 0.2-0.5 keV, the uncertainties in the data are less than 0.1.*

interpolates the pixels with respect to the background and filles the holes. After that, the images are free from point sources and they still show the vignetting. Now all the images corresponding to the same energy band are added and smoothed. In fact the smoothed images are the desired exposure maps which can be enhanced in a last step. The azimuthal averaged profile of the exposure maps is fitted with a polynomial of degree three which is then converted into images again. These then are the final improved exposure maps. The flow chart of Fig. 17 shows this procedure in a more visual fashion. Note, that the fit causes deviations in the outer FOV due to the fixed polynomial degree. In particular, the deviation of the fit increases towards the outer boundaries of the fit interval. However, this deviation is not crucial since the galaxies observed are confined to the inner FOV and thus the deviation is not affecting the region of interest.

The improved exposure maps have pixel coordinates. If they are used to correct a specific observation they have to be converted to the corresponding sky coordinates. This can easily be done by multiplying the improved exposure map with the detector mask image which is generated during the data reduction as described in the next sections. Finally, I draw a comparison of the SAS exposure map and the improved one to the observational data. For that purpose the azimuthal averaged radial profile of all three maps are shown in Fig. 16. The improvement is clearly visible but it still is not perfect. For off–axis angles exceeding 10.′0 the correction is still not appropriate. The consequence is then that the noise is raised when the image is divided by the exposure

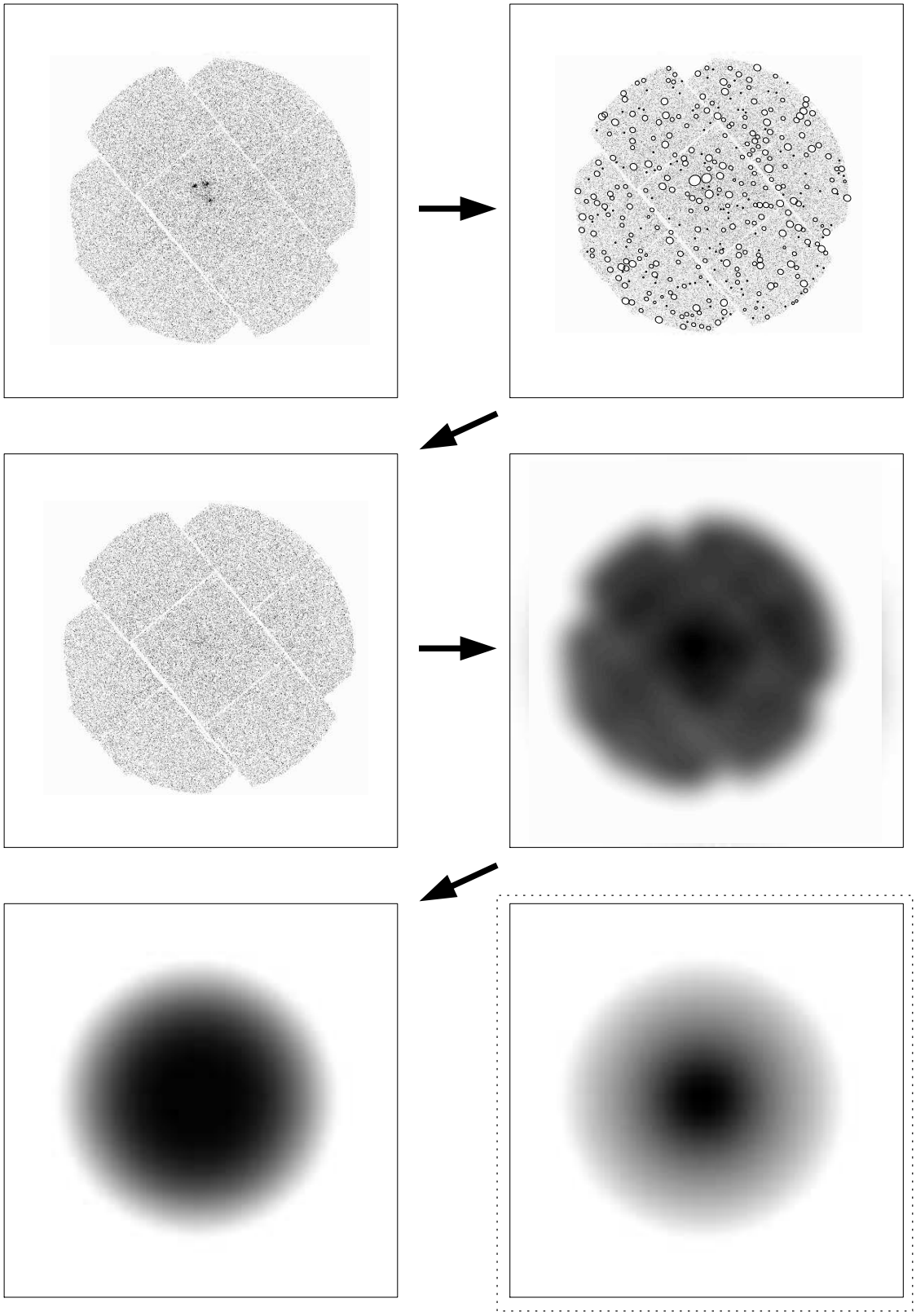

Fig. 17: *Following the arrows starting in the upper left corner: i) calibrated image, ii) cheese image (the circles mark the cheese holes), iii) filled hole image, iv) smoothed image, v) final exposure map. The dotted box displays the SAS exposure map.*

map. However, the galaxies discussed in this thesis do not extend into the edges of the FOV. Hence the deficiency in the outer FOV is negligible. It should be noted that the exposure map is assumed to be rotational symmetric for simplicity. Strictly this is not true. The CCDs number two and five show up with artificially higher count rates (up to a factor of two) in individual pointings. Fortunately this effect is not visible in the raw data of the pointings studied here. Moreover the angular extend of the galaxies of interest is smaller than the affected area in most cases. However one should keep this in mind when analyzing an XMM–Newton dataset. In the next section we will go further with the data reduction procedures.

4.4 Energy Bands and Hardness Ratios

Here, we tie up to Sec. 4.1 again. With the improved exposure maps every data set can be investigated now. After the calibration and flare filtering images for different energy bands are calculated. The energy bands are defined in Tab. 3. In X–ray astronomy the energy bands are not well defined as in the optical regime. Mostly they are defined with respect to the scientific goal. In this case the soft emission is of interest so the low energy end ($0.2-1.0\,\mathrm{keV}$) is splitted into two bands B2 and B3. Below this range the calibration works not well (due to the background effects described in Sec.4.1) and hence the energy regime below $0.2\,\mathrm{keV}$ is left out. This also applies to energies above $12\,\mathrm{keV}$. The PS band is used to detect point sources. This broad band gives a better signal–to–noise (S/N). From the optical it is well known to calculate colors of the sources in order to analyze their spectral types. A similar tool is known in X–ray astronomy. In contrast to the optical the intensities in the individual bands are not divided but the differences and totals of two bands are divided. In a formal way this looks:

$$\mathrm{HR1} = \frac{\mathrm{M}-\mathrm{S}}{\mathrm{M}+\mathrm{S}} \qquad\qquad \mathrm{HR2} = \frac{\mathrm{H}-\mathrm{M}}{\mathrm{H}+\mathrm{M}},$$

where HR denotes the two hardness ratios and S, M, and H are the soft, medium, and hard energy band respectively. Note that, depending on the spectral properties of the source considered the bands can be chosen accordingly. By definition the HR are between -1 and +1.

Having the HR of a real source it is useful to compare it to a model source. If the HR of both the model and the real source match within the uncertainties one can derive the physical properties of the real source from the model parameters. This can be done in the following fashion.

If we calculate a theoretical spectrum of an X–ray emitter and fold this spectrum with the telescope response (as depicted in Sec. 4.1, Eqn. 1 & 2) and calculate the counts in the individual bands, we can plot the theoretical HR for that source. Nowadays, several tools are available for calculating model spectra and count rates for several

Tab. 3: *X–ray band definitions and energy boundaries*

Band	E_{min} [keV]	E_{max} [keV]	Comment
PS	0.2	5.0	used for point source detection
B1	0.1	0.2	not calibrated
B2	0.2	0.5	
B3	0.5	1.0	
B4	1.0	2.0	
B5	2.0	5.0	
B6	5.0	8.0	
B7	8.0	12.0	not used
B8	12.0	15.0	not used

X–ray telescopes, e.g. the *sherpa* package coming with CIAO or the WWW pages of *WEBSpec*[10] and *PIMMS*[11].

Since the vast majority of X–ray sources are either power law sources or plasma sources it is useful to calculate the Hardness ratios for two model spectra with different parameters, i.e. different sources. For a real source there is one effect we have to account for, namely the photoelectric absorption of the X–rays. The absorbing material can be an intrinsic absorber (e.g. the accretion disk in an XRB) or the Galactic foreground which comes always into play. The photoelectric absorption of the interstellar medium (ISM) was studied by Morrison & McCammon (1983) and it is characterized by the cross section which is displayed in Fig. 18. The cross section is proportional to E^{-3} so that the soft photons are more diluted than the hard photons which leads to an apparent *hardening* of the spectrum. The physical process here is absorption of photons in the K– and L–shell of atoms or ions. At higher energies also Compton scattering and pair production can attenuate the X–ray photons, where the Compton effect is dominant in the $0.1 - 10\,\mathrm{MeV}$ regime and the pair production occurs around 1 MeV, the summed rest mass of an electron and a positron (511 keV each).

The main absorbers turns out to be hydrogen and helium. This absorption has to be accounted for when a model spectrum is calculated. Therefore, the packages provide an absorption model which can be applied to every plasma model or power law model. Here, the total absorption is traced by the HI column density. The plasma model has parameters temperature (T), metal abundance, and normalization which is the emission measure of the plasma. The power law model has parameters photon index and normalization. For the absorption only the absorbing column density of atomic hydrogen is a parameter. Equipped with these tools, we calculate the HR for an absorbed plasma

[10] http://heasarc.gsfc.nasa.gov/webspec/webspec.html
[11] http://cxc.harvard.edu/toolkit/pimms.jsp

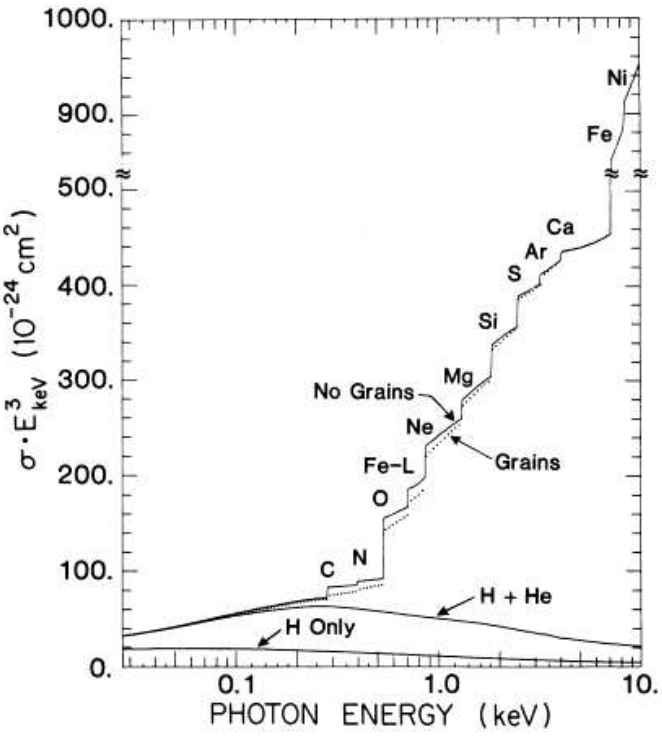

Fig. 18: *Photoelectric absorption cross section as a function of photon energy. The main absorption, especially in the soft energy regime below 1 keV, is dominated by the hydrogen content of the ISM. (Morrison & McCammon, 1983)*

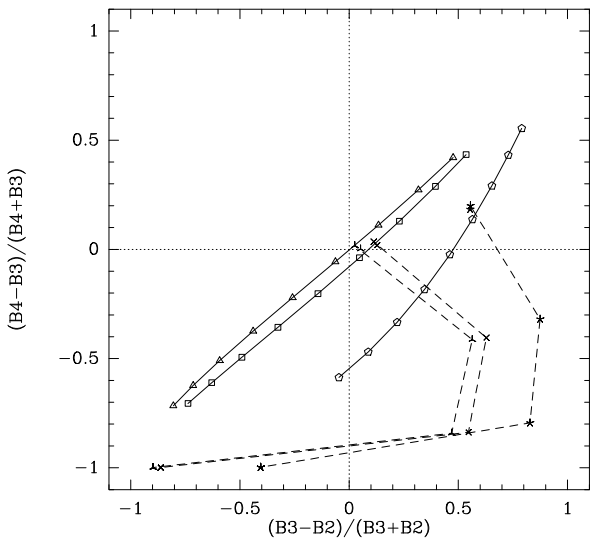

Fig. 19: *Calculated HR for different model spectra. The solid lines represent power law spectra while the dashed lines correspond to plasma emission sources. Both types of curves have increasing absorbing column densities from left to right (*1×10^{19} *cm*$^{-2}$, 1×10^{20} *cm*$^{-2}$, 1×10^{21} *cm*$^{-2}$*). For the power laws the photon index increases from top right (*$\gamma = 0$*) to bottom left (*$\gamma = 4$*) in steps of 0.5. The plasma spectra have increasing temperature from the bottom left (*$\log T\,[\mathrm{K}] = 5.0$*) to the right (*$\log T\,[\mathrm{K}] = 7.0$*) in steps of 0.5. Note the degeneracy of the HR in the fourth quadrant.*

of different temperatures ranging from $\log T\,[\mathrm{K}] = 5.0$ to 7.0 in steps of 0.5 and for an absorbed power law with photon indices ranging from 0 to 4 in steps of 0.5. Moreover, the absorbing column density has different values $1 \times 10^{19}\,\mathrm{cm}^{-2}$, $1 \times 10^{20}\,\mathrm{cm}^{-2}$, and $1 \times 10^{21}\,\mathrm{cm}^{-2}$ which leads to three curves for the plasmas and for the power laws each. The result is shown in Fig. 19.

The shape of the curves depends severely on the telescope response, e.g. using a thicker filter damps the number of soft photons and hence the spectrum appears to be harder. This causes the curves in Fig.19 to be shifted to the right. However, there is still an ambiguity: the high temperature plasma sources ($\log T > 6.0$) can still be confused with the highly absorbed power law sources. This ambiguity is not easy to resolve since the HR are often used when the source has too few photons to extract a highly significant spectrum. However, the concept of energy bands which leads to the HR is a very powerful tool to disclose the physical nature of a source even when its intensity is very low.

In the chapter about the galaxy sample the reader will see that the energy band definitions given in Tab.3 minimize the overlap of plasma models and power–law models in contrast to the band definitions given in the literature. In this sense the energy bands defined here provide a better classification of the point sources found.

4.5 Source Detection and Source Free Images

Now having the calibrated event lists and the different images for the individual energy bands it is advisable to search for point sources in the observed sky region. This is done for each camera and each energy band separately with the SAS task `eboxdetect`. Here, the exposure map and the detector mask (which is simply an image with value 1 at the pixels which work and otherwise zero) are needed for the input parameter for `eboxdetect`. The detector mask can be calculated with the task `emask`. With this mask and with the exposure map the sliding box algorithm of `eboxdetect` generates a source list which holds the position of the found point sources in pixel coordinates for each camera.

However, this holds true only for the calculation of exposure maps in the automatic pipeline. To identify the "real" (i.e. 4-σ) sources within an observation it is advisable to smooth a 0.2-5.0 keV image with a 2d-Gauss function with a FWHM of half of the PSF. This energy interval encompasses the energies predominantly produced by the bulk of all X–ray point sources. After setting the lower image cut value to 4-σ above the background the sources can be identified by eye. The `Karma`–package provides the function to get the source position and hence a source list.

The source list, is the input parameter for the calculation of cheese images which are already displayed in Fig. 17 in the upper right corner. These cheese images are needed when the diffuse emission is in the scope of the observation performed. Replacing the bright point sources with the appropriate (integrated intensity and surface brightness) photon noise can disclose the faint extended emission if present. Of course, this depends on the net exposure time and so on the detection limit which can be achieved.

Cheese images are calculated with the task `esplinemap`. Here, a two dimensional spline is fitted to the background including the sensitivity provided by the exposure map. This leads to the desired cheese images for each energy band and camera.

As with the calculation of the exposure maps, the cheese images of the real observation, too, has to be filled with photon noise. The source detection provides a list of source coordinates and also with the cut–out radii of the sources. Unfortunately, the radii calculated by SAS are wrong, namely too small. This shortcoming was solved with the development of a small C–routine which takes the cheese image and the coordinate list as input parameters and calculates the radii of the holes. The radii of the holes typically range between 2 and 20 pixels, whereas the hole radii calculated by SAS are typically between 4 and 6 pixels.

The routine selects all photons in a circle at the source positions within an initial radius of 1 pixel. For each selected region the statistic is evaluated, i.e. the number of encircled photons. If this is zero, the radius is increased by one pixel until the statistic is different from zero, i.e. the inner rim of the hole has been reached. This iterative approach is confident since it is performed on the cheese images themselves. With the

coordinates and cut–out radii of the sources the cheese holes can be refilled with the CIAO–task `dmfilth`. The outcome are the desired source free images. The coordinates and cut–out radii can be utilized to calculate source mask images with which in turn the images containing the point sources can be multiplied. This is useful to obtain images with the point sources only which makes it easy to derive the counts of an individual source.

4.6 Spectral Extraction

The EPIC–MOS and EPIC–*pn* instruments not just have imaging capabilities but also spectral resolution ($E/\Delta E \approx 50$ at 6.5 keV). This feature makes it possible to extract an X–ray spectrum out of the event list. Here, the number of counts per PI channel is extracted. But since the number of counts depends on the position on the chip (vignetting) and moreover depends on the filter transmission, the quantum efficiency and the size and shape of the PSF, these counts have to be corrected, i.e. calibrated. Therefore, the so called *redistribution matrix file* (RMF) and *ancillary region file* (ARF) have to be calculated using the SAS software. These files contain information about the interrelation of PI channels and photon energy in physical units as well as the effective area in the chosen energy range and chip position. The RMF gives the probability in which PI channel a photon with an specific energy is found. The formal context here is given by Eqn. 3.

Spectral extraction can be performed within the SAS package. After the filtered event list is loaded one can select the region from which the spectrum should be taken. Since the selected region does not only contain photons from the source but also photons from unrelated emission one must also select a source free region in the vicinity of the source of interest. This source free region serves as the background field. Since the difference of two Poisson distributions (the source and background spectrum are in fact Poisson distributed) is not a Poisson distribution, it is recommended to model the background and not subtracting it from the source spectrum! Both fields, the source and the background, are converted into FITS files holding the spectral information, i.e. intensity versus energy. After that the RMF and ARF are calculated using the dedicated SAS tasks `rmfgen` and `arfgen`. Now the user holds four files, the source spectrum, the background spectrum and the RMF and ARF files. These can be combined or grouped with the FTOOLS package. The task `grppha` puts these files into a single file and lets the user define the binning of the energy channels in order to achieve a significant signal–to–noise per energy bin. It is also possible to have an adaptive binning where `grppha` chooses the bin size in a way that each bin contains at least a certain number of photons.

In order to analyze the measured spectrum one needs model spectra to compare with. For this purpose *sherpa* (Freeman et al., 2001) provides a vast number of models for emission and absorption related to an atomic database. These individual models have

to be combined to a source–model. For example, the spectrum of an accreting source may be described by a power–law component. But since the emitted photons of the real source are diluted by the Galactic foreground one has to introduce a photoelectric absorption term to the source–model. In this special case the source model can be defined in *sherpa* as:

$$\text{source} = \text{absorption} \cdot \text{powerlaw} \tag{4}$$

If the source contains also an additional plasma component the source–model has to be expanded to:

$$\text{source} = \text{absorption} \cdot (\text{powerlaw} + \text{plasma}) \tag{5}$$

With this the source–model setup can be adjusted to the real source. However, the setup is based on an "educated guess" about the source physical nature. This guess consists of the parameters of the source components. For example the absorption component has only one parameter, i.e. the absorbing column density in units of $10^{22}\,\mathrm{cm}^{-2}$.

After having a physically meaningful source–model it is fitted to the observed spectrum by adjusting the parameters of each source–model term, which is automatically done by *sherpa*. Again the user can specify which parameters are fixed or thawed, i.e. free. Moreover the value range of thawed parameters can be adjusted.

4.6.1 Statistics

In general the fitting procedure itself is done by *sherpa* whereas the fitting method is set by the user. The different fitting methods decompose into two different types: single–shot and scatter–shot techniques. The former start from a guessed set of parameters and then try to improve the parameters in a continuous fashion, the latter try to look at parameters over the entire permitted range to see if there are better minima than near the starting guessed set of parameters. The single–shot techniques are much faster with respect to calculation time while the scatter–shot techniques can locate a decent minimum over the entire parameter range. It is advisable to use both techniques on the same dataset and also run the fit procedure more than once to see whether the minima found are stable.

In X–ray astronomy the number of photons per energy bin is quite low, necessitating the use of Poisson statistics which is defined as:

$$p(D_i|M_i) = \frac{M_i^{D_i}}{D_i!} \cdot e^{-M_i} \tag{6}$$

This is the probability to find D_i photons in bin i if the photons are independently measured at a constant rate M_i. In Poisson statistics the uncertainty σ_i of the data is just the square root of the number D_i of photons. For data exceeding 5 photons per bin one can also apply the Gaussian statistics defined as:

$$p(D_i|M_i) = \frac{1}{\sigma_i\sqrt{2\pi}} \cdot e^{-\frac{(D_i-M_i)^2}{2\sigma_i^2}} \tag{7}$$

Finding the appropriate model for the observed spectrum is equivalent to find the maximum likelihood of the Poisson distributed data which is defined as:

$$\mathscr{L} = \prod_i \mathscr{L} = \prod_i p(D_i|M_i) \tag{8}$$

This can be simplified when maximizing the logarithm of the likelihood $\mathscr{L}$ since the Stirling approximation can be applied ($\log n! \simeq n\log n - n$) and therefore the factorials are eliminated. However, the maximum likelihood method provides no goodness–of–fit which is needed to evaluate the model. Therefore, it is common to use the Gaussian statistics which provide a goodness–of–fit method by evaluating the χ^2 statistics which is defined as:

$$\chi^2 \equiv \sum_i \frac{(D_i - M_i)^2}{\sigma_i^2} \tag{9}$$

where D_i is the source data in bin i, M_i is the model data in bin i and σ_i corresponds to the estimated error of the i^{th} datum. The χ^2 approach is in general only valid for Gaussian distributions (i.e. $D_i > 5$ for all i) but *sherpa*s Chi–Gehrels statistics is designed for low–count data which makes it suitable for X–ray spectra (Freeman et al., 2001). The goodness–of–fit indicator commonly used is the reduced χ^2 which is $\chi^2_{red} = \chi^2_{obs}/P$ where P is the number of degrees of freedom. A good fit is characterized by $\chi^2_{red} \simeq 1$.

However, the reduced χ^2 can be lower than one. Then the fit is "too good" which means that there are more free parameters than independent data points. Thus, the fit has to be optimized so that the reduced χ^2 is close to one. For the case that this is achieved the statistical conclusion is only that this fit is a possible model, but it is not *the* model. Imagine that the fit is based on a physical model of the source of interest.

5 The Dwarf Galaxy Sample

5.1 Results

With the basic data reduction steps explained in the previous chapter, I will now discuss the sample of dwarf irregular galaxies. Here, the first three galaxies are treated in more detail to see the data reduction in a more practical way. The remaining five galaxies are discussed a little more briefly but they are treated with the same attention.

The selection criteria for the galaxy sample of the thesis at hand are a) the angular size must match the XMM–Newton field–of–view (30.′0), b) high resolution HI data is available, c) a low attenuating Galactic HI column density along the line of sight (as derived from the Leiden/Dwingeloo survey by Hartmann & Burton, 1997), d) the data is free accessible via the archives. In total eight dIrrs are in the sample, star burst as well as non–star burst dIrrs, which decompose into two subsamples: According to their HI masses the low–mass sample contains Holmberg I, Sextans A, NGC 1569, NGC 4449 and NGC 5253 (58-300$\times 10^6\,M_\odot$), while the high–mass sample consists of Holmberg II, IC 2574 and NGC 4214 (550-640$\times 10^6\,M_\odot$). The total mass of a galaxy, of course, is a better parameter when the issues of galactic winds or outflows are of interest. However, X–ray point sources will be searched in the HI distribution of a galaxy. Hence, the HI masses here are a more natural parameter. The main features of all these and their basic properties as they appear in the literature are given as well as a short table of key data for each dwarf galaxy.

The first XMM–Newton observations of dwarf galaxies as proposed by Walter & Kerp (2002) consists of the three galaxies Holmberg I, IC 2574 and Sextans A. The observational key data (for all galaxies analyzed in the thesis at hand) is given in Tab.4. All of them were observed in the PrimeFullWindow mode which provides the largest field of view. This is desired for the following reason. Many authors report on outflows of hot X–ray emitting gas (in some cases together with Hα) in galaxies (see e.g. Bregman et al., 1995; Strickland et al., 1997; Shopbell & Bland-Hawthorn, 1998; Strickland et al., 2002) ranging out to a few kpc. For example, an X–ray outflow of 10 kpc size in a distance of 3 Mpc appears as a $\approx$10 arcmin feature in the XMM–Newton FOV, which is 1/3 of the total FOV. Hence, the PrimeFullWindow mode is sufficient for the analysis performed.

5.1.1 Holmberg I

The well know group of galaxies in the so–called M 81–M 82 galaxy group is the most nearby condensation in the local supercluster. The group consists of M 81, a massive spiral, M 82, an irregular star burst galaxy, and also smaller objects like NGC 3077 and NGC 2976. Holmberg I and II are irregular dwarf galaxies within that group.

Tab. 4: *Observational key data of the dIrr sample. Total exposure time, Net exposure time per camera, Filter, Science mode (PrimeFullWindow)*

Observation	Total [s]	MOS1 [s]	MOS2 [s]	PN [s]	Filter	Mode
Holmberg I	26612	17000	19980	17592	THIN1	PFW
IC 2574	21617	19160	17681	14179	MEDIUM	PFW
Sextans A	24623	10198	9788	6097	MEDIUM	PFW
Holmberg II	12640	9568	9600	5198	THIN1	PFW
NGC 1569	18204	15296	15200	12160	MEDIUM	PFW
NGC 4214	20272	13568	12840	13888	MEDIUM	PFW
NGC 4449	15870	13376	14272	11584	THIN1	PFW
NGC 5253	47037	34720	36672	28736	THIN1	PFW

Tab. 5: *Holmberg I*

Morphological type	dIrr	
Position (J2000.0)	$\alpha = 09^{h}40^{m}30\overset{s}{.}61$ $\delta = 71^{d}11^{m}5\overset{s}{.}59$	
Distance	3.8 Mpc	(Karachentsev et al., 2002)
HI mass (10^6 $M_\odot$)	110	(Ott et al., 2001)

Holmberg I is a metal poor ([Fe/H] ≈ -2.0 dex) dIrr with a quiet phase of current star formation showing a prominent hole in its HI distribution in the very center. This hole or shell is assigned to past stellar activity. Ott et al. (2001) present evidence for a blow–out of material due to stellar winds and supernova explosions providing an energy input of about 2.0×10^{53} erg. This is equivalent to roughly 200 Type II supernovae in a stellar cluster. The SFR, calculated from B–band luminosity of the galaxy, is $0.65\,M_\odot\,yr^{-1}$.

Very recent, Vorobyov et al. (2004) investigated the creation of the center giant shell by numerical hydrodynamical modeling of supernova–driven shell formation. From the surface density contrast they can derive the total mass of face–on dIrrs and reproduce the morphology of Holmberg I. The mechanical input for creating the hole is about 3.0×10^{53} erg which corresponds to ≈300 Type II supernovae. Some basic parameters of Holmberg I are given in Tab.5.

After XMM–Newton data calibration, the flare filters are applied to the light curves and a filtered event list is computed for the three imaging instruments separately. The event lists are calculated in a very conservative way setting `FLAG==0 && PATTERN==0`. This setting ensures that no pile–up is present in the point sources which would intro-

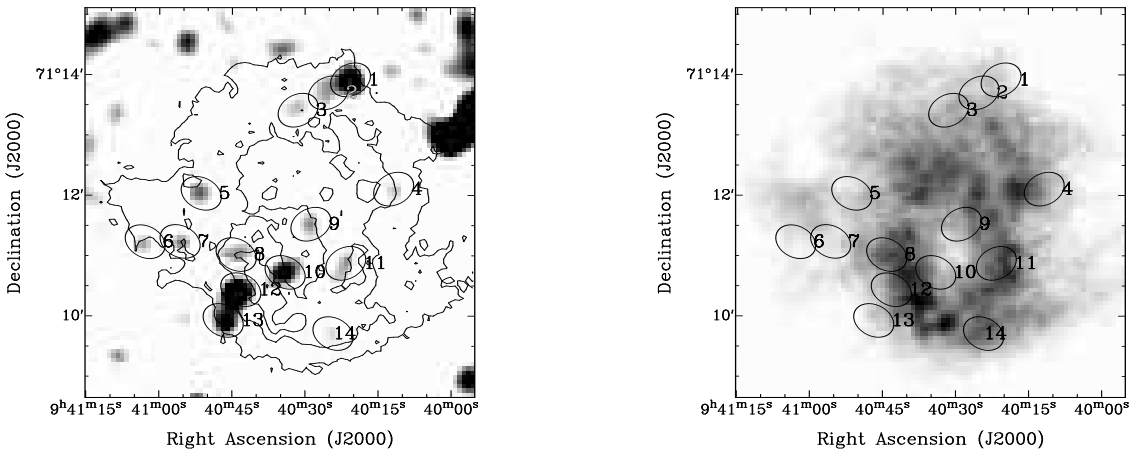

Fig. 20: **Left**:*Smoothed image of the combined EPIC–MOS1 and 2 Holmberg I maps in the PS band. The contours show the* HI *distribution (starting at 10% of the peak intensity growing in steps of 30%) shown in grey scale on the* **right** *(peak 0.3 Jy/Beam). Circles indicate the point sources which are above the 4-σ limit of the background. Numbers correspond to Tab.6.* HI *map published by Ott et al. (2001)*

duce wrong fluxes and luminosities. It is to note, that the point source detection, in contrast to the exposure map calculation, is done by eye throughout all observations since this procedure is very reliable even for the faintest point sources.

5.1.1.1 X–ray point sources In more detail, for finding the point sources I use the combined EPIC–MOS1 and 2 (M1M2) images in the 0.2-5.0keV energy range (PS band). This broad band provides an improved signal–to–noise (S/N) ratio in contrast to the narrower bands defined in Tab.3, which is increased further by using two cameras. Of course, the EPIC–*pn* camera is more sensitive (roughly the sensitivity of both EPIC–MOS cameras together) since it is not blocked by the RGS but due to the numerous gaps between the CCDs the use of the M1M2 maps is more reliable in the sense that less point sources are affected by the EPIC–*pn* gaps. The Combined M1M2 data has only very few gaps left since both instruments are rotated by 90^{o} relative to each other. The S/N can further be increased using a 2D–Gaussian to smooth the image. The FWHM of the Gaussian (2 pixels) is half of the telescopes PSF so that the low intensity sources are not smeared out too much. The averaged background level in the smoothed M1M2 image outside the HI distribution is $6.4\pm1.6\,\mathrm{cts\,pixel}^{-1}$. The numbers are not integers due to the Gaussian filter. In Fig.20 the smoothed map of the M1M2 images is displayed. A source is detected if its intensity exceeds the 4-σ threshold above the noise of the background.

Only point sources within the HI distribution, given by the outer contour in Fig.20, are considered. The point source examination reveals 14 point source above the 4-

σ threshold. Now having the coordinates of the point sources, two different count rates are calculated: a) the source counts in the broad 0.2-5.0 keV band for deriving the flux of the individual source and b) the source counts in B2, B3 and B4 band to calculate the hardness ratios (HR) of the sources. All counts are now extracted from the photon image of the EPIC–*pn* camera which is in general more sensitive (by a factor of 2) than the EPIC–MOS cameras. The counts are extracted within a circle with diameter 3.5×PSF. This ensures that statistically 99% of the source counts are included in the analysis. Since these counts are still enhanced by the background of the SXRB and also instrumental backgrounds, a source free background region outside the HI distribution of Holmberg I has to be investigated. These counts are then subtracted from the individual source regions for the fluxes as well as for the HR, giving the excess photons of the sources.

Note, that the sources are identified in the M1M2 data, but the counts are derived from the EPIC–*pn* data. Thus, a source can be absent in the EPIC–*pn* data after background subtraction. Nevertheless, the source is included in the source list, although it might give zero fluxes for the source in the EPIC–*pn* data.

The flux of each source can be calculated with the *PIMMS* package available at the CHANDRA WWW pages. This converts the excess count rates ($\mathrm{cts\,s^{-1}}$) to flux units ($\mathrm{erg\,cm^{-2}\,s^{-1}}$). For this aim, one has to provide information about the observational setup, namely the camera and filter used, the input energy band (0.2-5.0 keV), the output energy band (0.2-8.0 keV) and also the source model for which the flux should be calculated. In this case a power–law model is assumed with a photon index of $\Gamma \simeq 1.5$. The value for Γ here is adopted from the SXRB studies by Hasinger et al. (2001) which is a reasonable value. A better value can be obtained from the HR diagram. However, the uncertainties in the HR diagram are up to 50% in some cases (depending on the source counts in each band). Hence, the uncertainty in the flux calculation is good within a factor of 1.5. Here, the unabsorbed flux is calculated assuming a Galactic foreground absorption of $2.5 \times 10^{20}\,\mathrm{cm^{-2}}$ taken from the Effelsberg 100 m single dish data. For the luminosities one has to provide a distance to the galaxy. Here, the distance given in Tab.5 is assumed. The complete source list is displayed in Tab.6.

After background subtraction some of the sources show none or negative counts in the B2, B3, B4 energy bands although they are classified as detected in the PS band. This is because the S/N in the B2–B4 bands is not as good as in the broad source detection band which is also a combination of two cameras. These sources are marked with a star in Tab.6. Hence, they are excluded from the HR diagram.

In this regard, the lower flux limits for point sources in the individual bands can be estimated as follows. The count rate in a background region ($\gg$1000 pixels) is normalized to 3.5 × PSF[12]. The uncertainty of the background is the square root of the counts

[12]This is the diameter of the PSF times 3.5 which gives the normalization area. This ensures that 90% of the source photons are detected.

Tab. 6: *The XMM–Newton X–ray point sources found in Holmberg I. The flux units are 10^{-15} erg cm^{-2} s^{-1} in the PS band, the luminosity units are 10^{37} erg s^{-1}, the luminosity uncertainty is of the order of the relative flux uncertainty. The stars mark sources with zero or less counts in one band after background subtraction. The last three columns give the background corrected counts in the corresponding band.*

ID	Right Ascension (J2000.0)	Declination (J2000.0)	Flux	Luminosity	B2	B3	B4
1*	$09^h40^m20\overset{s}{.}71$	$71^o\ 13'\ 55\overset{''}{.}25$	2.45 ± 0.65	0.42	1	6	0
2	$09^h40^m25\overset{s}{.}21$	$71^o\ 13'\ 42\overset{''}{.}20$	4.02 ± 0.84	0.69	3	11	3
3*	$09^h40^m31\overset{s}{.}52$	$71^o\ 13'\ 24\overset{''}{.}78$	1.57 ± 0.52	0.27	7	-1	-2
4	$09^h40^m11\overset{s}{.}71$	$71^o\ 12'\ 06\overset{''}{.}48$	2.62 ± 0.68	0.45	4	3	3
5	$09^h40^m51\overset{s}{.}31$	$71^o\ 12'\ 02\overset{''}{.}00$	2.80 ± 0.70	0.48	4	4	2
6*	$09^h41^m02\overset{s}{.}98$	$71^o\ 11'\ 14\overset{''}{.}01$	0.52 ± 0.30	0.09	0	0	-2
7	$09^h40^m55\overset{s}{.}78$	$71^o\ 11'\ 14\overset{''}{.}10$	3.32 ± 0.76	0.57	7	6	1
8*	$09^h40^m44\overset{s}{.}09$	$71^o\ 11'\ 01\overset{''}{.}16$	1.92 ± 0.58	0.33	3	2	0
9*	$09^h40^m28\overset{s}{.}80$	$71^o\ 11'\ 31\overset{''}{.}69$	4.54 ± 0.89	0.78	13	10	0
10	$09^h40^m34\overset{s}{.}19$	$71^o\ 10'\ 43\overset{''}{.}82$	10.48 ± 1.35	1.81	14	25	11
11	$09^h40^m21\overset{s}{.}61$	$71^o\ 10'\ 52\overset{''}{.}55$	3.67 ± 0.80	0.63	12	8	1
12	$09^h40^m43\overset{s}{.}18$	$71^o\ 10'\ 26\overset{''}{.}37$	9.78 ± 1.31	1.68	6	16	20
13*	$09^h40^m46\overset{s}{.}76$	$71^o\ 09'\ 55\overset{''}{.}89$	2.10 ± 0.61	0.36	-3	6	4
14	$09^h40^m24\overset{s}{.}30$	$71^o\ 09'\ 42\overset{''}{.}95$	4.19 ± 0.86	0.72	9	7	1

Tab. 7: *Holmberg I flux limits for individual XMM–Newton bands. The flux units are* 10^{-15} *erg cm*$^{-2}$ *s*$^{-1}$

Band	background counts	flux limit
B2	5±0.5	0.57±0.06
B3	4±0.3	0.29±0.02
B4	4±0.3	0.41±0.03
PS	15±1.4	2.77±0.26

found in the large background region, which is then also normalized to the 3.5×PSF area. A source then is significant when the total counts of a source (including the background) is above the background itself. This is true for all sources found. Hence, the background corrected fluxes in Tab.6 represent the excess fluxes of the sources. The flux limits for point sources are given in Tab.7. The flux limits for all dIrr observations are derived in the same fashion as explained here using large background regions. In the case of CHANDRA observations the number of pixels in the background field are even larger (>60000 pixels) since the higher angular resolution require smaller pixel sizes.

As every observation in the X–ray regime is contaminated by the overall X–ray background (XRB) radiation one has to disentangle the point sources found in a galaxy from the extra galactic contribution. The XRB consists of superposed individual objects such as AGN and quasi–stellar objects (Hasinger et al., 2001). Unfortunately the XMM–Newton does not allow one to resolve faint sources because the telescope is confusion limited due to the angular resolution of the mirrors. The overall spectrum of the superposed XRB sources can be described by a power–law with $I(E) \propto E^{-\Gamma}$ with $\Gamma \approx 1.5$ (see also Gendreau et al., 1995). The number of XRB sources at a certain flux level is given by the log(N)–log(S) relation in Hasinger et al. (2001) which is based on the XMM–Newton observation of the Lockman hole (Lockman et al., 1985). To demonstrate that the point sources found in Holmberg I are not dominated by XRB sources, the log(N)–log(S) relation for the Holmberg I data is shown in Fig.21.

Furthermore, the X–ray colors, i.e. the hardness ratios(HR), are studied to find out whether or not XRB sources are detected. Sources unrelated to the galaxy (cosmic background sources) are strongly absorbed by the total gas content, preferentially by the HI, of the galaxy. Hence, they will appear as hard X–ray sources in the B3 and B4 bands, because the photoelectric absorption cross section $\sigma \propto E^{-3}$. For that aim, the HR of all sources with non–negative and non–zero counts in any band are plotted in Fig.22, together with the theoretical curves for thermal plasma and power–law sources.

The distribution of the X–ray point sources in the HR diagram in general shows that the sources are roughly of the same kind. There is considerable scatter which may

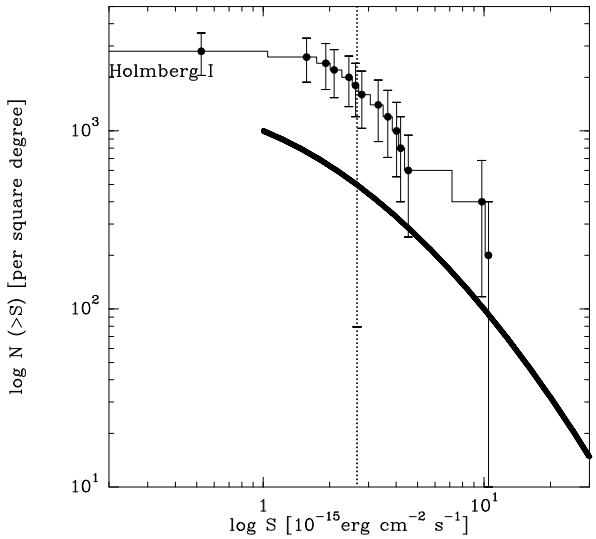

Fig. 21: *The cumulative log(N)–log(S) relation for Holmberg I (XMM–Newton data) scaled to the area of 1 square degree in order to compare to the data obtained from the XMM–Newton Lockman hole observation by Hasinger et al. (2001) (thick line). The Holmberg I data is well above the XRB data and hence the contamination with XRB sources is negligible. The dotted vertical line corresponds to the flux limit in the PS band. Note, that the XRB data corresponds to a foreground absorption given by the column density of the Lockman hole, which is the lowest column density region on the sky. Thus, the thick line is an upper limit.*

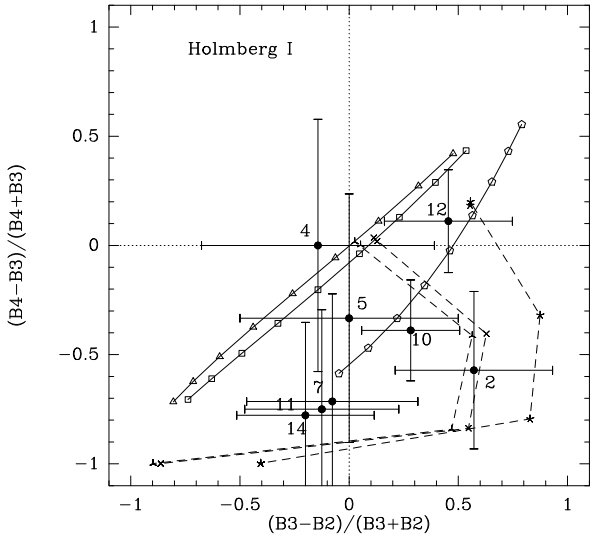

Fig. 22: *XMM–Newton HR for the point sources found in Holmberg I. The numbers correspond to the IDs of Tab.6. All errorbars correspond to an uncertainty of 1-σ. The dashed and solid lines are described in detail in the caption of Fig.19 and the accompanying text.*

reflect the few photons detected in each source. Source ID 2 whose errorbars are not in the power–law regime compared to the underlying model curves may be the only outlier. This source is most likely a plasma source with an absorbing column density of at least $1 \times 10^{20}\,\mathrm{cm}^{-2}$ according to its position in the HR diagram. But since the Galactic foreground is 2.5 times higher it is more likely to be $\approx 1 \times 10^{21}\,\mathrm{cm}^{-2}$ which is consistent within the 1-σ errorbars. All other sources are most likely power–law sources which argues for the classification of X–ray binaries, some of them (IDs 7, 11, 14) with very steep photon indices. This argues for relatively soft sources and indeed they do not have high count rates above 1.0 keV. Source ID 12 is the hardest source found. Its photon index ranges between $\Gamma \approx 1.5$–2.0. The flux is estimated to $9.78 \pm 1.31 \times 10^{-15}\,\mathrm{erg\,cm^{-2}\,s^{-1}}$ according to a luminosity of $1.68 \times 10^{37}\,\mathrm{erg\,s^{-1}}$ (assuming a distance of 3.5 Mpc). The luminosity is comparable to X–ray binaries which typically range between $L_X(0.1-2.4\,\mathrm{keV}) \approx 10^{36}-10^{37}\,\mathrm{erg\,s^{-1}}$.

To disentangle the nature of the sources, a search for optical counterparts is feasible because the optical monitor (OM) of the XMM–Newton was used during the observation. This small telescope operates in the UV regime with a band pass of 160-600 nm. According to the XMM–Newton handbook this detects mostly B0 and A0 stars which radiate in the UV at high temperatures. Therefore, their lifetime is short and so the OM traces young stars probably in star forming regions.

In Fig.23 the point source locations are shown as circles on top of the OM image. The contours resemble the HI distribution. At the high UV emission also the highest HI column densities are present. Moreover, Ott et al. (2001) find that the bulk of the Hα emission is located right at the location in the southeast where the UV is found. These regions are very close to the location of the brightest X–ray point sources found by XMM–Newton (except source ID 1 which is at the opposite side of the galaxy). The fainter sources appear to be more uniformly spread across the galaxy. This is also true for the old red stars as pointed out by Ott et al. (2001). Here, we have a first hint for the distribution of X–ray point sources.

The peculiar source ID 12, which is the second brightest, shows hardly UV emission. Also a SIMBAD[13] database lookup gave no hint to any counterparts in other wavelength. Since it is located at the outer rim of the large central HI shell where the column density is moderate, it may be an XRB source because the log(N)-log(S) relation only tells statistically that the data is not contaminated. However, since the source is the second brightest in the galaxy I assume it to be a HMXB (according to its luminosity). These (especially when they are isolated) do not have to show up in the OM.

Source ID 2 is very close to source ID 1 in the smoothed M1M2 image. The angular offset from peak to peak is only $28\farcs0$ (about twice the PSF). Both have no OM counterparts and also SIMBAD gave no results in other wavelength. Here, it may be

[13] http://simbad.u-strasbg.fr/Simbad

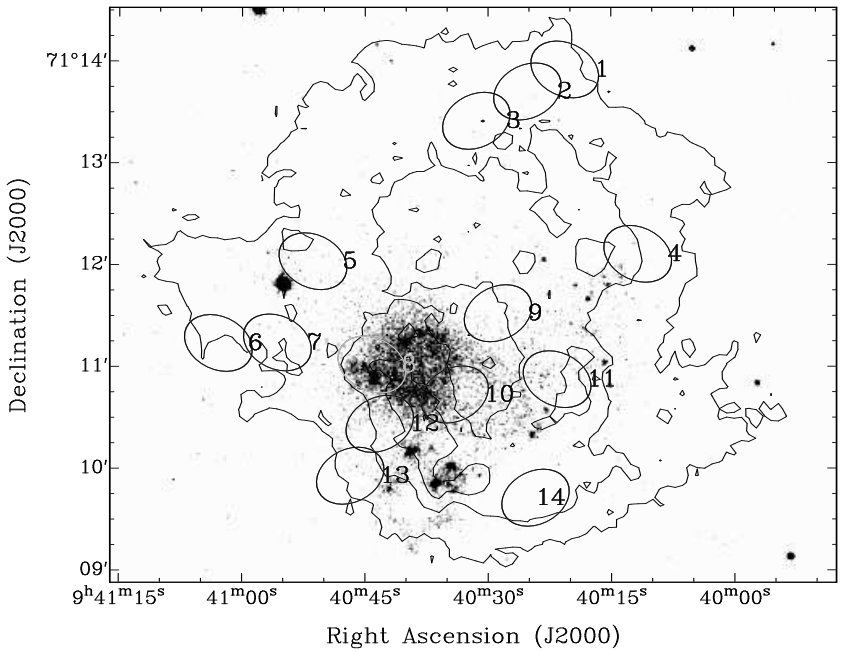

Fig. 23: *The OM map of Holmberg I with* HI *contours and the source positions. In the south-east prominent UV emission is clearly visible. This is associated with the brightest X–ray point sources found in the galaxy.*

possible that both sources are in fact one single extended source. But, as pointed out before, ID 2 is likely a plasma source while ID 1 has significant counts only in the B3 band. In addition their fluxes differ by a factor of 1.6. Within the flux uncertainties they differ by $0.08 \times 10^{-15}\,\mathrm{erg\,cm^{-2}\,s^{-1}}$. Within $2-\sigma$ uncertainties they are equal but still the difference in the individual bands is present. In the Hα data published by Ott et al. (2001) one can spot a little emission feature which spatially agrees with the position of ID 2. Also the HI shows a shell–like structure at this position. This argues for ID 2 to be a supernova remnant but the luminosity, according to Tab.6 is far below the value given by Fabbiano (1996). So far, the nature of ID 1 and 2 remains unclear.

Sources ID 8 and ID 10 have optical counterparts. ID 8 is clearly seen in th OM while ID 10 is not, but both show up in the DSS2[14] red and DSS2 blue images provided by the Catalogs and Surveys Branch of the Space Telescope Science Institute. As well as for the X–ray sources a 4-σ clip level is applied to the DSS2 images. ID 10 shows the highest luminosity of all Holmberg I X–ray sources and from the HR diagram it is characterized as a power–law source with index ≈ 3 and an absorbing column density of at least $1 \times 10^{21}\,\mathrm{cm^{-2}}$. This, again, speaks for an X–ray binary, maybe even a HMXB. Source ID 8 is also an peculiar source since the counts in the B2 and B3 band are quite low and B4 has no counts at all, but it is associated with the UV and DSS2 sources. The luminosity is in the range of X–ray binaries so likely it is one.

[14]Digitized Sky Survey

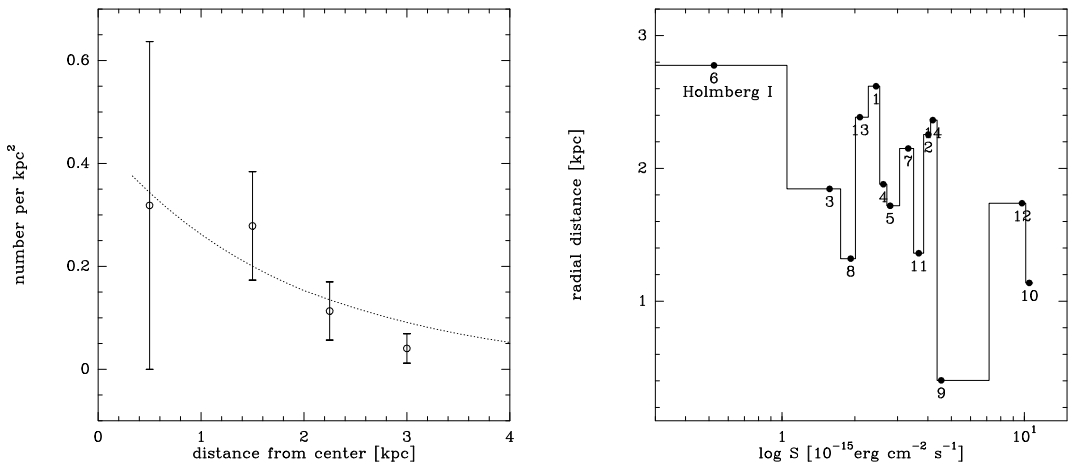

Fig. 24: **Left**: *The radial number density distribution of XMM–Newton point sources declines with increasing radius, with the morphological center taken as the origin. The dotted line is an exponential fit to the data. The bin size is 1 kpc.* **Right**: *Radial distances as a function of XMM–Newton source flux with the morphological center as the origin. Although the significance is not very high due to the low number of point sources, a general trend becomes apparent: the luminous sources tend to show up at smaller radii than the fainter ones. Numbers correspond to the source IDs.*

All remaining sources (ID 3,6,9,13) do not show up in the HR diagram. Sources ID 3 shows up in the DSS2 blue and DSS2 red. All others do not have any counterparts in the optical but from their luminosities and/or hardness ratios, it is concluded that they may be isolated X–ray binaries as well as ID 3.

According to the standard model of the HI shells found in dIrrs it is expected to find X–ray emission within the shells. Comparing the point source positions with the HI data shows that none of the X–ray sources is located in HI shells, except source ID 2 which is also associated with Hα emission. Only the OM shows emission in the HI shell in the south of the galaxy located at α=09$^{\rm h}$40$^{\rm m}$35$\overset{\rm s}{.}$09, δ=71$^{\rm o}$ 10$'$ 0$\overset{''}{.}$33 (J2000.0) with a linear size of 0.5 kpc. The column density at this position is $N_{\rm Hi} = 6 \times 10^{20}\,{\rm cm}^{-2}$. Quoting Ott et al. (2001) the number of SNe explosions, based on the energetic input of 1.7×10^{51} erg, can not be higher than two. As pointed out by Kerp et al. (2002) the soft X–ray emission of SNe is absorbed in situ by the shell when the HI column density exceeds a value of $N_{\rm Hi} = 5 \times 10^{20}\,{\rm cm}^{-2}$. This may be the cause why X–ray emission is not detected in this particular shell.

As seen from the previous investigation, the point sources represent a heterogeneous mixture of different types. In this case the sources are most likely X–ray binaries which trace the old stellar population and therefore the evolution of the stars as a whole. To study the properties of the X–ray source population, their spatial distribution is regarded.

In Fig.24 the radial distribution of the found sources is shown. Having the morpho-

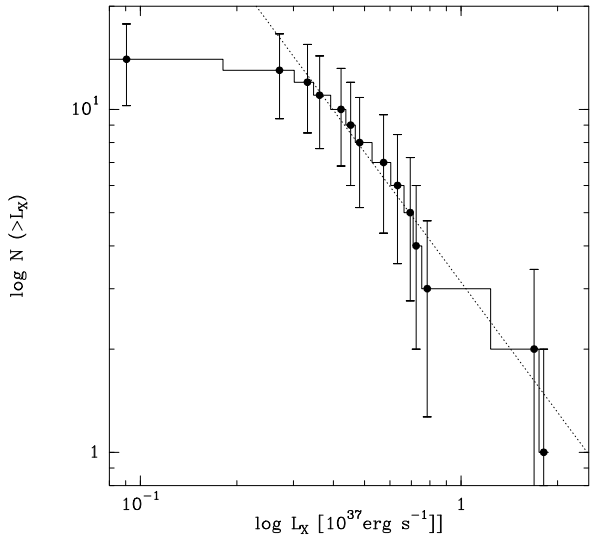

Fig. 25: *XLF of Holmberg I (XMM–Newton data). The dotted line is a fitted power–law with index* -1.06 ± 0.10. *Within the uncertainties the XLF appears to be unbroken, implying that no intense star burst occurred in the galaxy. Incompleteness due to the detection limit occurs at* 0.25×10^{37} *erg* s^{-1}.

logical center as the reference point the number density of the sources decreases with increasing radius. This is also seen by Ott et al. (2001) for the optical stellar surface brightness distribution. Also the reported change in slope of the surface brightness distribution with respect to the morphological center is suspected in the number density distribution. The radius at which the slope changes in both distributions is about 1.2 kpc. Of course, the errorbar for the point below 1 kpc is too large to constrain this reliably. An exponential fit to the data gives an characteristic radius of $r_o = 1.9 \pm 0.8$ kpc. The radial distribution can be constrained more, when regarding the fluxes of the sources.

The radial distance as a function of flux is displayed in the same view graph on the right hand side. Here, a general trend may become apparent, that the luminous sources tend to show up at smaller radii than the fainter ones. The lifetime of X–ray binaries depends on the companion star. For HMXB the companion has a lifetime of 10^6-10^7 yr. In contrast LMXB have longer lifetimes and thus they remain active longer but at lower luminosities (Wu, 2001). Here, the bright sources may still be associated with the young star forming regions whereas the faint sources dispersed through the galaxy and hence reflect the overall star formation history. Moreover, the bright sources exceeding a flux of 5×10^{-15} erg cm^{-2} s^{-1} are located at a radius of roughly 1.4 kpc. This is of the same order as the radius where the slope changes for the surface brightness distribution reported by Ott et al. (2001). Although the uncertainties are high, the coincidence is surprising.

Migrating from fluxes to luminosities one can study the X–ray luminosity function

(XLF). This provides a tool to investigate the star formation history. If the star formation was continuous and uniform then the XLF should appear unbroken whereas a star burst would form new HMXB and hence the XLF will show a break in its slope. In general, spiral galaxies, for example, show a steeper slope than ellipticals. In Fig.25 the XLF for Holmberg I is given. Within the uncertainties the XLF appears to be unbroken when a power–law is fitted to the data. The power–law index is -1.06 ± 0.10. Deviations from the power–law only show up at the very low luminosity end ($\approx 0.25 \times 10^{37}\,\mathrm{erg\,s^{-1}}$) which has to be attributed to the detection limit for the faint sources. The derived slope is comparable to galaxies like NGC 1291 or NGC 3184 which themself are spirals. This issue will be discussed later again, when data from a more extended sample will be studied in order to increase the significance.

So far, only the point sources were regarded. Since the XMM–Newton has a large collecting area and sensitivity it is suspected to detect very low intensity diffuse emission as well. This issue will be discussed in the following paragraph.

5.1.1.2 Diffuse soft X–ray emission To reveal diffuse soft X–ray emission a different approach is needed in contrast to the point source analysis. First of all, the point sources have to be removed from the photon images to make sure that only the extended emission is detected. This is done by cutting holes at the positions of the point sources with radii corresponding to the $3.5\times$PSF area. The resulting images are frequently referred to as *cheese images* (see Fig.17). To avoid any discontinuities at the edges of the cutted point sources the holes must be refilled. The commonly used approach here is to fill the holes with artificial photons. This is constrained by two means: a) the surface density of the artificial data must resemble the surface density of the surroundings of the holes and b) the counts per pixel of the artificial data must meet the ones of the surroundings as well. With that, the discontinuities can be minimized. To do so, the CIAO package provides a task (`dmfilth`) which filles all holes with the desired artificial data resembled from a source free background region.

The relevant energy regime needed for this analysis is below 1.0 keV. This follows from previous X–ray missions which did not report on any diffuse hot gas exceeding a temperature of 10^7 K which corresponds to a photon energy of about 1 keV. Therefore, the bands B2 and B3 are used to investigate the diffuse soft emission and the photon maps of these bands are treated as described.

Equipped with the point source subtracted, refilled images in B2 and B3 the search for diffuse soft X–ray emission can be performed. Since the images consist of a low number of individual photons (as compared to radio, IR or optical images with a vast number of photons per pixel) scattered across the FOV it is nearly impossible to identify extended emission in the photon maps. A very powerful tool to visualize extended emission anyway is the so–called *adaptive smoothing*. Here, the idea is to convolve the photon image with an automatically adjusted kernel size until a certain S/N is achieved.

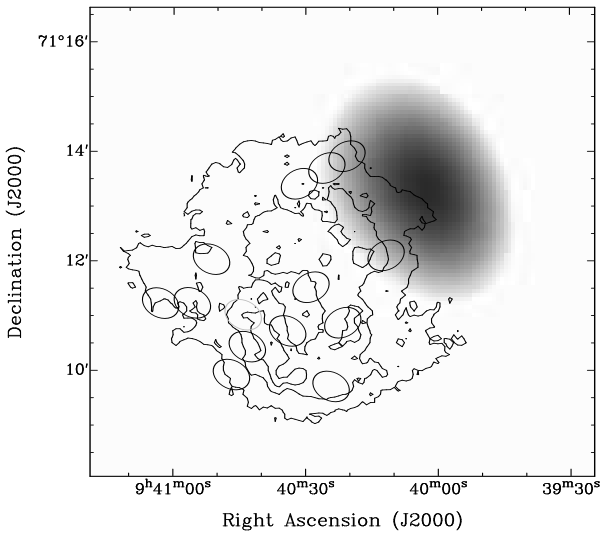

Fig. 26: *Adaptively smoothed image of the 0.2-1.0 keV EPIC–*pn *map. Point sources were subtracted and detector gaps are filled. The emission is clearly off-set from the central shell by* ≈ 3.5 *arcmin.*

The resulting image shows the emission with more or less uniform significance as defined by the minimum S/N. Pixels in the photon image which already are above the S/N are not smoothed and hence point sources are preserved. Since the photon images are vignetted they have to be corrected with the new enhanced exposure maps as described in Sec.4.3. Because of the variety of the smoothing kernels faint X–ray emission might become detectable even in the vicinity of individual bright X–ray sources.

Caution is advised with adaptively smoothed images. Since the flux is redistributed across the image, it should only be used for a qualitative impression of the emission only. For quantitative studies the corrected photon images need to be used. Furthermore, tests with the adaptive smoothing algorithm (in particular the `asmooth` task provided by CIAO) showed, that the variability of the kernel sizes can produce positional off–sets of the diffuse emission in question. This off–set can be about 1 arcmin in extreme cases.

After the point sources are subtracted the holes and also the gaps between the detector CCDs are filled. The exposure map correction is applied to the combined B2 and B3 band image of the EPIC–*pn* image and then adaptively smoothed with a minimal S/N of 4. Any residual point source contributions are identified and also cleaned from the photon image and then again adaptively smoothed until no point sources show up. The resulting image is then clipped to 4-σ above the background. In Fig.26 the 0.2-1.0 keV image of the EPIC–*pn* camera is displayed.

Diffuse soft X–ray emission is detected and completely located inside the central 10 arcmin of the FOV where the exposure map correction works very well (cf. Fig. 16). To independently test the reality of the diffuse X–ray emission, the number of

counts within the 4-σ limit are integrated and the intensity difference to a background field (i.e. the excess emission) in the processed photon images is calculated. In the B2–band there is an X–ray excess of $(6.1 \pm 0.7) \times 10^{-4}\,\mathrm{cts\,s^{-1}\,arcmin^{-2}}$ and in the B3–band $(2.2 \pm 0.2) \times 10^{-4}\,\mathrm{cts\,s^{-1}\,arcmin^{-2}}$. The higher energy bands do not show up with excess X–ray emission. Since the emission feature seen in the adaptively smoothed image is confirmed by the excess counts in the B2 and B3 band, more details can probably be obtained by considering the spectral information provided by the EPIC–*pn* data.

The spectrum is extracted from the EPIC–*pn* event list considering the 4-σ contour of the diffuse emission feature and excluding all point sources. In order to find the best–fit model different channel binnings are assumed and also different reasonable source models are fitted to them. In particular, the following emission terms and source models are evaluated:

The individual terms in the models denote:

AG: Galactic foreground absorption (*fixed parameter*: column density $N_{\mathrm{Hi}}^{\mathrm{Gal.}} = 2.5 \times 10^{20}\,\mathrm{cm^{-2}}$)

MP: MEKAL–plasma, accounting for the diffuse emission component (*fixed parameter*: abundance 0.2 solar, *free parameters*: temperature [keV], thermal normalization, which is the emission measure (EM) in units [$\mathrm{pc\,cm^6}$])

AI: intrinsic absorption, accounting for any absorption related to Holmberg I (*fixed parameter*: column density $N_{\mathrm{Hi}}^{\mathrm{int.}} = 0.5 \times 10^{21}\,\mathrm{cm^{-2}}$, mean value of Holmberg I taken from Ott et al. (2001))

PL: power–law, accounting for any residual point source backgrounds (*fixed parameter*: photon index $\Gamma = 1.5$, (Hasinger et al., 2001))

- **Model M1**: source = $AG \cdot (MP + (AI \cdot PL))$

  This approach is based on the idea that all emitters (MP, PL) are attenuated by the Galactic foreground (AG). In addition any residual point sources are attenuated by parts of the ISM (AI) of Holmberg I and/or intrinsic absorption in the possible point source population. The values are given above.

- **Model M2**: source = $AG \cdot (MP + PL)$

  Here, any residual point sources are assumed to be situated in front of the ISM or slightly immerged in the galaxy. However, M1 should yield better results since the spectrum is not background subtracted due to the statistical implications of Poisson distributed data (see Sec.4.6.1).

- **Model M3**: source = $AG \cdot MP$

Tab. 8: *Different spectral model fits for different binning of the data. The uncertainties in all values are of the order 10% as calculated by* COVAR *of the sherpa package.*

Binning	Model	MP kT [keV]	MP EM [10^{-3} pc cm^{-6}]	PL Γ	AI $N_{\rm Hi}^{\rm int.}$ [10^{21}cm^{-2}]	red.χ^2
G25	M1	0.05	3.46	1.5	0.5	3.34
G5	M1	0.04	17.14	1.5	0.5	0.83
C20	M1	0.07	1.28	1.5	0.5	1.39
G25	M2	0.04	7.80	1.5	—	3.10
G5	M2	0.03	17.14	1.5	—	0.81
C20	M2	0.06	2.79	1.5	—	1.31
G25	M3	0.04	15.03	—	—	12.50
G5	M3	0.09	45.73	—	—	3.84
C20	M3	0.06	2.86	—	—	4.81

This is the most simple model that can be assumed, but also here the constraints mentioned for M2 apply. Even so it is evaluated for completeness, although no reasonable results are expected.

The MP component in model M1 is not absorbed by the AI term because it must be located in front of the HI distribution. Otherwise it would not be seen due to the softness of this component. For the extracted spectrum three different spectral binnings are evaluated, namely:

- **G25**: The photons are binned so that at least 25 photons per bin are reached.
- **G5**: The photons are binned so that at least 5 photons per bin are reached.
- **C20**: Here, 20 spectral channels are combined in one bin, i.e. a constant binning.

The used fit method is the *sherpa* default POWELL method together with the CHI GEHRELS statistics. In Tab.8 all combinations are listed together with the χ^2 statistics.

No matter which model is assumed, the G25 binned spectrum produces exceptional high χ^2 values. Of course, the uncertainties in each bin get quite low since 25 photons at least are grouped. Therefore, the model is hardly to fit to the data and the deviations

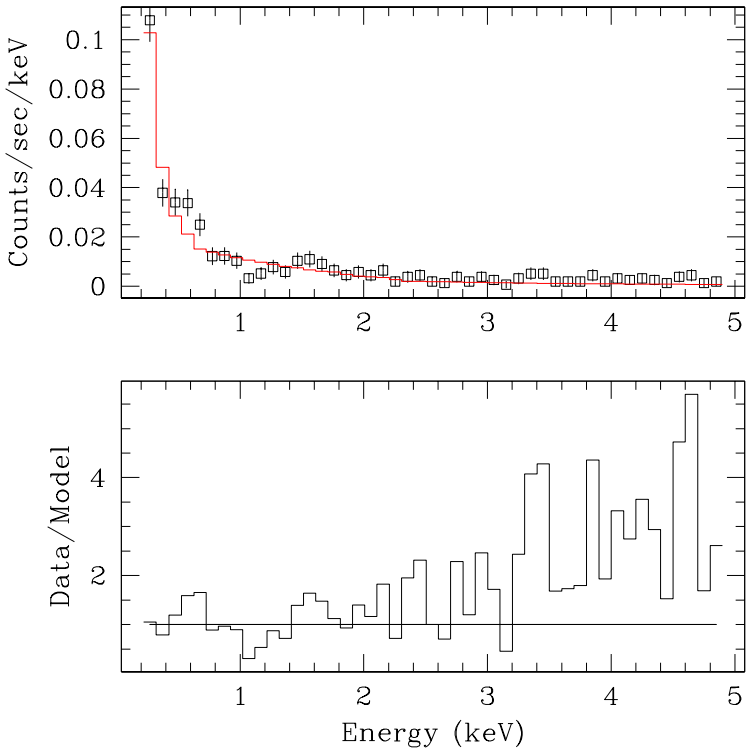

Fig. 27: *The diffuse emission spectrum of Holmberg I (XMM–Newton data points in the upper panel) together with the best fit model M2/C20 (solid line in the upper panel). The lower panel shows the ratio of data/model.*

between model and data do not agree within the uncertainties, hence the χ^2 is very different from one. The χ^2 of the G5 are comparable to the ones of the C20 spectrum. For the M3 model all the χ^2 are far away from one which is expected since the model setup is too simple because it does not account for any residual point sources, especially the background.

The remaining models are M1 and M2 together with the G5 and C20 binning. Any residual point sources have fixed intrinsic absorption according to the mean value given above. Physically it is advisable to set the intrinsic absorption to the column density value of Holmberg I. This ensures that extragalactic sources are attenuated by the whole galaxy. However, only a small fraction of the emission region is covered by the HI disk of Holmberg I, leading to a slightly higher χ^2 value.

Therefore, model M2 is more accurate which does not account for the intrinsic absorption and thus provides less free parameters which makes it more reliable. From the statistics only models M2/G5 and M2/C20 are acceptable (χ^2=0.81 and 1.31, respectively) but model M2/C20 provides a more reasonable emission measure. The

spectrum is given in Fig.27 together with the fitted model and the ratio of data/model.

According to the M2/C20 model one can calculate the plasma parameters. Therefore, I adopt the frequently used equations for the plasma parameters as given by e.g. Summers et al. (2004). These relevant equations for emission integral (EI), electron density (n_e), Pressure (P), equivalent HI mass (M) and thermal energy (E_{th}) are:

$$\begin{aligned} EI &= EM \times 4\pi D^2 / 10^{-14} && (10)\\ n_e &\sim (EI/Vf)^{1/2} && (11)\\ P &\sim 2 n_e k T && (12)\\ M &\sim n_e m_e V f && (13)\\ E_{th} &\sim 3 n_e k T V && (14) \end{aligned}$$

where f is a filling factor, EI the emission integral, m_p the proton rest mass and k is the Boltzmann constant. The volume V of the emitting region is $V = 6.55 \times 10^{65}\,\mathrm{cm}^3$ (assuming spherical symmetry).

The calculated plasma parameters are then:

$$\begin{aligned} T &= 10^{5.8}\,\mathrm{K} && (15)\\ n_e \cdot f^{1/2} &= 2.67 \times 10^{-2}\,\mathrm{cm}^{-3} && (16)\\ P \cdot f^{-1/2} &= 4.65 \times 10^{-12}\,\mathrm{dyn\,cm}^{-2} && (17)\\ M \cdot f^{-1/2} &= 15 \times 10^{6} M_{\odot} && (18)\\ E_{th} &= 4.57 \times 10^{54}\,\mathrm{erg} && (19) \end{aligned}$$

The assumption of spherical symmetry and a filling factor of unity give reasonable values for n_e, P, M and E_{th}. However, all plasma properties are calculated assuming collisionally ionized equilibrium (CIE). As pointed out by Breitschwerdt & Schmutzler (1999) this assumption is not realized in most astrophysical plasmas, hence the figures are only estimates.

Not only because of the CIA assumption, the interpretation of these figures given above turns out to be difficult. The main question is whether the diffuse emission detected in the imaging instruments of XMM–Newton is related to Holmberg I or not. A scenario can be outlined referring to previous work done by Ott et al. (2001) as follows. The central HI depletion is very likely produced by ≈ 120 supernova events which went off on a timescale of 4×10^7 yr. The age of the shell itself is between 60 and 100 Myr, depending on the analysis, and the energy needed to create the shell is a few 10^{53} erg. Also it is very likely that the shell broke up and blew the material out of the disk of Holmberg I. If one now attributes the diffuse X–ray emission

to the creation of the shell, the cooling time of the plasma has to be estimated to make sure that the plasma would still be visible. To do so, the cooling function Λ of Sutherland & Dopita (1993) is used and the value of the timescale turns out to be $t_{\rm cool} = 3/2 \cdot (NkT)/(\Lambda n_i n_e) \approx 15$ Myr for a 0.2 solar metalicity plasma. Provided the sound speed in this plasma (93.5 km s^{-1}), it could reach 1.5 kpc distances on the given timescale of 15 Myr which is, of course, not high up in the halo. The escape velocity of Holmberg I is 48 km s^{-1} taking the total mass of being 8.6×10^8 M$_\odot$ (Ott et al., 2001). Compared to the sound speed, this in turn argues for the idea that the extended X–ray emission can be attributed to the creation of the central shell.

The derived pressure corresponds to ≈ 900 K cm^{-3}. According to Breitschwerdt & Schmutzler (1999); de Avillez & Breitschwerdt (2004) the typical pressure in galactic halos is about a factor of 5-10 higher. But also they state that the filling factor f is of the order 0.2. Taking this value the pressure gains to values comparable to the typical halo pressures. Hence, the diffuse gas can survive in the halo environment.

Very recently, Vorobyov et al. (2004) performed a numerical simulation of an expanding shell in Holmberg I. Their favored model indeed is able to reproduce the HI properties found by observations. Moreover, this model produces a blow–out scenario with a mass loss of 1-2 % of the total gas mass. This gas fraction is just the gas which is at radial velocities exceeding the escape velocities of the galaxy. Provided the total gas mass being 8.6×10^8 M$_\odot$ the lost gas mass is $\approx 17 \times 10^6$ M$_\odot$, when the 2 % estimate is taken into account. This is in agreement with the gas mass of the hot gas detected in X–rays. From the blow–out model follows that the shell broke out of the disk 15 Myr ago which is the same time scale as the cooling time of the coronal gas. Here, we may see the gas expelled in the blow–out as the hot X–ray emitting gas phase.

A counter–argument here is the spatial off–set of the diffuse hot gas with respect to the morphological center of the HI distribution. On the contrary, the diffuse emission is located right at the position where the velocity dispersion of the HI reaches systematically higher values compared to the rest of the galaxy. Moreover, the morphological center does not match the dynamical center (Ott et al., 2001), which is off–set towards the north. From the morphology of the atomic gas the southern edge is sharp as compared to the northwestern side. All this argues for a motion of the galaxy through the ambient medium towards the southern direction, where the famous M 81, M 82, NGC 3077 triplet is located. Ott et al. (2001) suggest that ram–pressure compresses the galaxy at the southern part. This would also explain the disturbed northwestern part of the galaxy. In the context of the diffuse emission it is likely that, if the hot gas stems from blow–out from the central shell, it is stripped off in the direction of the northwest due to the same ram-pressure effects.

But even if no ram–pressure effects are called to account for the off–set it is still possible to basically explain the off-set. The inclination angle of the galaxy is $i = 15 - 20^{\rm o}$ (Vorobyov et al., 2004). Provided the projected off–set of 2.5 kpc of the diffuse hot gas, a distance can be derived from the inclination angle. The perpendicular distance then

is $7-10$ kpc which is well above the galaxy in the halo. Together with the timescale of the break out (15 Myr) a mean escape speed of $\approx 550\,\mathrm{km\,s^{-1}}$ for the hot gas is calculated. This value, however, is about a factor of 6 smaller than the sound speed in the coronal gas. Hence, the ram–pressure effect is more likely than the geometric effect for explaining the off–set.

All these different indications lead to a still not strong evidence. The central HI feature may be attributed to the diffuse emission in the northwest. However, the distance of the coronal gas, calculated from the sound speed and the cooling time scale, is too low to be in good agreement with the blow–out scenario.

5.1.1.3 Summary Observations of Holmberg I in the X–ray as well as in the UV are presented. The analysis of the X–ray point source population reveals 14 point source in total above the 4-σ threshold, confined to the HI distribution of the galaxy. Hardness ratios are calculated for all sources having positive counts in all energy bands considered. All but one of these appear as power–law sources (X–ray binaries) in the HR diagram, one is more consistent with the emission process of an absorbed plasma source ($N_{\mathrm{HI}} \approx 1 \times 10^{21}\,\mathrm{cm^{-2}}$). According to the optical counterparts, ID 8 and 10 show up in the UV range making them good candidates for HMXB whereas the remaining sources are more likely LMXB.

An analysis of the spatial distribution of the point sources is presented as well. The radial distribution of the X–ray point sources, with respect to the morphological center, shows a decline towards larger radii when the fluxes of them are ignored. This is consistent with what Ott et al. (2001) found for the surface brightness profiles in the optical. The faint sources tend to be distributed at larger radii than the bright ones. The implication here is, that the bright sources are associated with the star forming region in the southeast, which is located nearer to the morphological center, whereas the faint sources are wider distributed - they have propagated through the galaxy body.

The luminosity function appears to have no breaks within the uncertainties. It can be approximated by a power–law with slope -1.06$\pm$0.10. The absence of breaks means that no burst of star formation has occurred over a time scale of about 10^7 yr, which is the typical nuclear time scale of an HMXB (see e.g. Grimm et al., 2003).

Point source subtracted images are calculated to reveal any diffuse emission associated with the galaxy. At the soft energy regime (0.2-1.0 keV) diffuse emission is detected in the northwest of the galaxy where the velocity dispersion of the neutral gas reaches maximal values.

A spectral analysis of the diffuse emission is performed, taking into account the Galactic foreground absorption and also any residual point source contribution due to the X–ray background. Modeling the diffuse emission with a MEKAL–plasma model, the best fit model of the extracted spectrum yields a temperature of $\log(T[\mathrm{K}]) = 5.8$ and a corresponding HI mass of $15 \times 10^6\,\mathrm{M_\odot}$. This value is in agreement with the mass loss

calculated by Vorobyov et al. (2004). The origin of the blow–out scenario proposed by Ott et al. (2001); Vorobyov et al. (2004) is also suggested by the detection of the diffuse emission. The derived physical plasma parameters lead to a distance of the coronal gas of only 1.5 kpc which is not high above the plane. Thus, the blow–out is still questionable.

The diffuse emission shows a projected spatial off-set from the morphological center of Holmberg I. The spatial off–set is about 2.5 kpc. This off–set is addressed to the movement of the galaxy towards the south through the ambient medium. This is well confined by the HI study taken out by Ott et al. (2001). The off–set can then be explained by ram–pressure effects if the hot gas is blown out of the central shell. However, the inclination angle of the galaxy allows to explain the off–set without regarding ram–pressure effects. But this geometric explanation is not likely since the distance to the plane would be too high by a factor of five.

5.1.2 IC 2574

The second galaxy in the sample is IC 2574. It is also a member of the M 81–M 82 group of galaxies. As well as the Holmberg I and II dIrrs, IC 2574 shows an ISM dominated by holes and shells. Up to now 48 shells are known (Walter & Brinks, 1999). These shells are mostly expanding and show star forming regions traced by Hα emission predominantly located at the rims of the expanding shells. Particularly for one prominent shell towards the northeast Walter (2001) found that the shell is associated with a stellar cluster in its center. The ages of the shell and the cluster are comparable and this, together with the energetic input, argues for the 'standard model', i.e. massive star clusters can create super giant shells in galaxies.

Within this shell X–ray observations with ROSAT, XMM–Newtonand CHANDRA revealed a point source of ≈ 8 pc size (upper limit) which can be attributed to a cooling neutron star (Brinks et al., 2003). Besides the power–law component there is also a plasma component in the X–ray spectrum which can be attributed to a supernova remnant having an upper age limit of about 2000 yr. It is very likely that this SNR is one of the shell forming objects.

This 'standard model' is also supported by the work of Sánchez-Salcedo (2002). They derived kinematic ages for the shells and an asymmetry between the approaching and the receding side is found. Together with their photometry and the HI properties they claim the 'standard model' to be correct since all alternative scenarios are facing problems to explain the measured abundance and properties of the expanding shells.

As with Holmberg I in the previous section the same analysis steps are applied to the data observed by the XMM–Newton telescope. The observational key data is displayed in Tab.4, basic parameters are given in Tab.9. The difference here is the use of the MEDIUM filter in contrast to the THIN1 filter used in the Holmberg I observation.

Tab. 9: *IC 2574*

Morphological type	dIrr	
Position (J2000.0)	$\alpha = 10^h28^m27\overset{s}{.}40$ $\delta = 68^d24^m44\overset{s}{.}78$	
Distance	4.0 Mpc	(Karachentsev et al., 2002)
HI mass (10^6 $M_\odot$)	600	(Walter & Brinks, 1999)

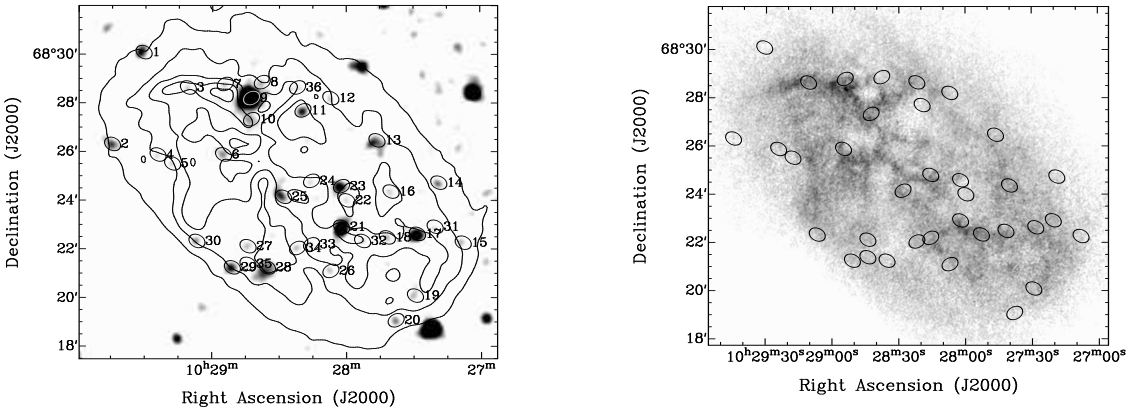

Fig. 28: **Left**:*Smoothed image of the combined EPIC–MOS1 & 2 IC 2574 maps in the PS band. The contours (starting at 10% of the peak intensity and growing in steps of 20%) show the* HI *distribution shown in grey scale (peak 2406 K km s*$^{-1}$*) on the* **right**, *circles indicate the point sources which are above the 4-*σ *limit of the background. Numbers correspond to Tab.11.* HI *map published by Walter & Brinks (1999)*

This has to be accounted for when deriving hardness ratios or dealing with spectra. In the latter case this is done automatically since the RMF and ARF are calculated accordingly. The first task performed is the detection of X–ray point sources

5.1.2.1 X–ray point sources The smoothed M1M2 image in the PS band is examinated to find point sources exceeding the 4-σ background threshold. Restricting the galaxy body to its HI distribution 36 point sources are identified. In Fig.28 (left) the location of these point sources are superimposed on the smoothed M1M2 image. The right hand side of the figure shows the HI map with the point sources overlayed as circles.

Equipped with the coordinates of each point source, the counts of each can extracted. Again different energy bands are considered: the PS band for flux calculation and the B2-B4 bands for the HR. As performed for Holmberg I the counts are extracted from

Tab. 10: *IC 2574 flux limits for individual XMM–Newton bands, taking at least 7000 pixels outside the* HI *distribution into account. The flux units are* 10^{-15} *erg cm*$^{-2}$ *s*$^{-1}$

Band	background counts	flux limit
B2	5 $\pm$0.3	0.63$\pm$0.04
B3	4 $\pm$0.3	0.35$\pm$0.03
B4	4 $\pm$0.2	0.49$\pm$0.02
PS	18$\pm$0.6	2.93$\pm$0.09

the EPIC–*pn* data. The detection limits for the individual bands are given in Tab.10. Here, the limits are comparable to the ones of the Holmberg I observation although they are slightly higher given the lower exposure times in the bands as shown in Tab.4.

Given the background corrected counts in th PS band the fluxes are calculated using a Galactic foreground absorption of 2.1×10^{20} cm^{-2} and a power–law index of $\Gamma = 1.5$ which is again a mean value. From the fluxes one can derive the luminosities adopting a distance to IC 2574 of 4 Mpc (Karachentsev et al., 2002). In Tab.11 I summarize the X–ray point sources found, giving the coordinates, fluxes, luminosities and counts in the B2-B4 bands.

The source list provides the following information. From the 36 sources found in the PS band of the M1M2 images, 15 source turn out to be insignificant in the B2–B4 bands of the EPIC–*pn* data. This can be addressed to the lower exposure time in the EPIC–*pn* data. Especially two sources (ID 3 and 15) show negative counts even in the EPIC–*pn* PS band data. They only show up in the smoothed M1M2 PS band. In the B2–B4 bands (each of which is less significant than the PS band) both have virtually zero counts after correcting for the background emission. All remaining 21 sources are considered to be detected.

The contamination of the data by XRB objects is evaluated with the help of the log(N)-log(S) diagram. Figure 29 shows that the IC 2574 data points are well above the extra galactic background. This positive off–set makes sure that statistically no point sources from the XRB contribute to the point sources found. However, it is still possible to have one XRB source in the data. Contamination occurs below 1.0×10^{-15} erg cm^{-2} s^{-1}.

Now, hardness ratios can be calculated for the detected sources. The HR diagram is show in Fig.30 where the model curves are nearly the same as explained in the caption of Fig.19. The only difference here is that now the MEDIUM filter is used and therefore the theoretical models have to account for this. Since the thicker filter dilutes the X–rays especially in the soft energy regime the curves appear “harder” and accordingly they are shifted to the right in the HR diagram.

The interpretation of the HR diagram turns out to be not as straight forward as in the

Tab. 11: *The XMM–Newton X–ray point sources found in IC 2574. The flux units are 10^{-15} erg cm^{-2} s^{-1} in the PS band, the luminosity units are 10^{37} erg s^{-1}, the luminosity uncertainty is of the order of the relative flux uncertainty. The stars mark sources with zero or less counts in one band after background subtraction. The daggers mark peculiar sources in the HR diagram. The last three columns give the background corrected counts in the corresponding band.*

ID	Right Ascension (J2000.0)	Declination (J2000.0)	Flux	Luminosity	B2	B3	B4
1	$10^h29^m30\overset{s}{.}75$	$68^o\ 30'\ 05\overset{''}{.}66$	12.79 ± 1.67	2.45	12	26	13
2	$10^h29^m44\overset{s}{.}75$	$68^o\ 26'\ 19\overset{''}{.}03$	9.32 ± 1.42	1.78	11	16	10
3*	$10^h29^m10\overset{s}{.}91$	$68^o\ 28'\ 39\overset{''}{.}14$	—	—	0	2	0
4	$10^h29^m24\overset{s}{.}21$	$68^o\ 25'\ 53\overset{''}{.}53$	3.90 ± 0.92	0.75	4	4	5
5*	$10^h29^m17\overset{s}{.}88$	$68^o\ 25'\ 31\overset{''}{.}94$	1.08 ± 0.48	0.21	2	1	0
6	$10^h28^m55\overset{s}{.}02$	$68^o\ 25'\ 54\overset{''}{.}12$	3.90 ± 0.92	0.75	4	7	2
7	$10^h28^m54\overset{s}{.}31$	$68^o\ 28'\ 48\overset{''}{.}13$	1.95 ± 0.65	0.37	2	3	3
8	$10^h28^m37\overset{s}{.}71$	$68^o\ 28'\ 52\overset{''}{.}66$	5.64 ± 1.11	1.08	5	6	9
9	$10^h28^m42\overset{s}{.}44$	$68^o\ 28'\ 13\overset{''}{.}47$	154.1 ± 5.78	29.50	121	208	249
10*	$10^h28^m42\overset{s}{.}43$	$68^o\ 27'\ 21\overset{''}{.}27$	0.43 ± 0.31	0.08	0	2	0
11†	$10^h28^m19\overset{s}{.}53$	$68^o\ 27'\ 43\overset{''}{.}15$	4.77 ± 1.02	0.91	9	4	8
12†	$10^h28^m06\overset{s}{.}88$	$68^o\ 28'\ 13\overset{''}{.}58$	4.55 ± 0.99	0.87	8	4	8
13*	$10^h27^m46\overset{s}{.}38$	$68^o\ 26'\ 29\overset{''}{.}04$	0.87 ± 0.43	0.17	4	1	0
14*	$10^h27^m18\overset{s}{.}83$	$68^o\ 24'\ 44\overset{''}{.}19$	3.47 ± 0.87	0.66	0	3	13
15*	$10^h27^m07\overset{s}{.}91$	$68^o\ 22'\ 16\overset{''}{.}03$	—	—	0	0	0
16*	$10^h27^m40\overset{s}{.}12$	$68^o\ 24'\ 22\overset{''}{.}81$	0.87 ± 0.43	0.17	1	1	3
17	$10^h27^m28\overset{s}{.}36$	$68^o\ 22'\ 38\overset{''}{.}23$	19.29 ± 2.04	3.69	18	35	25
18*	$10^h27^m41\overset{s}{.}74$	$68^o\ 22'\ 29\overset{''}{.}73$	3.04 ± 0.81	0.58	0	7	3
19*	$10^h27^m29\overset{s}{.}23$	$68^o\ 20'\ 05\overset{''}{.}99$	7.15 ± 1.25	1.37	0	20	8
20	$10^h27^m37\overset{s}{.}90$	$68^o\ 19'\ 05\overset{''}{.}23$	5.42 ± 1.08	1.04	5	10	6
21	$10^h28^m2\overset{s}{.}20$	$68^o\ 22'\ 56\overset{''}{.}01$	28.40 ± 2.48	5.43	15	49	43
22†	$10^h27^m59\overset{s}{.}82$	$68^o\ 24'\ 01\overset{''}{.}25$	3.90 ± 0.92	0.75	5	3	5
23	$10^h28^m02\overset{s}{.}19$	$68^o\ 24'\ 36\overset{''}{.}06$	15.39 ± 1.83	2.95	17	20	18
24*	$10^h28^m15\overset{s}{.}58$	$68^o\ 24'\ 49\overset{''}{.}15$	3.69 ± 0.89	0.71	7	6	1
25	$10^h28^m28\overset{s}{.}18$	$68^o\ 24'\ 09\overset{''}{.}97$	18.86 ± 2.02	3.61	5	15	42
26*	$10^h28^m06\overset{s}{.}93$	$68^o\ 21'\ 07\overset{''}{.}28$	0.22 ± 0.22	0.04	1	0	0
27*	$10^h28^m43\overset{s}{.}90$	$68^o\ 22'\ 08\overset{''}{.}05$	0.43 ± 0.31	0.08	0	0	1
28	$10^h28^m35\overset{s}{.}23$	$68^o\ 21'\ 15\overset{''}{.}93$	8.67 ± 1.37	1.66	3	19	11
29	$10^h28^m50\overset{s}{.}96$	$68^o\ 21'\ 15\overset{''}{.}77$	11.49 ± 1.58	2.20	13	17	12
30†	$10^h29^m06\overset{s}{.}72$	$68^o\ 22'\ 20\overset{''}{.}77$	11.49 ± 1.58	2.20	5	2	12
31	$10^h27^m20\overset{s}{.}48$	$68^o\ 22'\ 55\overset{''}{.}47$	4.77 ± 1.02	0.91	2	10	7
32*	$10^h27^m52\overset{s}{.}76$	$68^o\ 22'\ 21\overset{''}{.}15$	1.73 ± 0.61	0.33	4	2	0
33	$10^h28^m15\overset{s}{.}58$	$68^o\ 22'\ 12\overset{''}{.}55$	4.12 ± 0.94	0.79	3	7	4
34*	$10^h28^m21\overset{s}{.}87$	$68^o\ 22'\ 03\overset{''}{.}84$	1.52 ± 0.57	0.29	4	2	0
35	$10^h28^m43\overset{s}{.}88$	$68^o\ 21'\ 24\overset{''}{.}55$	3.90 ± 0.92	0.75	6	5	5
36*	$10^h28^m21\overset{s}{.}90$	$68^o\ 28'\ 39\overset{''}{.}69$	1.30 ± 0.53	0.25	3	4	0

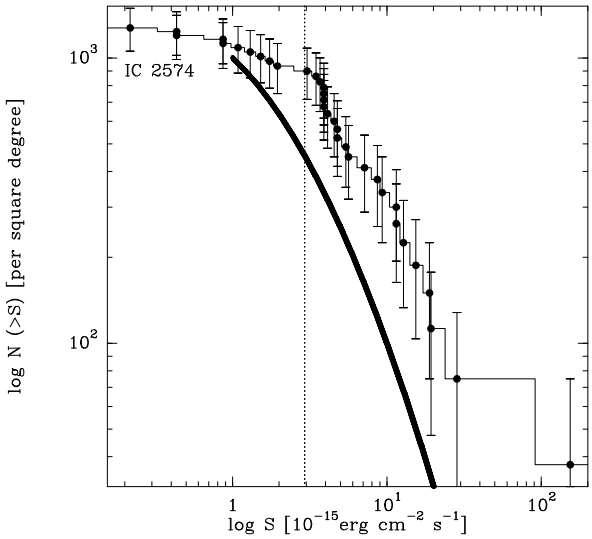

Fig. 29: *The cumulative log(N)–log(S) relation for IC 2574 (XMM–Newton data) scaled to the area of 1 square degree in order to compare to the data obtained from the XMM–Newton Lockman hole observation by Hasinger et al. (2001) (thick line). The data is well above the XRB data and hence the contamination with XRB sources is negligible. The dotted vertical line corresponds to the flux limit in the PS band. Again, as for the Holmberg I case, the thick line is an upper limit.*

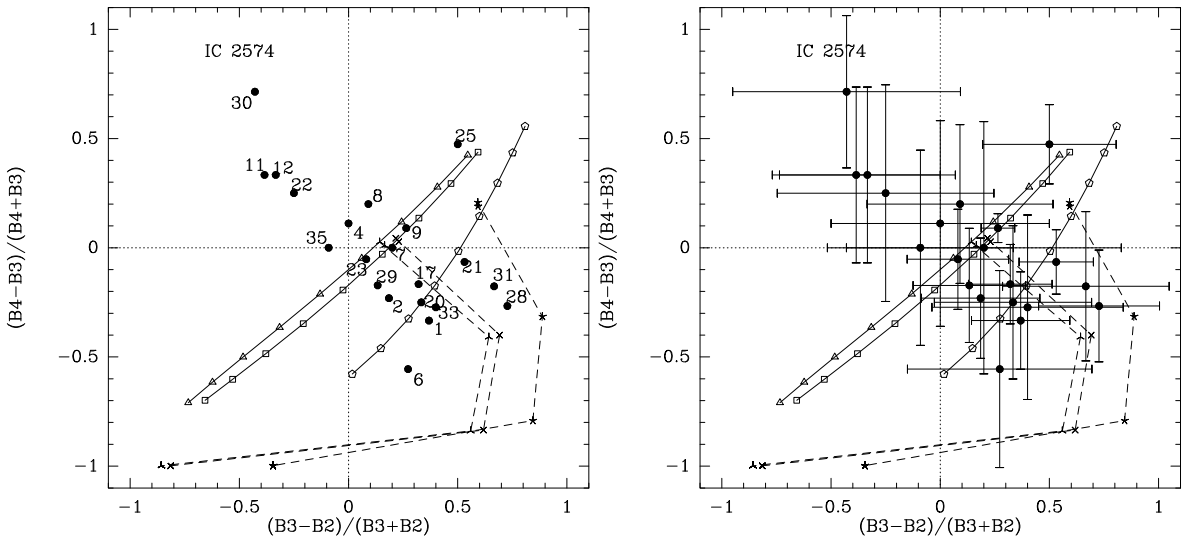

Fig. 30: *XMM–Newton HR for the point sources found in IC 2574. The numbers (***left***) correspond to the IDs of Tab.11. All errorbars (***right***) correspond to an uncertainty of 1-*σ*. The dashed and solid lines are described in detail in the caption of Fig.19 and the accompanying text.*

Holmberg I observation. At first glance there are four peculiar sources showing up in the upper left of the diagram, namely the source ID 11, 12, 22 and 30. These are not intersecting the model curves within their 1-σ uncertainties. According to the source list of Fig.11 their luminosities are not unusual and also the counts in the B2-B4 band are not extremely low. Also the re–examination of the photon images do not show any special features. The position in the HR diagram is due to the lower counts in the B3 band compared to the B2 and B4 band. Examining the B5 and B6 bands it turns out that ID 30 shows up with 30 cts and 8 cts respectively (after background subtraction). The other 3 sources are not significant. At least ID 30 can be identified with a very hard source. Together with its luminosity of $2.2 \times 10^{37}\,\mathrm{erg\,s^{-1}}$ it is likely an X–ray binary. However, the nature of the other 3 sources deviating from the model curves remains unclear. It is speculated that these sources may be faint background sources, reasonable since the log(N)-log(S) relation is statistical.

All other sources are, within their uncertainties, situated in the power–law regime of the model curves making them good candidates for being X–ray binaries. But there is one very prominent source having the maximum luminosity of all sources found in IC 2574, which is source ID 9. This source is very well known and was observed also with the CHANDRA telescope (Brinks et al., 2003). The authors claim that this source is likely a young supernova remnant (SNR) with an absorbed ($N_{\mathrm{Hi}} \approx 8.0 \times 10^{20}\,\mathrm{cm^{-2}}$) thermal plasma component of kT$=$ 2.4 keV combined with a power–law component. Its position in the HR diagram is fully consistent with this finding.

To disentangle the nature of the remaining sources, a comparison with the OM and DSS2 images is performed. The OM image of the UV emission is displayed in Fig.31. First, the sources which do not show up in either of these three wavelength are IDs 1,2,4,14,15,16,18,20,27,28,29,31,33,35. Except IDs 14-16,18,27 all have hardness ratios which are compatible with power–laws, hence they are regarded as being isolated X–ray binaries which do not have to show up in the optical. Source ID 15, which has no counts in the 0.2-2.0 kev range cannot be identified. It also does not show up at higher energies. The remaining sources (IDs 14,16,18,27) with no hardness ratio information, have at least luminosities which are also compatible with X–ray binaries.

The sources with optical counter parts in at least one of the three wavelengths are then IDs 3, 5-10, 13, 17, 19, 21, 23-26, 32, 34, 36. Here, only the sources IDs 3, 5, 10, 13, 19, 26, 32, 34, 36 have no hardness ratios. The classification of them being X–ray binaries only stems from their luminosities and is therefore questionable. Source ID 3, cannot be identified due to its zero flux in the EPIC–*pn* data. The remaining sources, namely IDs 6-8, 17, 21, 23, 24 do all show up in the OM and hence they are considered as X–ray binaries, most likely HMXB. At this point I would like to summarize the correlation analysis in a table (Tab.12).

Some of the sources are in spatial agreement with HI shells. There are six shells (Walter & Brinks, 1999) which are associated with X–ray point sources. Shell S1 is located at $\alpha = 10^{\mathrm{h}}28^{\mathrm{m}}43\overset{\mathrm{s}}{.}24$, $\delta = 68^{\mathrm{o}}28'17\overset{''}{.}81$(J2000.0) and the accompanying sources

Tab. 12: *IC 2574 X–ray to optical correlation. Here, the abbreviations denote: L→LMXR, H→HMXB, S→SNR, I→isolated binary*

ID	HR	OM	DSS2 red	DSS2 blue	Luminosity [10^{37} erg s^{-1}]	Classification
1	√				2.45	L
2	√				1.78	L
3		√		√	0.00	?
4	√				0.75	L
5			√	√	0.21	L
6	√	√	√	√	0.75	H
7	√	√	√	√	0.37	H
8	√	√			1.08	H
9	√	√	√	√	29.5	S
10		√	√	√	0.08	L
11	√				0.91	I
12	√				0.87	I
13			√		0.17	L
14					0.66	L
15					0.00	?
16					0.17	L
17	√	√			3.69	H
18					0.58	L
19			√		1.37	L
20	√				1.04	L
21	√	√			5.43	H
22	√				0.75	L
23	√	√			2.95	H
24		√	√	√	0.71	L
25	√	√	√	√	3.61	H
26			√		0.04	L
27					0.08	L
28	√				1.66	L
29	√				2.20	L
30	√				2.20	L
31	√				0.91	L
32		√	√	√	0.33	L
33	√				0.79	L
34			√		0.29	L
35	√				0.75	L
36		√	√	√	0.25	L

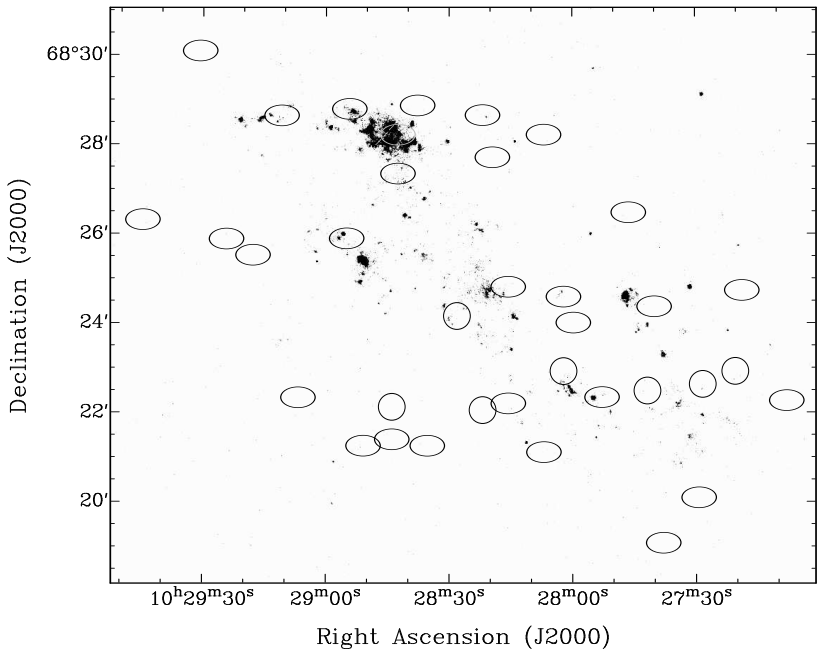

Fig. 31: *The OM map of IC2574 with* HI *contours and the source positions. Numbers were skipped for clarity. In the north prominent UV emission is clearly visible. This is associated with the brightest X–ray point source found in the galaxy.*

are ID 9 in the very center and ID 7,8,10 surrounding this shell. Shell S2 is located at $\alpha = 10^{\rm h}28^{\rm m}22\overset{\rm s}{.}68$, $\delta = 68^{\rm o}27'17\overset{''}{.}04$(J2000.0) with source ID 11 at its northern rim. Shell S3 has central coordinates $\alpha = 10^{\rm h}27^{\rm m}59\overset{\rm s}{.}0$, $\delta = 68^{\rm o}24'9\overset{''}{.}95$(J2000.0) with source ID 22 in the center and ID 23 at the northern rim. The next shell associated with X–ray point sources is shell S4 at $\alpha = 10^{\rm h}28^{\rm m}32\overset{\rm s}{.}10$, $\delta = 68^{\rm o}21'55\overset{''}{.}10$. The X–ray source near to S4 is ID 28. More far away there are additional point sources (ID 27,34,35) which may be associated with S4 as well. Shell S5 is centered on α=$10^{\rm h}28^{\rm m}49\overset{\rm s}{.}51$, $\delta = 68^{\rm o}26'20\overset{''}{.}29$(J2000.0). Here, only ID 6 is in the vicinity at the southeast rim of the shell. The last shell is S6 with position $\alpha = 10^{\rm h}28^{\rm m}21\overset{\rm s}{.}88$, $\delta = 68^{\rm o}\ 24'\ 14\overset{''}{.}34$(J2000.0), showing ID 24 and 25 on its rim in the west and east respectively.

To get a better handle on the associated X-ray point sources, the results of Walter & Brinks (1999) (hereafter WB99) are used. The shells S1-S6 are regarded as the primary shells while the WB99 shells are smaller, hence, secondary shells. If a point source is located on the rim of a primary shell it is attributed to this shell unless it is not in positional agreement with a secondary shell.

Concerning the expansion of the shells only S1 and S6 are found to be still expanding. Shells S2-S5 are concerned to be total blown out shells. Following WB99 these are most likely very old shells. It is suggested that the X–ray point sources found on the rims originated from the old stellar population which created the shells. Due to turbulence the sources are likely be dispersed an swept up towards the expanding direction,

outwards off the shell. ID 22 in S3 might be a relict source still located inside the shell or it is located outside the shell on the line–of–sight, but due to projection it appears inside the shell.

In the case of S6 it is suggested that source ID 25 is associated with the WB99–shell 28 since the positional agreement is perfect within the PSF of XMM–Newton. Note, that S6 and WB99–shell 28 are not identical but they are tangent to each other. Accordingly, this source is likely one of the sources driving the WB99–shell 28 and not associated with S6. For the shell S1 it turns out that ID 9 is located in the very center and it is very likely being a SNR driving the expansion of the shell as pointed out by Brinks et al. (2003). However, the associated source ID 7 agrees perfect with the location of the WB99–shell 42, and ID 10 with that of WB99–shell 33. Hence, they are not related to shell S1. In contrast to that ID 8 is not correlated with any of the WB99–shells so it is more likely to be a relic source of S1.

In total there are 14 X–ray point sources associated with HI shells where 4 of them are in the very centers of the shells taking the PSF of the XMM–Newton. Regarding 10 ks CHANDRA observation having a much better resolution ($1''$) the position can not be constrained further. These four sources are also detected in the UV and DSS2 images (cf. Tab.12) as well as in the WB99 Hα images which argues for them being HMXB in young star forming regions, as depicted in WB99.

Having the likely classification of the X–ray point sources, a spatial analysis can be carried out. The radial distribution must account for two issues, the position angle of the galaxy and the inclination angle. With this the deprojected distances to the galaxy center can be derived. I adopt the inclination angle of $i = 75^{\rm o}$ and an position angle of $PA = 52^{\rm o}$ from Martimbeau et al. (1994). The number density point sources as a function of deprojected radius is given in Fig.32 (left).

As in contrast to Holmberg I the number density does not decline towards larger radii. One can spot a significant peak at 4-5 kpc distance from the dynamical center. Below that peak the number density decreases slightly toward smaller radii and above the peak it declines towards larger radii. According to the right hand side panel of Fig.32 all sources within the 4-5 kpc range have fluxes below $1 \times 10^{-14}\,{\rm erg\,cm^{-2}\,s^{-1}}$. These are assumed to be LMXB and hence are old objects ($\approx 10^{10}$ yr) except source ID 9.

If now the positions of these objects in the disk of IC 2574 are regarded, the following asymmetry turns out. With respect to the minor axis of the galaxy, most sources show up at the approaching side, which is in the southwest. Only three of the sources are on the receding side (one of which is ID 9). This asymmetry is not the only one addressed to IC 2574. Recently Sánchez-Salcedo (2002) studied the ages of the HI shells found by WB99. Their conclusion is that the shells on the approaching side are about twice as old than the shells at the receding side. Moreover, there was less recent star formation at the approaching side which is in good agreement with the asymmetry found for the LMXB population at 4-5 kpc radii. Since all other sources, not belonging to the 4-

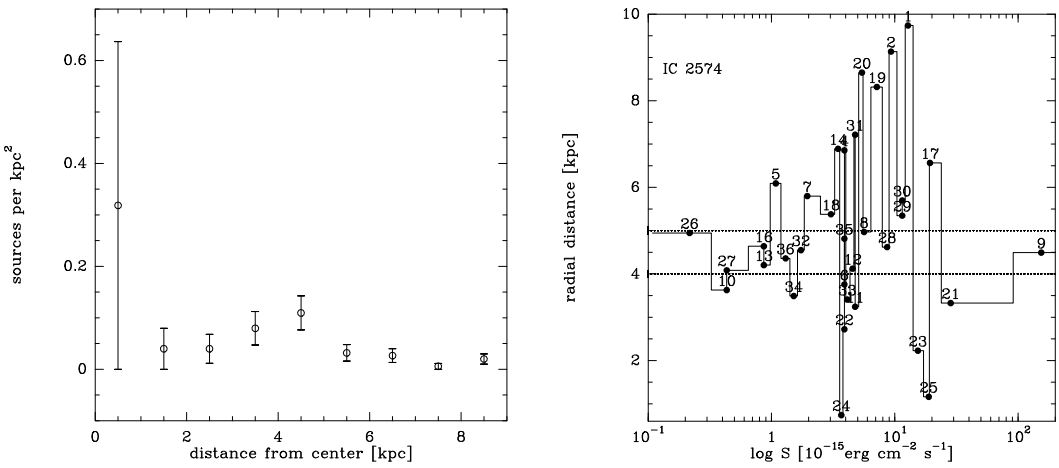

Fig. 32: **Left**: *The radial distribution of XMM–Newton point sources peaks at a radius of about 4.5 kpc.* **Right**: *Radial distances as a function of source flux. The radial range where the peak occurs in the number density is marked by the dotted lines.*

5 kpc structure, are distributed uniformly across the whole galaxy, it is concluded that the 4-5 kpc sources belong to the old shells.

Furthermore, this LMXB population is correlated with an HI ring–like structure (see Fig.33) at a radial distance of 4.5 kpc. It seems as if the number density of the LMXB resembles the HI ring. The assumption made for calculating the deprojected radii of the point sources is that they are all located in a plane. If this assumption is not true, the correlation is just due to projection effects. This can be examined when the HI data cube is studied deeper. For example, if the galaxy is warped then also the HI ring is only a projected effect. Hence, the eye might be cheated by the warp and the projection on the sky and the correlation is not real. This is also very likely since the LMXB are old objects whereas the HI (and also the asymmetry in recent star formation, as pointed out by Sánchez-Salcedo (2002)) is related to chronological young structures. However, a tilted ring analysis (e.g. Begeman, 1989) of the HI data cube is beyond the scope of this thesis.

In contrast to Holmberg I, here the radial distance as a function of flux does not show the tendency to decrease towards higher fluxes. Regarding Fig.32 (right) most sources are situated outside a 3 kpc range. Only four sources are confined below the 3 kpc distance. The star formation in the galaxy is not uniformly distributed. Rather the number of X–ray point sources is low in the center and increases towards the outer parts of the galaxy, showing also the 4-5 kpc structure with old stellar populations. Also the 4-5 kpc sources seem to be an underlying old population in contrast to the younger and smoother distributed sources. Hence, a break feature is expected in the XLF.

To study the issue of star formation closer the XLF of IC 2574 is inspected. The XLF is shown in Fig.34. Different to Holmberg I the XLF shows a kink at 1×10^{37} erg s^{-1}.

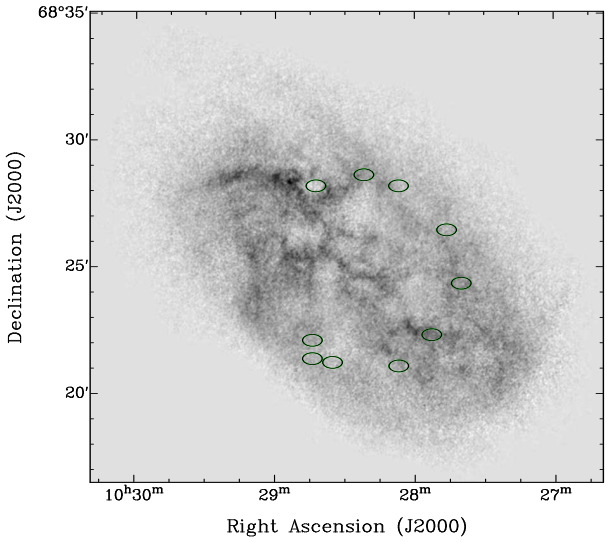

Fig. 33: *Again the* HI *map now showing the positions of the LMXB found in the 4-5 kpc radius, indicated by the black ellipses. The neutral gas at these positions shows an enhancement in column density, forming a ring–like structure. Also note the asymmetry between the receding and approaching side of the galaxy (northeast and southwest respectively).*

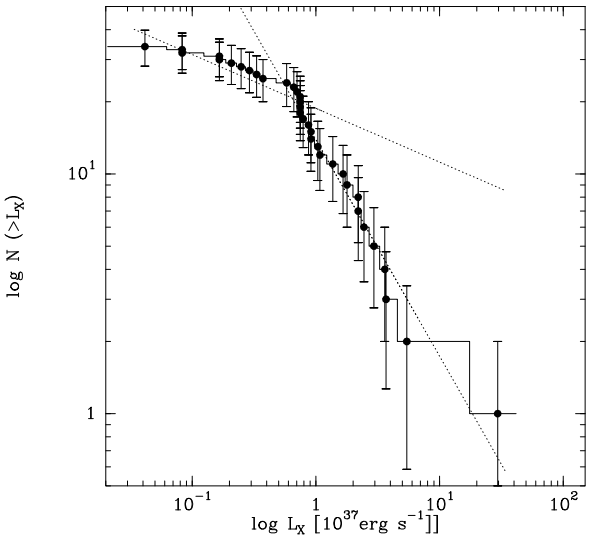

Fig. 34: *X–ray luminosity function of IC 2574 (XMM–Newton data). At* 1×10^{37} *erg s*$^{-1}$ *the slope changes significantly. The dotted lines show the broken power–law fits with slope. The slopes are* $\beta = -0.22 \pm 0.02$ *and* $\beta = -0.90 \pm 0.08$*. Here, the break in the slopes reflects the different binary populations of LMXB and HMXB.*

The XLF then cannot be fitted by a single power–law but by a broken power–law. The power–law indices for the sources below 1×10^{37} erg s^{-1} is -0.22±0.02 and for the brighter sources it is -0.90±0.08. The interpretation of the break turns out to be difficult since there are no studies of dIrrs regarding this issue.

In general, a break in the XLF can have different causes. Considering a galaxy having faced a recent star burst, the number of LMXB will increase more than the number of HMXB. Hence, a break will show up in the XLF. Moreover, for massive galaxies a break of the XLF at $L_X \approx 2 \times 10^{37}$ erg s^{-1} is reported for the bulge population in M 31 (for a nice review see Fabbiano & White, 2003, and references therein). It is suggested, that the break marks episodes of star formation. There are also reports of a break near the Eddington–limit. Assuming a neutron star of $1.4 M_{\odot}$ the Eddington–luminosity is 2×10^{38} erg s^{-1}. In this regard, a break is attributed to a transition between neutron star and black hole binaries. Another cause for breaks in the XLF is a confusion effect with cosmic background sources (i.e. detection incompleteness). As reported by Humphrey & Buote (2004) the break in the XLF can be eliminated by applying Monte Carlo simulations.

However, all the reported effects for breaks in the XLF are at luminosities exceeding the break luminosity found in IC 2574 by at least one order of magnitude. Interestingly, below the break luminosity I find 10 sources in total (ID 5, 7, 13, 16, 19, 26, 27, 32, 34, 36). Six of them belong to the 4-5 kpc–ring sources (ID 13, 16, 26, 27, 32, 36) and only three of the sources are on the receding side of the galaxy (ID 5, 7, 36). The sources above the break luminosity are distributed uniformly across the galaxy. I conclude that the break in the XLF is caused by the underlying old population of LMXB in the 4-5 kpc ring found in IC 2574 and also reflects the different star formation rates in the two halves of the galaxy (Sánchez-Salcedo, 2002).

5.1.2.2 Diffuse emission The search for diffuse emission is carried out in the same fashion as in Holmberg I. Indeed, an extended soft component in the B2 and B3 band is found, displayed in Fig.35 together with the HI contours and the point source positions marked by circles. To make sure, that the emission is real, the number of excess photons in the region of interest is calculated with respect to a source free background field. The excess in the B2 band turns out to be $(2.1 \pm 0.3) \times 10^{-4}$ cts s^{-1} arcmin^{-2} and in the B3 band $(2.9 \pm 0.3) \times 10^{-4}$ cts s^{-1} arcmin^{-2}. The higher energy bands do not show up with excess emission.

To find out whether or not the diffuse emission is related to IC 2574, the plasma properties are derived from the spectral information contained in the EPIC–*pn* data. For this purpose the spectrum is extracted from a 4-σ region excluding the point sources. The spectrum is again grouped to the G25, G5 and C20 binning as described in the Holmberg I section. The models assumed for the diffuse emission are the same as for the Holmberg I data, i.e. the argumentation here is the same. The figures for the fitting

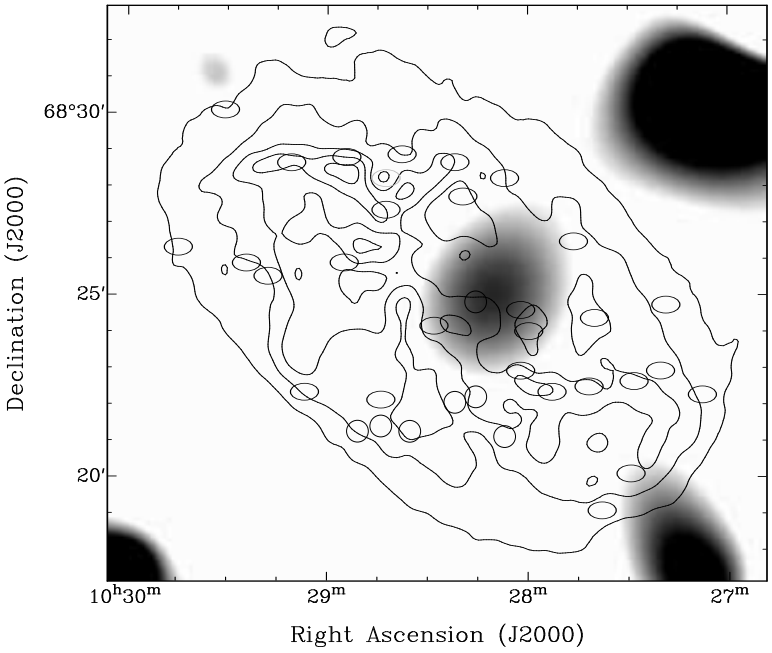

Fig. 35: *Adaptively smoothed image of the 0.2-1.0 keV EPIC–*pn *map. Point sources were subtracted and detector gaps are filled. The features outside the* HI *distribution are due to the exposure map correction which raises the noise at the outer FOV.*

is given in Tab.13. The intrinsic column density is the mean value for IC 2574 adopted from Martimbeau et al. (1994).

The model in favor here is M1/C20 owing to the χ^2. The spectrum and the fitted model is given in Fig.36. In contrast to Holmberg I where the XRB is hardly attenuated by the galaxy itself, here the diffuse emission is completely within the galaxy. Thus the XRB is attenuated by the whole galaxy. Therefore, the M2 models are not physically meaningful. From that M1/C20 values, the other parameters can be calculated using equations 10 to 14. They turn out to be:

$$T = 10^{6.1}\,\mathrm{K} \quad (20)$$

$$n_e \cdot f^{1/2} = 7.12 \times 10^{-3}\,\mathrm{cm}^{-3} \quad (21)$$

$$P \cdot f^{-1/2} = 2.47 \times 10^{-12}\,\mathrm{dyn\,cm}^{-2} \quad (22)$$

$$M \cdot f^{-1/2} = 1.0 \times 10^{7} M_{\odot} \quad (23)$$

$$E_{th} = 5.75 \times 10^{54}\,\mathrm{erg} \quad (24)$$

Again, spherical symmetry is assumed and the filling factor f is assumed to be one. Therefore, the same precautions are recommended as in the Holmberg I study, with regard to the figures. Having the plasma properties the question now is whether the

Tab. 13: *Different spectral model fits for different binning of the data. The uncertainties in all values are of the order 10% as calculated by* `COVAR` *of the sherpa package.*

Binning	Model	MP kT [keV]	MP EM [10^{-3} pc cm^{-6}]	PL Γ	AI $N_{\rm Hi}^{\rm int.}$ [10^{21} cm^{-2}]	red.χ^2
G25	M1	0.10	0.54	1.5	1.1	1.33
G5	M1	0.10	0.56	1.5	1.1	0.45
C20	M1	0.11	0.41	1.5	1.1	0.80
G25	M2	0.09	0.48	1.5	—	1.62
G5	M2	0.09	0.50	1.5	—	0.49
C20	M2	0.10	0.35	1.5	—	0.96
G25	M3	0.12	0.39	—	—	9.83
G5	M3	0.12	0.40	—	—	1.55
C20	M3	0.13	0.35	—	—	6.12

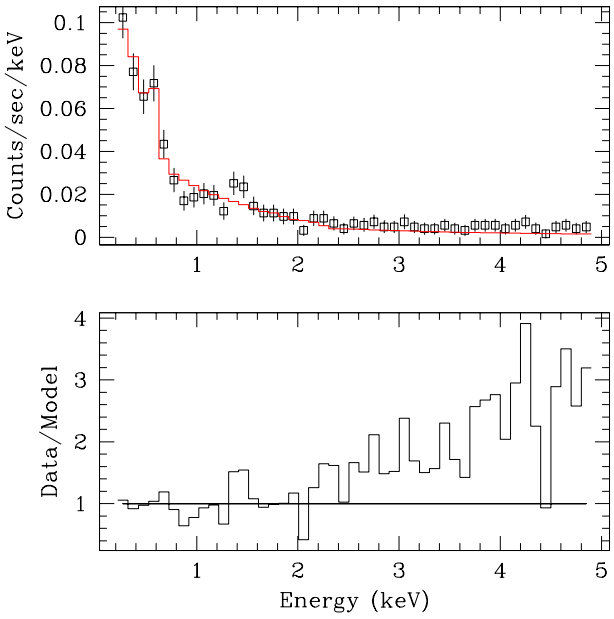

Fig. 36: *The diffuse emission spectrum of IC 2574 (XMM–Newton data points in the upper panel) together with the best fit model M1/C20 (solid line in the upper panel). The lower panel shows the ratio of data/model.*

emission can be attributed to IC 2574 with its large number of shells. The linear size of the plasma is 4.5 kpc which gives a volume of the emitting region of about $V = 1.55 \times 10^{66}\,\mathrm{cm}^3$.

All calculated plasma parameters are higher than for the Holmberg I case. However, the assumption of spherical symmetry and not least the uncertain filling factor impose overestimations on the pressure and the mass of the plasma. From the plasma parameters one can calculate characteristic timescales and from that, upper limits for the height the plasma can reach. The cooling time of the plasma for 0.2 solar metalicity is ≈ 110 Myr where i make use of the cooling function by Sutherland & Dopita (1993). The speed of sound in that plasma is $\approx 130\,\mathrm{km\,s}^{-1}$. Based on these figures the plasma can reach an upper limit distance perpendicular to the plane of ≈ 15 kpc.

Morphologically, the peak of the plasma emission is located at the WB99 shell 20. But since IC 2574 is inclined this positional coincidence must not be real. The position of the plasma also depends on the height of the plasma above the galactic plane (if it was produced in a blow–out scenario). The plane of the disk is inclined by 70^{o}. For this fixed angle the projected position of the plasma is a line parallel to the minor axis, when the perpendicular height of the plasma is varied from 0-15 kpc. Hence, good candidates for the origin of the plasma are WB99 shell 22 and 26, since these are located on this projection line.

The deprojected linear distance between WB99 shell 20 and the plasma peak intensity is 1.5 kpc. This distance is too low leading to a perpendicular distance of the plasma of about 2 kpc. Additionally, WB99 shell 20 did not suffer from a total blow–out according to WB99. WB99 shell 26 is further away (about 4 kpc deprojected) and for the deprojected distance of the plasma it gives 4.2 kpc.

The pressure of the plasma has to be of the order of the halo pressure. If the plasma pressure is higher, the plasma would expand and cool down adiabatically. If the plasma pressure is lower than the surrounding pressure, it cannot break out of the shell. The pressure consideration of the plasma gives a pressure of $2.47 \times 10^{-12}\,\mathrm{dyn\,cm}^{-2}$. This corresponds to $\approx 1000\,\mathrm{K\,cm}^{-3}$ which is suitable to let the plasma survive in the halo of the galaxy (see Breitschwerdt & Schmutzler, 1999; de Avillez & Breitschwerdt, 2004). The escape velocity of IC 2574 can only be calculated as an lower limit since the total mass is unknown. From the HI mass alone the escape velocity gives $\approx 30\,\mathrm{km\,s}^{-1}$. Compared to the speed of sound in the plasma the diffuse emission component can be driven into the halo.

The mass of the diffuse gas is about 1% of the HI mass of the galaxy. Together with the thermal energy of the plasma it is more likely that the plasma stems from more than one shell forming event, i.e. from more than one shell in the ISM of IC 2574.

5.1.2.3 Summary XMM–Newton observation of IC 2574 are presented together with the UV image taken by the OM. The analysis of the X–ray data revealed 36

point sources in the HI distribution of IC 2574. Two sources must be excluded due to their low signal–to–noise. Confusion with the extra galactic background is statistically unlikely. The hardness ratios exhibit four peculiar sources one of which is classified as an X–ray binary whereas the other three are unclear.

One source (ID 9) has a hardness ratio which is fully consistent with the findings of Brinks et al. (2003). In total there are 14 sources associated with HI shells four of which are in the very centers of shells. These are considered to be high–mass X–ray binaries.

The spatial analysis reveals an excess of predominantly old (10^{10} yr) population in a 4-5 kpc galactocentric distance. These point sources can be identified with an HI ring–like structure. Nearly all of these sources are on the approaching side of the galaxy where predominantly old shells are found. This asymmetry in age is reflected in the asymmetry in old X–ray point source populations.

Six of these ten old sources are below a break in the X–ray luminosity function. It is argued that the break stems from the underlying old stellar population of LMXB on the approaching side of the disk, giving rise to different star formation rates in the two halves of the galaxy. However, the global origin of the asymmetry remains unknown.

The careful analysis of extended soft X–ray emission shows a hot plasma ($T = 10^{6.1}$ K) component projected on the HI disk of IC 2574. The inclination of the disk makes it difficult to pin down the origin of the plasma component. From the plasma parameters follows that the gas cannot be higher than 15 kpc above the plane. Regarding the inclination of the galaxy a value of ≈ 4 kpc is calculated for the case that WB99–shell 26 is the origin of the plasma. However, the thermal energy and mass of the plasma leads to to the picture that more than one shell produced the hot gas.

5.1.3 Sextans A

Sextans A is a dIrr located at the edge of the local group. Its HI distribution is dominated by two distinct clumps where the star formation is taking place (Skillman et al., 1988). According to Wilcots & Hunter (2002) it has an unusual HI structure which argues for an undisturbed galaxy (see also Barnes & de Blok, 2004), at least for the last 6 to 10 Gyr. Hence, the star formation is triggered by internal processes. However, the average star formation derived from the B–band luminosity is $\approx 5.0\,\mathrm{M}_{\odot}\,\mathrm{yr}^{-1}$.

This is also supported by the distribution of stars in Sextans A. van Dyk et al. (1998) found that the young stars are situated at the inner rim of the prominent HI shell whereas the oldest population shows a uniform distribution across the galaxy. Hence, the internal processes are very likely star formation due to supernovae events resulting in neutral gas pile–up and compression with sequential star formation in recent times. According to Skillman et al. (1988) Sextans A has a high HI surface density and they

Tab. 14: *Sextans A*

Morphological type	dIrr	
Position (J2000.0)	$\alpha = 10^h11^m1^s.96$ δ = -04^{d}41^{m}18^s.43	
Distance	1.4 Mpc	(Dolphin et al., 2003)
HI mass (10^6 $M_\odot$)	58	(Skillman et al., 1988)

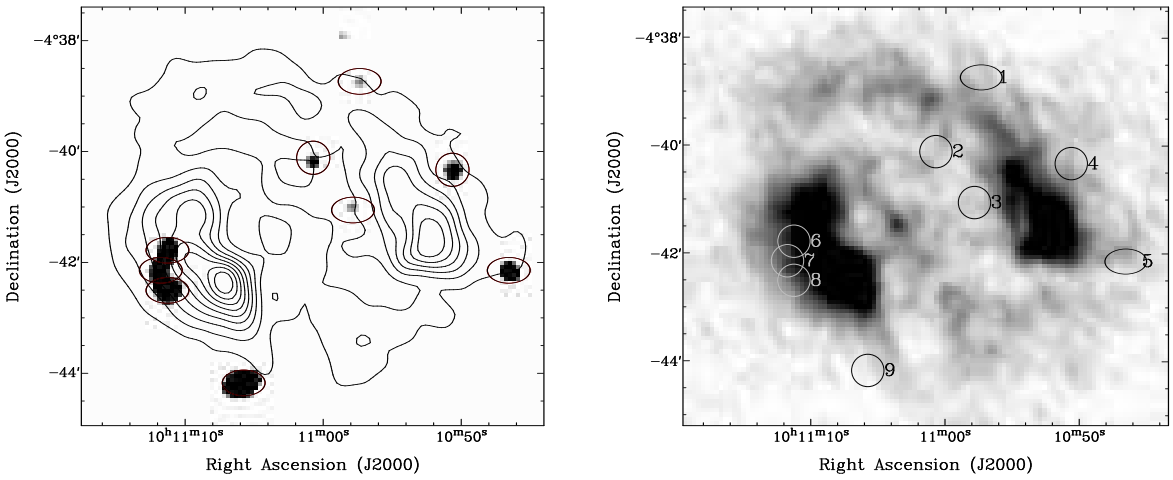

Fig. 37: **Left**:*Smoothed image of the combined EPIC–MOS1 & 2 Sextans A maps in the PS band. The contours (starting at 10% peak growing in steps of 10%) show the* HI *distribution shown in grey scale (peak 0.6 Jy/Beam) on the* **right**, *circles indicate the point sources which are above the 4-*σ *limit of the background. Numbers correspond to Tab.15.* HI *map by Skillman et al. (1988)*

suggest that this may be an important factor to massive star formation in dIrrs. Basic data of Sextans A is given in Tab.14.

The XMM–Newton observation of Sextans A has the lowest net exposure times in the sample so far (cf. Tab.4). This, of course, is due to the contamination of unrelated X–ray counts in the light curves. However, the same techniques as in the previous observations are used.

5.1.3.1 Point sources After clipping the M1M2 data to a 4-σ background level, 9 X–ray point sources are detected within the HI distribution of Sextans A. The M1M2 map together with the neutral gas map and the positions of X–ray point sources are displayed in Fig.37. Also the ID s of the point sources are plotted and refer to Tab.15.

As with two sources in IC 2574, the counts for source ID 3 are negative in the EPIC–*pn* PS band. Comparing to Tab.4 the exposure time here is about 6 ks leading to a lower

Tab. 15: *The XMM–Newton X–ray point sources found in Sextans A. The flux units are 10^{-15} erg cm^{-2} s^{-1} in the PS band, the luminosity units are 10^{37} erg s^{-1}, the luminosity uncertainty is of the order of the relative flux uncertainty. The stars mark sources with zero or less counts in one band after background subtraction. The last three columns give the background corrected counts in the corresponding band.*

ID	Right Ascension (J2000.0)	Declination (J2000.0)	Flux	Luminosity	B2	B3	B4
1*	$10^h10^m57^s.25$	-04° 38′ 44.″10	2.47 ± 0.87	0.05	0	3	3
2*	$10^h11^m00^s.75$	-04° 40′ 06.″75	3.09 ± 0.98	0.06	2	6	-1
3*	$10^h10^m57^s.84$	-04° 41′ 03.″30	—	—	-3	2	-4
4*	$10^h10^m50^s.56$	-04° 40′ 19.″79	5.25 ± 1.27	0.11	0	0	12
5	$10^h10^m46^s.49$	-04° 42′ 08.″54	7.71 ± 1.54	0.16	3	9	10
6	$10^h11^m11^s.22$	-04° 41′ 46.″80	8.95 ± 1.66	0.18	6	4	14
7	$10^h11^m11^s.80$	-04° 42′ 08.″55	14.19 ± 2.09	0.29	15	16	8
8	$10^h11^m11^s.22$	-04° 42′ 30.″30	9.56 ± 1.72	0.19	7	17	2
9	$10^h11^m05^s.69$	-04° 44′ 10.″35	19.13 ± 2.43	0.39	11	14	21

Tab. 16: *Sextans A flux limits for individual XMM–Newton bands. The flux units are 10^{-15} erg cm^{-2} s^{-1}*

Band	background counts	flux limit
B2	5±0.3	1.82±0.11
B3	6±0.3	1.27±0.06
B4	7±0.4	2.04±0.12
PS	31±1.0	12.41±0.37

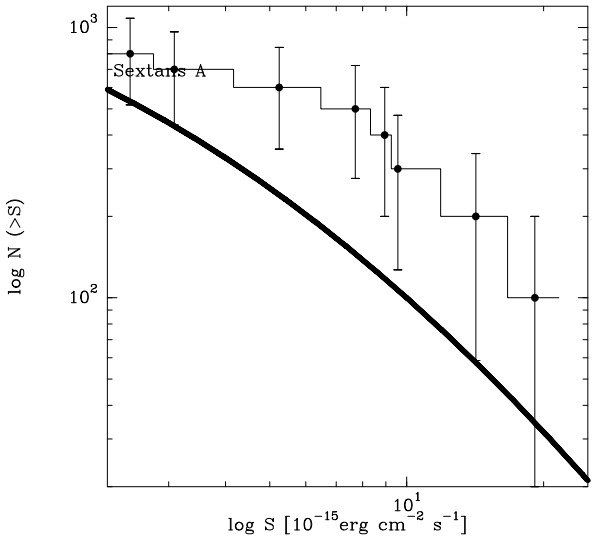

Fig. 38: *The cumulative log(N)–log(S) relation for Sextans A (XMM–Newton data) scaled to the area of 1 square degree in order to compare to the data obtained from the XMM–Newton Lockman hole observation by Hasinger et al. (2001) (thick line). The data is well above the XRB data and hence the contamination with XRB sources is statistically low. Note, that the Thick line refers to the absorbing column density of the Lockman hole, hence it is the upper limit for the XRB.*

signal–to–noise in the EPIC–*pn* data in contrast to the combined M1M2 data. Therefore, ID 3 disappears in the EPIC–*pn* data. The detection limits are given in Tab.16. Due to the lower exposure time, the flux limits are higher in the individual bands, as well as in the broad PS band. However the limiting luminosities in the individual bands are comparable to the other observations presented so far. In this regard the contamination by XRB sources is carried out in the log(N)–log(S) plot displayed in Fig.38.

Although the flux limits are higher than in the previous observations, the number of sources per square degree at a certain flux is higher than the XRB sources. Therefore, the detected point sources of Sextans A are statistically belonging to the galaxy. With the individual source counts in the B2–B4 band the hardness ratios can be calculated for sources with more than zero counts in each of these bands. The hardness ratios in a graphic fashion are shown in Fig.39.

Sources ID 9,5 and 7 are located on the power–law tracks. Source ID 9 is situated left of the power–laws with the lowest absorbing column density. Since the Galactic foreground column density is $3.1 \times 10^{20}\,\mathrm{cm}^{-2}$, source ID 9 is expected to show up more to the right. Within 2-σ uncertainties this is fulfilled. Only from the HR these three sources are concerned to be X–ray binaries. In contrast, source ID 8 is found in the plasma–model regime. The absorption at the source positions in the HR plot is degenerated but fully consistent with the Galactic foreground. Source ID 6 is located in the upper left of the HR diagram. This area is not covered by the model lines

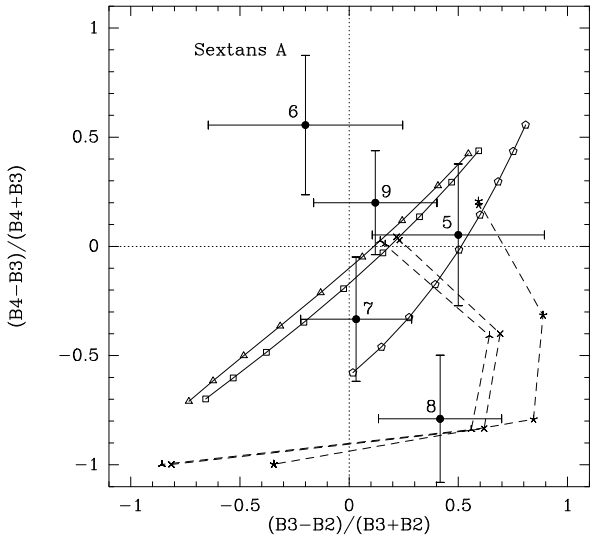

Fig. 39: *XMM–Newton HR for the point sources found in Sextans A. The numbers correspond to the IDs of Tab.15. All errorbars correspond to an uncertainty of 1-σ. The dashed and solid lines are described in detail in the caption of Fig.19 and the accompanying text.*

because this would require an absorption which is far too low, compared to the Galactic foreground. Also the source does not show up at higher energies (B6–band). So far, the nature of the source is unclear. Since the log(N)-log(S) relation provides only statistical information, the source may be a background source.

To get a better handle on the physical origin of the sources a correlation analysis with other wavelengths is performed. Again, the XMM–Newton observation was carried out using the OM. Three sources also appear in the UV image of the OM, namely ID 2,3 and 8. The same holds true for the DSS2 red and blue images. Therefore, and also because of their luminosities, the sources ID 2 and 3 are concerned to be LMXB. Source ID 8, however, is classified as a plasma source according to its HR. In the UV it is detected down to a wavelength of ≈ 250 nm. The X–ray luminosity is $1.9 \times 10^{36}\,\mathrm{erg\,s^{-1}}$ and the temperature $\approx 10^{5.5}$ K. These values argue for an old supernova remnant, which is also confirmed by the fact that the source is not variable.

Source ID 6 has no optical counter parts and hence it is likely a background source. The sources which do not show up in the HR (due to their low counts in the bands) or in the optical can only be evaluated on basis of their luminosities. These are compatible with the luminosities of accreting X–ray binaries, most likely LMXB.

To carry out the spacial analysis I adopt a distance to Sextans A of 1.3 Mpc (Dolphin et al., 2003) and a face–on orientation (Barnes & de Blok, 2004). In Fig.40 the radial distances of the X–ray point sources is plotted against their fluxes. As one can see from the diagram nearly all sources are located outside a 1.0 kpc distance from the geometric center defined by the HI distribution of the galaxy. Only two of the nine sources are inside the high column density region in the west. These two sources (ID 2

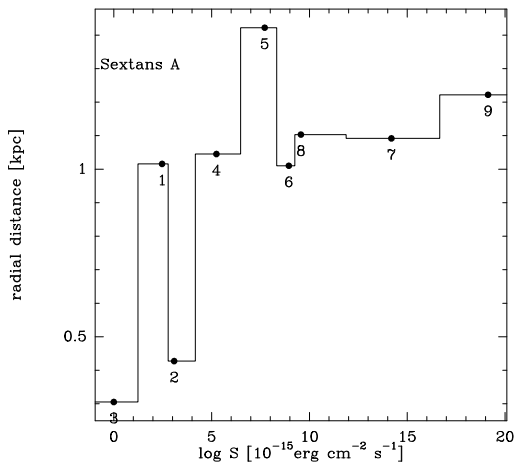

Fig. 40: *Radial distances as a function of source flux (XMM–Newton data). Nearly all sources are located outside a 1 kpc radius.*

and 3) are associated with the boxy shaped stellar body of the galaxy.

The star formation history of Sextans A was studied by Dohm-Palmer et al. (1997a,b, 2002). From their work it follows that the star formation was very uniform in the last 100 to 600 Myr. Recently, i.e. younger than 100 Myr the star formation is gained by a factor of 20. The most recent star formation (< 50 Myr) is more densely concentrated than the star formation of the past, which is distributed across the whole galaxy.

Moreover, the star formation seems to avoid the center of the galaxy which is confirmed by the distribution of the X–ray point sources. In general, the X–ray point sources resemble the old population and appear in the outer parts of the galaxy. The actual star formation is concentrated at the densest HI clump (Skillman et al., 1988) as well as the brightest HII region (Hodge et al., 1994), where virtually no X–ray point sources are found. The few X–ray point sources show that there was no prominent burst of star formation in Sextans A which is also satisfied by the fact, that it did not interact with other objects in its environment (Wilcots & Hunter, 2002; Barnes & de Blok, 2004). The origin of the star formation is attributed to a bar feature, which is aligned with the central HI depletion (Skillman et al., 1988). This bar then is assumed to trigger the star formation at its outer parts where the X–ray population is concentrated. Hence, since a bar in a galaxy produces non–circular motions of the material in the center (e.g. Bosma, 1981), it is concluded that the X–ray point sources are in the outskirts of the galaxy due to dissipation and internal diffusion.

The result that the X–ray point sources mimic the old population, which is produced in a uniform star formation across long time scales (1 Gyr) should also be reflected in the XLF. It is expected that the XLF shows no breaks as discussed in the context of the IC 2574 observation. In Fig.41 the XLF of Sextans A is shown. It turns out that the XLF, indeed, has no breaks. The power–law fit gives a slope of $\beta = 0.72 \pm 0.14$.

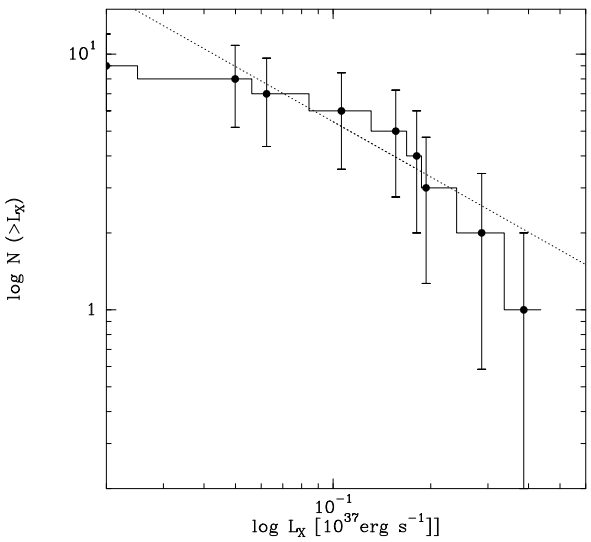

Fig. 41: *X–ray luminosity function of Sextans A (XMM–Newton data). The dotted line shows the power–law fits with slope* $\beta = -0.72 \pm 0.14$. *Here, the XLF has a constant slope which reflects the uniform star formation history.*

5.1.3.2 Diffuse emission Examining the point source subtracted, vignetting corrected XMM–Newton images gives no indication of diffuse soft X–ray emission. This can have two different causes. First of all, the exposure time of the observation may be too short to reveal diffuse emission. Second, there is no diffuse emission associated with Sextans A. I like to discuss the effect of lower exposure time first.

The exposure time is related to the limiting fluxes which can be detected in an observation. Referring to Tab.16 the limiting fluxes in the B2 and B3 bands are of the order 10^{-15} erg cm^{-2} s^{-1} whereas the flux limits in the Holmberg I and IC 2574 observations are an order of magnitude lower.

Provided the distance to the three galaxies, one can convert the flux limits to luminosity limits. It turns out, that the limiting luminosities are of the order 10^{34} erg s^{-1} in all three cases. Especially the limiting luminosities for Sextans A are about a factor of 3.5 lower than for the other observations (in the B2 band) and a factor of 2.0 lower in the B3 band. It follows that the shorter exposure time for the Sextans A observation is not the cause for the non–detection of diffuse soft X–ray emission.

This then implies that there is virtually no diffuse soft X–ray emission associated with Sextans A down to the luminosity limits given from the exposure time and distance. However, this finding is satisfied with the low star formation in the past of the galaxy. Since there were no times of star bursts in the past which could have produced coronal gas, the non–detection fits well into the evolution of Sextans A.

5.1.3.3 Summary The XMM–Newton observation of Sextans A gives the following picture. Above the 4-σ threshold nine X–ray point sources are detected in the M1M2 map (PS band). The contamination with the extra galactic X–ray background is negligible argued on the log(N)–log(S) relation. All sources turn out to be X–ray binaries except one source (ID 8). This is classified as an old, already cooled down ($T \approx 10^{5.5}$ K) supernova remnant, based on the non–variability and the position in the hardness ratio diagram. The nature of one source (ID 3) remains unclear, since it has too less photons in the B2–B3 bands and no optical counterpart in the UV and DSS2 red and blue images.

The spacial analysis of the X–ray point source population agrees very well with the findings of Dohm-Palmer et al. (2002). The distribution of the X–ray point sources fits to the star formation history of the galaxy and the dynamics suggested by Skillman et al. (1988). This is furthermore confined by the X–ray luminosity function which shows no breaks. The single power–law fit gives $\beta = 0.72 \pm 0.14$ for the slope.

Diffuse soft X–ray emission is not found within the galaxy or its vicinity. Since the limiting luminosities in the B2–B4 bands are lower than in the Holmberg I and IC 2574 observations (due to the small distance of Sextans A) it is concluded that there is no such extended emission component. This also follows from the shallow stellar activity in the past of Sextans A.

5.1.4 Holmberg II

Holmberg II is a well studied dIrr with a prominent ISM showing holes and expanding shells in the HI distribution. The HI gas mass is six times higher than for Holmberg I. The holes were studied with ROSAT (Kerp et al., 2002) to find evidence for hot gas in the vicinity of the shells. Since it is thought that these holes correspond to stellar activity it is expected to find hot gas but up to now this is not found. The reasons may be insufficient sensitivity for small holes or may be the gas is blown out in the case of large holes and cannot be detected anymore. Bureau & Carignan (2002) investigated HI data of Holmberg II and found that ≈80% of the total mass is dark which is true for most dwarf galaxies. Also there is more mass in the gas than in the stars. However, the galaxy is dark matter dominated only in the outer parts which is a common feature of massive spirals.

The question how star formation is triggered in dwarf galaxies like Holmberg II was studied by Stewart et al. (2000). They claim that massive star formation is not smoothly distributed across the galaxy. The FUV profile of Holmberg I appears to be flat, as well as the profiles in other optical bands arguing for local processes which trigger the star formation in dIrrs. The ages of star forming regions were analyzed with B, Hα, and FUV photometry which give a preference for young regions in dense HI regimes and old regions in HI voids. They conclude that local star formation on the one hand is

Tab. 17: *Holmberg II*

Morphological type	dIrr, Im	
Position (J2000.0)	$\alpha = 08^{h}19^{m}11\overset{s}{.}21$ $\delta = 70^{d}43^{m}39\overset{s}{.}61$	
Distance	3.1 Mpc	(Karachentsev et al., 2002)
HI mass (10^6 $M_\odot$)	644	(Bureau & Carignan, 2002)

triggered by the energy input of massive stars ionizing their surroundings and produce compact HII regions around aging clusters. The large–scale star formation on the other hand is triggered by supernovae which give enough energy input to account for the properties of HI holes seen in Holmberg II.

Another interesting feature about Holmberg II is an ultraluminous compact X–ray source called Holmberg II X–1. It is variable and shows a soft excess which is attributed to blackbody radiation from a disk around the compact core. However, the major variability is seen in the power–law component of the source spectra (Dewangan et al., 2004). The compact source can be identified with an optical counterpart which is consistent with a star with spectral type between O4V and B3 Ib (Kaaret et al., 2004b). The object photoionizes its surroundings which show up as an He II region. The lower bound of the X–ray luminosity is $\approx 5.0 \times 10^{39}$ erg s^{-1}. With respect to the Eddington limit the compact object has at least a mass of 25 $M_\odot$. Basic properties are listed in Tab.17.

The XMM–Newton data of Holmberg II is the first one in this thesis obtained from the archive. After proton filtering the exposure times are about 9.6 ks for the EPIC–MOS instruments and 5.2 ks for the EPIC–*pn*. The OM was used in this observation and data at other wavelength are available, such as Hα, L and C band radio data, DSS2 red and blue optical data. These will be used to identify X–ray sources in addition to the hardness ratios.

5.1.4.1 Point sources Taking the smoothed M1M2 image in the PS band reveals 62 X-ray sources in total. The image is given in Fig.42 (left), on the right hand side the HI distribution is shown. Since the brightest source in the galaxy outshines all other sources, a logarithmic representation of the grey scale is used. As one can see the bright source ID 4 shows a star shaped pattern around its center. At this point it is not clear whether this star like shape is the intrinsic shape of the X–ray emission or an artefact from the mirror support structure, which has also a "spider" shaped pattern. The identification of point sources in the vicinity of this bright source is therefore not unambiguous. To get a better handle on this issue the mirror support structure is overplotted on the blow up of the bright source in Fig.43 (left). Here, the pattern of the

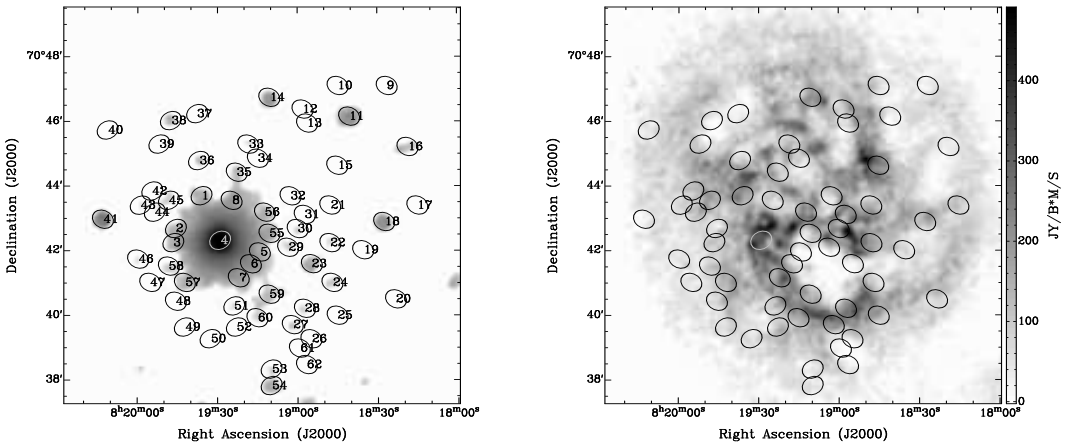

Fig. 42: **Left**:*X–ray point sources within the* HI *distribution of Holmberg II. The grey scale image is a logarithmic representation of the M1M2 PS band data, the circles mark the 62 point sources detected above 4-*σ *background level.* **Right**: *The* HI *column density map with the X–ray point sources overlayed as circles. The peak is 491 Jy/Beam·m/s.* HI *map by Kerp et al. (2002)*

support structure seems to be correlated with intensity enhancements in the image, but it is still not clear whether these are artefacts or not.

There are 11 peculiar sources surrounding the central bright source ID 4 (Fig.43). From their symmetric distribution and also from their equidistant offset from the central source (within the PSF) they are most likely artefacts from the mirror supports. Since the spacial resolution of the XMM–Newton telescope is not appropriate to disentangle the "spider" feature, CHANDRA data is taken from the archive to reveal the point source distribution in the very neighborhood of the ID 4 source. The CHANDRA event list is filtered with respect to the PS band. Then the image is adaptively smoothed to improve the signal–to–noise, gaining the signal of possible point sources.

The image is given in Fig.43 (right) clipped to the 4-σ background threshold. As one can see, no sources show up in the vicinity of the bright source ID 4. The different detection limit of the CHANDRA data yields a limiting flux in the PS band of $S = 2.76 \times 10^{-17}\,\mathrm{erg\,cm^{-2}\,s^{-1}}$ for a background area of ≈52000 pixels. With respect to this flux limit no point source at the "spider" location is found in the CHANDRA data.

Nevertheless, sources ID 1, 55, 56, 57 and 58 show a little bridge–like feature which connects the sources to the "spider" structure and hence they are more isolated than the other surrounding sources. It is concluded, that the source ID 2, 3, 6 and 58 are artefacts due to the spider shaped mirror support structure of the XMM–Newton telescope. Accordingly, these sources are excluded from further analysis. The remaining sources and their parameters are given in Tab.18. Sources ID 5, 7 and 8 can be identified with the ROSAT sources 9, 11 and 7 respectively found by Kerp et al. (2002) (see their Tab. 2).

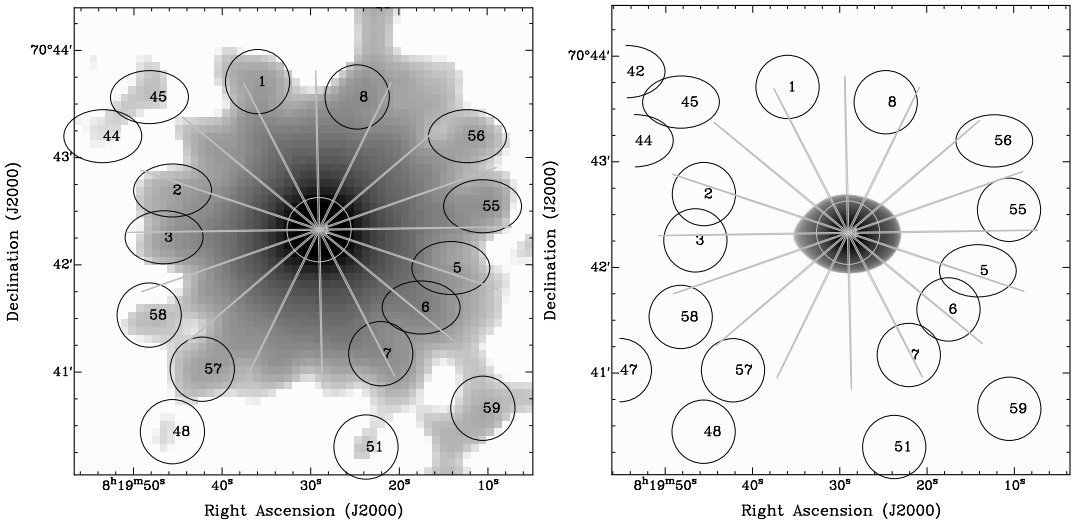

Fig. 43: **Left**: *Zoom in of the bright X–ray source observed by XMM–Newton The overlayed spider–like lines corresponds to the mirror support structure of the telescope. Sources ID 1, 2, 3, 5, 6, 7, 8, 55, 56, 57 and 58 are peculiar since they may be artefacts from diffraction due to the mirror supports. However, ID 1, 55, 56, 57 and 58 are more isolated and further off the central bright source.* **Right**: *Adaptively smoothed CHANDRA image in the PS band showing the same region.*

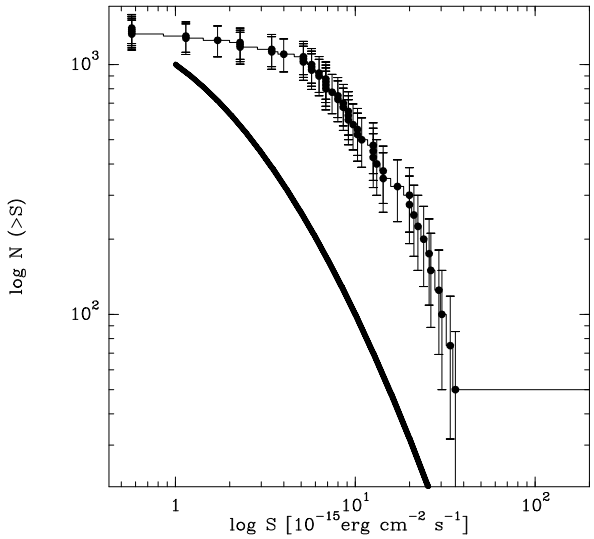

Fig. 44: *The cumulative log(N)–log(S) relation for Holmberg II (CHANDRA data) scaled to the area of 1 square degree in order to compare to the data obtained from the XMM–Newton Lockman hole observation by Hasinger et al. (2001) (thick line). The data is well above the XRB data (which is an upper limit) and hence the contamination with XRB sources is statistically low, especially since the thick line is an upper limit.*

Tab. 18: *The X–ray point sources found in Holmberg II (CHANDRA data). The flux units are 10^{-15} erg cm^{-2} s^{-1} in the PS band, the luminosity units are 10^{37} erg s^{-1}, the luminosity uncertainty is of the order of the relative flux uncertainty. The stars mark sources with one or less counts in one band after background subtraction. The last three columns give the background corrected counts in the corresponding band.*

ID	Right Ascension (J2000.0)	Declination (J2000.0)	Flux	Luminosity	B2	B3	B4
1	$08^h19^m36.03$	$70^o\ 43'\ 42.60$	25.71 ± 3.83	2.86	12	21	10
4	$08^h19^m29.01$	$70^o\ 42'\ 19.94$	5765 ± 57.39	641.64	2308	4070	2889
5	$08^h19^m14.10$	$70^o\ 41'\ 58.13$	43.98 ± 5.01	4.89	27	29	17
7	$08^h19^m22.00$	$70^o\ 41'\ 10.32$	62.83 ± 5.99	6.99	18	50	34
8	$08^h19^m24.61$	$70^o\ 43'\ 33.88$	22.28 ± 3.57	2.48	13	15	9
9	$08^h18^m26.43$	$70^o\ 47'\ 06.26$	6.86 ± 1.98	0.76	6	8	2
10*	$08^h18^m44.93$	$70^o\ 47'\ 06.63$	5.71 ± 1.81	0.64	3	8	0
11	$08^h18^m40.57$	$70^o\ 46'\ 10.00$	30.27 ± 4.16	3.37	12	20	13
12	$08^h18^m58.17$	$70^o\ 46'\ 23.32$	10.28 ± 2.42	1.14	10	3	4
13	$08^h18^m56.42$	$70^o\ 45'\ 57.20$	5.14 ± 1.71	0.57	4	3	3
14	$08^h19^m10.49$	$70^o\ 46'\ 45.20$	14.28 ± 2.86	1.59	7	2	9
15*	$08^h18^m45.03$	$70^o\ 44'\ 38.73$	9.14 ± 2.29	1.02	6	10	1
16	$08^h18^m18.61$	$70^o\ 45'\ 12.97$	6.86 ± 1.98	0.76	4	5	3
17*	$08^h18^m15.22$	$70^o\ 43'\ 24.12$	2.29 ± 1.14	0.25	3	0	0
18	$08^h18^m27.54$	$70^o\ 42'\ 53.98$	29.13 ± 4.08	3.24	13	17	15
19*	$08^h18^m35.49$	$70^o\ 42'\ 01.95$	4.00 ± 1.51	0.45	8	4	-1
20	$08^h18^m23.29$	$70^o\ 40'\ 30.33$	8.00 ± 2.14	0.89	7	5	4
21	$08^h18^m47.72$	$70^o\ 43'\ 24.82$	5.14 ± 1.71	0.57	4	5	2
22*	$08^h18^m47.76$	$70^o\ 42'\ 15.22$	3.43 ± 1.40	0.38	3	5	0
23	$08^h18^m54.81$	$70^o\ 41'\ 36.18$	10.85 ± 2.49	1.21	10	5	5
24*	$08^h18^m46.93$	$70^o\ 41'\ 01.26$	1.71 ± 0.99	0.19	-2	5	0
25*	$08^h18^m45.22$	$70^o\ 40'\ 00.33$	0.57 ± 0.57	0.06	-3	-1	-1
26*	$08^h18^m54.88$	$70^o\ 39'\ 16.98$	3.43 ± 1.40	0.38	5	0	2
27	$08^h19^m01.87$	$70^o\ 39'\ 43.17$	12.57 ± 2.68	1.40	8	10	4
28*	$08^h18^m57.48$	$70^o\ 40'\ 13.56$	6.28 ± 1.89	0.70	5	8	0
29	$08^h19^m03.56$	$70^o\ 42'\ 06.73$	9.14 ± 2.29	1.02	4	10	2
30	$08^h19^m00.04$	$70^o\ 42'\ 41.49$	8.57 ± 2.21	0.95	7	6	4
31*	$08^h18^m57.39$	$70^o\ 43'\ 07.56$	0.57 ± 0.57	0.06	3	1	-1
32*	$08^h19^m02.64$	$70^o\ 43'\ 42.42$	2.29 ± 1.14	0.25	3	5	-1

Tab. 19: *Table.18—continued*

ID	Right Ascension (J2000.0)	Declination (J2000.0)	Flux	Luminosity	B2	B3	B4
33	$08^h19^m18.44$	$70^o\ 45'\ 18.25$	10.28 ± 2.42	1.14	10	7	2
34	$08^h19^m14.93$	$70^o\ 44'\ 52.13$	9.71 ± 2.36	1.08	9	5	2
35	$08^h19^m22.85$	$70^o\ 44'\ 26.08$	13.14 ± 2.74	1.46	5	14	2
36	$08^h19^m36.91$	$70^o\ 44'\ 47.85$	7.43 ± 2.06	0.83	10	4	3
37*	$08^h19^m37.80$	$70^o\ 46'\ 14.85$	1.14 ± 0.81	0.13	2	2	0
38	$08^h19^m47.48$	$70^o\ 46'\ 01.77$	12.57 ± 2.68	1.40	8	7	7
39	$08^h19^m51.87$	$70^o\ 45'\ 18.25$	5.14 ± 1.71	0.57	3	5	2
40*	$08^h20^m11.24$	$70^o\ 45'\ 44.17$	0.57 ± 0.57	0.06	-2	0	-1
41*	$08^h20^m12.91$	$70^o\ 42'\ 58.85$	1.14 ± 0.81	0.13	2	3	-1
42*	$08^h19^m54.49$	$70^o\ 43'\ 51.23$	6.86 ± 1.98	0.76	13	2	1
43*	$08^h19^m58.87$	$70^o\ 43'\ 25.10$	0.57 ± 0.57	0.06	0	0	3
44	$08^h19^m53.60$	$70^o\ 43'\ 12.09$	12.57 ± 2.68	1.40	7	8	9
45	$08^h19^m48.33$	$70^o\ 43'\ 33.87$	19.99 ± 3.38	2.22	10	18	8
46*	$08^h19^m59.72$	$70^o\ 41'\ 45.04$	8.00 ± 2.14	0.89	9	1	2
47*	$08^h19^m55.32$	$70^o\ 41'\ 01.58$	9.14 ± 2.29	1.02	9	5	0
48*	$08^h19^m45.67$	$70^o\ 40'\ 26.83$	5.71 ± 1.81	0.64	3	8	0
49*	$08^h19^m42.16$	$70^o\ 39'\ 38.99$	2.29 ± 1.14	0.25	3	2	0
50	$08^h19^m32.53$	$70^o\ 39'\ 17.25$	8.57 ± 2.21	0.95	9	5	3
51	$08^h19^m23.76$	$70^o\ 40'\ 18.13$	33.70 ± 4.39	3.75	21	23	13
52	$08^h19^m22.89$	$70^o\ 39'\ 38.98$	19.99 ± 3.38	2.22	15	20	2
53	$08^h19^m09.78$	$70^o\ 38'\ 20.59$	26.28 ± 3.87	2.92	15	18	11
54	$08^h19^m09.79$	$70^o\ 37'\ 50.14$	35.99 ± 4.53	4.01	16	30	9
55	$08^h19^m10.57$	$70^o\ 42'\ 32.90$	23.99 ± 3.70	2.67	11	18	15
56	$08^h19^m12.32$	$70^o\ 43'\ 12.06$	22.28 ± 3.57	2.48	11	23	5
57	$08^h19^m42.17$	$70^o\ 41'\ 01.64$	14.28 ± 2.86	1.59	11	13	2
59	$08^h19^m10.61$	$70^o\ 40'\ 39.80$	17.14 ± 3.13	1.91	6	15	8
58	$08^h19^m48.31$	$70^o\ 41'\ 32.07$	6.28 ± 1.89	0.70	6	3	3
60	$08^h19^m15.01$	$70^o\ 39'\ 56.33$	21.14 ± 3.48	2.35	11	16	9
61*	$08^h18^m59.27$	$70^o\ 38'\ 59.64$	5.71 ± 1.81	0.64	7	3	0
62*	$08^h18^m56.66$	$70^o\ 38'\ 29.15$	6.86 ± 1.98	0.76	9	1	3

Tab. 20: *Holmberg II flux limits for individual CHANDRA bands normalized to the area of 3.5 PSF. The flux units are 10^{-15} erg cm^{-2} s^{-1}*

Band	background counts	flux limit
B2	4±0.2	1.37±0.07
B3	2±0.2	0.48±0.05
B4	2±0.1	0.67±0.03
PS	10±0.5	4.43±0.22

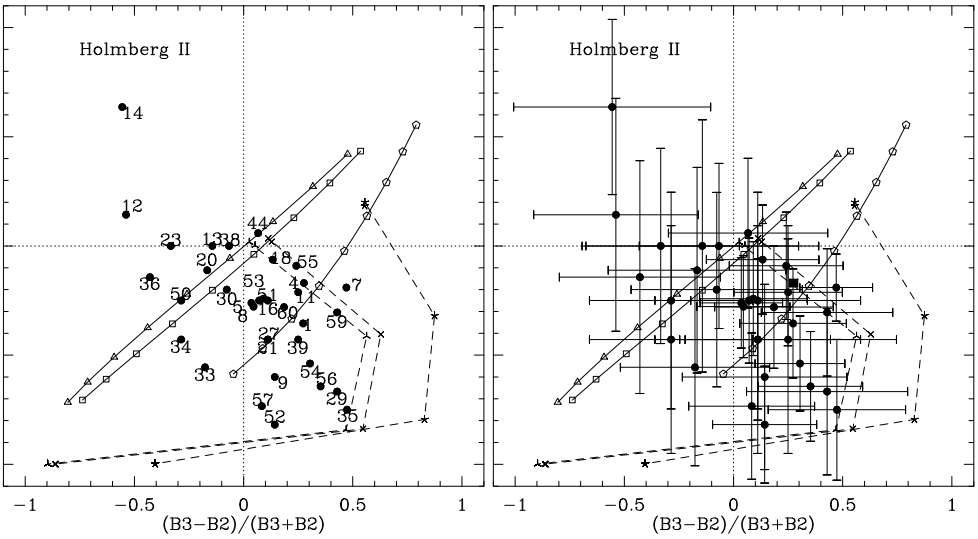

Fig. 45: *CHANDRA HR for the point sources found in Holmberg II. The numbers correspond to the IDs of Tab.18. All errorbars correspond to an uncertainty of 1-σ. The dashed and solid lines are described in detail in the caption of Fig.19 and the accompanying text.*

To make sure that the sources found are related to the galaxy and not to the extra galactic background the log(N)-log(S) relation is evaluated in Fig.44. Again, the sources are well above the background and hence it is concluded that the contamination is statistically low.

The limiting flux for point sources is again calculated for the 3.5 PSF area. Separate for all the bands, namely PS and B2–B4, the limiting flux together with the background counts is given in Tab.20. From the B2–B4 counts the hardness ratios are calculated. In contrast to the previous sections here the HR diagram is given in two versions, a) the sources with their ID number corresponding to Tab.18 and b) the sources with their uncertainties. According to Tab.18 the sources marked with stars have one or less counts in either the B–bands and hence they are not regarded for the HR diagram. The resulting HR diagram is shown in Fig.45.

The HR diagram reveals a large number of sources related to accreting power–law models. Deviating from this are the sources ID 12, 14, 29, 35 and 52. Sources ID 12 and 14 are in the upper left corner where no models are physically meaningful. Within the 2-σ uncertainties source ID 12 is compatible with a power–law model, whereas ID 14 is still off. The investigation of the higher bands B5 and B6 does not show any counts above the background. Hence, the nature of source ID 14 remains unclear.

The three other sources are in the plasma regime of the model curves. They are compatible with a absorbing column density of about $1 \times 10^{21}\,\mathrm{cm}^{-2}$ and a temperature of log(T[K])≈5.5. From the HR diagram they are supposed to be supernova remnants.

The brightest source ID 4 is located right on the track for a plasma absorbed by a column density of only $1 \times 10^{19}\,\mathrm{cm}^{-2}$. Due to its high counts in the B–bands the uncertainties are very low so that these do not reach out to plasma models with higher absorbing column densities. One can read the temperature of the plasma from the position of the source in the HR to be between log(T[K])=6.0 and 6.5. According to Kerp et al. (2002) this source was analyzed with ROSAT and their hardness ratio gave a plasma model with $N_{\mathrm{HI}} = 3 \times 10^{20}\,\mathrm{cm}^{-2}$ and log(T[K])=7.0. These figures do not agree at first glance. However, Dewangan et al. (2004) studied the bright source very recently with XMM–Newton. Their results state that this ultra luminous X–ray source (ULX) is not well described by a single plasma component. They rather favor a multi–component model consisting of a plasma, a blackbody and a power–law model absorbed intrinsically and by the Galaxy. In conclusion the ULX is likely a blackhole binary which in addition shows a variable flux, which is in agreement with X–ray observations at different times. The variation is about a factor of four in luminosity between the high and low luminosity states at April and September 2002, respectively.

Hence, the deviation from the values by Kerp et al. (2002) are not surprising. Moreover, the properties of the ULX are changing with its flux. The observation presented here is from 2002 April, 10, where the source had its brightest luminosity of $6.4 \times 10^{39}\,\mathrm{erg\,s}^{-1}$. According to Dewangan et al. (2004) the source is soft in the low and hard in the high flux state where the time scale on which the flux changes is about half a year. Therefore, the position of the source in the HR diagram changes on time scales of about half a year. However, the flux derived from the observation presented here is comparable to the results of Dewangan et al. (2004) and Kerp et al. (2002), which is also true for the luminosity. Hence, the source is most likely a blackhole binary with variable flux.

The nature of the remaining sources, although they are in the power–law regime of the HR diagram, will be further studied taking observation at other wavelengths. This is advisable, as in the previous sections, since the HR of power–law and plasma models intersect in the diagram. Fortunately, a variety of other observations are available. These are namely Hα, radio L–band (21 cm) and C–band (6 cm) and DSS2 red and blue images. Images of these wavelengths are given in Fig.46-51 with superimposed X–ray source positions.

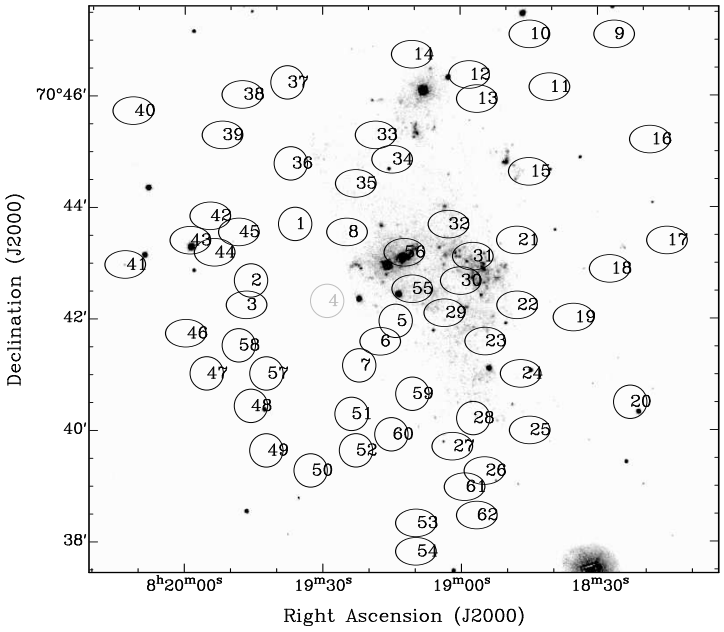

Fig. 46: *Holmberg II as seen by XMM–Newton OM. Source positions and ID numbers correspond to Tab.18.*

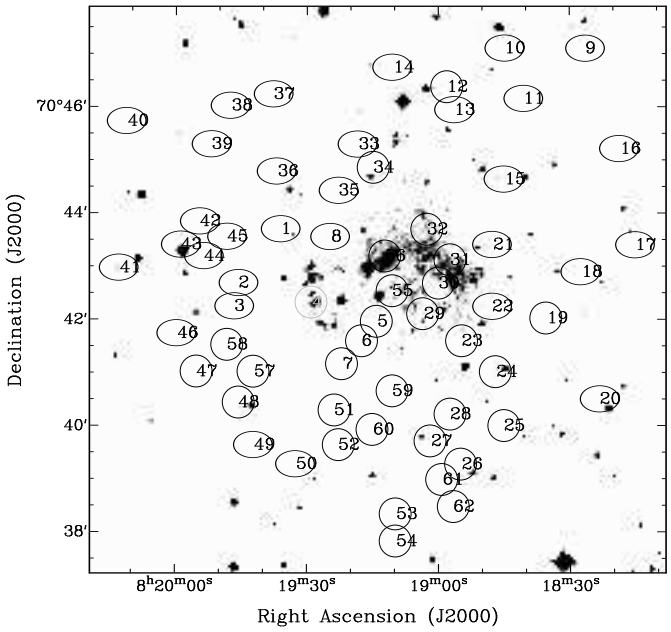

Fig. 47: *Holmberg II in the DSS2 blue optical image. Source positions and ID numbers correspond to Tab.18.*

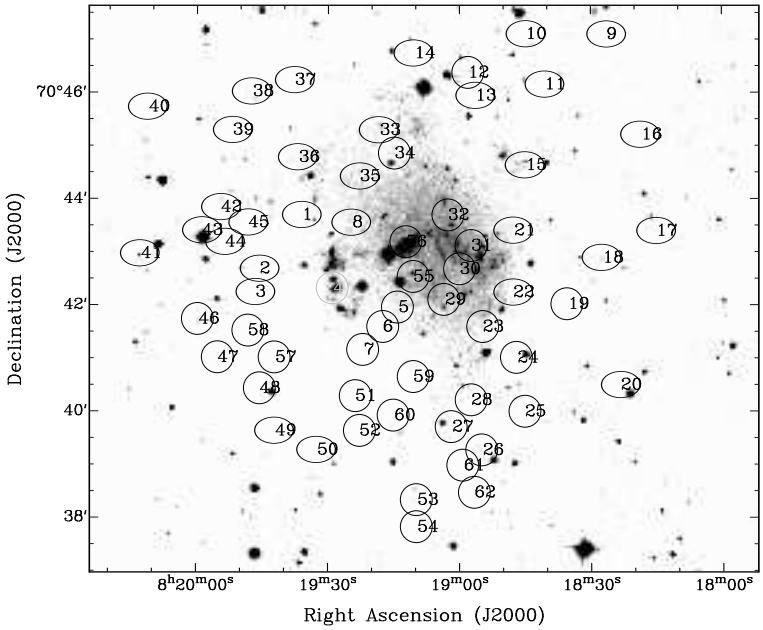

Fig. 48: *Holmberg II in the DSS2 red optical image. The emission is more extended than in the DSS2 blue data. Source positions and ID numbers correspond to Tab.18.*

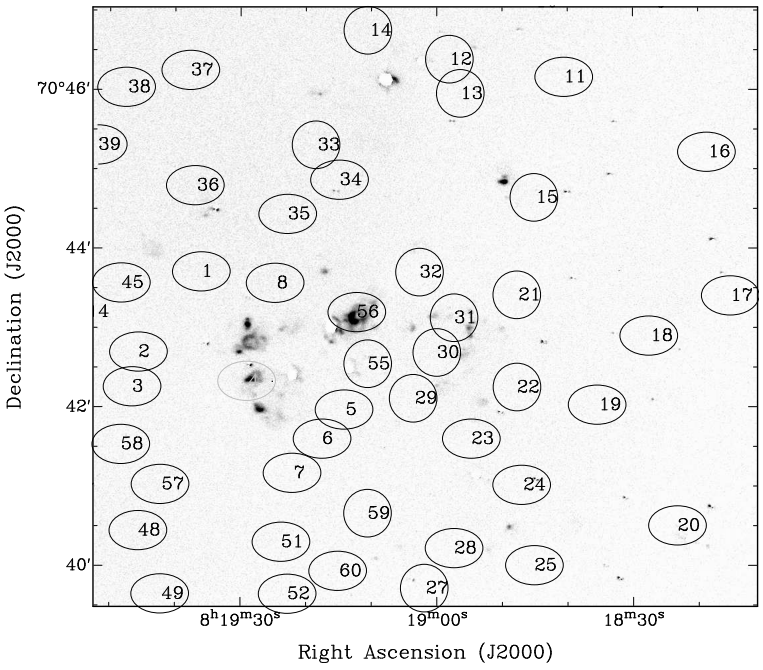

Fig. 49: *Holmberg II seen in Hα. See also Fig.52 for details of the emission around source ID 56. Note, that the FOV is smaller than for the other observations. Source positions and ID numbers correspond to Tab.18. Map by Kerp et al. (2002)*

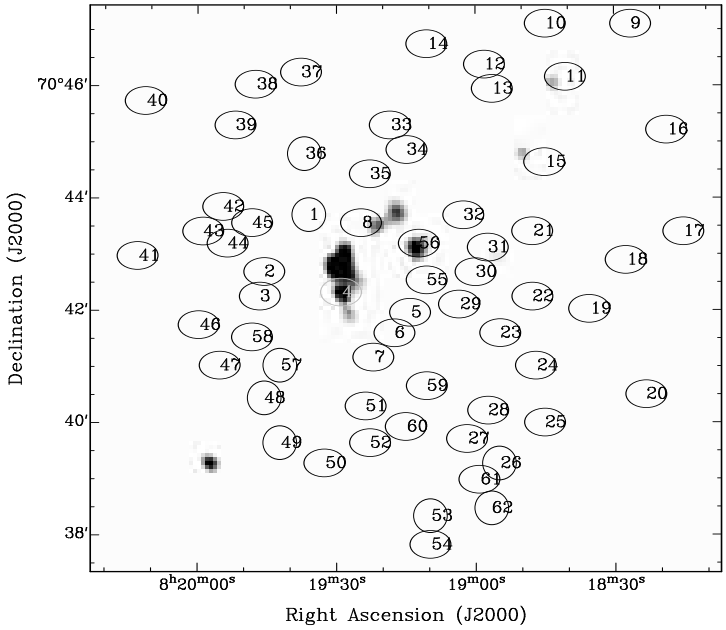

Fig. 50: *Holmberg II in the radio continuum emission at 6 cm wavelength (C band). Source positions and ID numbers correspond to Tab.18. The greyscale image is clipped to 0.1-0.6 mJy/Beam. Map by Kerp et al. (2002)*

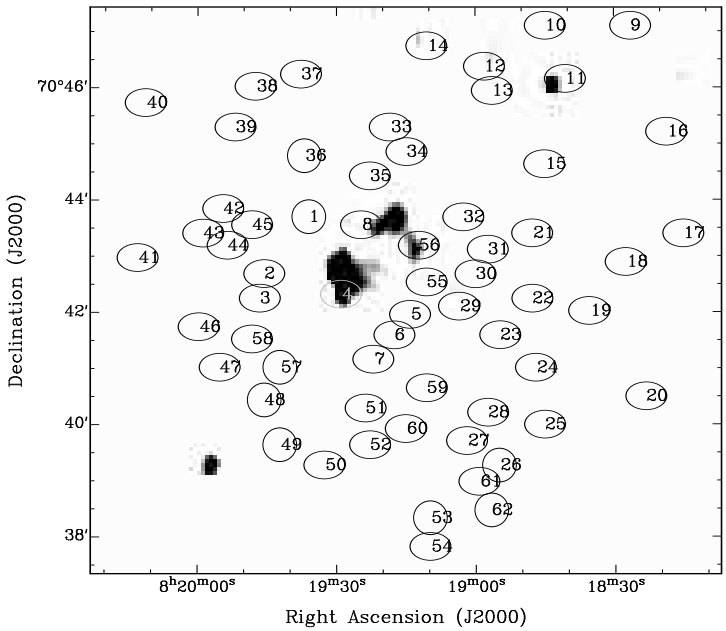

Fig. 51: *Holmberg II in the radio continuum emission at 21 cm wavelength (L band). Source positions and ID numbers correspond to Tab.18. The greyscale image is clipped to 0.2-0.7 mJy/Beam. Map by Kerp et al. (2002)*

Starting with the Hα data, which traces young star forming regions, there are two sources located at Hα regions, namely ID 4 and 56. These two are also seen in the radio continuum data and the DSS2 images. With the discussion above concerning ID 4 it is expected that this source shows up in all these wavelength. Source ID 56 is, according to its HR, a plasma source with a temperature of about $10^{5.5}$ K. Comparing its position with the HI data, it is located at a high column density region between three shells (Puche et al., 1992). Its appearance in the radio continuum bands indicates that the source or at least its environment produces synchrotron radiation. From the L and C–band data one can derive the spectral index of the sources ID 4 and 56. These give $\alpha = -0.66$ and $\alpha = -0.05$, respectively. The former spectral index argues for ID 4 being a supernova remnant while the latter spectral index is consistent with a non–thermal emission for source ID 56, likely an HII region (for a discussion on spectral indices, see e.g. Uyanıker et al., 2004, and references therein). In addition ID 56 shows up in the OM which also supports the idea of an HII region.

ID 56 shows the following picture (see also Fig.52): in Hα appears a bow–like structure surrounding a depleted region in the neutral gas. This might be a small HI shell which is not described in Puche et al. (1992). The radio continuum investigation gives a spectral index which is characteristic for non–thermal emission, typical for HII regions. The X–ray peak intensity is situated at the HI depletion although this is uncertain because the PSF size is of the order of the shell size in HI. However, the HR of the X–ray source is in agreement with a plasma model which indicates that the source is a supernova remnant. The radio emission peak is located on the Hα peak intensity, where also the OM data has its maximum. In summary, ID 56 is maybe hot gas filling an HI cavity and on the rim of the cavity new stars show up in an HII region, where also the DSS2 maps show their peak intensity. If this picture applies, then source ID 56 would be a fine example for the "standard model" of shells in dwarf irregular galaxies. However, this is probably not the creation process for *all* shells in Holmberg II, especially not for the shells at the outskirts of the galaxy HI distribution (see e.g. Bureau & Carignan, 2002).

Regarding the radio continuum images source ID 8 (ROSAT source 7 in Kerp et al. (2002)) is associated with C–band and L–band emssion. In the Hα maps this source is not detected. The power–law index is in agreement with the one found by Kerp et al. (2002) making it likely beeing an X–ray binary. Also sources ID 5 and 7 are in agreement with the findings of Kerp et al. (2002) who identified them as X–ray binaries.

Source ID 30 is associated with faint Hα emission in the southeast of its position. This Hα region is again located on the rim of an HI shells and indicates probably star formation due to swept up material from the shell creation by stellar activity, as described by the "standard model" of these shells. Source ID 30 is also visible in the DSS2 maps and according to its HR it fits well to a power–law model with index $\Gamma \approx 2$ and an intrinsic absorption of more than 10^{20} cm^{-2}. Last its luminosity is in agreement

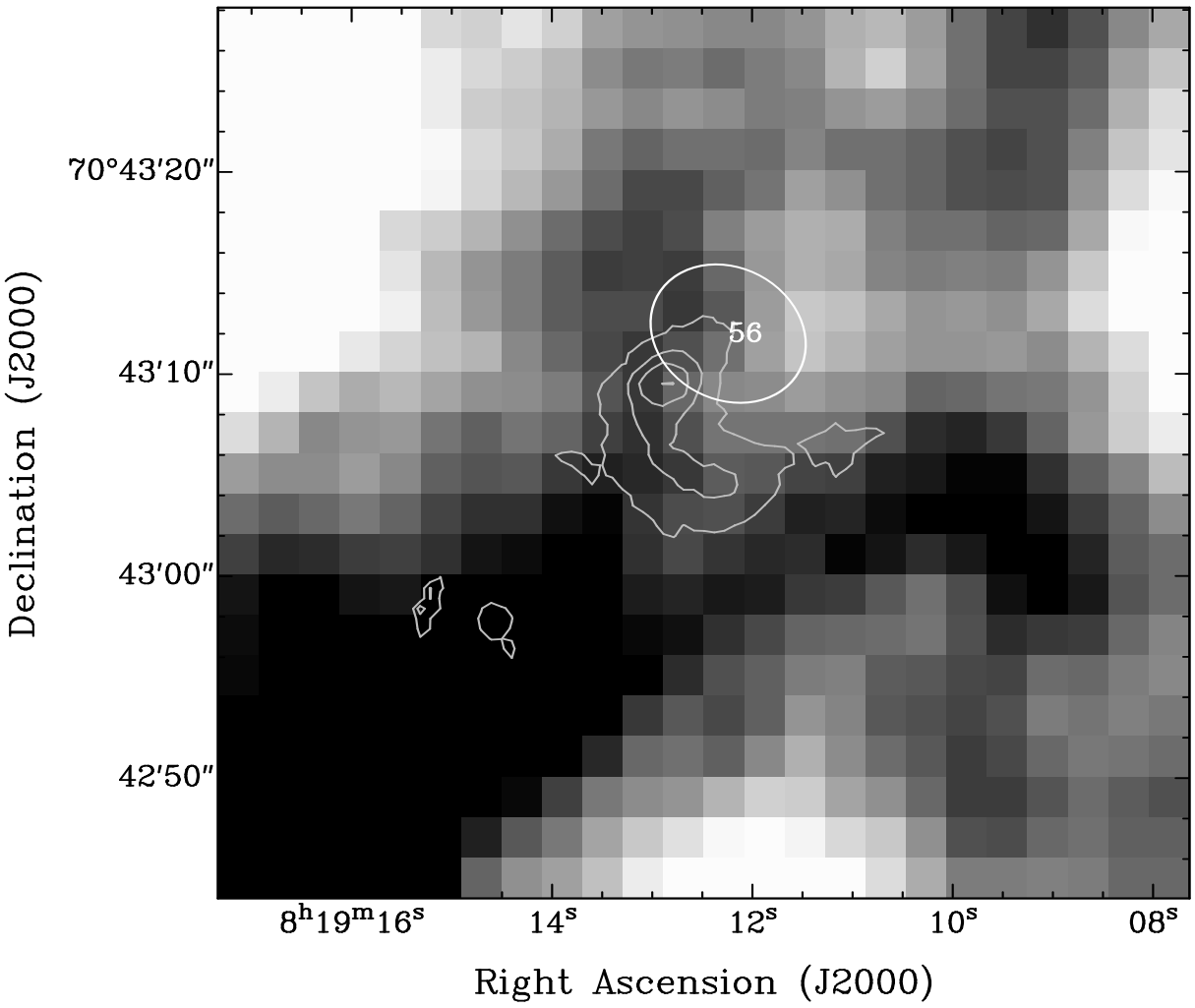

Fig. 52: *Blow–up of source ID 56 (numbered circle). The grey color image shows the* HI *distribution, the contours correspond to the Hα emission. The Hα emission shows a bow–like shape around a shell feature in the neutral gas where the peak of the X–ray intensity is situated.*

with an XRB and it is seen in the OM data, which makes it a good candidate for a HMXB.

In the remaining DSS2 images there are more sources associated with the optical wavelengths. Here, source ID 43 is related to emission in both, the blue and red filter as well as in the OM. However, the source shows only 3 counts in the B4 band and no counts in any other band after background correction. The flux is close to the detection limit and hence the classification remains unclear.

Several sources are located within the stellar body of Holmberg II which are ID 29, 31, 32, 55. Sources ID 31 and 32 show only counts in the B2 and B3 bands which makes a classification impossible. Sources ID 29 and 55 are located at the rim of two HI shells. The hardness ratio of ID 29 is comparable to a plasma model with $N_{\rm HI} \geq 1 \times 10^{21}$ cm^{-2} and a temperature of log(T[K])$\geq$ 5.5. Together with its luminosity it is concerned to be a supernova remnant. Source ID 55 has a HR which is in the "unclear" region where power–law and plasma model curves overlap. If one assumes it to be a plasma source, the parameters are $N_{\rm HI} \geq 1 \times 10^{21}$ cm^{-2} and log(T[K])$\geq$ 6.0 with a luminosity of $L_X = 2.67 \times 10^{37}$ erg s^{-1}. These figures are reasonable for a supernova remnant. But also if one assumes the source to be a power–law source (i.e. XRB) the values yield $N_{\rm HI} \geq 1 \times 10^{21}$ cm^{-2} and $\Gamma \approx 1.5$ and these are also in the physically allowed range. Together with its appearance in the OM also the interpretation of the source being an HMXB is possible.

The remaining sources have no counterparts in other data than X–rays. Hence, their nature can only be evaluated on the basis their luminosities and of the hardness ratios which is, as stated previously, not unambiguous. The likely classification of all sources is given in Tab.21 together with the respective luminosities and correlations with the other observations.

With the classification performed, now the statistical properties regarding the spatial distribution can be evaluated. First of all, the X–ray sources within HI shells, based on the studies by Puche et al. (1992) are identified. It turns out that only a few sources are in the very center of HI shells. These are ID 5, 11, 37 and 61. Source ID 5 is situated in the center of Puche et al. (1992) shell 32 and according to its HR it is an X–ray binary. Source ID 11 is inside shell 8 of Puche et al. (1992). In the vicinity there is also a radio continuum source with a spectral index of $\alpha = -1.46$ indicating that this source is a non–thermal synchrotron source. From the hardness ratio of ID 11 it can also be a plasma source which would fit nicely into the picture of the standard model. However, the radio continuum spectrum is very steep and it is more likely that the radio source is a background source not associated with Holmberg II. Both other sources ID 37 and 61 are not showing up in the hardness ratio diagrams and hence their nature remains unclear.

Nearly all other X–ray sources are on the rims of shells except sources ID 20, 40, 41, 46, 47 which are at the very edge of the HI distribution. Source ID 20 is compatible

Tab. 21: *Holmberg II X–ray to optical/radio correlation and X–ray luminosities. Here, the abbreviations denote: L→LMXR, H→HMXB, S→SNR, I→isolated binary, — →no classification. The sources with empty fields do only show up in the X–ray images and they are assumed to be XRB since no other types of sources can be related to these.*

ID	HR	OM	DSS2 red	DSS2 blue	Hα	C–band	L–band [10^{37} erg s^{-1}]	Luminosity	Classification
1	√						2.86	L	
4	√		√	√	√	√	641.64	S	
5	√							4.89	L
7	√							6.99	L
8	√					√	√	2.48	L
9	√						0.76	L	
10							0.64		
11	√						3.37	S?	
12	√						1.14	L	
13	√						0.57	L	
14	√						1.59	—	
15		√						1.02	
16	√						0.76	L	
17							0.25		
18	√						3.24	L	
19							0.45		
20	√	√						0.89	H
21	√						0.57	L	
22		√						0.38	
23	√	√						1.21	H
24		√						0.19	
25							0.06		
26							0.38		
27	√	√						1.40	H
28							0.70		
29	√	√	√	√				1.02	S
30	√	√	√	√	√			0.95	H
31		√	√	√				0.06	—
32		√	√	√				0.25	—

Tab. 22: *Table.21—continued*

ID	HR	OM	DSS2 red	DSS2 blue	Hα	C–band	L–band [10^{37} erg s^{-1}]	Luminosity	Classification
33	√						1.14	L	
34	√	√						1.08	H
35	√						1.46	S	
36	√						0.83	L	
37							0.13		
38	√						1.40	L	
39	√						0.57	L	
40							0.06		
41		√						0.13	
42							0.76		
43		√	√	√				0.06	H?
44	√						1.40	L	
45							2.22		
46							0.89		
47							1.02		
48							0.64		
49							0.25		
50	√						0.95	L	
51	√						3.75	L	
52	√						2.22	S	
53	√						2.92	L	
54	√						4.01	S or L	
55	√	√	√	√				2.67	S or H
56	√	√	√	√	√	√	√	2.48	S
57	√						1.59	S	
59	√						1.91	S or L	
60	√						2.35	L	
61							0.64		
62							0.76		

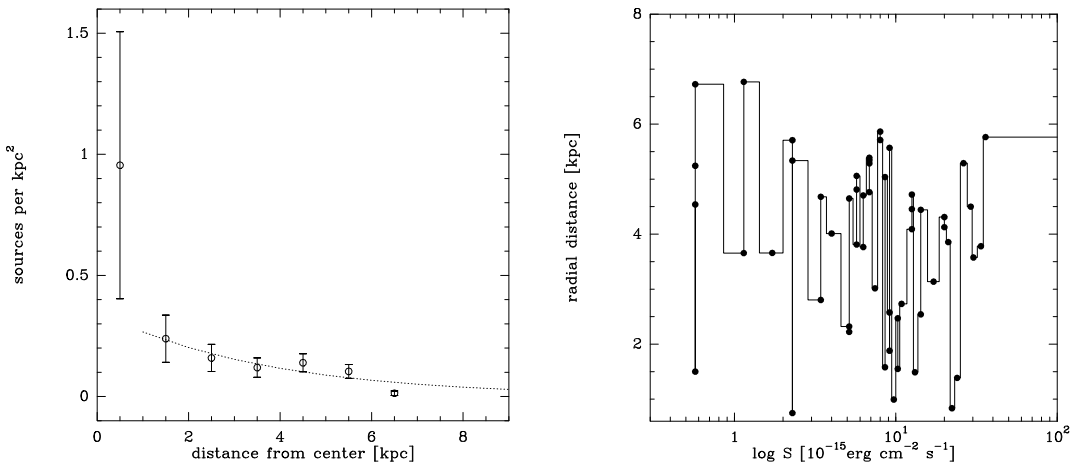

Fig. 53: **Left**: *The radial distribution of CHANDRA point sources. The dotted line shows an exponential fit to the data, excluding the very uncertain point in the center.* **Right**: *Radial distances as a function of source flux.*

with a power–law source, the other four have no HR. The vast majority of all X–ray sources are on the rims of HI holes which is not surprising, since the neutral gas of Holmberg II is dominated by holes and shells. Interestingly, the X–ray point sources fit very well into the picture of induced star formation on the rims of the HI shells. In general, the creation process of the shells itself is unclear in most cases, since most of the shells are empty (Bureau & Carignan, 2002).

As with the previous data, the radial distribution of the sources is investigated. Corrected for the inclination of $i = 47^{\mathrm{o}}$ the distribution of the point sources with respect to the morphological center is shown in Fig.53 (left). The radial distribution shows a general decline of the point source density towards the outer regions of the galaxy. The data, excluding the uncertain point in the very center, is fitted with an exponential function of the form $f(r) = a \cdot \exp(r/r_{\mathrm{o}})$, giving $a = 0.4 \pm 0.08$ and $r_{\mathrm{o}} = 3.6 \pm 0.9$. The general exponential decline is also seen in the R, B, U and FUV profiles (Stewart et al., 2000).

Up to 4 kpc the distribution follows the exponential decline while it is slightly off outside the 4 kpc radius. This small deviation disappears if one regards 2-σ uncertainties to the data points. Hence, it is attributed to the general appearance of the galaxy: it is dominated by the shells in the neutral gas and the point sources are more on the eastern than on the western side of the galaxy. This is also reflected in the distribution of the X–ray sources as a function of flux, as displayed in Fig.53 (right). Here, the point sources do not show any particular behavior concerning the dependency on the flux.

To get a deeper insight in the star formation of Holmberg II the XLF is evaluated. In Fig.54 the XLF is plotted. As in the IC 2574 case the XLF shows a break at $\approx 0.8 \times 10^{37}\,\mathrm{erg\,s^{-1}}$. Hence, a broken power–law is fitted to the data giving two slopes $\beta = -0.18 \pm 0.02$ for $L_X < 0.08 \times 10^{37}\,\mathrm{erg\,s^{-1}}$ and $\beta = -1.27 \pm 0.05$ for higher lu-

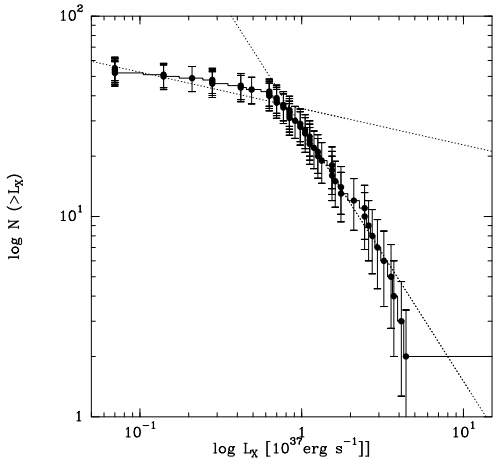

Fig. 54: *X–ray luminosity function of Holmberg II (CHANDRA data). The dotted lines correspond to a fit of a broken power–law with a break at* 0.8×10^{37} *erg s*$^{-1}$ *and slopes of* $\beta = -0.18 \pm 0.02$ *for* $L_X < 0.08 \times 10^{37}$ *erg s*$^{-1}$ *and* $\beta = -1.27 \pm 0.05$ *above this value.*

minosities. Following the discussion of the IC 2574 XLF the break luminosity here is also too low to be explained by a recent star burst or confusion effects. According to Stewart et al. (2000) the star formation in Holmberg II is sustaining and had no major burst in the past ≈ 10 Myr, although the star formation was not distributed uniformly across the HI body.

Moreover, the sources below the luminosity break are more concentrated at the south-western part of the galaxy and less at the northeastern part. This distribution is also traced by the FUV as reported by Stewart et al. (2000). The young star forming regions (2.5-4.5 Myr) are located at the highest HI column density region in the southwest, whereas the older ones (> 4.5 Myr) are in the north. Hence, the break in the XLF is attributed to the different ages of the X–ray point source population, reflecting the non–uniform star formation.

5.1.4.2 Diffuse emission Examination of the data with regard to diffuse soft emission in the X–ray regime covered by the B2-B4 bands gives no detection. With the net exposure time of 5198 s in the EPIC–*pn* data, the faint emission of coronal gas is hardly detectable. The flux limit in the B2 band for example yields a luminosity limit of about 1.6×10^{36} erg s^{-1}, but this refers to point sources since the flux is normalized to 3.5×PSF. For extended emission the flux limit in the B2 band amounts to 1.6×10^{-15} erg s^{-1} arcmin^{-2} equivalent to a luminosity of 2.0×10^{36} erg arcmin^{-2}. Down to this limit no diffuse soft emission is found in the processed data.

Following the argumentation of Bureau & Carignan (2002) this nondetection is to expect. They argue that the standard model, where supernovae and energetic stellar populations create the shells, is only valid for a small fraction of the holes found by Puche

et al. (1992). This is satisfied by the considerations outlined by Bureau & Carignan (2002):

The correlations presented by Puche et al. (1992) reflect physical properties of the host galaxy and not the creation mechanism of the shells. The Hα images show that many walls between the shells are lacking Hα emission and also the small holes are not preferentially filled with Hα emitters. Moreover the vast majority of the larger shells are not filled with coronal gas. Only the X–ray sources found outside the stellar body (Kerp et al., 2002) are good candidates for being supernova remnants; at least they indicate that the star formation in the past was located well outside the regions of recent star formation. Furthermore, Bureau & Carignan (2002) point out that the radio continuum observations by Tongue & Westpfahl (1995) only reveal the large energy input from supernovae in the inner part of the galaxy, not in the outer regions where shells are also found. The last argument is that inside the shells no underlying stellar component is found. Hence, the standard model is unlikely if one follows Bureau & Carignan (2002).They more favor a shell creation mechanism due to ram pressure effects and turbulent viscous stripping which is produced by the propagation of Holmberg II through the IGM of the M 81 group or at least a small subgroup of the M 81 group.

If this picture is correct, then no diffuse soft X–ray emission is expected, most of the shells can be explained by the ram–pressure and the remaining shells are products of subsequent supernovae, namely the shells filled with hot gas, as are found in the present investigation.

5.1.4.3 Summary With the XMM–Newton observation of Holmberg II taken from the archive the following results are obtained. In total there are 55 X–ray point sources detected within the HI distribution of Holmberg II. The log(N)-log(S) relation of these is well above the extragalactic background. In agreement with previous observations an ultra luminous X–ray source is detected. In addition ten of the sources can be attributed to supernova remnants (ID 4, 11, 29, 35, 52, 54-59). Here, the radio continuum data is used to constrain their nature. Four of them (ID 11, 54, 55, 59) may be also X–ray binaries, since their hardness ratios are in the ambiguous region where power–law and plasma models intersect.

Furthermore, 21 X–ray binaries are identified, which are most likely LMXB according to their luminosities. However, there is also a fraction of 24 sources which cannot be identified, since their flux is so low in the B bands that hardness ratios are very uncertain. Only three of them are correlated with optical emission in the DSS2 red and blue. Probably the unclear sources are isolated X–ray binaries which do not have to show up in the optical.

The spacial inspection of the point sources reveals an exponential decline of the number density with increasing radius from the morphological center. This is also seen in

the optical R, B, U and also FUV data by Stewart et al. (2000). The distribution of the point sources with respect to their fluxes is uniformly. The XLF shows a break at $0.8\times10^{37}\,\mathrm{erg\,s^{-1}}$ and hence a broken power–law fit is performed which yields slopes of $\beta = -0.18 \pm 0.02$ for $L_X < 0.08 \times 10^{37}\,\mathrm{erg\,s^{-1}}$ and $\beta = -1.27 \pm 0.05$ above. It is concluded that the break stems from different ages of the X–ray point source population which is pronounced towards the southwestern side of the galaxy (i.e. the southwest population is younger).

The search for diffuse emission in the soft bands B2 and B3 gave no result. It is concluded that the non–detection is not due to the relatively short exposure time of about 5200 s but rather it is simply not there, following the argumentation of Bureau & Carignan (2002). They attribute the HI morphology to ram–pressure effects and only in some cases to supernovae and energetic stellar activity, which is confirmed by the investigation of the XMM–Newton data.

5.1.5 NGC 1569

In contrast to the aforementioned galaxies this, NGC 1569, is a star burst dwarf galaxy. According to Stil & Israel (2002) the neutral ISM is characterized by turbulent motion. The velocity dispersion is twice that of other dIrrs. Although there is rotation in the outer parts of the HI distribution, the inner part (0.6 kpc, which is the major fraction of the optical galaxy) does not rotate at all. And even in the outer parts the turbulence due to the star burst is dominating.

This star burst is ≈25 Myr ago (Anders et al., 2004) and may be the cause for the turbulent ISM. The star clusters formed in this star burst show an offset of X–ray point sources with respect to the cluster center (Kaaret et al., 2004a). This offset can be explained assuming that the X–ray point sources are binary systems. The brighter X–ray sources are located nearer to the clusters indicating that they are younger objects.

Since NGC 1569 contains two prominent super star clusters (known as NGC 1569–A and –B) it was expected to find supernova remnants in these clusters. However, Greve et al. (2002) report that the immediate surroundings have no supernova remnants. They argue that the supernova remnants are absent because of a violent and turbulent outflow of material which does not allow supernova remnants to form.

Very recently Lisenfeld et al. (2004) found evidence for a convective wind which causes electrons to escape the halo of the galaxy. This is supported by X–ray observations (Martin et al., 2002) which give evidence for a shocked wind interacting with a gaseous halo. Apparently the wind itself is enriched by metals due to stellar evolution.

For this object XMM–Newton data and also CHANDRA data is investigated. The exposure time for the XMM–Newton data is 12160 s in the EPIC–*pn* instrument and

Tab. 23: *NGC 1569*

Morphological type	dIrr	
Position (J2000.0)	$\alpha = 04^{h}30^{m}48\overset{s}{.}81$ $\delta = 64^{d}51^{m}2\overset{s}{.}12$	
Distance	2.0 Mpc	(Makarova & Karachentsev, 2003)
HI mass (10^6 $M_\odot$)	130	(Stil & Israel, 2002)

the CHANDRA data amounts to 100220 s exposure time. With the very long exposure time of the CHANDRA one can hope to resolve the XMM–Newton sources very nicely. Since no HI FITS data were available only the outer contours of the HI content of the galaxy can be used. Here, the HI map of Mühle et al. (2005) (see Fig.55) is circumferenced by an ellipse (see Fig.56). The lowest column density encircled is $\approx 5 \times 10^{20}\,\mathrm{cm}^{-2}$. In addition the OM data can be used provided in the UVW 2 filter band (180-250 nm) and DSS2 in red and blue filter.

5.1.5.1 Point sources The smoothed XMM–Newton image of the combined M1M2 detectors (Fig.56) shows a bright source in the very center of NGC 1569. It is surrounded by diffuse emission. In the north this diffuse emission shows an arch–like shape while in the south there are two streaks towards the southwest. The east also shows an enhancement towards the radial direction. This morphology is in agreement with Fig. 5 of Martin et al. (2002) where they denote the archs and streaks as 'filaments'. According to this figure the arch is identified with filaments 11 and 13 while the streaks in the south correspond to filament 6 and 7. The XMM–Newton data, however, is dominated by the central emission and the morphology on scales smaller than one arcminute remains unclear for now. Since the angular resolution (i.e. PSF size) is too low to reveal point sources, the CHANDRA data of NGC 1569 is used provided by the archive.

The picture of X–ray emission becomes more clear in the CHANDRA data. Due to its higher angular resolution ($0\overset{''}{.}5$) and, in this case, the very long exposure time, the point source content can be separated from the diffuse emission. The adaptively smoothed CHANDRA image (minimal signal–to–noise of 5) in the PS band is shown in Fig.57. From this image the positions of point sources are taken. The detection limits in the individual bands are given in Tab.24. Martin et al. (2002) do not give any detection limits for their CHANDRA data but as the reader will see in the following, the detection limit in the present work is lower, thus fainter sources (down to the detection limit given in Tab.24) are detected here.

In total 62 point sources are found above the 4-σ threshold within the HI distribution of the galaxy. To ensure that the contribution of background sources is negligible, the

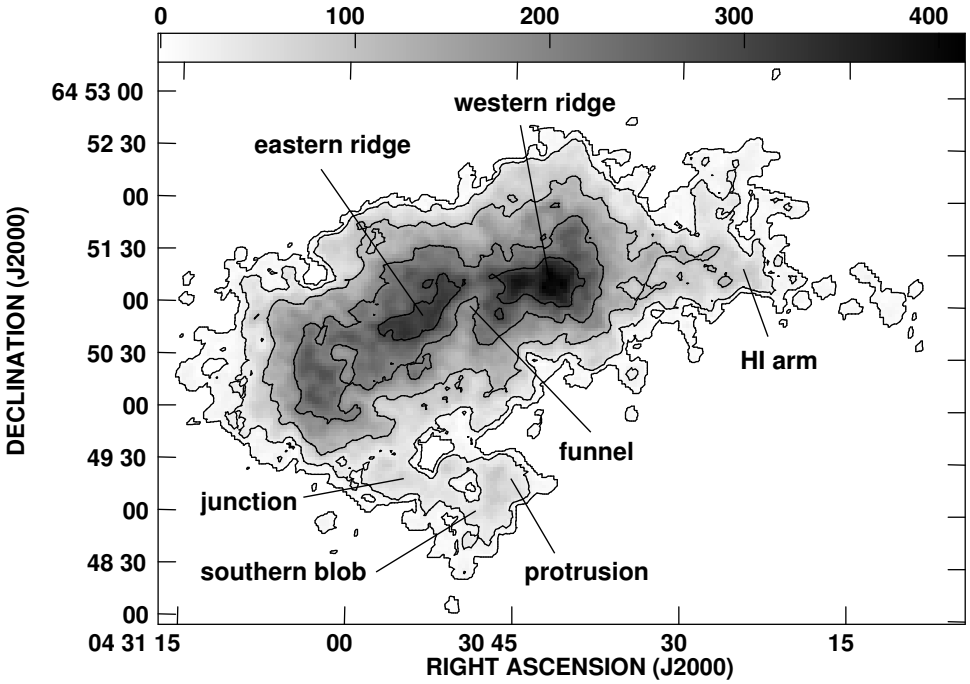

Fig. 55: HI *map of NGC 1569 taken from Mühle et al. (2005). The contour lines denote column densities at 0.5, 2.0, 4.0, 6.0* $\times 10^{21}$ cm^{-2}.

Tab. 24: *NGC 1569 flux limits of the CHANDRA data for individual bands normalized to the area of 3.5 PSF. The flux units are* 10^{-17} $erg\,cm^{-2}\,s^{-1}$.

Band	background counts	flux limit
B2	0.53±0.03	8.58±0.51
B3	0.35±0.03	1.59±0.13
B4	0.46±0.03	1.81±0.11
PS	1.94±0.10	14.17±0.71

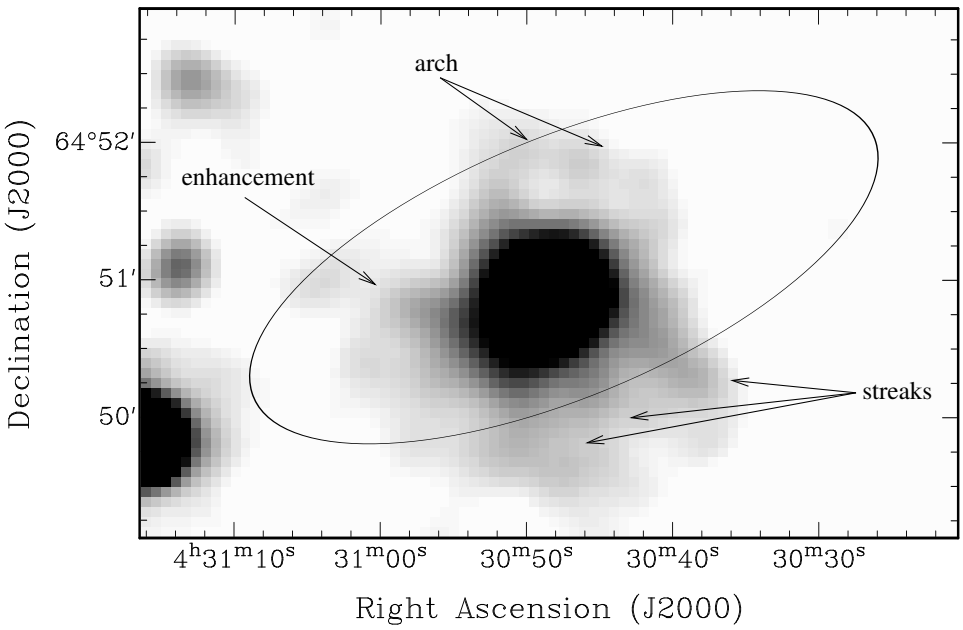

Fig. 56: *X–ray emission within the* HI *distribution of NGC 1569. The grey scale image shows the XMM–Newton M1M2 smoothed data in the PS band, clipped to 4-*σ *background level. The* HI *data (see Fig.55) is represented by the ellipse encompassing the* HI *distribution of the galaxy at a column density level of* $\approx 5 \times 10^{20}$ cm^{-2}.

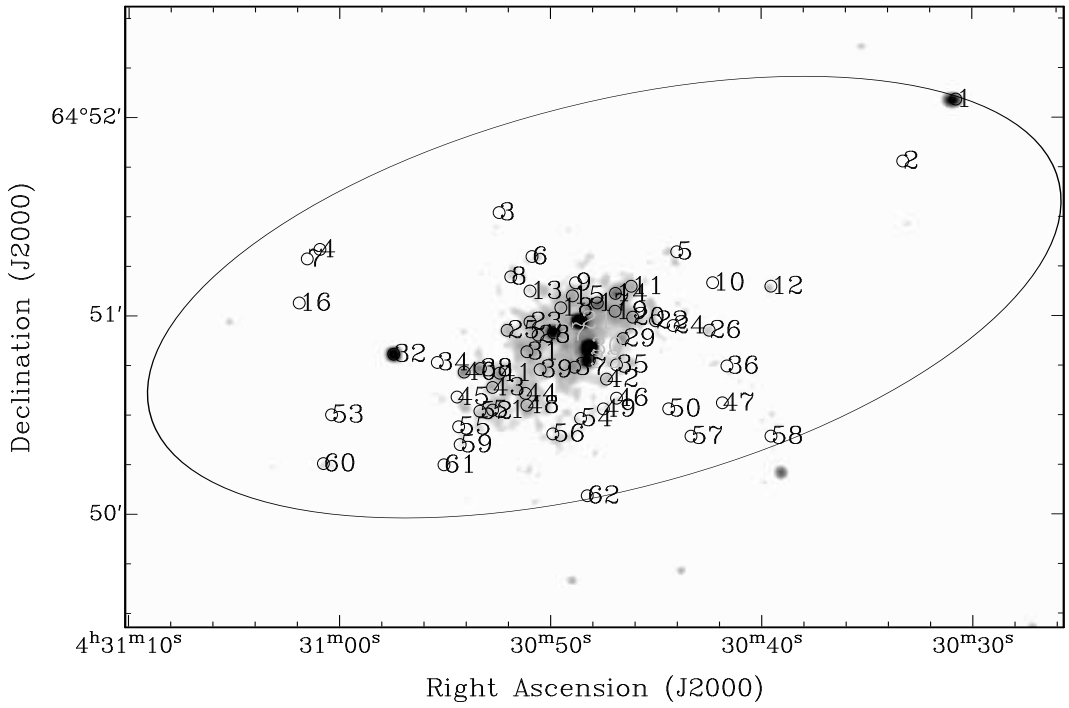

Fig. 57: *Gaussian smoothed CHANDRA image in the PS band, clipped to 4-σ above background. The grey scale image is a square root representation of the data. The circles mark the X–ray point sources found. Note the patchy structure of the X–ray emission in the center of the galaxy. The big ellipse represents the* HI *contour at* $N_{\rm HI} \approx 5 \times 10^{20}\ cm^{-2}$.

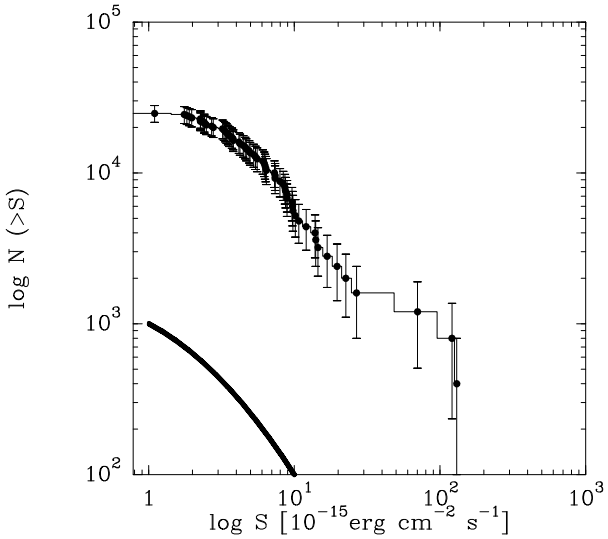

Fig. 58: *Comparison of the log(N)-log(S) relation of NGC 1569 (CHANDRA data) with the extragalactic X–ray background. With respect to the uncertainty of the number of point sources in the galaxy, the relation is well above the extragalactic relation derived by Hasinger et al. (2001). The thick line, again, represents the upper limit of the XRB.*

log(N)-log(S) relation of the point sources, scaled to the area of one square degree, is evaluated and displayed in Fig.58. Unfortunately, Martin et al. (2002) do not give the log(N)-log(S) relation and also not the detection limits. According to their Table 1 the faintest source detected above 3-σ has a flux of 6.1×10^{-17} erg s^{-1} cm^{-2} which is comparable to the flux limit in the PS band of the data presented here. Based on this, the number of point sources should be more or less equal but Martin et al. (2002) restrict their point source detection to sources which are smaller than 2 times the size of the CHANDRA PSF while I do not restrict the point sources found.

The detected point sources with position, flux, luminosity and counts in the B bands are given in Tab.25. In contrast to the work of Martin et al. (2002) where the source detection was done with the `celldetect` algorithm, here the source "detection" by eye reveals ≈30 % more point sources. This generally shows the uncertainty in automated tasks with respect to the more straight forward approach of image smoothing, noise estimation and clipping. In particular, the image is smoothed with a 2-D Gaussian of half the PSF size, which provides a Gaussian noise. From that the noise uncertainty is simply the standard deviation. Clipping the image data to $4-\sigma$ above the background noise then gives the point sources.

Since only a very small number of point sources have one or less counts (ID 2, 19, 25 and 50) the hardness ratios can be given for all remaining point sources. The HR diagrams are given in two different ways, one with the source IDs and one with the uncertainty (i.e. errorbars), both displayed in Fig.59. The HR diagram shows, again, two sources in the upper left corner (ID 12, 16). Within 2.5-σ uncertainties ID 12 and

Tab. 25: *The X–ray point sources found by CHANDRA in NGC 1569. The flux units are 10^{-15} erg cm^{-2} s^{-1} in the PS band, the luminosity units are 10^{37} erg s^{-1}, the luminosity uncertainty is of the order of the relative flux uncertainty. The stars mark sources with one or less counts in one band after background subtraction. The last three columns give the background corrected counts in the corresponding band.*

ID	Right Ascension (J2000.0)	Declination (J2000.0)	Flux	Luminosity	B2	B3	B4
1	$04^h30^m30.96$	$64^o\ 52'\ 5.47$	16.80 ± 1.11	0.97	10	49	109
2*	$04^h30^m33.28$	$64^o\ 51'\ 46.79$	1.10 ± 0.28	0.06	5	0	0
3	$04^h30^m52.43$	$64^o\ 51'\ 31.64$	2.78 ± 0.45	0.16	8	12	9
4	$04^h31^m0.93$	$64^o\ 51'\ 20.32$	1.90 ± 0.37	0.11	2	10	6
5	$04^h30^m44.02$	$64^o\ 51'\ 19.81$	3.80 ± 0.53	0.22	4	14	24
6	$04^h30^m50.89$	$64^o\ 51'\ 18.36$	4.17 ± 0.55	0.24	3	21	26
7	$04^h31^m1.54$	$64^o\ 51'\ 17.37$	1.76 ± 0.36	0.10	7	5	6
8	$04^h30^m51.89$	$64^o\ 51'\ 11.96$	4.46 ± 0.57	0.26	4	27	22
9	$04^h30^m48.80$	$64^o\ 51'\ 10.48$	6.28 ± 0.68	0.36	6	30	33
10	$04^h30^m42.32$	$64^o\ 51'\ 10.45$	2.41 ± 0.42	0.14	5	6	7
11	$04^h30^m46.10$	$64^o\ 51'\ 9.49$	8.62 ± 0.79	0.50	2	54	49
12	$04^h30^m39.46$	$64^o\ 51'\ 8.96$	1.98 ± 0.38	0.11	4	2	5
13	$04^h30^m50.96$	$64^o\ 51'\ 7.53$	4.97 ± 0.60	0.29	2	22	38
14	$04^h30^m46.95$	$64^o\ 51'\ 7.03$	12.05 ± 0.94	0.70	2	62	80
15	$04^h30^m48.96$	$64^o\ 51'\ 6.05$	9.72 ± 0.84	0.56	2	68	46
16	$04^h31^m1.92$	$64^o\ 51'\ 4.08$	2.27 ± 0.41	0.13	10	3	10
17	$04^h30^m47.72$	$64^o\ 51'\ 4.08$	14.54 ± 1.03	0.84	7	79	83
18	$04^h30^m49.50$	$64^o\ 51'\ 3.10$	10.15 ± 0.86	0.59	3	63	53
19*	$04^h30^m46.95$	$64^o\ 51'\ 1.62$	14.03 ± 1.01	0.81	1	87	89
20	$04^h30^m46.10$	$64^o\ 51'\ 0.14$	9.79 ± 0.85	0.57	5	65	55
21	$04^h30^m48.65$	$64^o\ 50'\ 59.16$	70.19 ± 2.26	4.06	22	253	463
22	$04^h30^m45.02$	$64^o\ 50'\ 58.66$	5.26 ± 0.62	0.30	6	39	22
23	$04^h30^m50.89$	$64^o\ 50'\ 58.68$	8.69 ± 0.80	0.50	2	48	55
24	$04^h30^m44.17$	$64^o\ 50'\ 57.67$	3.58 ± 0.51	0.21	9	18	13
25*	$04^h30^m52.04$	$64^o\ 50'\ 56.22$	6.07 ± 0.67	0.35	1	22	49
26	$04^h30^m42.47$	$64^o\ 50'\ 56.19$	3.44 ± 0.50	0.20	3	26	13
27	$04^h30^m49.81$	$64^o\ 50'\ 55.72$	26.73 ± 1.40	1.55	9	111	161
28	$04^h30^m50.58$	$64^o\ 50'\ 54.25$	13.88 ± 1.01	0.80	8	77	81
29	$04^h30^m46.56$	$64^o\ 50'\ 53.25$	7.96 ± 0.76	0.46	4	58	30
30	$04^h30^m48.11$	$64^o\ 50'\ 50.80$	130.40 ± 3.09	7.55	60	710	827
31	$04^h30^m51.12$	$64^o\ 50'\ 49.33$	10.74 ± 0.89	0.62	6	67	56

Tab. 26: *Table.25—continued*

ID	Right Ascension (J2000.0)	Declination (J2000.0)	Flux	Luminosity	B2	B3	B4
32	$04^h30^m57.45$	$64^o\ 50'\ 48.84$	22.57 ± 1.28	1.31	8	36	171
33	$04^h30^m48.11$	$64^o\ 50'\ 46.86$	120.90 ± 2.97	7.00	53	625	784
34	$04^h30^m55.36$	$64^o\ 50'\ 46.38$	2.27 ± 0.41	0.13	4	9	6
35	$04^h30^m46.87$	$64^o\ 50'\ 45.38$	6.43 ± 0.69	0.37	4	37	33
36	$04^h30^m41.63$	$64^o\ 50'\ 44.86$	3.29 ± 0.49	0.19	3	23	13
37	$04^h30^m48.88$	$64^o\ 50'\ 44.40$	19.65 ± 1.20	1.14	8	88	123
38	$04^h30^m53.28$	$64^o\ 50'\ 44.41$	7.31 ± 0.73	0.42	8	36	38
39	$04^h30^m50.50$	$64^o\ 50'\ 43.91$	8.91 ± 0.81	0.52	3	63	47
40	$04^h30^m54.05$	$64^o\ 50'\ 43.43$	6.21 ± 0.67	0.36	4	29	37
41	$04^h30^m52.43$	$64^o\ 50'\ 42.44$	8.91 ± 0.81	0.52	9	48	43
42	$04^h30^m47.34$	$64^o\ 50'\ 40.95$	5.41 ± 0.63	0.31	4	41	19
43	$04^h30^m52.74$	$64^o\ 50'\ 38.51$	7.38 ± 0.73	0.43	6	42	36
44	$04^h30^m51.20$	$64^o\ 50'\ 36.54$	9.64 ± 0.84	0.56	4	64	50
45	$04^h30^m54.44$	$64^o\ 50'\ 35.56$	4.68 ± 0.58	0.27	7	26	23
46	$04^h30^m46.87$	$64^o\ 50'\ 35.05$	3.80 ± 0.53	0.22	8	28	11
47	$04^h30^m41.86$	$64^o\ 50'\ 34.04$	1.83 ± 0.37	0.11	4	10	5
48	$04^h30^m51.12$	$64^o\ 50'\ 33.09$	8.40 ± 0.78	0.49	6	54	42
49	$04^h30^m47.49$	$64^o\ 50'\ 32.10$	4.90 ± 0.60	0.28	6	35	20
50*	$04^h30^m44.41$	$64^o\ 50'\ 32.09$	2.41 ± 0.42	0.14	1	11	11
51	$04^h30^m52.74$	$64^o\ 50'\ 32.11$	7.38 ± 0.73	0.43	4	47	41
52	$04^h30^m53.36$	$64^o\ 50'\ 31.13$	6.36 ± 0.68	0.37	6	41	30
53	$04^h31^m0.38$	$64^o\ 50'\ 30.63$	2.27 ± 0.41	0.13	2	14	6
54	$04^h30^m48.57$	$64^o\ 50'\ 29.15$	4.60 ± 0.58	0.27	9	28	17
55	$04^h30^m54.36$	$64^o\ 50'\ 26.70$	4.24 ± 0.56	0.25	9	18	20
56	$04^h30^m49.88$	$64^o\ 50'\ 24.73$	5.55 ± 0.64	0.32	4	37	27
57	$04^h30^m43.33$	$64^o\ 50'\ 23.72$	2.71 ± 0.44	0.16	2	13	12
58	$04^h30^m39.55$	$64^o\ 50'\ 24.19$	3.51 ± 0.51	0.20	6	23	11
59	$04^h30^m54.28$	$64^o\ 50'\ 21.29$	3.73 ± 0.52	0.22	8	17	18
60	$04^h31^m0.76$	$64^o\ 50'\ 15.87$	3.22 ± 0.48	0.19	7	16	13
61	$04^h30^m55.05$	$64^o\ 50'\ 15.38$	2.49 ± 0.43	0.14	4	15	8
62	$04^h30^m48.27$	$64^o\ 50'\ 5.53$	3.36 ± 0.50	0.19	4	15	16

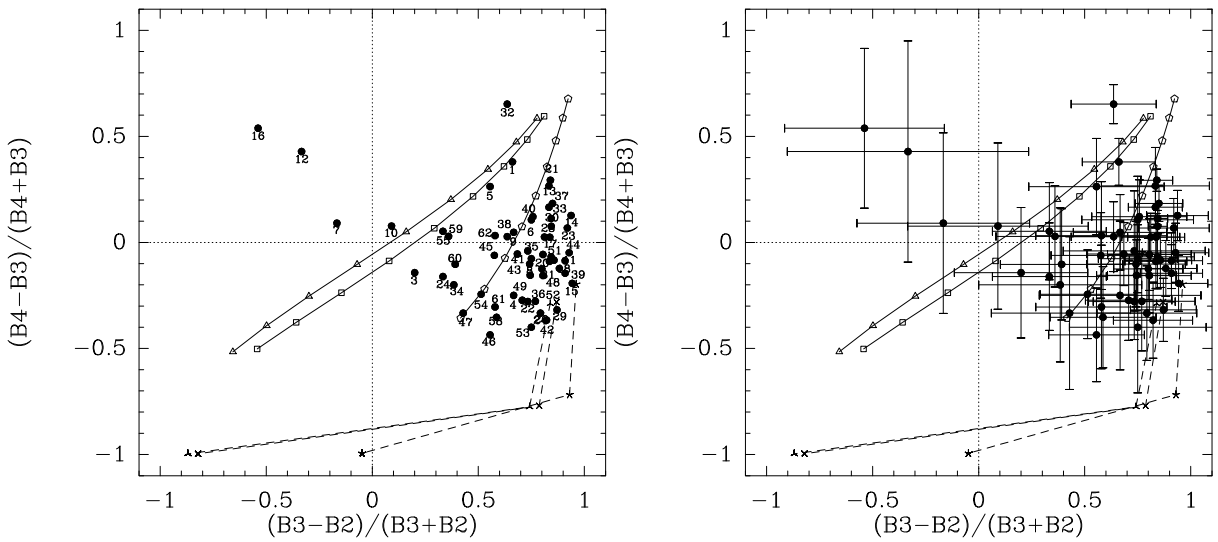

Fig. 59: *HR for the point sources found in NGC 1569 (CHANDRA data). The numbers correspond to the IDs of Tab.25. All errorbars correspond to an uncertainty of 1-σ. The dashed and solid lines are described in detail in the caption of Fig.19 and the accompanying text.*

ID 16 are in the range of the power–law models. According to the count rates in each B band (B2=10 cts, B3=3 cts, B4=10 cts) ID 16 cannot be a background AGN since the B2 band is not heavy absorbed and the source is located at an HI column density of $\approx 2.0 \times 10^{21}\,\mathrm{cm}^{-2}$. This column would absorb X–rays below 0.5 keV essentially (see e.g. Kerp et al., 2002). On the other hand the DSS2 red and blue images reveal an optical counterpart at the position in question, leading to the picture of a foreground star producing the X–ray emission. This argumentation is also true for the source ID 12 which shows up at even higher column densities ($\approx 5.0 \times 10^{21}\,\mathrm{cm}^{-2}$).

All other sources occupy the right hand region in the diagram. Here, the plasma sources are more separated from the power–law sources than in the XMM–Newton HR diagram. Even so, there are also sources in the transition region between plasma and power–law models. In the following I give a list of source IDs in the three regions:

- Plasma sources: 11, 15, 18, 20, 22, 26, 29, 31, 36, 39, 42, 44, 48, 49, 51, 53, 56
- Power–law sources: 1, 3, 5-10, 12-14, 16, 17, 21, 23, 24, 27, 28, 30, 32-34, 37, 38, 40, 41, 43, 45, 47, 55, 57-62
- Transition region: 4, 18, 35, 46, 52, 54

First of all, the number of plasma sources is high in contrast to the galaxies investigated before. Since the number of supernova remnants in dwarf galaxies is expected to be not so high, due to their low star formation rate, the high number of plasma sources

here is attributed to the bipolar outflow of hot gas as reported by many authors (see e.g. Martin et al., 2002; Stil & Israel, 2002; Anders et al., 2004; Lisenfeld et al., 2004). The point sources are then high density regions within the diffuse component. This is supported by the patchy appearance of the emission morphology.

At this point, I like to point to an issue concerning the models in the HR diagram. Referring to Martin et al. (2002) the source ID 40 is found to be a supernova remnant. They argue that the radio continuum spectral index of $\alpha = -0.9$ is typical for an evolved supernova remnant. Also they find a shell in the optical line emission in [OIII] and [SII]. Moreover this source shows up in their HR diagram at a position which is compatible with a black body emission model. In this investigation, the source shows up as a power–law source in Fig.59.

At first glance, these two findings seem to contradict each other. To disentangle this appearant contradiction one has to evaluate the behavior of different models in the HR diagram. Therefore, the black body model of *sherpa* is used to calculate tracks for different temperatures of $10^{5.0...7.0}$ K, where the exponent increases in steps of 0.5 (from bottom to top in Fig.60) and for absorbing column densities of $N_{HI} = 1 \times 10^{19...20...21}$ cm^{-2} (from left to right in the same figure). For these models of black body emission in the HR diagram one finds an interesting fact: for temperatures below $10^{5.5}$ K the black body models occupy the same region as the plasma models and for higher temperatures they are in the region of high absorbed ($N_{HI} \approx 10^{21}$ cm^{-2}) power–law models. Hence, the contradiction is due to the degeneracy of the black body and power–law models in the HR diagram.

In this context I would like to note, that the behavior of the model curves in the HR diagram is quite sensitive to the choice of the X–ray bands. The separation of power–law and plasma models turns out to be better in the present work than in the work of Martin et al. (2002) although they claim that their energy bands were chosen carefully.

Comparing Fig.60 with Fig.59 reveals that source ID 40 is in agreement with a power–law and a black body model. As described by Martin et al. (2002) this source is a supernova remnant. With the discussion of the black body models in the HR diagram the X–ray source may not be the supernova remnant itself but the residual compact object inside the remnant which might be a cooling neutron star, explaining the black body radiation. However, a cooling neutron star is only visible in X–rays for a short time and hence it is hard to tell whether the X–rays come from the hot gas filled shell or from the central object. In summary this source exemplifies how the different emission models overlap in the HR diagram and more over it shows that source identification on the basis of X–ray data alone can lead to substantial misinterpretations, hence, additional data in other wavelengths are always eligible.

From the power–law sources eight are very bright (ID 1, 17, 21, 27, 30, 32, 33). Except source ID 1 all of them have optical counterparts in both DSS2 blue and red. In the XMM–Newton OM only ID 17, 21, 27 and 30 have optical counterparts. These

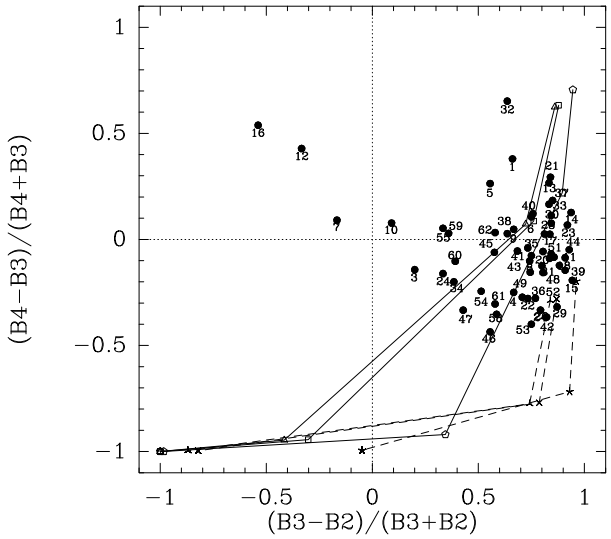

Fig. 60: *HR for the point sources found in NGC 1569 (CHANDRA data). The numbers correspond to the IDs of Tab.25. The solid lines represent black body models with temperatures of $10^{5.0...7.0}$ K, where the exponent increases in steps of 0.5 (from bottom to top) and absorbing column densities of $N_{HI} = 1 \times 10^{19...20...21}$ cm^{-2} (from left to right). Compare this to Fig.59.*

are interpreted as HMXB while the others are most likely LMXB. The four brightest sources in the central region of NGC 1569 (ID 21, 27, 30, 33) were investigated by Heike et al. (2003) recently. They found that ID 30 is a stellar black hole and the other three sources are binary systems. These findings are based on the variability of the sources.

The plasma sources are likely not all supernova remnants according to their patchy morphology. All of them are located south of the major axis of the galaxy. Since the galaxy is inclined by 60^{o}, the asymmetry is attributed to the inclination; we look at the "bottom" of the galaxy which is not obscured by the HI disk, as in contrast to the "top" (north) of the galaxy which is obscured by the disk itself (see also Stil & Israel, 2002). Since the absorption of the disk at the leading edge of the galaxy attenuates soft X–rays, no soft plasma sources are visible north of the major axis.

In other words, if the plasma sources are dense plasma regions within the bipolar outflow (e.g. Martin et al., 2002) (or accumulated material on the line of sight, i.e. projection effects), one would expect to detect only the emission south of the major axis and not north of it, because this emission would be absorbed by the leading edge of the gas disk. This finding is in concordance with Martin et al. (2002) - see their sketch Fig.13.

The only source deviating from this geometric effect is source ID 53. It is located in the very east of the HI disk at a low column density region compared to its surroundings. Here, the source may be hot gas filling the cavity but on the other hand the DSS2 images show a bright star at this position. Hence, the object is more likely a foreground

star.

The sources in the HR diagram transition region are more difficult to identify. Most of these, except ID 4 are also located beneath the major axis. It is concluded that these sources are also related to the hot gas outflow and represent even dense regions within the hot gas or are features arising from projection effects within the hot gas. Source ID 4 is situated in the northwest at the edge of the HI distribution. This location does not argue for source ID 4 belonging to the diffuse outflow of the galaxy. Since there is no counterpart in the optical this source is most likely an isolated accreting binary system or a background source like an AGN.

5.1.5.2 Super star clusters (SSC) In the center of NGC 1569, right between the eastern and western high column density HI regions (see e.g. map in Stil & Israel (2002), their Fig. 3, upper panel), there are two super star clusters (SSC) frequently referred to as SSC-A and SSC-B. As reported by Greve et al. (2002) SSC-A decomposes into two sub–clusters. The SSC are associated with UV emission in the OM data showing young hot stars within the SSC. The number of stars in each SSC is about $10^{5...6}$. Given the positions of both SSC no X–ray point sources are correlated with them. Figure61 shows the X–ray point sources as circles superimposed on the adaptively smoothed CHANDRA image together with the SSC positions marked with crosses and OM contours.

The SSC are not correlated positionally with any X–ray point source. Only ID 21 is close to SSC-A. The region of UV emission is also filled with diffuse X–ray emission, which is most likely gas heated by the stellar activity at this region. As reported by Martin et al. (2002) the region may be the cause for the outflow of coronal gas. This is also supported by the detection of supernova remnants and radio supernovae within an area of ≈ 300 pc diameter around SSC-A and B (Greve et al., 2002). Moreover, locally metal–enriched gas has not been found (Kobulnicky & Skillman, 1997) which also argues for the blow–away of the material due to stellar activity. Finally, the metal–enriched material is found in the outflow detected in X–rays as reported by Martin et al. (2002)

In the region of UV emission and its surroundings there are 11 X–ray point sources detected with CHANDRA which are power–law sources (ID 14, 17, 21, 23, 27, 28, 30, 33, 35, 37, 42) and some plasma sources which are, as described above, attributed to the outflow of coronal gas, except source ID 20 which is in positional agreement with a thermal radio source (source No. 6 of Greve et al., 2002) which they claim is most likely an HII region.

The SSC clusters are correlated with the UV as well as with the diffuse X–ray emission. The old X–ray binary systems are located outside the UV emission. The UV emission itself is coming from the young stars in the SSC as they are in positional agreement within the PSF of the OM. The accreting X–ray sources are older objects

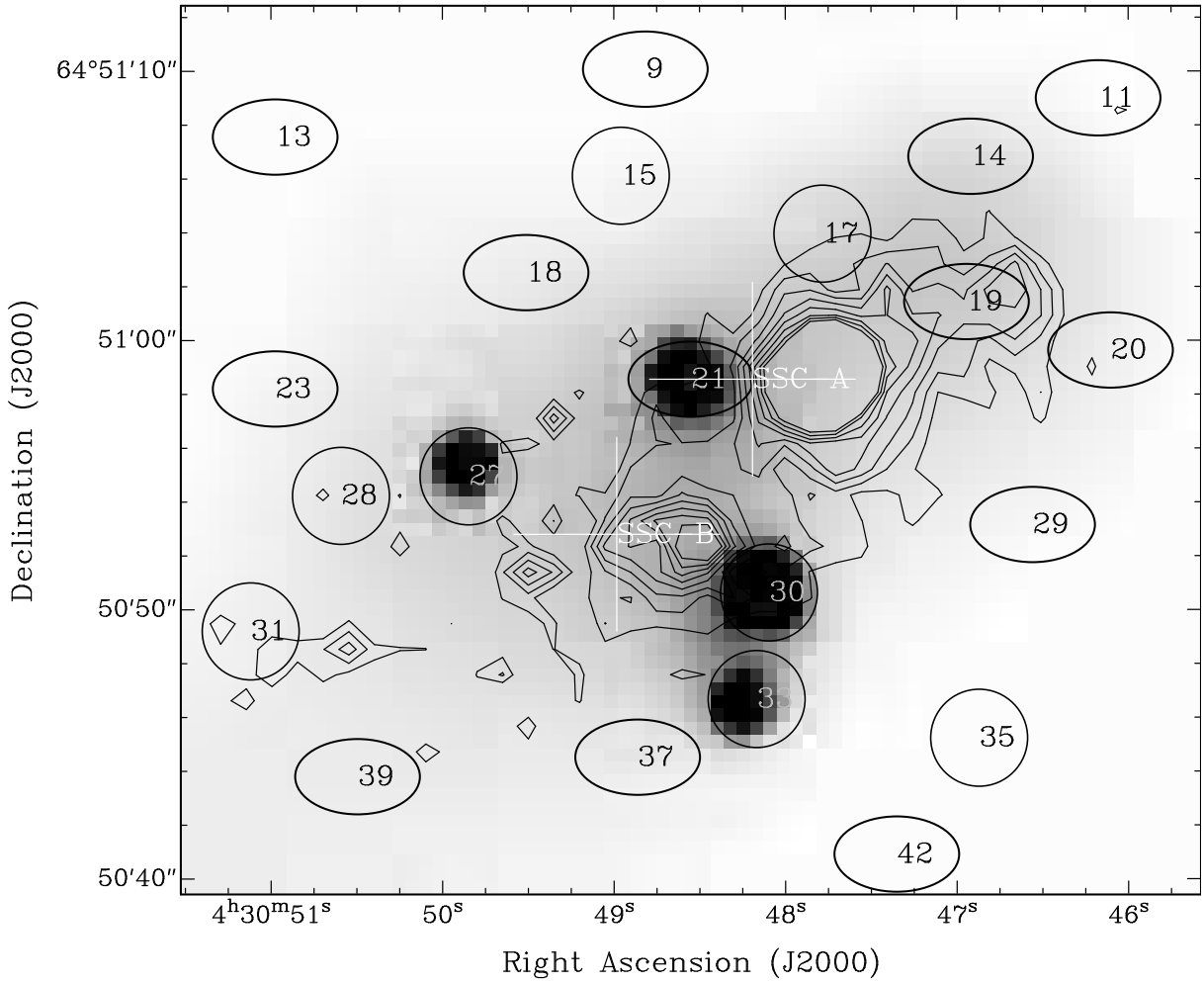

Fig. 61: *X–ray point sources as circles superimposed on the adaptively smoothed CHANDRA image together with the SSC positions marked with crosses. The SSC are not in positional agreement with X–ray point sources. The positional offset of the SSC positions and the UV data likely stems from the PSF of the OM of about 1″. The main diffuse X–ray emission comes from the region between both SSC. Contours correspond to the UV emission of XMM–Newton OM starting with 4-σ above background.*

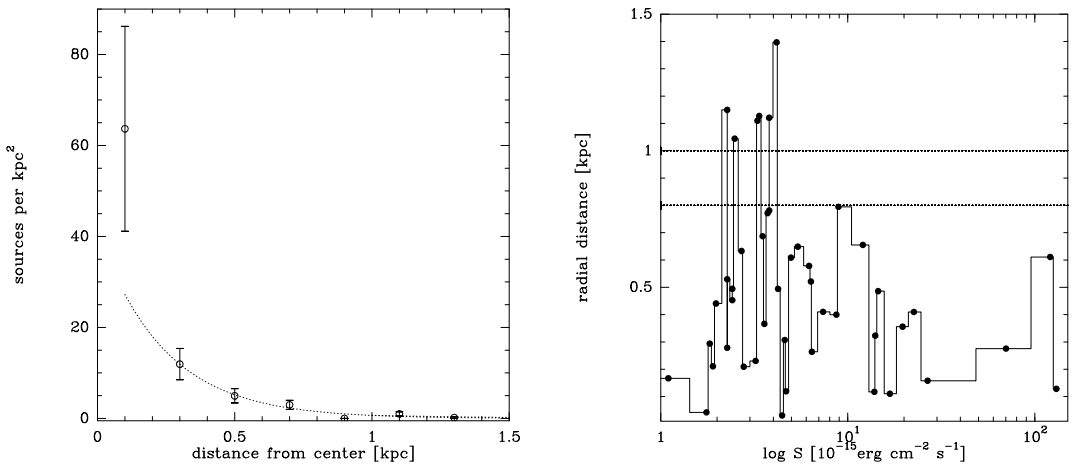

Fig. 62: **Left**: *The radial distribution of CHANDRA point sources in NGC 1569. The dotted line shows an exponential fit to the data, excluding the very uncertain point in the center.* **Right**: *Radial distances as a function of source flux. The dotted lines mark the region where no point sources are found. This corresponds to the drop in the left hand view graph.*

which may have been generated within the SSC and now they dissipated towards the outer edge of the region of high stellar activity.

As with the investigations performed before, the spatial distribution of the X–ray point sources of NGC 1569 are regarded in the following. All plasma sources which are attributed to density or line of sight effects in the diffuse outflow are excluded from this analysis, since they would give rise to features — e. g. in the XLF — which are not related to stellar components.

First, the number of sources per square degree as a function of center distance is given in Fig.62 (left) together with the source center distances as a function of flux (right). The (deprojected) surface density of the X–ray point sources declines exponentially. The fit to the data, excluding the uncertain inner data pint, gives a characteristic radial scale length of $r_o = 0.24 \pm 0.01$ kpc. Between radii of 0.8 and 1.0 kpc no sources are detected.

This is also seen in the flux dependency of the distances. Here, the ring between 0.8 and 1.0 kpc is devoid of point sources. Neither in the HI maps nor in the optical maps a cause can be identified for this devoidance. Hence this is likely by chance. Moreover, the sources with fluxes exceeding $S = 2 \times 10^{-14}$ erg cm^{-2} s^{-1} are confined to the inner part of the galaxy within a radius of 0.6 kpc with respect to the morphological center. This trend is only seen in Holmberg I so far.

Converting the fluxes to luminosities (provided a distance to NGC 1569 of 2.2 Mpc (Israel, 1988)) one obtains the XLF of NGC 1569. The view graph is shown in Fig.63. In contrast to Martin et al. (2002); Belczynski et al. (2004) the XLF here is well constrained since the number of point sources in the present work is higher.

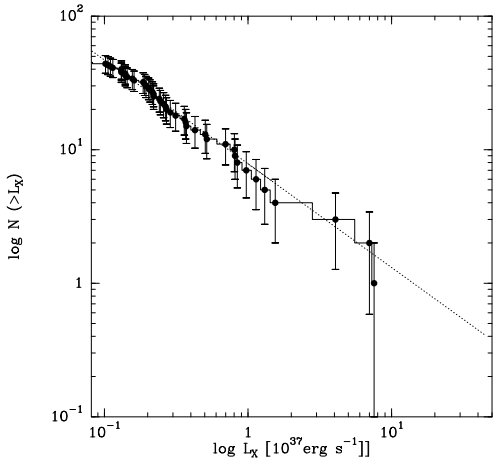

Fig. 63: *X–ray luminosity function of NGC 1569 (CHANDRA data). The dotted lines correspond to a fit of a power–law with a slope of* $\beta = -0.78 \pm 0.02$.

Within the uncertainties the XLF can be fitted by a single power–law with slope $\beta = 0.78 \pm 0.02$ which is steeper than the slope of 0.5 adopted by Martin et al. (2002). This "unbroken" behavior of the XLF, which is also reported by Belczynski et al. (2004), is interpreted as a uniform star formation although a star burst has occurred 25 Myr ago (Anders et al., 2004). However, this star burst is not visible in the XLF. The age of the SSCs is about 10 Myr and it appears that the X–ray binary population is not yet affected by this burst. Only a slight undulation is visible in the XLF which is not significant within the uncertainties. However, the XLF models by Belczynski et al. (2004) suggest a young population not older than 70 Myr which shows that the times at which star bursts occurred are not well confined.

As pointed out by authors Anders et al. (e.g. 2004); Lisenfeld et al. (e.g. 2004); Martin et al. (e.g. 2002) this burst may have produced the outflow of hot material blown in the halo of NGC 1569. This outflow is visible in Hα as well as in X–rays. This issue will be discussed in the following.

5.1.5.3 Diffuse emission As described above, Martin et al. (2002) report about a bipolar outflow of hot X–ray emitting gas perpendicular to the plane of NGC 1569. To visualize the diffuse emission source subtracted CHANDRA images in the B–bands are calculated and adaptively smoothed. Figure 64 shows the diffuse emission in the B–bands as contours on top of the UV images of the OM in the inner region of the galaxy ($\approx 2\farcm5$ diameter) where the bulk of the diffuse emission is thought to come from.

The spatial distribution of the soft diffuse X–ray emission is in concordance with the interpretation of an outflow perpendicular to the plane of the galaxy. With respect to the peak intensities in each band, the diffuse emission is confined in the north

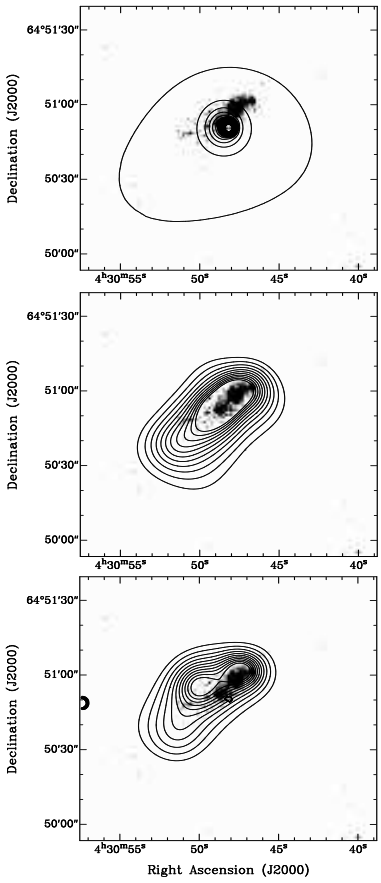

Fig. 64: *From top to bottom the B2, B3 and B4 band emission of NGC 1569 (point source subtracted CHANDRA data). The contour levels start at 3 %, 20 % and 20 % of the peak intensity, respectively. The B2 band emission is more diffuse than the B4 band emission which itself shows two peaks. The B3 band emission is oriented parallel to the major axis of the galaxy.*

($\delta = 64^{\circ}51'15''$ (J2000.0)) and extends towards the south. This is expected when the observer looks at the bottom of the galaxy.

To derive the physical parameters of the coronal gas of NGC 1569 a spectrum of the region encircled by the lowest contour line of the B2 band emission (see Fig.64) is analyzed. After calculating weighted RMF and ARF information the spectrum is fitted with *sherpa*.

The first models which are assumed to be the sources of the X–ray emission are the ones described in connection with IC 2574 and Holmberg I. It turns out that these are not good approximation of the data; their reduced χ^2 are above 1.8. To improve the model, a second plasma term is introduced leading in total to an intrinsically power–law component (for residual point sources) and two plasma components, all three absorbed by the Galactic foreground.

The model yields then $AG \cdot (MP_1 + MP_2 + (AI \cdot PL))$.

The power–law component accounts for the XRB which is absorbed by the galaxy. The two plasma components account for the coronal gas of NGC 1569. All these components are then absorbed by the Galaxy.

The abundance of the plasma terms is set to 0.2 solar. The intrinsic absorption column is set to $2.2 \times 10^{21}\,\mathrm{cm}^{-2}$, which is the mean value for NGC 1569. The power–law index is set to 1.5 as in the previous spectral model for Holmberg I and IC 2574. The fit yields a χ^2 of 1.3 which is close to the best value (1.2) derived by the models of Martin et al. (2002). The difference here is, that they need intrinsic absorption for all three emission components to achieve the same goodness of fit. In this sense the approach here is more natural since it only needs one intrinsic absorption component for the XRB.

The fit yields the following temperatures for the two plasma components:

- $T_1 = 10^{6.9}\,\mathrm{K}$ (first plasma term, MEKAL model)
- $T_2 = 10^{6.6}\,\mathrm{K}$ (second plasma term, MEKAL model)

Since NGC 1569 is situated only 11° above the Galactic plane, the absorbing column density is quite high, $N_{\mathrm{HI}} = 2.1 \times 10^{21}\,\mathrm{cm}^{-2}$. The figure from the fit matches nicely the value given by Burton (1985). The emission measures of both components are $\mathrm{EM_{cold}} = 1.8 \times 10^{-4}\,\mathrm{pc\,cm}^{-6}$ and $\mathrm{EM_{hot}} = 2.4 \times 10^{-4}\,\mathrm{pc\,cm}^{-6}$.

As described above, the diffuse emission is modeled by two thermal plasma components (MEKAL model). The fit procedure yields two slightly different values for both temperature components. The temperatures are in agreement with the model favored by Martin et al. (2002) within the uncertainties which are of the order 10-20 %. Taking the additional parameters from the fit (i.e. the emission integral) one can calculate the

electron density n_e, pressure P and equivalent hydrogen mass M of the plasma components. Again, spherical symmetry of the emission region (volume $V = 1.4 \times 10^{64}\,\mathrm{cm}^3$) is assumed. The values are given below and the spectrum is given in Fig.65.

hot plasma component:

- $T = 10^{6.9}\,\mathrm{K}$
- $n_e \cdot f^{1/2} = 3.18 \times 10^{-2}\,\mathrm{cm}^{-3}$
- $P \cdot f^{-1/2} = 6.97 \times 10^{-11}\,\mathrm{dyn\,cm}^{-2}$
- $M \cdot f^{-1/2} = 0.4 \times 10^6\,M_\odot$
- $E_{th} = 1.61 \times 10^{54}\,\mathrm{erg}$

cold plasma component:

- $T = 10^{6.6}\,\mathrm{K}$
- $n_e \cdot f^{1/2} = 2.92 \times 10^{-2}\,\mathrm{cm}^{-3}$
- $P \cdot f^{-1/2} = 3.20 \times 10^{-11}\,\mathrm{dyn\,cm}^{-2}$
- $M \cdot f^{-1/2} = 0.4 \times 10^6\,M_\odot$
- $E_{th} = 7.34 \times 10^{53}\,\mathrm{erg}$

The uncertainties in these figures are dominated by the unknown value of the filling factor f, as discussed e.g. in the Holmberg I case. Martin et al. (2002) estimate the X–ray gas mass to be $3.5 \times 10^6\, f^{0.5}\,\mathrm{M}_\odot$. In contrast to Martin et al. (2002) the mass of the coronal gas is here lower by a factor of four. If the filling factor f is assumed to be 0.1, the discrepancy vanishes. Also different sizes of the extraction region of the spectral information and the different spectral model particularly yield different normalization values. This has influences on the mass estimation and pressure as well. Moreover, Martin et al. (2002) show, that the inferred mass of the coronal gas depends on the metalicity. In particular, the mass decreases with increasing α–element abundance – for example for Z_α=0.1$\mathrm{Z}_\odot$ the mass may be $10^7\,\mathrm{M}_\odot$, for Z_α=10$\mathrm{Z}_\odot$ the mass drops to $10^6\,\mathrm{M}_\odot$. Since I assumed 0.2 solar metalicity for the coronal gas, the mass will decrease further when I adopt the preferred value of Martin et al. (2002) of 1.0 solar. Hence, the mass discrepancy stems from the combined effects of assumed filling factors, assumed abundances and the assumed geometry of the emission region.

With these numbers upper limits for the sound speed and hence, time and distance scales can be derived. The sound speed in both phases is $v_h = 330\,\mathrm{km\,s}^{-1}$ and $v_c =$

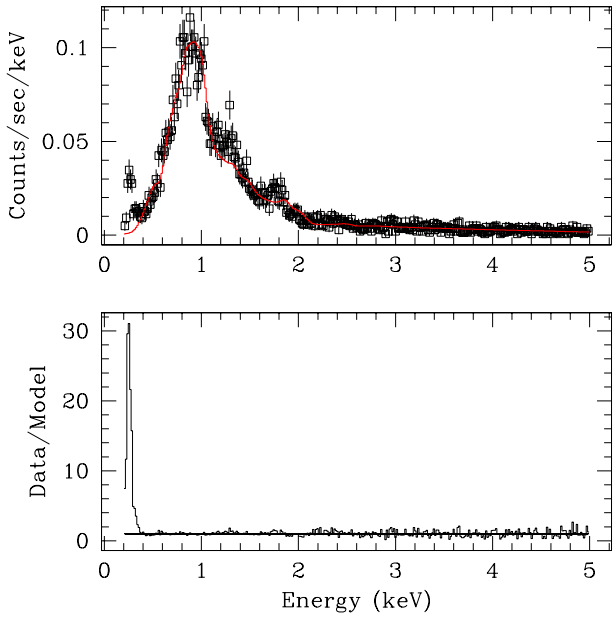

Fig. 65: *The diffuse emission spectrum (CHANDRA data) of NGC 1569 (data points in the upper panel) together with the best fit model (solid line in the upper panel). The lower panel shows the ratio of data/model.*

230 km s^{-1} for the hot and cold phase, respectively. The cooling times amount to $t_{\rm cool,hot} = 163$ Myr and $t_{\rm cool,cold} = 90$ Myr. The distances the gas can reach on these time scales are 55 kpc and 22 kpc respectively. Hence the picture of the bipolar outflow of hot gas is very well justified.

The XMM–Newton data of NGC 1569, which was not analyzed by Martin et al. (2002), as described in the beginning of this section, has a poor spatial resolution to identify the point sources, but still it is more sensitive to the diffuse emission. Thus, the spectral information is extracted from the same region as the CHANDRA data. The same model is applied to the data fixing the galactic foreground to the value given above. The brightest point source in the center of the extraction region is subtracted and the power–law index is a free parameter to account for any residual point sources. The spectrum is given in Fig.66 together with the fitted model.

The XMM–Newton data yields an unsatisfying χ^2 of 0.28 and the following parameters:

hot plasma component:

- EM$= 1.9 \times 10^{-4}$ pc cm^{-6}
- $T = 10^{7.0}$ K

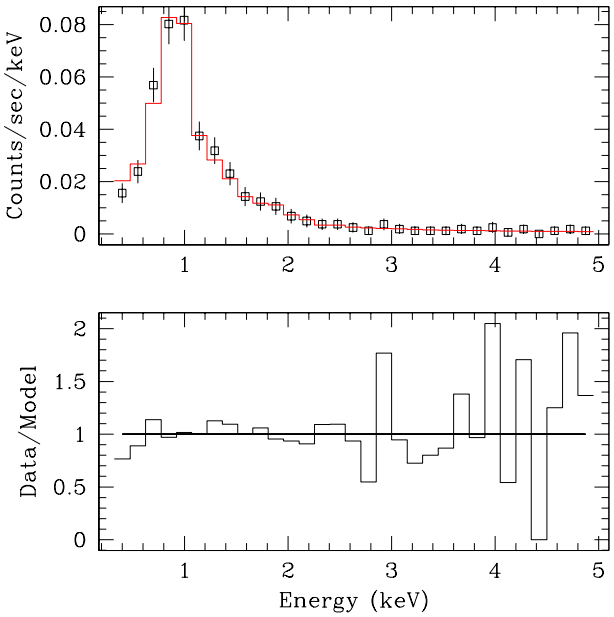

Fig. 66: *The diffuse emission spectrum (XMM–Newton data) of NGC 1569 (data points in the upper panel) together with the best fit model (solid line in the upper panel). The lower panel shows the ratio of data/model.*

- $n_e \cdot f^{1/2} = 2.83 \times 10^{-2}\,\mathrm{cm}^{-3}$
- $P \cdot f^{-1/2} = 7.83 \times 10^{-11}\,\mathrm{dyn\,cm}^{-2}$
- $M \cdot f^{-1/2} = 0.3 \times 10^{6}\,M_{\odot}$
- $E_{th} = 1.60 \times 10^{54}\,\mathrm{erg}$
- $v = 370\,\mathrm{km\,s}^{-1}$
- $t_{\mathrm{cool}} = 230\,\mathrm{Myr}$
- $d = 88\,\mathrm{kpc}$

cold plasma component:

- EM$= 1.1 \times 10^{-4}\,\mathrm{pc\,cm}^{-6}$
- $T = 10^{6.8}\,\mathrm{K}$
- $n_e \cdot f^{1/2} = 2.17 \times 10^{-2}\,\mathrm{cm}^{-3}$
- $P \cdot f^{-1/2} = 3.78 \times 10^{-11}\,\mathrm{dyn\,cm}^{-2}$

- $M \cdot f^{-1/2} = 0.2 \times 10^6 M_\odot$
- $E_{th} = 7.7 \times 10^{53}$ erg
- $v = 295\,\mathrm{km\,s^{-1}}$
- $t_{\mathrm{cool}} = 190$ Myr
- $d = 55$ kpc

The temperatures are slightly higher, while the electron densities are smaller which leads to a smaller mass estimate and longer cooling times. The differences are likely due to the imperfect calibrations of the two telescopes (i.e. the RMF and ARF) and also the different binning of the data might play a role here. The attempt of fitting other models, e.g. with only one plasma component or with a fixed power–law index yields comparable results but with $\chi^2 < 0.28$. However, the values are in the same range as the CHANDRA results and the interpretation of outflowing gas still holds true when the XMM–Newton data is taken into account.

5.1.5.4 Summary The XMM–Newton observation of NGC 1569 shows the limitation of the $14''$ PSF size of the telescope. With this resolution only one point source is detected in the galaxy. Taking the CHANDRA data this point source is resolved into 62 individual objects. The log(N)-log(S) provides the information that the detected point sources are negligible contaminated by unrelated sources.

In contrast to Martin et al. (2002), here, ≈30 % more point sources are found, showing the problems of automated point source search algorithms. The investigation reveals that the bulk of X–ray point sources are accreting binary systems, three of which are HMXB. Moreover, one HII region and one stellar blackhole binary are found. Also the SNR detected by Martin et al. (2002) is confirmed while the X–ray emission mights stem from the central object and not from the SNR itself. However, this interpretation is questionable due to the short life times of neutron stars.

The hardness ratio of one particular source (ID 40) shows that the blackbody and plasma models in the HR diagram are not easy to disentangle. More precise, below a temperature of $10^{5.5}$ K the blackbody models are the same as plasma models while for temperatures above they run like the power–law models. Hence, additional data is always required. Also the choice of the X–ray bands in the present work turns out to be less ambiguous.

The SSC–A and B in NGC 1569 are not correlated with any X–ray point source. However, there a 11 X–ray point sources surrounding the SSCs one of which is the HII region mentioned before. The XMM–Newton OM shows that the SSC region is also emitting UV radiation showing the young stellar population of NGC 1569.

The spatial distribution of the X–ray point sources shows no special features. Only between a radial distance of 0.8 and 1.0 kpc there is a devoidance of X–ray point sources, which may be casual. The number density of point sources drops exponentially towards larger radii with a characteristic scale length of $r_o = 0.24 \pm 0.01$ kpc. There is a trend, like in Holmberg I, that the most luminous sources occupy only the inner (<0.6 kpc) region of the galaxy.

The XLF of NGC 1569 turns out to be "unbroken" in agreement with Belczynski et al. (2004). Here, my results constrain the XLF much better than in previous investigations due to the more numerous point sources. Since the star burst is very young, old objects like X–ray binaries are not expected to introduce a break in the XLF. Hence, a single power–law behavior of the XLF is expected.

The diffuse emission of the galaxy is spatially confined in the north and extends to the south. This distribution is attributed to the inclination of the galaxy of $i = 60^o$. The observer looks at the "bottom" of the galaxy. The spectral information of the CHANDRA data is used to determine the emission model of the diffuse emission. The data can be approximated with a two thermal components and an absorbed power–law model for residual point sources, all three absorbed by the Galactic foreground. In addition to Martin et al. (2002), the XMM–Newton data is taken into account, fitting the same model to the data extracted from the same region as the CHANDRA data. The parameters based on the XMM–Newton spectral data is in broad agreement with the CHANDRA data.

The temperatures for the hot and cold plasma components of the CHANDRA data turn out to be log(T[K])=6.9 and log(T[K])=6.6, respectively. In concordance with Martin et al. (2002) the general picture of a bipolar outflow of coronal gas is confirmed with the figures for time scales and distance estimates. The difference in mass is attributed to the uncertain filling factor f of the coronal gas, different extraction regions, concerning the spectral information and a metalicity dependant mass estimate. The XMM–Newton data deviates only slightly from the CHANDRA results.

5.1.6 NGC 4214

Like NGC 1569, NGC 4214 is a metal–poor dwarf star burst galaxy (Walter et al., 2001). The irregular nature of this galaxy is supported by the fact that the peaks of HI and CO do not show a clear correlation. There are three detections of molecular gas (one in the center, one in the northwest and one in the southeast). A comparison with the optical shows that the star formation has not started yet in the northwest region while it started in the southeast recently. The central molecular clump is associated with an evolved star burst.

CHANDRA and XMM–Newton observations reveal diffuse X–ray emission around two of the three star burst regions, mainly with the oldest and less with the young

Tab. 27: *NGC 4214*

Morphological type	dIrr	
Position (J2000.0)	$\alpha = 12^h15^m39\overset{s}{.}75$ $\delta = 36^d19^m36\overset{s}{.}17$	
Distance	2.7 Mpc	(Drozdovsky et al., 2002)
HI mass (10^6 $M_\odot$)	550	(Drozdovsky et al., 2002)

region (Hartwell et al., 2004). From the spectral fits the authors suggest a blow–out in the future for NGC 4214. There is also evidence for ionized gas flowing out of wind driven bubbles when they approach the steep density gradient from HI clouds to HI holes (Wilcots & Thurow, 2001; Maíz-Apellániz et al., 1999). However, Schwartz & Martin (2004) report on sight lines which intersect expanding shells in NGC 4214 which give evidence for a trapped ionization front.

After proton filtering the exposure time of the archival data set of NGC 4214 amounts to ≈13 ks in all instruments. The OM was not used. In addition HI data and the DSS2 images are used in the following. The investigation of the smoothed M1M2 data in the PS band reveals a number of X–ray point sources.

Additionally to the XMM–Newton data also CHANDRA data is available in the archive. This observation is used to disentangle the point sources in the very center of the galaxy where the XMM–Newton PSF is too large to resolve individual sources. Unfortunately, both data sets show a significant positional offset of about 15 arcsec. This is also reported by Hartwell et al. (2004). In contrast to their paper here the declaration of coordinates always refers to the individual observation, i.e. CHANDRA or XMM–Newton.

5.1.6.1 Point sources Clipping the M1M2 image to the 4-σ background level one spots 71 X–ray point sources within the HI distribution of NGC 4214. The M1M2 map is given in Fig.67 (left), together with the HI distribution of the galaxy (right). Here, I find more sources in the XMM–Newton data than Hartwell et al. (2004) in their CHANDRA data. This is because their luminosity limit is about an order of magnitude higher than the luminosity limit of the XMM–Newton data presented here.

The elongated source ID 3 appears as a linear pattern of pixels in the photon image which is probably a cosmic ray event, hence it is rejected from further analysis. All other sources are then evaluated in the log(N)–log(S) diagram to investigate the contamination by background sources. The resulting diagram is depicted in Fig.68.

As with the other observations so far, the found X–ray sources are statistically not contaminated with background sources. Many sources are very faint and therefore

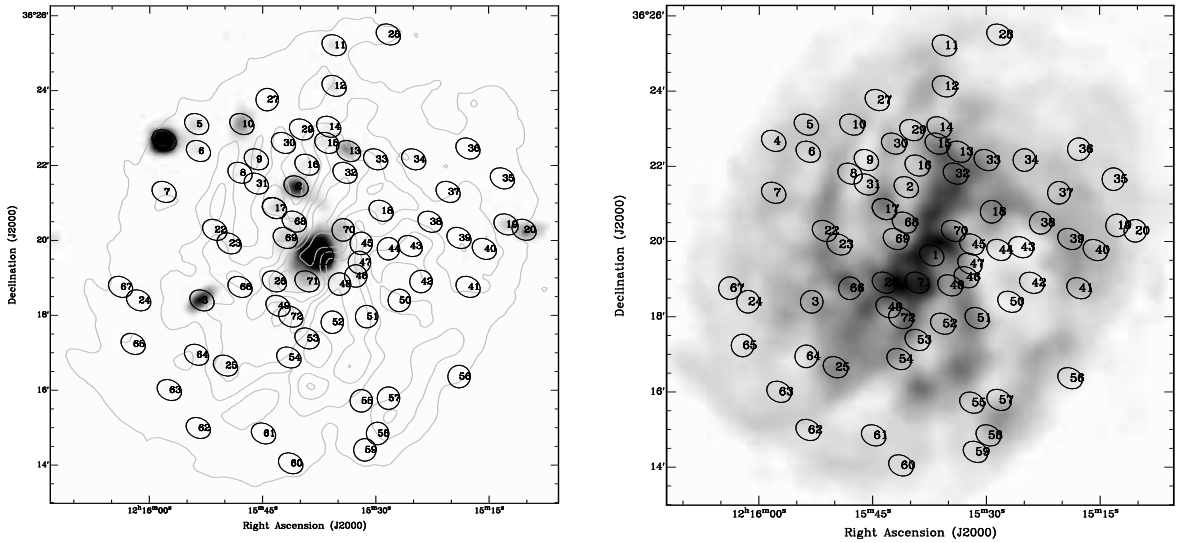

Fig. 67: **Left**:*X–ray point sources within the* HI *distribution of NGC 4214 in the M1M2 map in the PS band (XMM–Newton data). The grey scale image is a logarithmic scaling, the circles mark the 72 point sources detected above 4-*σ *background level. Contours (starting at 10% of the peak intensity, growing in steps of 10%) correspond to the* HI *map on the* **right**: *The* HI *column density map with the X–ray point sources overlayed as circles. The peak here is 1750 Jy/Beam·m/s. The* HI *map is from Walter et al. (2001).*

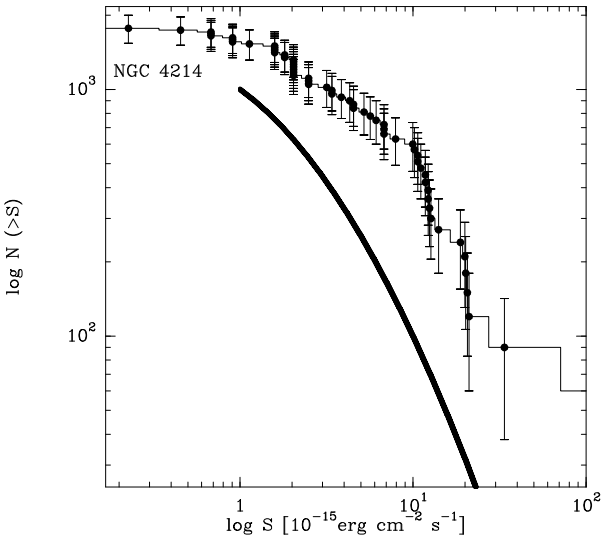

Fig. 68: *Comparison of the log(N)-log(S) relation of NGC 4214 (XMM–Newton data) with the extragalactic X–ray background. With respect to the uncertainty of the number of point sources in the galaxy, the relation is well above the extragalactic relation derived by Hasinger et al. (2001), which gives the upper limit for the XRB.*

Tab. 28: *NGC 4214 flux limits of the XMM–Newton data for individual bands normalized to the area of 3.5 PSF. The flux units are 10^{-15} erg cm^{-2} s^{-1}*

Band	background counts	flux limit
B2	8±0.5	1.01±0.06
B3	7±0.5	0.63±0.04
B4	12±0.7	1.48±0.09
PS	43±1.4	7.12±0.23

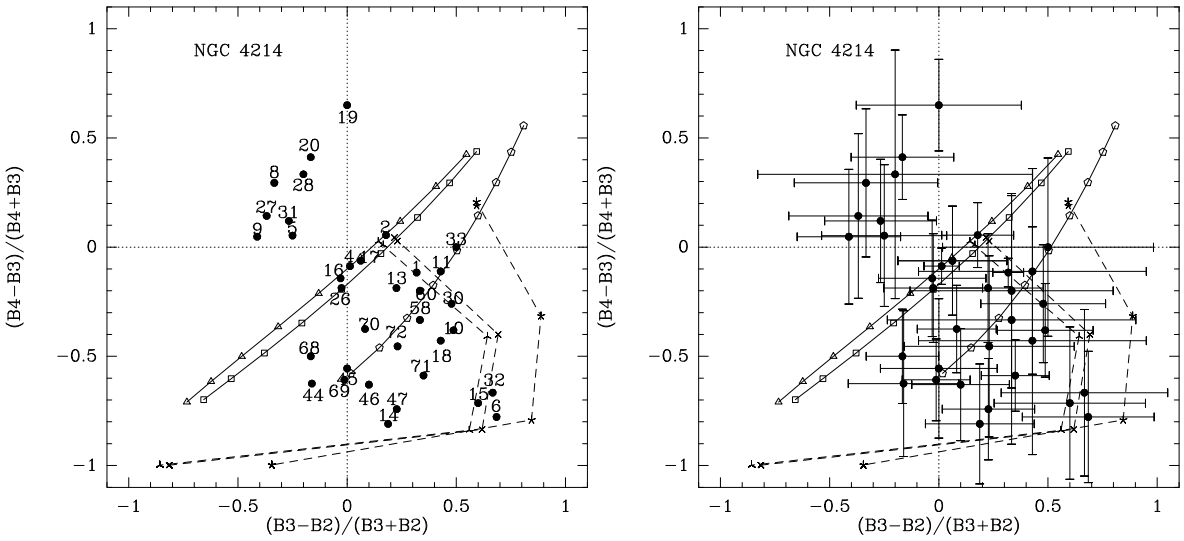

Fig. 69: *HR for the XMM–Newton point sources found in NGC 4214. The numbers correspond to the IDs of Tab.29. All errorbars correspond to an uncertainty of 1-σ. The dashed and solid lines are described in detail in the caption of Fig.19 and the accompanying text.*

their hardness ratios cannot be evaluated. Nevertheless they are listed in the point source catalog displayed in Fig.29. There are also sources listed (as with the other observations) which have virtually no flux in the EPIC–*pn* data. On the other hand they appear in the M1M2 data because the combined MOS-1 and MOS-2 data has twice the exposure time and the image is smoothed giving a better signal–to–noise. However, they are listed nevertheless. The corresponding detection limits are calculated in the same fashion as for the previous galaxies and are presented in Tab.28

From here, the hardness ratios can now be evaluated taking the XMM–Newton data. For 34 sources the hardness ratios are given in Fig.69, the other 36 sources have less than two counts in at least one B–band and are hence excluded from the HR. The work of Hartwell et al. (2004) shows again, that the band definitions are a crucial point for the HR. Their HR diagram simply cannot distinguish between their model curves wihtin the uncertainties due to their band definitions.

Tab. 29: *The X–ray point sources found by XMM–Newton in NGC 4214. The flux units are 10^{-15} erg cm^{-2} s^{-1} in the PS band, the luminosity units are 10^{37} erg s^{-1}, the luminosity uncertainty is of the order of the relative flux uncertainty. The stars mark sources with one or less counts in one band after background subtraction. The last three columns give the background corrected counts in the corresponding band.*

ID	Right Ascension (J2000.0)	Declination (J2000.0)	Flux	Luminosity	B2	B3	B4
1	$12^h15^m37.26$	$36^o\ 19'\ 38.10$	157.90 ± 5.98	16.33	134	259	205
2	$12^h15^m40.50$	$36^o\ 21'\ 26.85$	33.75 ± 2.76	3.49	30	43	48
4	$12^h15^m58.15$	$36^o\ 22'\ 40.70$	109.0 ± 4.97	11.27	152	156	131
5	$12^h15^m53.83$	$36^o\ 23'\ 6.84$	9.97 ± 1.50	1.03	15	9	10
6	$12^h15^m53.46$	$36^o\ 22'\ 23.34$	4.30 ± 0.99	0.45	3	16	2
7*	$12^h15^m58.14$	$36^o\ 21'\ 18.05$	2.04 ± 0.68	0.21	10	8	-3
8	$12^h15^m48.06$	$36^o\ 21'\ 48.58$	6.80 ± 1.24	0.70	12	6	11
9	$12^h15^m45.90$	$36^o\ 22'\ 10.34$	11.78 ± 1.63	1.22	24	10	11
10	$12^h15^m47.70$	$36^o\ 23'\ 6.88$	10.65 ± 1.55	1.10	10	29	13
11	$12^h15^m35.45$	$36^o\ 25'\ 13.05$	2.49 ± 0.75	0.26	2	5	4
12*	$12^h15^m35.46$	$36^o\ 24'\ 7.80$	0.68 ± 0.39	0.07	4	-1	4
13	$12^h15^m33.66$	$36^o\ 22'\ 23.39$	12.69 ± 1.70	1.31	12	19	13
14	$12^h15^m36.18$	$36^o\ 23'\ 2.55$	7.93 ± 1.34	0.82	13	19	2
15	$12^h15^m36.54$	$36^o\ 22'\ 36.45$	2.04 ± 0.68	0.21	3	12	2
16	$12^h15^m39.06$	$36^o\ 22'\ 1.65$	10.19 ± 1.52	1.05	17	16	12
17	$12^h15^m43.38$	$36^o\ 20'\ 52.04$	12.23 ± 1.66	1.26	15	17	15
18	$12^h15^m29.34$	$36^o\ 20'\ 47.68$	2.04 ± 0.68	0.21	2	5	2
19	$12^h15^m12.78$	$36^o\ 20'\ 25.78$	14.05 ± 1.78	1.45	7	7	33
20	$12^h15^m10.26$	$36^o\ 20'\ 17.04$	20.16 ± 2.14	2.08	21	15	36
22*	$12^h15^m51.30$	$36^o\ 20'\ 17.21$	5.21 ± 1.09	0.54	8	1	6
23*	$12^h15^m49.50$	$36^o\ 19'\ 55.47$	4.53 ± 1.01	0.47	11	11	-2
24*	$12^h16^m1.37$	$36^o\ 18'\ 24.01$	1.59 ± 0.60	0.16	0	4	7
25*	$12^h15^m49.85$	$36^o\ 16'\ 39.72$	—	—	0	0	-7
26	$12^h15^m43.38$	$36^o\ 18'\ 54.59$	11.78 ± 1.63	1.22	20	19	13
27	$12^h15^m44.46$	$36^o\ 23'\ 46.04$	3.85 ± 0.93	0.40	13	6	8
28	$12^h15^m28.25$	$36^o\ 25'\ 30.42$	1.81 ± 0.64	0.19	3	2	4
29*	$12^h15^m39.78$	$36^o\ 22'\ 58.20$	—	—	0	1	1
30	$12^h15^m42.30$	$36^o\ 22'\ 36.45$	6.80 ± 1.24	0.70	6	17	10
31	$12^h15^m45.90$	$36^o\ 21'\ 31.19$	11.10 ± 1.59	1.15	19	11	14
32	$12^h15^m34.02$	$36^o\ 21'\ 48.59$	2.04 ± 0.68	0.21	2	10	2
33	$12^h15^m30.05$	$36^o\ 22'\ 10.33$	2.04 ± 0.68	0.21	2	6	6
34*	$12^h15^m25.01$	$36^o\ 22'\ 10.30$	2.04 ± 0.68	0.21	6	0	7
35*	$12^h15^m13.13$	$36^o\ 21'\ 39.73$	0.68 ± 0.39	0.07	5	-3	3
36*	$12^h15^m17.81$	$36^o\ 22'\ 27.64$	—	—	-4	2	1

Tab. 30: *Table.29—continued*

ID	Right Ascension (J2000.0)	Declination (J2000.0)	Flux	Luminosity	B2	B3	B4
37*	$12^h15^m20.33$	$36^o\ 21'\ 18.06$	0.23 ± 0.23	0.02	6	-2	4
38*	$12^h15^m22.86$	$36^o\ 20'\ 30.24$	0.91 ± 0.45	0.09	0	-1	5
39*	$12^h15^m18.90$	$36^o\ 20'\ 4.10$	3.17 ± 0.85	0.33	-2	6	3
40*	$12^h15^m15.66$	$36^o\ 19'\ 46.66$	0.91 ± 0.45	0.09	0	1	1
41*	$12^h15^m17.82$	$36^o\ 18'\ 45.79$	—	—	-5	-6	-8
42*	$12^h15^m23.94$	$36^o\ 18'\ 54.54$	—	—	4	-1	1
43*	$12^h15^m25.38$	$36^o\ 19'\ 51.10$	—	—	5	-2	-2
44	$12^h15^m28.26$	$36^o\ 19'\ 46.77$	6.80 ± 1.24	0.70	18	13	3
45	$12^h15^m31.86$	$36^o\ 19'\ 55.49$	5.66 ± 1.13	0.59	14	14	4
46	$12^h15^m32.58$	$36^o\ 19'\ 3.29$	12.46 ± 1.68	1.29	18	22	5
47	$12^h15^m32.22$	$36^o\ 19'\ 25.04$	10.65 ± 1.55	1.10	17	27	4
48*	$12^h15^m34.74$	$36^o\ 18'\ 50.25$	2.04 ± 0.68	0.21	5	9	-3
49*	$12^h15^m43.02$	$36^o\ 18'\ 15.44$	1.59 ± 0.60	0.16	5	15	-1
50*	$12^h15^m26.82$	$36^o\ 18'\ 24.11$	3.40 ± 0.88	0.35	12	0	5
51*	$12^h15^m31.14$	$36^o\ 17'\ 58.04$	—	0	4	5	-1
52*	$12^h15^m35.82$	$36^o\ 17'\ 49.35$	6.12 ± 1.18	0.63	13	10	0
53*	$12^h15^m39.06$	$36^o\ 17'\ 23.25$	2.49 ± 0.75	0.26	7	1	1
54*	$12^h15^m41.58$	$36^o\ 16'\ 52.80$	—	—	2	-6	-4
55*	$12^h15^m31.86$	$36^o\ 15'\ 43.19$	—	—	6	2	-1
56*	$12^h15^m18.91$	$36^o\ 16'\ 22.25$	—	—	0	1	-1
57*	$12^h15^m28.27$	$36^o\ 15'\ 47.52$	3.40 ± 0.88	0.35	3	0	13
58	$12^h15^m29.71$	$36^o\ 14'\ 50.98$	0.91 ± 0.45	0.09	2	4	2
59*	$12^h15^m31.51$	$36^o\ 14'\ 24.89$	—	—	0	-7	-2
60	$12^h15^m41.21$	$36^o\ 14'\ 3.15$	0.68 ± 0.39	0.07	3	6	4
61*	$12^h15^m44.81$	$36^o\ 14'\ 50.99$	0.45 ± 0.32	0.05	4	0	4
62*	$12^h15^m53.44$	$36^o\ 14'\ 59.64$	4.53 ± 1.01	0.47	13	1	5
63*	$12^h15^m57.40$	$36^o\ 16'\ 0.51$	2.49 ± 0.75	0.26	7	6	-2
64*	$12^h15^m53.81$	$36^o\ 16'\ 57.09$	—	—	4	-6	0
65*	$12^h16^m2.08$	$36^o\ 17'\ 14.41$	1.13 ± 0.51	0.12	8	2	-2
66*	$12^h15^m48.05$	$36^o\ 18'\ 45.88$	1.59 ± 0.60	0.16	10	3	-3
67*	$12^h16^m3.89$	$36^o\ 18'\ 45.73$	—	—	3	-4	-1
68	$12^h15^m40.86$	$36^o\ 20'\ 30.30$	19.93 ± 2.12	2.06	42	30	10
69	$12^h15^m41.94$	$36^o\ 20'\ 4.20$	21.07 ± 2.18	2.18	42	41	10
70	$12^h15^m34.38$	$36^o\ 20'\ 17.25$	18.80 ± 2.06	1.94	28	33	15
71	$12^h15^m39.06$	$36^o\ 18'\ 54.60$	20.61 ± 2.16	2.13	26	54	14
72	$12^h15^m41.22$	$36^o\ 17'\ 58.05$	1.59 ± 0.60	0.16	5	8	3

The sources in the HR diagram decompose into at least three components; plasma sources (ID 6, 14, 15, 32, 47, 71), power–law sources (ID 2, 4, 16, 17, 26, 44, 45, 68, 69, 70, 72) and yet unidentified sources (ID 1, 5, 8, 9, 10, 11, 13, 18, 19, 20, 27, 28, 30, 31, 33, 58, 60). From the unidentified ones, ID 5, 8, 9, 19, 20, 27, 28, 30 are in the "forbidden" region in the upper left corner of the HR plot, the others are in the ambiguous regime of the HR diagram. The positions of the "forbidden" sources in the galaxy are not in the center but more at the outer parts. In higher bands they also show no excess photons. Considering 2-σ uncertainties, all these sources reach the power–law regime, except ID 19 and 20, hence, their nature remains unclear.

To characterize the sources in the ambiguous region the DSS2 images in red and blue band are considered. It turns out that sources ID 1, 13, 18 and 33 show up in both bands, while ID 10 is slightly visible only in the red band. The other sources (ID 11, 30, 58 and 60) are not seen in the optical. Unfortunately, no additional observations are at hand making the classification very hard. The literature provides images and data in several wavelength (Hα and [OIII] by MacKenty et al. (2000), He I by Martin & Kennicutt (1997), UV and NIR by Fanelli et al. (1997)). Taking these, only source ID 1 is identified with an Hα source (MacKenty et al., 2000, their source XIIn). However, the data in the literature do not provide coordinates and therefore it is unfeasible to perform a source–to–source correlation reliably.

Here, the classification is only feasible on the basis of hardness ratios, as it was also done in the work of Hartwell et al. (2004). They argue, that most of the sources are HMXB because they are associated with the central young star forming region (e.g. Fanelli et al., 1997). This conclusion may be true but here the HR diagram in conjunction with the luminosities can be used to discriminate between HMXB and LMXB. It is moreover possible to separate accreting sources from plasma sources. Hence, from the 70 point sources found, six are plasma sources. Two of them (ID 47, 71) are located at the central source (ID 1) in the east and south, respectively. Three more are in the northeast and south of ID 13 and the last in the west of ID 4.

To get a better handle on the nature of the sources, additional data from the CHANDRA instrument is examined. The event list is selected in the PS band and then adaptively smoothed to increase the signal to noise for point sources and even faint diffuse emission. Due to the higher angular resolution of the CHANDRA mirrors ($\approx 0.5''$) one can hope to find substructure in the sources fond by XMM–Newton. The adaptively smoothed CHANDRA image in the PS band together with the XMM–Newton point source positions (shifted to the CHANDRA coordinates) is displayed in Fig.70. The lefthand side is clipped and scaled to reveal the components of the central source ID 1, the righthand side is clipped and scaled to reveal the diffuse emission components. The limiting flux in the CHANDRA PS band per 3.5×PSF is $S = 3.5 \pm 0.2 \times 10^{-17}\,\mathrm{erg\,cm^{-2}\,s^{-1}}$.

The CHANDRA data resolves the XMM source ID 1 into 4 distinct sources. One has a diffuse halo like appearance while the other three are point like, also reported

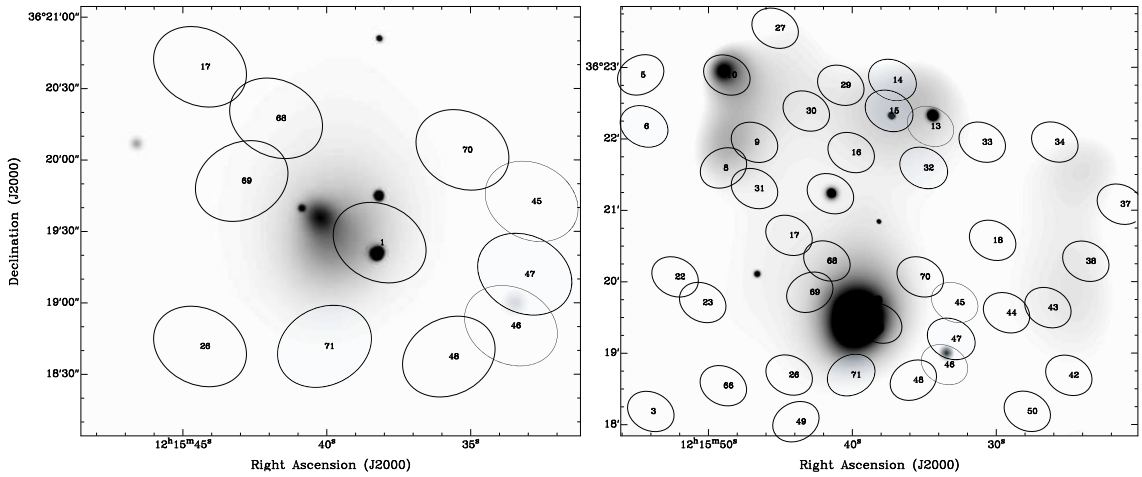

Fig. 70: *Both images show the adaptively smoothed CHANDRA ACIS-S3 data in the PS band clipped to 4-σ above background. The* **left** *shows the central region around XMM source ID 1 which is now resolved into four sources one of which is more diffuse and three point like ones. The* **right** *shows a larger region with another upper clipping of the image, which reveals some diffuse emission around XMM sources ID 8, 9 and ID 13, 14, 15.*

by Hartwell et al. (2004). The diffuse source is correlated with Hα emission in the very center of the young star forming region, where also CO is detected (Walter et al., 2001). The three point like sources are outside the CO region but still inside the star forming region. Moreover, the diffuse source is in positional agreement with the Hα cavity found by MacKenty et al. (2000, their source I-As). They report that the cavity is bordered towards the north and more open towards the south and west, matching nicely the shape of the diffuse X–ray emission of the CHANDRA data. Furthermore, they claim to have found a supernova remnant at the position of the diffuse X–ray source which nicely fits the picture.

To constrain this more a spectrum is extracted from the ACIS data (see Fig.75). Binned to at least 25 photons per bin, the spectrum is fitted with an M2 model which accounts for residual point sources and a plasma component, both absorbed by HI in the foreground. This model is more simple than the model suggested by Hartwell et al. (2004) which contains two plasma components. This finding will be discussed more in the section about the difuse emission below.

With a χ^2 of 1.22, the model yields a plasma temperature of $10^{6.3}$ K and a photon index for the power–law component of 1.5, which both are absorbed by an HI column density of 4.0×10^{21} cm^{-2}. The temperature is between the two temperatures derived by Hartwell et al. (2004). The spectrum is shown in Fig.71 together with the model. This result makes the supernova remnant hypothesis of MacKenty et al. (2000) almost certain. The final proof for hot gas originating from the diffuse emission is given in Fig.72 where the hardness ratio of this source is plotted together with the theoretical models calculated for the CHANDRA telescope. In conclusion, the model presented

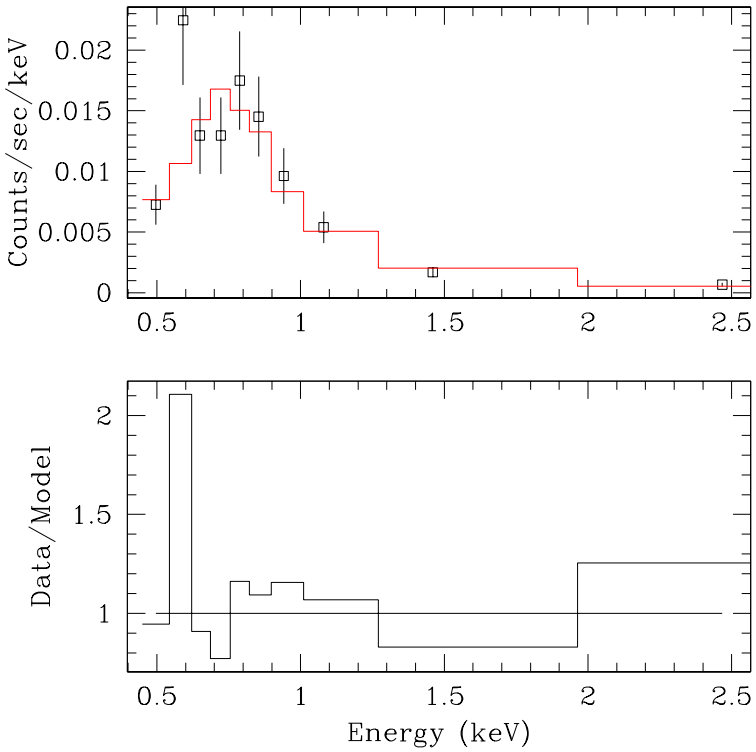

Fig. 71: *CHANDRA emission spectrum of the SNR candidate (the diffuses source in Fig.70) in NGC 4214 (data points in the upper panel) together with the best fit model (solid line in the upper panel). The lower panel shows the ratio of data/model.*

here is favored since it is simpler than the Hartwell et al. (2004) model and yields similar results.

The most northern source of the three compact ones is in positional agreement with the MacKenty et al. (2000) source IIIs which they argue is probably an old super star cluster. The X–ray emission then is most likely originating from an accreting binary system. The most luminous source in the very center of the XMM ID 1 source ellipse is in agreement with the MacKenty et al. (2000) source I-Hn, which they do not further discuss in their paper. Both are power–law sources according to their HR and hence they are classified as X-ray binaries. The small source at the western side of the hot diffuse gas is most likely a binary system as well, but the counts in the B bands are to low to give a hardness ratio for the source.

The CHANDRA data does not resolve other sources into smaller ones. In Fig.70 (right) there are two sources which do not show up in the XMM–Newton data: north of ID 1 and towards the west of ID 1. The former is visible in the XMM–Newton data as a very faint extension of source ID 2. Its hardness ratio cannot be calculated since it

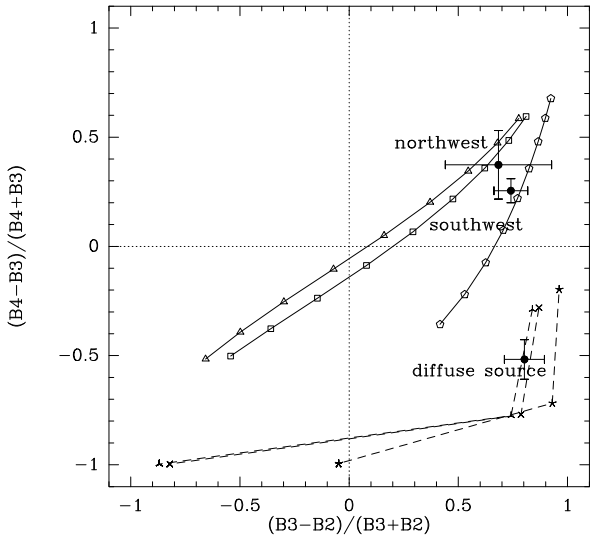

Fig. 72: *Hardness ratio of the central CHANDRA sources. The source in the northeast of the diffuse source has too few counts in the B2 band, hence it is left out here. The diffuse source is clearly a plasma source while the other two are power–law sources.*

has negative counts in the B2 band. The other source towards the west of ID 1 has also too less counts. The origin of these sources remains unclear.

Sources ID 8 and 9, which show up in the "forbidden" region in the XMM–Newton hardness ratio diagram, are at the edge of a diffuse emission component associated with source ID 10. Unfortunately both sources have too few counts to calculate a hardness ratio from the CHANDRA data. Also no counterparts are found in the literature or the DSS2 images making a classification impossible. I will come back to the sources ID 8 and 9 in the section concerning the diffuse emission of NGC 4214.

To summarize the classification of the point sources found, I give a list of source ID s:

- plasma sources:
  1, 6, 14, 15, 32, 47, 71
- power–law sources:
  2, 4, 16, 17, 26, 44, 45, 68, 69, 70, 72
- unclear:
  5, 8, 9, 10, 11, 13, 18, 19, 20, 27, 28, 30, 31, 33, 58, 60

Since supernova remnants are quite rare objects in contrast to X–ray binaries, most of the unclear objects are thought to be binary systems. The sources in the upper left region in the HR diagram are very hard which does not argue for plasma emission. Another possibility for these hard sources could be, that they are highly absorbed background sources like AGNs.

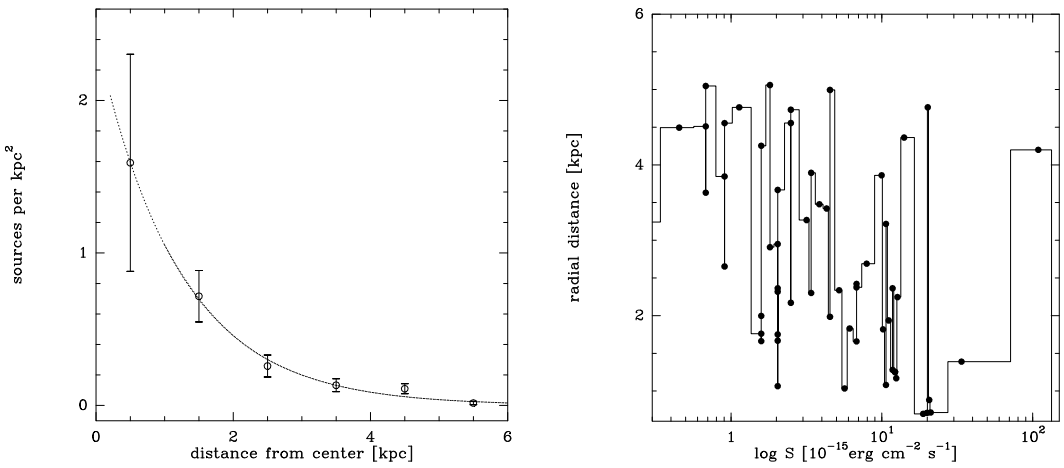

Fig. 73: **Left**: *The radial distribution of XMM–Newton point sources. The dotted line shows an exponential fit to the data, excluding the very uncertain point in the center.* **Right**: *Radial distances as a function of source flux.*

With the source positions at hand, one can now examine the spacial properties of these. The radial distance from the morphological center of the galaxy as a function of flux is given in Fig.73 together with the number density of the point sources towards increasing radii. The former shows no structure and is qualitatively comparable to Holmberg II. The latter is fitted with an exponential function of the form $f(r) = a \cdot \exp(r/r_o)$, giving $a = 2.4 \pm 0.08$ and $r_o = 1.2 \pm 0.05$ kpc. Compared to Holmberg II which has a comparable angular size and distance, this figure is smaller by a factor of three. This just means, that the point source density in NGC 4214 is higher in the center than in the Holmberg II case, or at least more concentrated towards the center. This is in line with the exponential brightness profile of the old stellar population (Schild, 1984), in general the X–ray binary population reflects the old stellar content of the galaxy.

Switching from fluxes to luminosities the XLF is obtained and plotted in Fig.74. As in the Holmberg II case the XLF shows a break at a luminosity of $\approx 0.8 \times 10^{37}$ erg s^{-1}. This break is not recognized by Hartwell et al. (2004) since their luminosity limit is too low (by a an order of magnitude) and they detect only 20 point sources. The slopes of the broken power–law fitted to the data are $\beta = -0.34 \pm 0.02$ and $\beta = -1.44 \pm 0.13$ for below and above the break luminosity, respectively. The slope fitted by Hartwell et al. (2004) to their 'unbroken' XLF is $\beta = -0.76 \pm 0.20$ which is (within the uncertainties) exactly the mean of the broken power–law slopes derived here. In this context they claim that the "luminosity functions of galaxies can now be studied in great detail", which is questionable since their data is not as sensitive as the data presented here.

The sources below the break luminosity are not randomly distributed across the HI body of the galaxy but they avoid the inner part completely. Inside a 2.1 kpc radius around the morphological center none of the sources below the luminosity break is found. Their distribution reaches out to the edge of the HI distribution. The sources

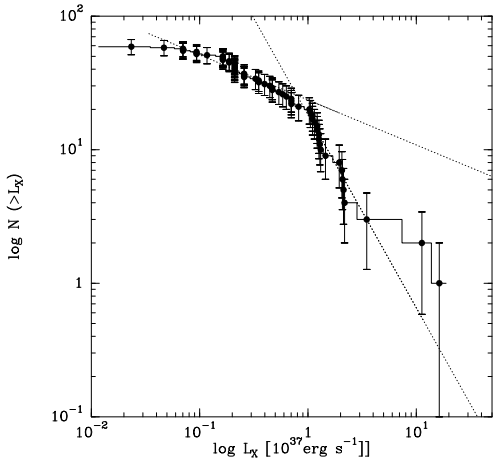

Fig. 74: *The XLF of NGC 4214 derived from XMM–Newton data. As in the Holmberg II case the XLF shows a break at* $\approx 0.8 \times 10^{37}$ *erg* s^{-1}*. The dotted lines correspond to a broken power–law fit with slopes* $\beta = -0.34 \pm 0.02$ *and* $\beta = -1.44 \pm 0.13$ *below and above the break, respectively.*

below the break are the ones for which no hardness ratios can be determined. Thus, it is concluded that these sources are faint old sources (likely LMXB) which are not related to the star formation sites in the center of the galaxy. Hence, the break in the XLF represents a general distinction between old and young objects. This again shows, together with the argumentation for the other galaxies with XLF breaks, that the breaks can have different origins (see also Fabbiano & White, 2003; Humphrey & Buote, 2004).

5.1.6.2 Diffuse emission Diffuse soft X–ray emission on small scales (<1 kpc) is seen in three regions: a) at the central source, b) around sources ID 13 and 15 and c) around sources ID 8 and 9. The extraction region for the spectra are displayed in Fig.75

In the XMM–Newton image sources ID 8 and 9 appear as two distinct peaks while the CHANDRA image reveals one diffuse peak right between the two sources. The two peaks are smeared into one due to the adaptive smoothing of the image. A significant CHANDRA spectrum of the emission associated with sources ID 8, 9 and 10, can be obtained by grouping the data to at least 25 photons per channel. This yields 175 photons in seven bins across an energy range of 0.2-8.0 keV. Applying an M2 model to the data, the fit gives for $\chi^2 = 1.4$ the following parameters: $N_{HI} = 3.5 \times 10^{21}$ cm^{-2}, $\Gamma = 0.63$ and $T = 10^{6.2}$ K. The spectrum is displayed in Fig.76. A query at the source position of ID 8 gave a very faint counterpart in the radio continuum at 20 cm, but no spectral index can be derived. However, the diffuse emission is morphologically connected to source ID 10 which is comparable with a plasma source, according to its hardness ratio. The temperature based on the HR diagram is also compatible with

log(T[K])=6.2 K.

Hence, the argumentation points to hot gas originating probably from a supernova remnant. One might think, that the hot gas stems from young hot stars heating the environment and producing the radio continuum emission (HII region), but the DSS2 images do not show stellar clusters at the position in question. This diffuse emission feature associated with sources ID 8 and 9 is not discussed by Hartwell et al. (2004). They only regard the central diffuse emission which is discussed below. First I present the diffuse emission associated with sources ID 13 and 15.

Also the source ID 13 and 15 are embedded in a diffuse emission region which is situated in the west of source ID 10 in a linear distance of about 2 kpc. Both sources and also the sources around (ID 14, 32, 33) are in the plasma regime of the HR diagram. A spectrum of the diffuse emission is extracted from the CHANDRA data excluding the point sources (see Fig.75). With a fixed foreground absorbing column density of $1.5 \times 10^{20}\,\mathrm{cm}^{-2}$ (Hartwell et al., 2004) the M2 model fit gives $T = 10^{5.7}\,\mathrm{K}$ and $\Gamma = 0.89$ ($\chi^2 = 1.8$). The spectrum is given in Fig.77. Since sources ID 13, 14, 15, 32 and 33 are correlated with a star cluster in the DSS2 blue it is concluded that the diffuse X–ray emission originates from an HII region. In contrast to the probable supernova remnant described above, here the star cluster argues for the HII region. However, since no additional data is avaliable for this region, the conclusion is not unappeasable.

Besides these two regions and the central source no diffuse emission is seen in the X–ray data with respect to the detection limits. Here the situation is quite similar to Holmberg II where the standard model for HI shells is only valid for a small fraction of shells. The main mechanism triggering the shell formation and thus the formation of stars is a drift of the galaxy through the ambient medium, where ram–pressure effects are responsible for the shell creation.

NGC 4214 itself formed stars over last few Gyr at a very low but constant rate of $\approx 0.5 - 1.0\,\mathrm{M}_\odot\,\mathrm{yr}^{-1}$ (Fanelli et al., 1997). They also claim that NGC 4214 is interacting with the nearby dwarf galaxy NGC 4190 at a linear distance of 36 kpc, yielding the star formation in the centrally concentrated star clusters, while the global star formation is not "burst–like". Hence, no high–energetic stellar events are expected in the outer parts of the galaxy and hot gas is virtually absent, except for the three cases where diffuse X–ray emitting gas is detected.

Having the spectra of the three diffuse emission features a), b), and c) more parameters can be calculated. These three X–ray features of the galaxy yield the following physical parameters, assuming spherical symmetry for the emitting volumes ($\mathrm{V_a} = 5.4 \times 10^{62}\,\mathrm{cm}^3$, $\mathrm{V_b} = 4.31 \times 10^{63}\,\mathrm{cm}^3$, $\mathrm{V_c} = 2.5 \times 10^{64}\,\mathrm{cm}^3$):

central SNR candidate a):

- EM$= 9.7 \times 10^{-4}\,\mathrm{pc\,cm}^{-6}$

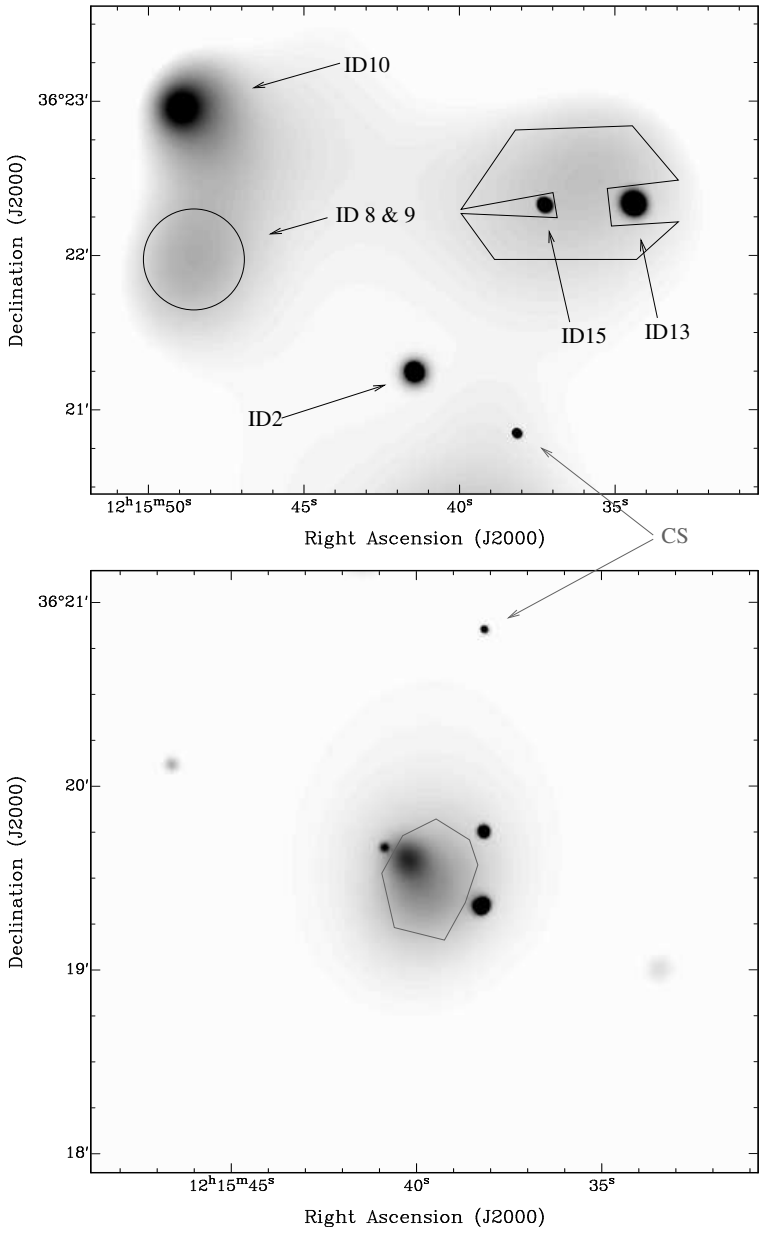

Fig. 75: *Spectral extraction regions of diffuse emission in the central region of NGC 4214 (CHANDRA data). The* **upper image** *shows the region around sources ID 8, 9, 10, 13 and 15 while the* **lower image** *shows the central source of NGC 4214. The CHANDRA source denoted as 'CS' is the same in both images. The extraction regions are shown in two images because the clipping is different in both in order to show the sources properly. The lower clip corresponds to 4-σ above background.*

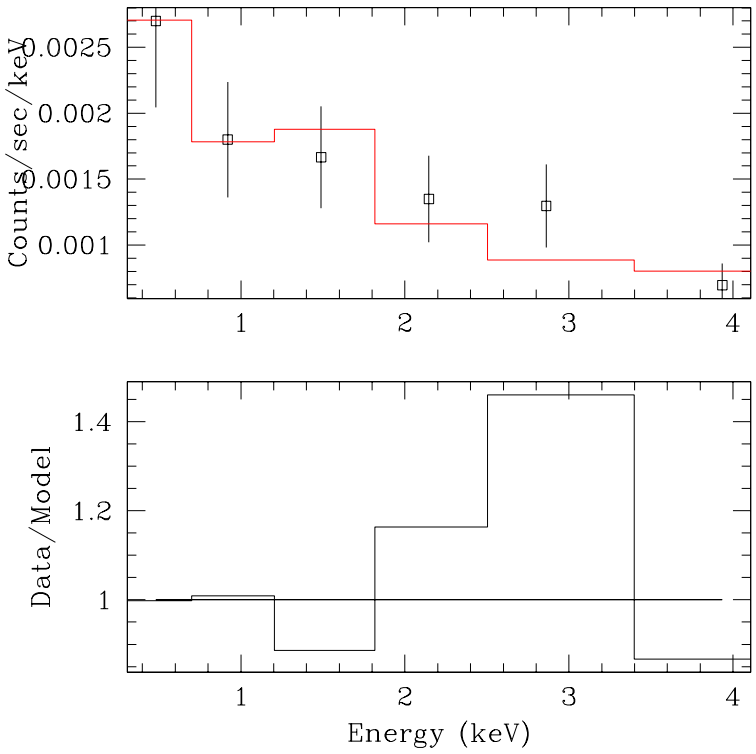

Fig. 76: *CHANDRA emission spectrum of the emission associated with sources ID 8, 9 and 10 in NGC 4214 (data points in the upper panel) together with the best fit model (solid line in the upper panel). The lower panel shows the ratio of data/model.*

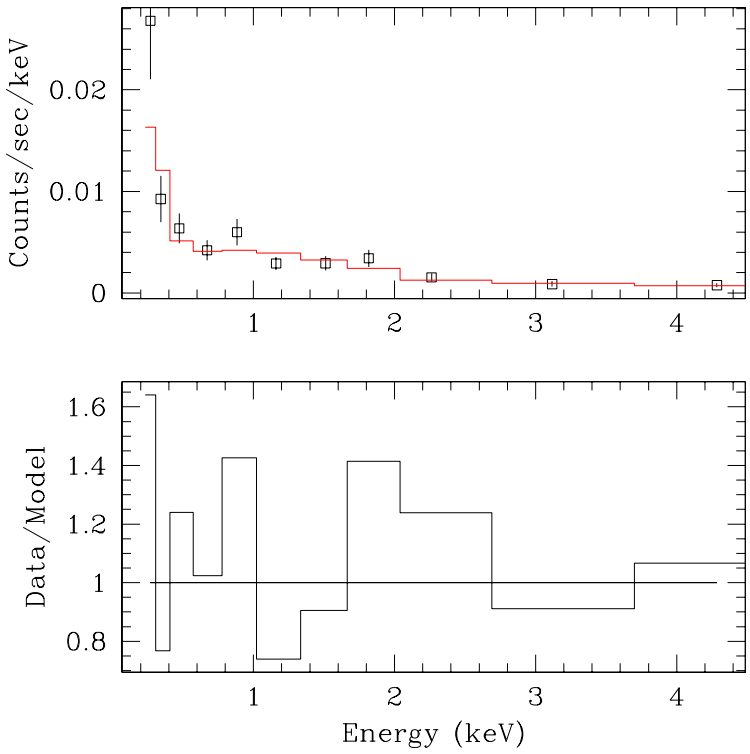

Fig. 77: *CHANDRA emission spectrum of the emission associated with sources ID 13 and 15 in NGC 4214 (data points in the upper panel) together with the best fit model (solid line in the upper panel). The lower panel shows the ratio of data/model.*

- $T = 10^{6.3}\,\mathrm{K}$
- $n_e \cdot f^{1/2} = 0.4\,\mathrm{cm}^{-3}$
- $P \cdot f^{-1/2} = 2.17 \times 10^{-10}\,\mathrm{dyn\,cm}^{-2}$
- $M \cdot f^{-1/2} = 0.2 \times 10^6\,M_\odot$
- $E_{th} = 1.8 \times 10^{53}\,\mathrm{erg}$
- $v = 165\,\mathrm{km\,s}^{-1}$
- $t_{\mathrm{cool}} = 3.3\,\mathrm{Myr}$
- $d = 0.5\,\mathrm{kpc}$

ID 8 & 9 b):

- EM$= 1.3 \times 10^{-4}\,\mathrm{pc\,cm}^{-6}$
- $T = 10^{6.2}\,\mathrm{K}$
- $n_e \cdot f^{1/2} = 5.2 \times 10^{-2}\,\mathrm{cm}^{-3}$
- $P \cdot f^{-1/2} = 2.3 \times 10^{-11}\,\mathrm{dyn\,cm}^{-2}$
- $M \cdot f^{-1/2} = 0.2 \times 10^6\,M_\odot$
- $E_{th} = 1.5 \times 10^{53}\,\mathrm{erg}$
- $v = 150\,\mathrm{km\,s}^{-1}$
- $t_{\mathrm{cool}} = 20\,\mathrm{Myr}$
- $d = 3\,\mathrm{kpc}$

ID 13 & 15 c):

- EM$= 1.5 \times 10^{-3}\,\mathrm{pc\,cm}^{-6}$
- $T = 10^{5.7}\,\mathrm{K}$
- $n_e \cdot f^{1/2} = 7.3 \times 10^{-2}\,\mathrm{cm}^{-3}$
- $P \cdot f^{-1/2} = 1.05 \times 10^{-11}\,\mathrm{dyn\,cm}^{-2}$
- $M \cdot f^{-1/2} = 1.5 \times 10^6\,M_\odot$

- $E_{th} = 4.0 \times 10^{53}\,\mathrm{erg}$
- $v = 85\,\mathrm{km\,s^{-1}}$
- $t_{\mathrm{cool}} = 4.7\,\mathrm{Myr}$
- $d = 0.4\,\mathrm{kpc}$

The values derived here show that the diffuse components are probably bound to the galaxy since the distances (d) they can reach are very small. Component a) is in broad agreement with the values of the softer component given by Hartwell et al. (2004). The deviations can be attributed to the uncertain filling factor and different extraction regions, and of course to the different models assumed. However, the simpler model presented here is more favored since it has less free parameters. The parameters of components b) and c) are in agreement with their classification given above. Since the diffuse emission of component c) is at high column densities of the neutral gas it is likely that the hot gas is in front of the neutral hydrogen. On the other hand, the diffuse emission component b) leaks into a low column density region while the likely origin of the emission is located towards higher column densities (see Fig.67). Here, the interpretation regarding the standard model is challenging.

5.1.6.3 Summary XMM–Newton and CHANDRA data are analyzed with respect to X–ray point sources and diffuse emission within the HI distribution of NGC 4214 as detected by the VLA. In total, 70 X–ray point sources are detected down to the detection limit in the PS band in contrast to the 20 sources detected by Hartwell et al. (2004).. The log(N)-log(S) relation shows that the detection is statistically not contaminated by background sources from the cosmic X–ray background.

There are 12 point sources which are very faint in the EPIC–*pn* data and they are only significant in the M1M2 smoothed data. The central region of the galaxy, where star formation is taking place today, is not well resolved by XMM–Newton . Thus, CHANDRA data is used to resolve the bright point source found by XMM–Newton. It turns out, that the single source decomposes into four sources in the CHANDRA data one of which is extended and associated with Hα emission and an Hα cavity detected by MacKenty et al. (2000). This X–ray source is most likely a supernova remnant.

A second supernova remnant is found in NGC 4214. This finding is confined by a very faint radio continuum source at the same position. In contrast to this, a third diffuse X–ray emission feature is interpreted as an HII region because it is associated with a star cluster visible in DSS2 red and blue band.

The remaining point sources are most probable accreting binary systems according to their hardness ratios. A discrimination between LMXB or HMXB is not easy since no additional data is available and the hardness ratio does not distinguish between these.

According to Hartwell et al. (2004) the sources in the center are HMXB since they are associated with the star forming region. This does not apply to the sources outside a radius of $\approx 2\,\mathrm{kpc}$ radius from the center and even the classification of Hartwell et al. (2004) is only rough and can be challenged. Especially because their choice of the bands is not very careful and leads to not well separated model curves in the HR diagram.

The spacial distribution of X–ray source in NGC 4214 is analyzed then. The source density drops exponentially from the center with $r_\mathrm{o} = 1.2\,\mathrm{kpc}$ which is a factor of three smaller than in the Holmberg II case. Thus, the sources in NGC 4214 are more concentrated towards the center than in Holmberg II. The exponential decline towards the outer rim is in concordance with the profile of the old stellar population in the galaxy found by Schild (1984). The radial distribution as a function of flux does not show a particular behavior; the sources are distributed randomly with respect to their fluxes.

Further the XLF is investigated. It turns out that it can be approximated by a broken power–law with indices $\beta = -0.34 \pm 0.02$ below the break luminosity of $0.8 \times 10^{37}\,\mathrm{erg\,s^{-1}}$ and $\beta = -1.44 \pm 0.13$ above. The break is interpreted as a distinction between old and young objects because the sources below the break are situated outside the star forming clusters in the center. Here, the break is absent in the XLF derived by Hartwell et al. (2004) due to the detection limit.

Diffuse soft X–ray emission is only detected at three plasma sources as described above. No hot halo or outflow is visible. This is also constrained by the spectra taken at the positions of the diffuse emission. The derived plasma parameters do not allow the gas to be expelled into the halo of NGC 4214. Since the star formation of the galaxy in the last few Gyr was quite low (Fanelli et al., 1997) the non–detection of a hot halo is expected. Here, the picture of NGC 4214 derived is quite similar to what is found for Holmberg II.

5.1.7 NGC 4449

The neutral interstellar medium of NGC 4449 is quite unusual as reported by Bajaja et al. (1994); Hunter et al. (1998, 1999): In the outer part of the optical galaxy the HI shows a ring–like structure with high velocity dispersion. In addition there are two counter–rotating gas systems around the optical galaxy. Furthermore, the neutral ISM is fragmented into clouds as observed in other galaxies. The inner structure appears as a bar which includes most of the optical galaxy whereas outside the bar the neutral gas is of filamentary structure. All this argues for a disruption of the galaxy due to an external perturbation and the gas has not relaxed up to now (see also Valdez-Gutiérrez et al., 2002). To give constraints on that scenario from the theoretical side Theis & Kohle (2001) performed N–body simulations. Their result is an interaction

Tab. 31: *NGC 4449*

Morphological type	dIrr, Im	
Position (J2000.0)	$\alpha = 12^h28^m12\overset{s}{.}13$ $\delta = 44^d06^m6\overset{s}{.}95$	
Distance	4.2 Mpc	(Karachentsev et al., 2003)
HI mass (10^6 $M_\odot$)	300	(Hunter et al., 1999)

of NGC 4449 with the companion galaxy DDO 125 and their model can reproduce the observational results. Because the neutral medium of the galaxy is highly perturbed, the X–ray investigation is performed only for the inner $5\overset{'}{.}0$.

The high energy regime was observed with CHANDRA. The analysis shows diffuse gas with a complex morphology (Summers et al., 2003). They suggest an expanding shell within an Hα cavity which is aligned with the diffuse X–ray emission. Here, the authors point to the huge HI halo which prevents the hot gas from being blown out although the expansion velocity is supposed to be $\approx$220 km s^{-1}. Individual X–ray point sources were studied by Miyawaki et al. (2004). They suggest that the X–ray emission of dwarf galaxies in general is enhanced by recent star formation.

The XMM–Newton observation (see Tab.4 for exposure times) of NGC 4449 reveals 15 X–ray point sources above the 4-σ background level in the PS band of the smoothed M1M2 images. Since there is a 29 ks CHANDRA observation available from the archive it is advisable to use this because the angular resolution is much better. Several XMM–Newton point sources decompose into two or three CHANDRA point sources. Hence, the XMM–Newton data is rejected.

After extracting PS band events from the CHANDRA event file, the image is adaptively smoothed and clipped to 4-σ background level. The X–ray point sources are identified by eye as before. Since the HI morphology of NGC 4449 shows large scale filaments and arms, only the inner part is regarded. The X–ray map together with source positions, IDs and HI contours of the inner region is displayed in Fig.78. The image reveals 20 X–ray point sources in total, together with diffuse emission in between the central sources. The detection limits for the B bands and PS band are given in Tab.32.

Here, the detection limits are very low compared to XMM–Newton. This is due to the small number of background counts in a large detector area (e.g. in the B2 band are 180 cts in 37044 pixels). Having the detection limits, the detected point sources are listed in Tab.33 with their positions, fluxes, luminosities and the counts in the B bands.

To make sure that the point sources are not contaminated by the extra galactic X–ray background, the log(N)-log(S) relation is again evaluated with respect to the number of

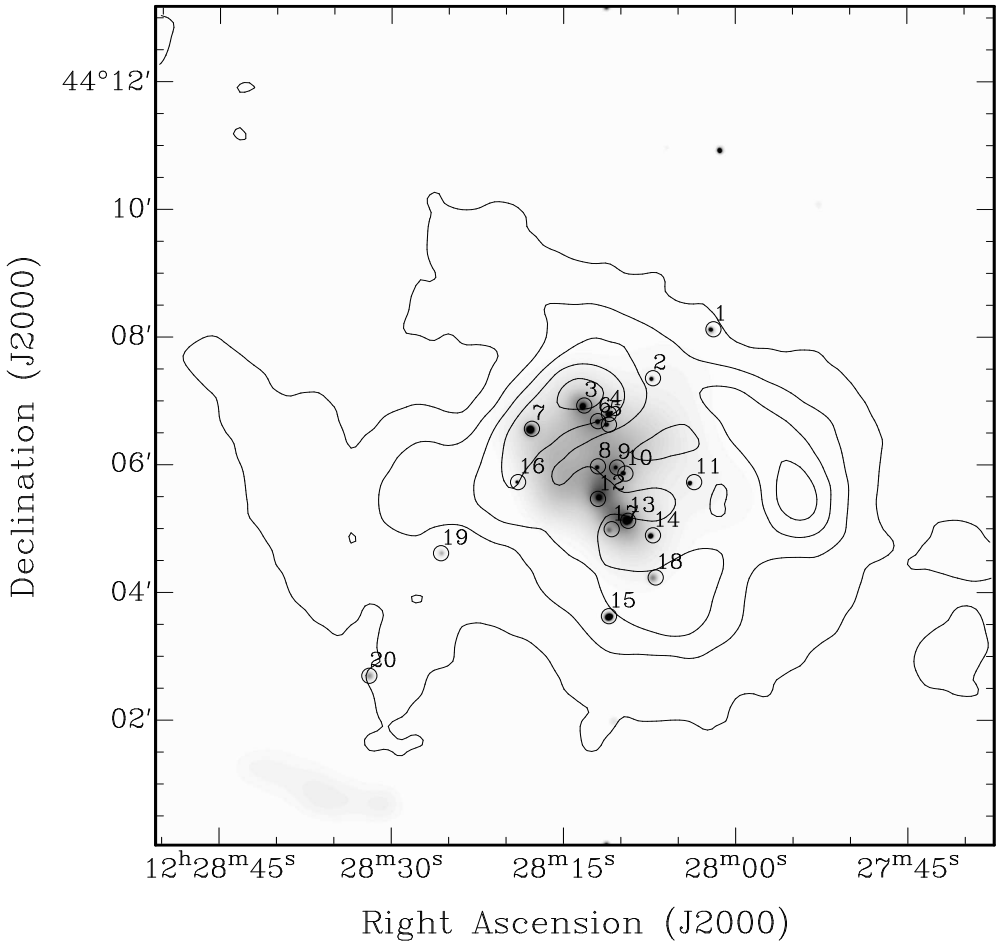

Fig. 78: *Adaptively smoothed CHANDRA image of NGC 4449 in the PS band with superimposed* HI *contours and point source positions. Diffuse emission is also seen in the center of the galaxy. The image is clipped to 4-*σ *background level. The contours show the* HI *distribution starting at 10% of the peak intensity and growing in steps of 20%. The peak is 0.55 Jy/Beam. The* HI *map is taken from Hunter et al. (1999).*

Tab. 32: *NGC 4449 flux limits of the CHANDRA data for individual bands normalized to the area of 3.5 PSF. The flux units are 10^{-17} erg cm^{-2} s^{-1}. The size of the background area is about 35000 pixels or more.*

Band	background counts	flux limit
B2	0.05±0.01	2.7±0.5
B3	0.10±0.01	1.5±0.2
B4	0.04±0.01	0.5±0.1
PS	0.30±1.01	7.5±0.2

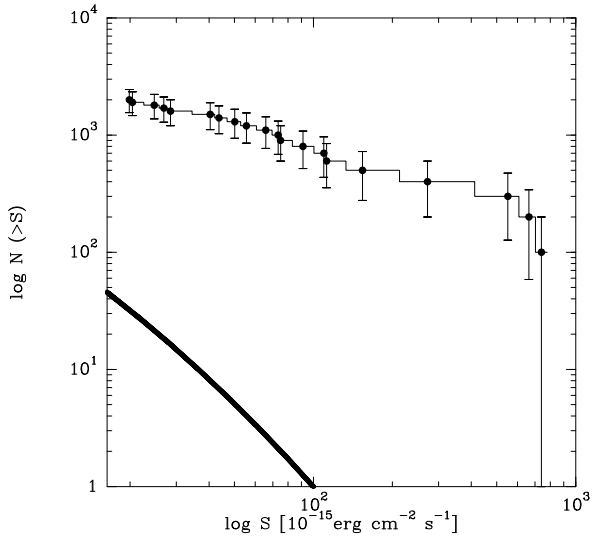

Fig. 79: *Comparison of the log(N)-log(S) relation of NGC 4449 (CHANDRA data) with the extragalactic X–ray background. With respect to the uncertainty of the number of point sources in the galaxy, the relation is well above the extragalactic relation derived by Hasinger et al. (2001) which is the upper limit for the XRB.*

Tab. 33: *The X–ray point sources found in NGC 4449 (CHANDRA data). The flux units are 10^{-15} erg cm^{-2} s^{-1} in the PS band, the luminosity units are 10^{37} erg s^{-1}, the luminosity uncertainty is of the order of the relative flux uncertainty. The stars mark sources with zero or less counts in one band after background subtraction. The last three columns give the background corrected counts in the corresponding band.*

ID	Right Ascension (J2000.0)	Declination (J2000.0)	Flux	Luminosity	B2	B3	B4
1	$12^h28^m2.02$	$44^o\ 08'\ 7.86$	75 ± 6.42	15.08	9	33	77
2	$12^h28^m7.23$	$44^o\ 07'\ 21.63$	43.65 ± 4.93	8.78	6	23	31
3	$12^h28^m13.17$	$44^o\ 06'\ 56.04$	153.9 ± 9.16	30.95	17	108	132
4	$12^h28^m10.97$	$44^o\ 06'\ 48.17$	551.2 ± 17.28	110.86	18	384	505
5	$12^h28^m11.16$	$44^o\ 06'\ 38.33$	65.81 ± 6.02	13.24	22	55	38
6	$12^h28^m11.89$	$44^o\ 06'\ 41.28$	109.6 ± 7.74	22.04	11	85	83
7	$12^h28^m17.83$	$44^o\ 06'\ 34.38$	740.4 ± 20.02	148.91	7	155	750
8	$12^h28^m11.98$	$44^o\ 05'\ 58.97$	40.41 ± 4.75	8.13	6	46	21
9	$12^h28^m10.42$	$44^o\ 05'\ 57.99$	55.54 ± 5.54	11.17	79	20	3
10	$12^h28^m9.69$	$44^o\ 05'\ 52.08$	112.3 ± 7.83	22.59	7	46	97
11	$12^h28^m3.85$	$44^o\ 05'\ 43.22$	73.38 ± 6.35	14.76	15	37	53
12	$12^h28^m11.79$	$44^o\ 05'\ 29.45$	50.14 ± 5.27	10.08	6	42	28
13	$12^h28^m9.33$	$44^o\ 05'\ 7.80$	663.6 ± 18.96	133.46	172	467	485
14	$12^h28^m7.23$	$44^o\ 04'\ 54.03$	91.22 ± 7.07	18.35	37	72	45
15	$12^h28^m11.06$	$44^o\ 03'\ 38.26$	272.3 ± 12.16	54.77	304	198	2
16	$12^h28^m19.01$	$44^o\ 05'\ 44.19$	26.9 ± 3.90	5.41	33	15	2
17	$12^h28^m10.93$	$44^o\ 04'\ 59.44$	28.52 ± 4.01	5.74	8	16	21
18	$12^h28^m7.05$	$44^o\ 04'\ 14.67$	19.87 ± 3.38	4.00	1	2	17
19	$12^h28^m25.58$	$44^o\ 04'\ 38.21$	20.41 ± 3.43	4.10	1	3	23
20*	$12^h28^m31.87$	$44^o\ 02'\ 42.04$	24.73 ± 3.75	4.97	0	5	22

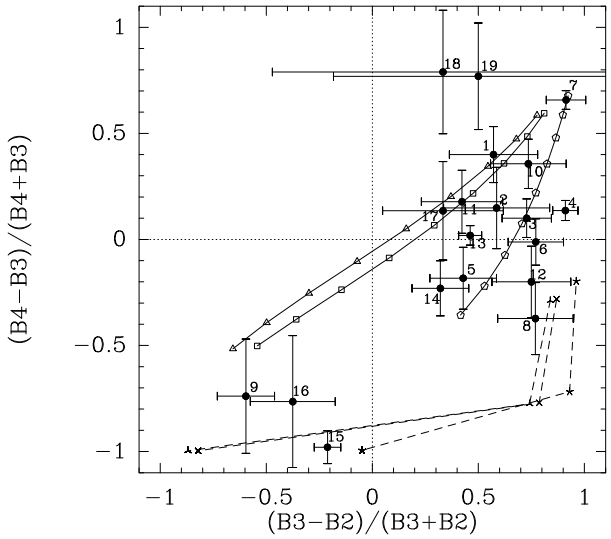

Fig. 80: *HR for the point sources found in NGC 4449 with CHANDRA. The numbers correspond to the IDs of Tab.33. All errorbars correspond to an uncertainty of 1-σ. The dashed and solid lines are described in detail in the caption of Fig.19 and the accompanying text.*

sources per square degree, according to Hasinger et al. (2001). The relation is shown in Fig.79. It turns out that the relation is well above the extragalactic background and hence, the detected sources belong to the galaxy.

With this information the nature of the detected point sources can be investigated. Only one source has zero counts in one of the B bands (ID 20) and hence it is excluded from this investigation. The first tool used is again the hardness ratio diagram of the sources. It is displayed in Fig.80.

The HR diagram shows five peculiar sources namely ID 9, 15, 16, 18 and 19. Sources ID 18 and 19 are comparable with the power–law models within 2-σ uncertainties. Source ID 18 is classified as a background AGN by Summers et al. (2003). This source is also seen in the XMM–Newton OM data in Fig.81. Source ID 19 might be an AGN as well but it is not further classified by Summers et al. (2003). The more interesting sources ID 9, 15 and 16 are in the very soft regime of the HR diagram. These sources are identified as super soft sources (SSS) one of which (ID 15) is also reported by Summers et al. (2003) and the remaining two by Ott (2003). Now, with the OM image the binary systems can be separated into LMXB and HMXB and the classification is given in Tab.34.

Having the sources and their physical nature, one can study their spatial distribution in the galaxy. Here, the inclination angle of $i = 56.2^{\mathrm{o}}$ (e.g. Hunter et al., 1999) has to be taken into account. The radial number density per square kiloparsec is shown in Fig.82 (left). It shows a nice exponential decline towards larger radii. Fitting an exponential function to the data gives a characteristic scale length of $r_{\mathrm{o}} = 0.66 \pm 0.01$ kpc. There are no special features in the exponential decline. This is in concordance with the

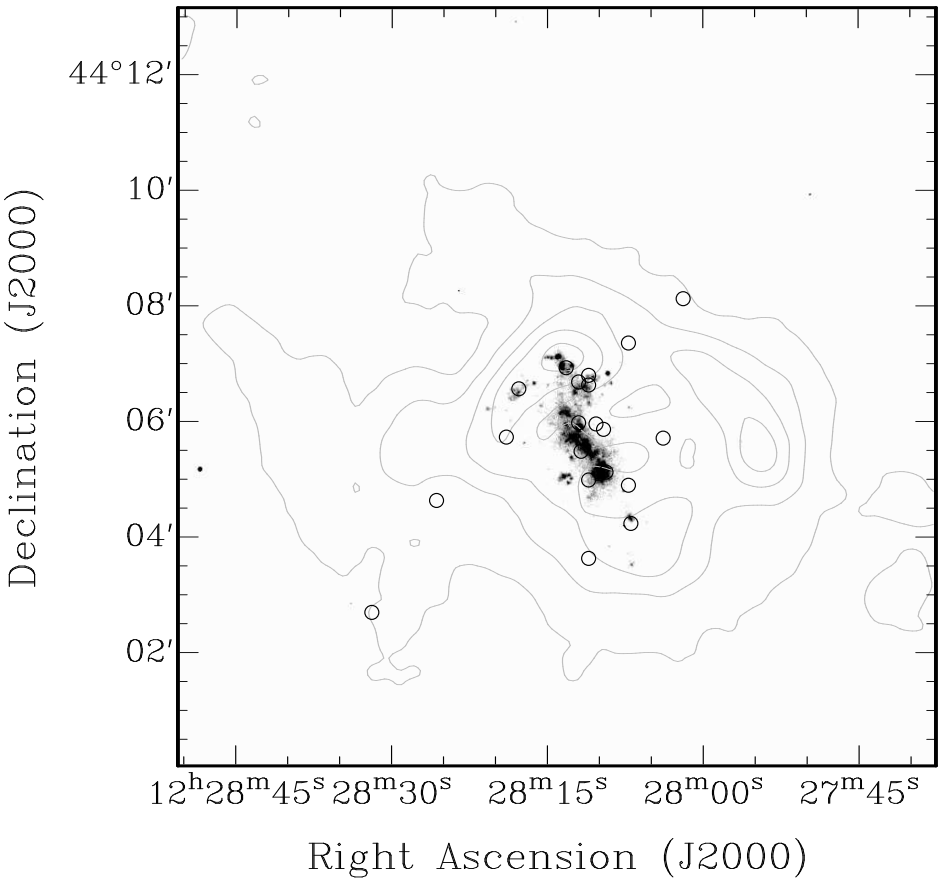

Fig. 81: *XMM–Newton optical monitor image of NGC 4449 in the UV regime (180-260 nm). The circles mark the position of the detected X–ray point sources. The contours are the same as in Fig.78*

Tab. 34: *The X–ray point sources of NGC 4449 and their most likely physical type. Here, L denotes LMXB, H denotes HMXB and S is for SSS and R for supernova remnant.*

ID	Source type	ID	Source type
1	L	11	L
2	L	12	R
3	H	13	H
4	H	14	L
5	H	15	S
6	H	16	S
7	H	17	L
8	R	18	AGN
9	S	19	L
10	L	20*	—

stellar body of NGC 4449 which shows scale lengths of $r_o = 0.84 \pm 0.01$ kpc and $r_o = 0.74 \pm 0.01$ kpc for the V and B band surface brightness profiles, respectively (Hunter et al., 1999).

Introducing the fluxes of all sources gives the view graph in Fig.82 (right). Nearly sources are located within a radius of 2 kpc with respect to the morphological center of the galaxy. Only six sources are outside this radius and hence they are not associated with the stellar body of the galaxy. They are very likely residuals of past star formation.

Converting the fluxes to luminosities, one obtains the XLF of NGC 4449 which is shown in Fig.83. It is fitted by an unbroken power–law with $\beta = -0.59 \pm 0.03$. This unbroken behavior does not argue for a past star burst phase of the galaxy. Hence, the star formation in the galaxy is not dominated by bursts before $\approx 10^7$ yr ago. The XLF derived by Summers et al. (2003) also shows no breaks and their fitted slope amounts to $\beta = -0.51$. Unfortunately they do not give any uncertainties to this value but in general the agreement is there.

5.1.7.1 Diffuse emission Diffuse emission in the soft X–ray regime is known for NGC 4449 (e.g. Summers et al., 2003). In their work they apply the following model to the diffuse emission component: $\mathrm{abs_{gal}}$[abs(mekal+mekal)]. Their idea here is to have two plasma components with different temperatures, both attenuated by the ISM of NGC 4449 and in addition attenuated by the Galactic foreground which they fix to $N_{\mathrm{HI}} = 1.4 \times 10^{20}\,\mathrm{cm}^{-2}$. Since they excluded point sources and subtracted the background from the spectral data they do not introduce a power–law component in first place. However, the subtraction of background data is not feasible due to the Poisson statistics. Further, they argue that an additional power–law component (with

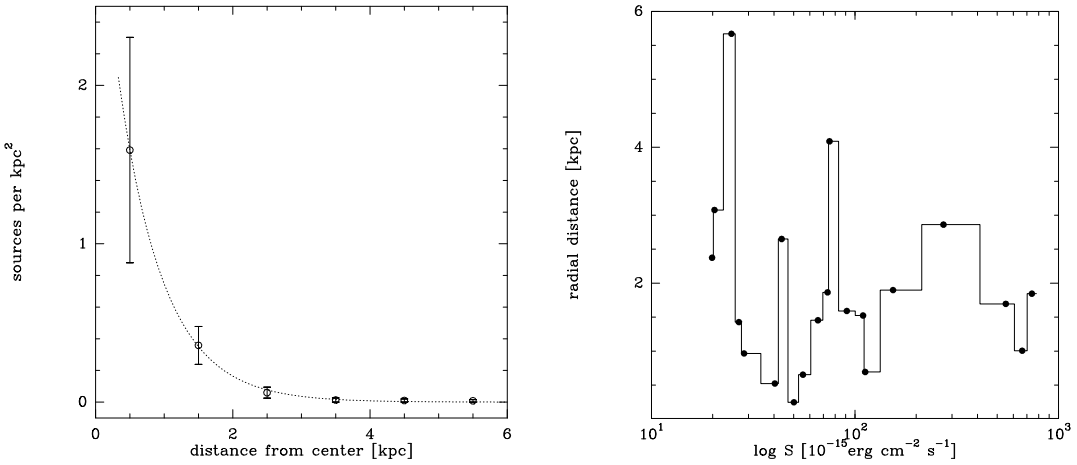

Fig. 82: **Left**: *The radial distribution of CHANDRA point sources. The dotted line shows an exponential fit to the data.* **Right**: *Radial distances as a function of source flux.*

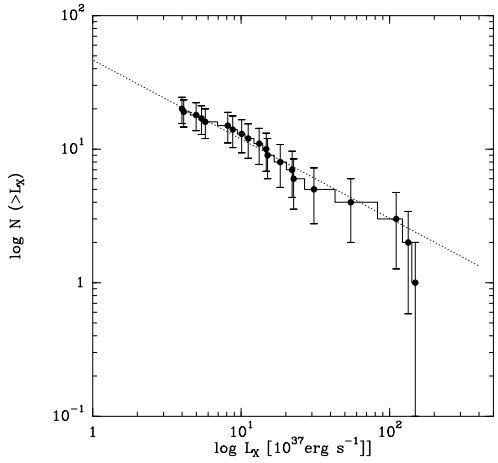

Fig. 83: *The XLF of NGC 4449 CHANDRA sources shows no breaks. The dotted line is a power–law fit with* $\beta = -0.59 \pm 0.03$. *Since the X–ray sources represent old objects (*10^7 *yr or older) these diagram shows that there was no pronounced star burst before that time. Recent star burst do not enter in this diagram.*

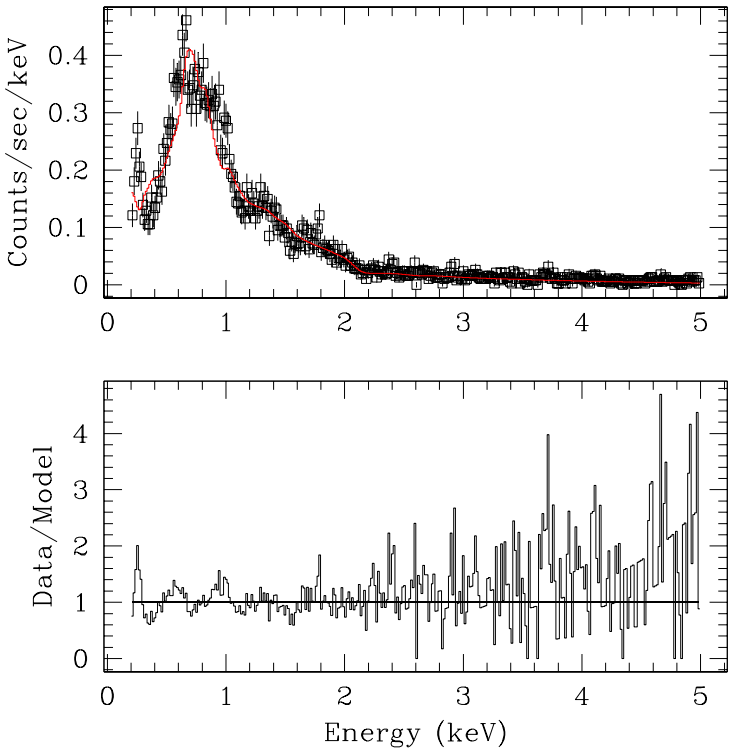

Fig. 84: *The diffuse CHANDRA emission spectrum of NGC 4449 (data points in the upper panel) together with the best fit model (solid line in the upper panel). The lower panel shows the ratio of data/model.*

a fitted power–law index of $\Gamma = 2.53$) does not improve the fit statistics. Their derived temperatures amount to $T_1 = 10^{6.5}$ K and $T_2 = 10^{7.0}$ K.

However, this model is physically not very striking because the attenuation by the Galactic foreground *and* the intrinsic absorption can be combined in one single absorption term. A physically more meaningful model is the model M1 introduced for IC 2574. The power–law index is again $\Gamma = 1.5$ and the Galactic foreground absorption is set to 1.4×10^{21} cm^{-2} (Miyawaki et al., 2004).

The spectral data is not background subtracted because the difference of two Poisson statistics is not a Poisson statistic anymore. Hence, the background as well as residual point sources here again is regarded with the (fixed) power–law component of the M1 model. With this model the χ^2 gives values well above 2.0. Hence, the model is not well determined. Therefore, a second plasma component is introduced, which is basically in agreement with the two–plasma component model given by Summers et al. (2003). This enhanced model still yields a χ^2 value of 2.3. However, the model can be fitted when the power–law index is regarded as a free parameter.

This gives $\chi^2 = 1.28$ but the power–law index $\Gamma = 2.7$ which is quite steep but in broad agreement with the power–law index given by Summers et al. (2003). The remaining parameters, however, are $T_1 = 10^{5.7}$ K and $T_2 = 10^{6.6}$ K which are lower than the temperatures derived by Summers et al. (2003). The discrepancy is attributed to the different models assumed. The fit also provides the parameters from which the following figures are calculated, assuming spherical symmetry of the emitting volume ($V = 4.4 \times 10^{65}\,\mathrm{cm}^3$):

cold plasma component:

- $T = 10^{5.7}\,\mathrm{K}$
- $n_e \cdot f^{1/2} = 5.24 \times 10^{-2}\,\mathrm{cm}^{-3}$
- $P \cdot f^{-1/2} = 7.25 \times 10^{-12}\,\mathrm{dyn\,cm}^{-2}$
- $M \cdot f^{-1/2} = 19 \times 10^6\,M_\odot$
- $E_{th} = 4.8 \times 10^{54}\,\mathrm{erg}$
- $t_{\mathrm{cool}} = 6\,\mathrm{Myr}$
- $v_{\mathrm{c}} = 83\,\mathrm{km\,s}^{-1}$

hot plasma component:

- $T = 10^{6.6}\,\mathrm{K}$
- $n_e \cdot f^{1/2} = 2.00 \times 10^{-2}\,\mathrm{cm}^{-3}$
- $P \cdot f^{-1/2} = 2.18 \times 10^{-11}\,\mathrm{dyn\,cm}^{-2}$
- $M \cdot f^{-1/2} = 7.3 \times 10^6\,M_\odot$
- $E_{th} = 1.37 \times 10^{55}\,\mathrm{erg}$
- $t_{\mathrm{cool}} = 130\,\mathrm{Myr}$
- $v_{\mathrm{c}} = 230\,\mathrm{km\,s}^{-1}$

Having the time scales and sound velocities, both plasma components show a different picture. The cold component is confined to the galaxy since it can only reach up to 500 pc from the disk, while the hot component can reach distances of 32 kpc (both upper limits).

The parameters of both components computed here are comparable to the parameters found by Summers et al. (2003), except the cooling times of the plasma components

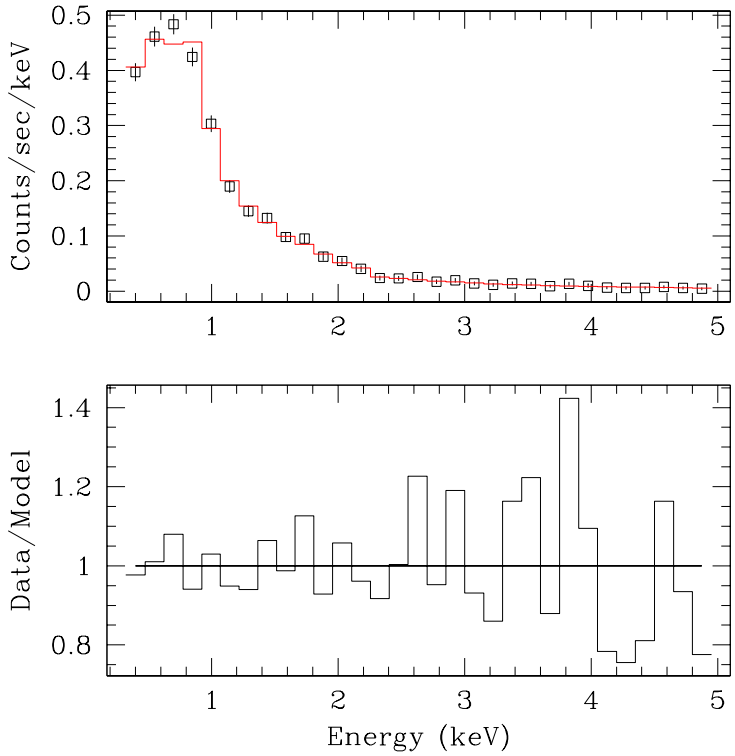

Fig. 85: *The diffuse emission spectrum of NGC 4449 (XMM–Newton data points in the upper panel) together with the best fit model (solid line in the upper panel). The lower panel shows the ratio of data/model.*

are a factor of ten higher in the model presented here. This discrepancy most likely stems from the different model and geometry assumed, which enters into the relation for the electron density. Also the unknown filling factor can introduce deviations in the cooling time. In summary, a multiphase environment model of the hot gas is needed and at least some of the hot gas can escape the galaxy, both in general agreement with the investigation performed by Summers et al. (2003).

Although the XMM–Newton data suffers from low angular resolution regarding the point sources, it is useful for spectral studies. Thus, the same region as for the CHANDRA spectrum is used to extract spectral data from the XMM–Newton data which was not performed by Summers et al. (2003). The point sources and background are not subtracted and the same model as for the CHANDRA data is applied. The XMM–Newton spectrum is displayed in Fig.85.

With the fixed value for the foreground absorption and the fixed $\Gamma = 1.5$ for the power–law index, the fit yields a $\chi^2 > 2$. When the power–law index is a free parameter, the χ^2 drops to 0.68 and the power–law index gives $\Gamma = 2.1$ which is slightly flatter than

for the CHANDRA data. The other parameters yield:

cold plasma component:

- $T = 10^{6.1}\,\mathrm{K}$
- $n_e \cdot f^{1/2} = 4.38 \times 10^{-2}\,\mathrm{cm}^{-3}$
- $P \cdot f^{-1/2} = 1.55 \times 10^{-11}\,\mathrm{dyn\,cm}^{-2}$
- $M \cdot f^{-1/2} = 16 \times 10^{6}\,M_{\odot}$
- $E_{th} = 1.0 \times 10^{55}\,\mathrm{erg}$
- $t_{\mathrm{cool}} = 19\,\mathrm{Myr}$
- $v_{\mathrm{c}} = 133\,\mathrm{km\,s}^{-1}$

hot plasma component:

- $T = 10^{6.8}\,\mathrm{K}$
- $n_e \cdot f^{1/2} = 1.85 \times 10^{-2}\,\mathrm{cm}^{-3}$
- $P \cdot f^{-1/2} = 2.9 \times 10^{-11}\,\mathrm{dyn\,cm}^{-2}$
- $M \cdot f^{-1/2} = 6.8 \times 10^{6}\,M_{\odot}$
- $E_{th} = 1.92 \times 10^{55}\,\mathrm{erg}$
- $t_{\mathrm{cool}} = 200\,\mathrm{Myr}$
- $v_{\mathrm{c}} = 280\,\mathrm{km\,s}^{-1}$

The values here are in broad agreement with the values derived from the CHANDRA data. The temperatures are slightly higher while the HI mass estimates are slightly lower. The discrepancy to the CHANDRA data is attributed to the differences in RMF and ARF files, i.e. the calibration. Also a different binning of the data can produce deviations in the fitted parameters. The reader may assume the deviations as an estimate for the uncertainties of the parameters.

The distance estimates the gas components can reach based on the cooling time and sound speed are 2.6 kpc for the cold and 58 kpc for the hot component. This supports the result from the CHANDRA data that the cold component is bound to the galaxy while the hot component can be vented into the halo.

5.1.7.2 Summary The XMM–Newton observation of NGC 4449 reveals 15 point sources in the inner 5.′0 of the galaxy. The outer parts are not regarded due to the impressive tidal debris seen in the HI data. Some of the XMM–Newton point sources decompose into individual point sources when the CHANDRA data of NGC 4449 is screened. Hence the XMM–Newton data is rejected since all XMM–Newton point sources are also detected in the CHANDRA data. The CHANDRA data contains 20 X–ray point sources. The log(N)-log(S) relation shows that the contamination by background sources is statistically negligible.

Only one source has zero counts in one of the B bands and hence it is excluded from the hardness ratio investigation. The HR diagram shows three super soft sources (SSS), two supernova remnants and accreting binary systems; eight LMXB and seven HMXB.

In concordance to Summers et al. (2003) one source is identified as a background AGN which is also visible in the XMM–Newton optical monitor in the 180-260 nm band.

The point source density dependence on radial distance from the galaxy center follows an exponential law with a scale length of $r_o = 0.66 \pm 0.01$ kpc. This value agrees with the exponential decline of the B and V band surface brightness. Only six X–ray sources are located outside a 2 kpc radius and they are interpreted as residuals of past star formation since they are all accreting binary systems.

The XLF of NGC 4449 is flat and can be approximated by a single power–law with index $\beta = -0.59 \pm 0.03$. This unbroken behavior is interpreted as a quiescent star formation without a burst before $\approx 10^7$ yr. A more recent star burst would not affect the XLF because the time is too short to produce accreting systems which by then would introduce breaks in the XLF.

Diffuse X–ray emission is a well known feature of NGC 4449 and as well found in this investigation. The attempt to fit a model to the total X–ray spectrum emerging from the diffuse region gives a two component plasma and a power–law model for the residual point sources in that region. The temperatures of the cold and hot plasma component are $10^{5.7}$ K and $10^{6.6}$ K respectively. The power–law component has a photon index of $\Gamma = 2.7$ which is much steeper than the value derived by Hasinger et al. (2001). The discrepancy between the temperatures here and the values derived by Summers et al. (2003) are attributed to the different model approach. The power–law index on the other hand is comparable to the one given by Summers et al. (2003) although they subtracted the background and the point sources. This shows that the subtractions of backgrounds regarding spectral data is questionable.

These values are in general agreement to the values found by Summers et al. (2003). The differences are attributed to the uncertain filling factor and a different extraction region. Of course the different spectral model introduced here yields different values for the parameters as well.

The calculated plasma parameters, cooling time and sound speed in the hot gas give upper estimates for the distance the gas can reach if it stems from a blowout due to

stellar activity. At least the hot component reaches sufficiently large distances to escape the galaxy in the future, while the cold component is bound to the galaxy. These findings for the diffuse emission are supported by the spectral data extracted from the XMM–Newton event list. The deviations to the CHANDRA data can be attributed to the differences in the associated RMF and ARF files, thus, the different calibrations for the two instruments. Also, the deviation may be interpreted as the uncertainty of the spectral investigations.

5.1.8 NGC 5253

NGC 5253 has a peculiar HI velocity field (Kobulnicky & Skillman, 1995) where the HI rotates around the optical major axis. In addition there is also a weak neutral gas component rotating around the minor axis. They claim that the gas dynamics together with the current star formation activity yields two scenarios, a) gravitational interaction with the nearby spiral M 83 or b) the accretion of a gas–rich companion on a highly elliptical orbit around NGC 5253.

In 1997 CO–line studies revealed that NGC 5253 appears to be the most CO–poor star burst galaxy known (Turner et al., 1997). They conclude, together with the previously known HI peculiarities, that the galaxy has recently accreted gas of extremely low metalicity. In addition to this a very young star cluster is observed in the very center of NGC 5253 using radio continuum observations (Turner et al., 1998). The diameter of these star forming regions is about a few tenths of a parsec which is an order of magnitude bigger than comparable regions in the Galaxy. Also the number of O–stars driving the ionization of these regions is significantly higher (200-1000 O–stars) than in the Galaxy. The region in the north of the dominant radio source may trace the very youngest star burst.

More recent, Strickland & Stevens (1999) observed NGC 5253 with ROSAT. They found at least five X–ray sources very nearby the central young star cluster and hence, they form superbubbles driven by these young clusters. The starburst in NGC 5253 appears to be fed by gas infalling along the optical minor axis of the galaxy while hot gas expanding from the starburst has a preferential direction along the major axis (Calzetti et al., 1999).

Summers et al. (2004) discovered several X–ray emitters with CHANDRA and XMM–Newton namely point sources and diffuse emission associated with superbubbles and probably star clusters therein. Again their analysis give evidence that the stellar ejecta may leave the gravitational potential well of the host galaxy and enrich the surrounding IGM.

The XMM–Newton observation of NGC 5253 taken from the archive shows one point source in the M1M2 map in the PS band. This source is located in the very center of the galaxy. Taking the CHANDRA data (59 ks exposure time) from the archive this

Tab. 35: *NGC 5253*

Morphological type	dIrr	
Position (J2000.0)	α = $13^h39^m56.^s29$ δ = -$31^d38^m38.^s30.^s$	
Distance	3.1 Mpc	(Freedman et al., 2001)
HI mass (10^6 $M_\odot$)	140	(Kobulnicky & Skillman, 1995)

Tab. 36: *NGC 5253 flux limits for individual CHANDRA bands normalized to the area of 3.5 PSF. The flux units are 10^{-17} erg cm^{-2} s^{-1}. The size of the background region is more than* $\approx$ 80000 *pixels.*

Band	background counts	flux limit
B2	0.1±0.01	2.7±0.3
B3	0.1±0.01	0.5±0.1
B4	0.1±0.01	0.4±0.1
PS	0.4±0.02	4.6±2.0

single point source fragments into several individual sources. In total I find 52 point sources, in contrast to the work of Summers et al. (2004) who found 31 point sources. The discrepancy is again due to the different point source detection used.

As in the NGC 4449 case some of these sources are not expected to be point sources but dense "blobs" in the diffuse hot gas phase or superbubbles surrounding SSC, as suggested also by Summers et al. (2004). This expectation is reasonable because the emission is very patchy in some regions of the galaxy, i.e. the emission is not point like but uneven extended.

The CHANDRA image in the PS band is given in Fig.86 together with the point source positions and the HI extend of the galaxy. Since no HI FITS data was available only an ellipse is given marking roughly the outer contour of the neutral gas where the column density drops below $N_{\rm HI} \approx 4.5 \times 10^{20}\,{\rm cm}^{-2}$ (see Kobulnicky & Skillman, 1995).

Decomposing the CHANDRA event list (59.09 ks exposure) into the B bands and PS band one can calculate the detection limits given in Tab.36. The flux of the point sources is then calculated assuming a power–law model with photon index of $\Gamma = 1.5$ and an absorbing column density of $2.5 \times 10^{20}\,{\rm cm}^{-2}$ from which the log(N)-log(S) relation is derived. The resulting diagram is shown in Fig.87. As with the previous observations the detected point sources are above the extragalactic background and are statistically not contaminated by unrelated sources. After this preparatory work

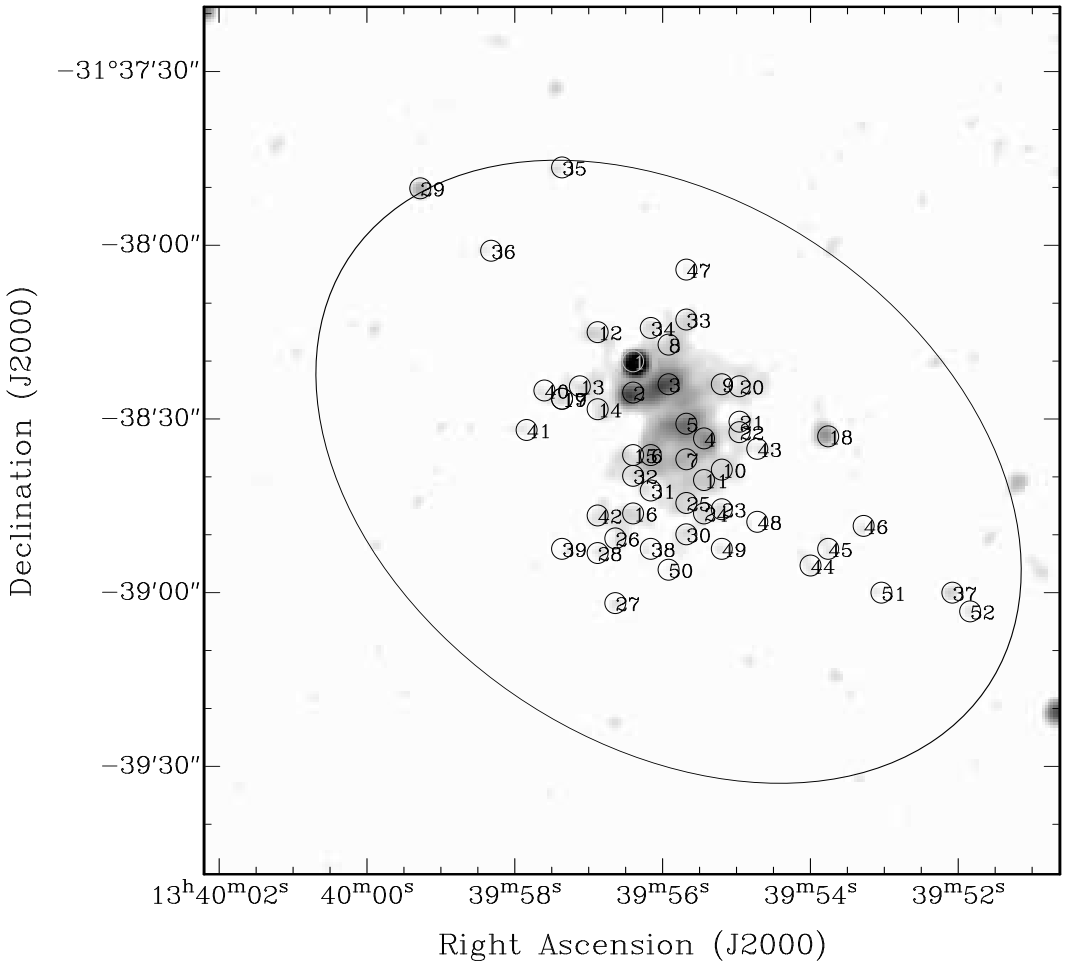

Fig. 86: *Adaptively smoothed image of the CHANDRA data in the PS band showing NGC 5253 with superimposed* HI *ellipse and point source positions. Some diffuse emission is also seen in the center of the galaxy. The image is clipped to 4-*σ *background level. The ellipse encircles the region where* $N_{\rm HI} \geq 4.5 \times 10^{20}$ *cm*$^{-2}$ *corresponding to the total* HI *intensity map by Kobulnicky & Skillman (1995).*

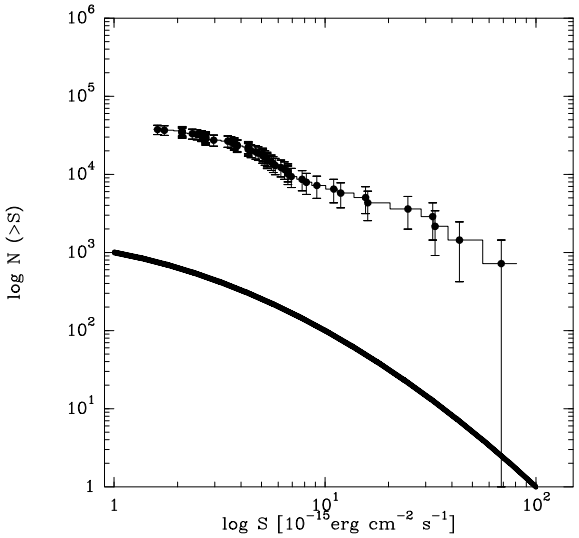

Fig. 87: *Comparison of the log(N)-log(S) relation of NGC 5253 (CHANDRA data) with the extragalactic X–ray background. With respect to the uncertainty of the number of point sources in the galaxy, the relation is well above the extragalactic relation derived by Hasinger et al. (2001) which, again, is the upper limit for the XRB.*

the list of point sources is given in Tab.37.

As expected there is a very high number of plasma sources (33), 12 power–law sources and seven yet unclear sources seen in the HR diagram (Fig.88). Here, the HR diagram is more telling than the one given by Summers et al. (2004) because the bands are chosen more carefully to avoid the ambiguity of different model curves.

From the unclear sources, ID 27 falls in the power–law regime when 2-σ uncertainties are regarded. Source ID 1 is the brightest source in the galaxy and it is also seen in radio continuum emission (Turner et al., 2000). Their conclusion with respect to the nature of this source is a very young gas–rich counterpart of super star clusters. Hence, the X–ray source is very likely hot gas produced by stellar winds.

The remaining unclear sources ID 9, 29, 30, 33, 42 are distributed randomly across the galaxy but ID 9 and 33 are closer to the diffuse emission. A cross–correlation with sources found in other wavelength[15], however, provides some further information. Within a search radius of $10''$ I find an HII region in a distance of $0.'1$ from ID 9 (Campbell & Terlevich, 1984). An X–ray source is found by NED at the position of ID 29 (Colbert et al., 2004) but the authors do not explicitly give the type of the source. Sources ID 30, 33 and 42 give no results in the cross–correlation.

The 12 power–law sources (ID 14, 18, 28, 32, 36, 37, 44-46, 50-52) are also distributed across the galaxy. They are not found in the very center which is dominated by young stellar populations. However, they all are within the stellar body of the galaxy as the

[15]NED is used for the cross–correlation, http://nedwww.ipac.caltech.edu/

Tab. 37: *The X–ray point sources found by CHANDRA in NGC 5253. The flux units are 10^{-15} erg cm^{-2} s^{-1} in the PS band, the luminosity units are 10^{37} erg s^{-1}, the luminosity uncertainty is of the order of the relative flux uncertainty. The stars mark sources with one or less counts in one band after background subtraction. The last three columns give the background corrected counts in the corresponding band.*

ID	Right Ascension (J2000.0)	Declination (J2000.0)	Flux	Luminosity	B2	B3	B4
1	$13^h39^m56.35$	-31° 38′ 20.08	68.48 ± 2.91	7.87	15.0	229.0	231.0
2	$13^h39^m56.46$	-31° 38′ 25.49	33.25 ± 2.03	3.82	10.0	193.0	59.0
3	$13^h39^m56.00$	-31° 38′ 24.02	43.39 ± 2.32	4.99	14.0	219.0	107.0
4	$13^h39^m55.38$	-31° 38′ 33.36	24.72 ± 1.75	2.84	12.0	131.0	49.0
5	$13^h39^m55.69$	-31° 38′ 30.90	32.39 ± 2.00	3.72	9.0	161.0	83.0
6	$13^h39^m56.12$	-31° 38′ 36.32	15.57 ± 1.39	1.79	5.0	83.0	32.0
7	$13^h39^m55.77$	-31° 38′ 36.81	15.95 ± 1.40	1.83	12.0	85.0	30.0
8	$13^h39^m55.85$	-31° 38′ 17.13	11.87 ± 1.21	1.36	9.0	66.0	17.0
9	$13^h39^m55.31$	-31° 38′ 24.02	7.79 ± 0.98	0.90	8.0	36.0	16.0
10	$13^h39^m55.15$	-31° 38′ 38.78	8.16 ± 1.00	0.94	6.0	44.0	9.0
11	$13^h39^m55.38$	-31° 38′ 40.74	9.15 ± 1.06	1.05	10.0	48.0	9.0
12	$13^h39^m56.93$	-31° 38′ 15.16	4.70 ± 0.76	0.54	6.0	21.0	5.0
13	$13^h39^m57.04$	-31° 38′ 24.51	5.19 ± 0.80	0.60	3.0	28.0	4.0
14	$13^h39^m56.81$	-31° 38′ 28.44	4.45 ± 0.74	0.51	4.0	16.0	10.0
15	$13^h39^m56.50$	-31° 38′ 36.32	11.00 ± 1.17	1.26	8.0	56.0	19.0
16	$13^h39^m56.42$	-31° 38′ 46.16	5.07 ± 0.79	0.58	5.0	26.0	4.0
17	$13^h39^m57.35$	-31° 38′ 26.48	4.33 ± 0.73	0.50	5.0	17.0	4.0
18	$13^h39^m53.77$	-31° 38′ 32.87	6.68 ± 0.91	0.77	6.0	19.0	23.0
19	$13^h39^m57.35$	-31° 38′ 26.48	4.33 ± 0.73	0.50	5.0	17.0	4.0
20	$13^h39^m54.85$	-31° 38′ 24.51	6.43 ± 0.89	0.74	9.0	30.0	7.0
21	$13^h39^m54.85$	-31° 38′ 30.41	5.07 ± 0.79	0.58	5.0	25.0	8.0
22	$13^h39^m55.04$	-31° 38′ 32.38	5.56 ± 0.83	0.64	5.0	27.0	10.0
23	$13^h39^m55.19$	-31° 38′ 45.66	5.32 ± 0.81	0.61	6.0	25.0	3.0
24	$13^h39^m55.42$	-31° 38′ 46.16	5.69 ± 0.84	0.65	6.0	26.0	6.0
25	$13^h39^m55.77$	-31° 38′ 44.68	6.68 ± 0.91	0.77	6	42	4
26	$13^h39^m56.54$	-31° 38′ 50.58	4.82 ± 0.77	0.55	3	22	5

Tab. 38: *Table.37—continued*

ID	Right Ascension (J2000.0)	Declination (J2000.0)	Flux	Luminosity	B2	B3	B4
27	$13^h39^m56.62$	-31° 39′ 1.90	2.10 ± 0.51	0.24	6	2	4
28	$13^h39^m56.85$	-31° 38′ 53.04	2.60 ± 0.57	0.30	2	9	6
29	$13^h39^m59.28$	-31° 37′ 50.07	3.71 ± 0.68	0.43	2	14	9
30	$13^h39^m55.69$	-31° 38′ 50.09	4.33 ± 0.73	0.50	6	20	6
31	$13^h39^m56.23$	-31° 38′ 42.22	6.18 ± 0.87	0.71	4	29	10
32	$13^h39^m56.39$	-31° 38′ 39.76	6.92 ± 0.92	0.80	9	26	15
33	$13^h39^m55.65$	-31° 38′ 12.70	5.32 ± 0.81	0.61	7	24	8
34	$13^h39^m56.16$	-31° 38′ 14.18	5.81 ± 0.85	0.67	9	25	6
35	$13^h39^m57.43$	-31° 37′ 46.62	2.10 ± 0.51	0.24	3	6	1
36	$13^h39^m58.39$	-31° 38′ 0.89	2.72 ± 0.58	0.31	3	7	6
37	$13^h39^m52.07$	-31° 38′ 59.93	2.35 ± 0.54	0.27	2	4	7
38	$13^h39^m56.19$	-31° 38′ 52.55	2.97 ± 0.61	0.34	8	11	2
39	$13^h39^m57.27$	-31° 38′ 52.55	2.10 ± 0.51	0.24	1	10	2
40	$13^h39^m57.62$	-31° 38′ 25.00	3.59 ± 0.67	0.41	4	12	3
41	$13^h39^m57.89$	-31° 38′ 31.89	2.72 ± 0.58	0.31	2	11	3
42	$13^h39^m56.85$	-31° 38′ 46.65	3.83 ± 0.69	0.44	6	14	5
43	$13^h39^m54.61$	-31° 38′ 35.33	3.83 ± 0.69	0.44	3	19	6
44	$13^h39^m54.00$	-31° 38′ 55.50	3.46 ± 0.65	0.40	5	14	6
45	$13^h39^m53.73$	-31° 38′ 52.55	3.71 ± 0.68	0.43	7	11	6
46	$13^h39^m53.30$	-31° 38′ 48.61	2.10 ± 0.51	0.24	5	4	5
47	$13^h39^m55.65$	-31° 38′ 4.34	2.47 ± 0.55	0.28	4	9	2
48	$13^h39^m54.81$	-31° 38′ 47.63	2.60 ± 0.57	0.30	4	9	2
49	$13^h39^m55.19$	-31° 38′ 52.55	2.72 ± 0.58	0.31	5	11	1
50	$13^h39^m55.89$	-31° 38′ 56.00	2.72 ± 0.58	0.31	4	10	4
51	$13^h39^m53.11$	-31° 38′ 59.93	1.73 ± 0.46	0.20	4	4	2
52	$13^h39^m51.84$	-31° 39′ 3.37	1.61 ± 0.45	0.18	1	5	2

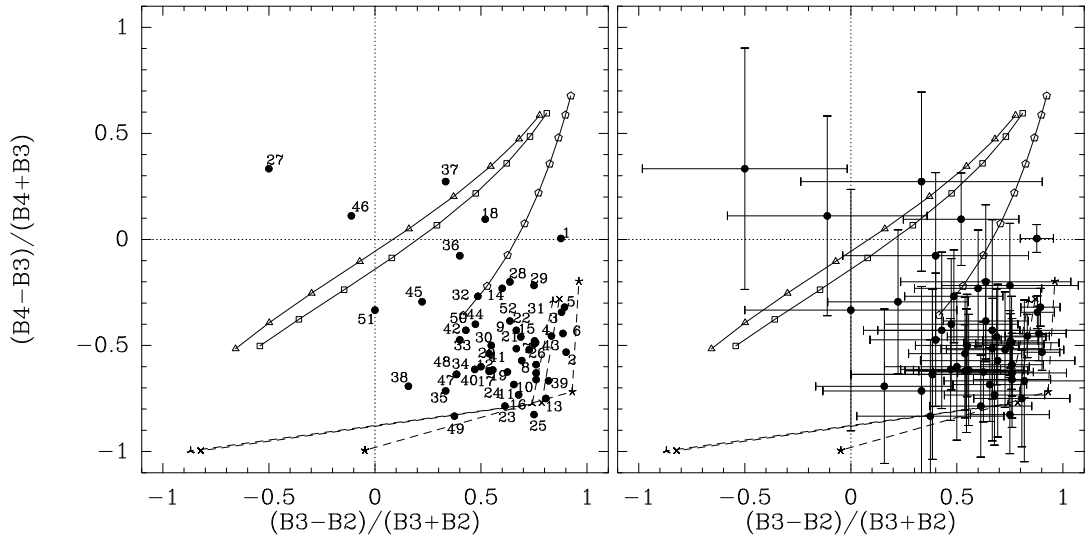

Fig. 88: *CHANDRA HR for the point sources found in NGC 5253. The numbers correspond to the IDs of Tab.37. All errorbars correspond to an uncertainty of 1-σ. The dashed and solid lines are described in detail in the caption of Fig.19 and the accompanying text.*

DSS2 red and blue bands show. Hence, they are classified as binary systems. Since they are quite faint ($L_X < 7.7 \times 10^{36}$ erg s^{-1}) they are most likely LMXB. Source ID 52 shows a bright foreground star in the DSS2 images thus it is probably not related to NGC 5253. The brightest power–law source is ID 18. Summers et al. (2004) fit a combined absorbed plasma+power–law model to the spectral data. This model can be rejected since the source is well within the power–law regime of the HR diagram.

From radio continuum observations only three supernova remnant candidates are reported by Turner et al. (1998). Two of them (sources B and K of Turner et al. (1998)) are identified with the X–ray sources ID 2 and 1 respectively, while the third supernova remnant candidate (source H in their paper) has no counterpart in the X–rays. This nondetection argues for the supernova remnant to be old, as pointed out by Turner et al. (1998). Moreover, they emphasize that it is behind a dust lane and hence the X–ray emission is attenuated. The very high number of plasma sources can be explained by the diffuse component seen in the X–ray data as follows.

The remaining plasma sources are confined to the inner region of the galaxy, less than 30″ from the morphological center which corresponds to 500 pc, assuming a distance of 3.1 Mpc to NGC 5253 (Freedman et al., 2001). Their spatial distribution follows the diffuse emission component as shown in Fig.89. The only outlier here is source ID 35 in the north west of NGC 5253. Cross-correlating the source position with NED (search radius 10″) gave no further insight, thus the origin of this source remains unclear. The other sources might be associated with superbubbles as suggested by Summers et al. (2004) or they might be clumps in the diffuse emission. These clumps can either be denser regions in the hot gas, due to turbulent motions or a line–of–sight

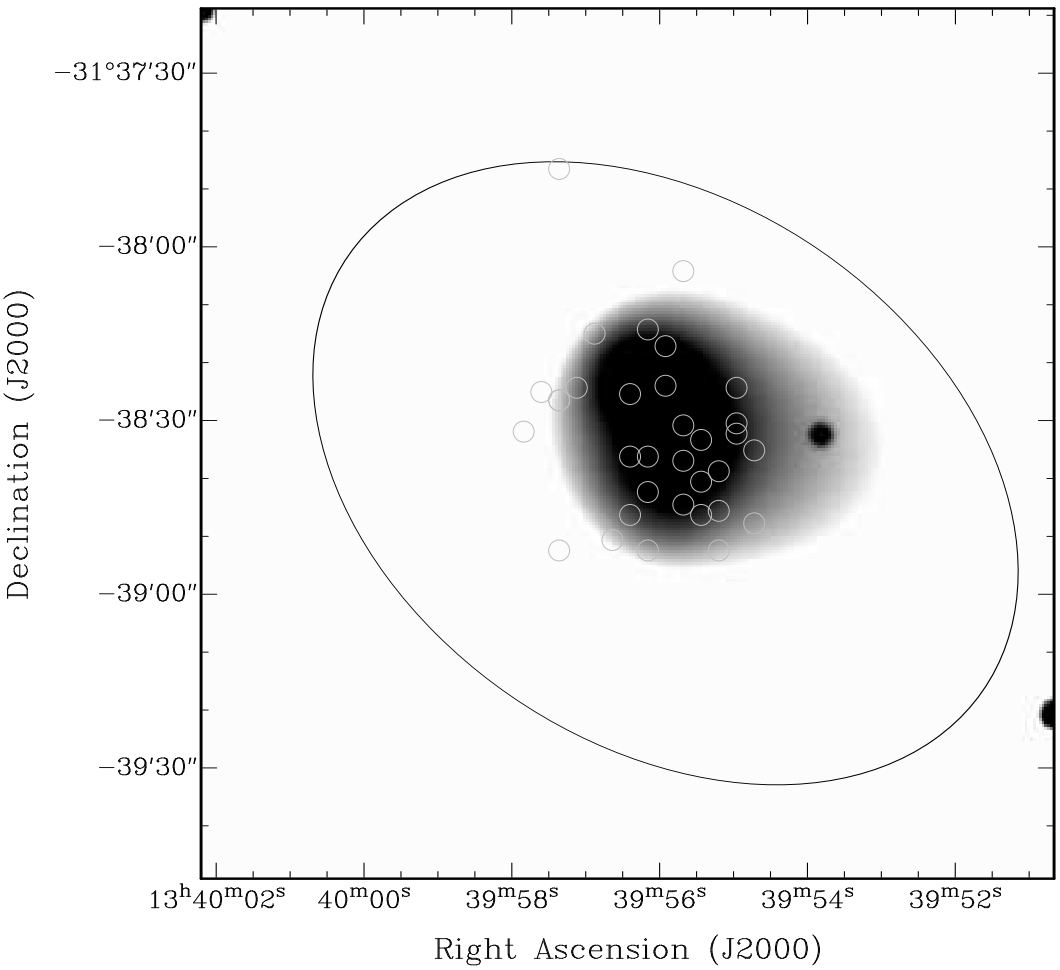

Fig. 89: *Adaptively smoothed CHANDRA image of NGC 5253 with superimposed* HI *ellipse and plasma source positions. Most of the plasma sources, derived from the HR diagram, are located within the diffuse emission component of the galaxy. Thus, the majority of the plasma sources are not supernova remnants but clumps in the diffuse emission component. The image is clipped to 4-*σ *background level.*

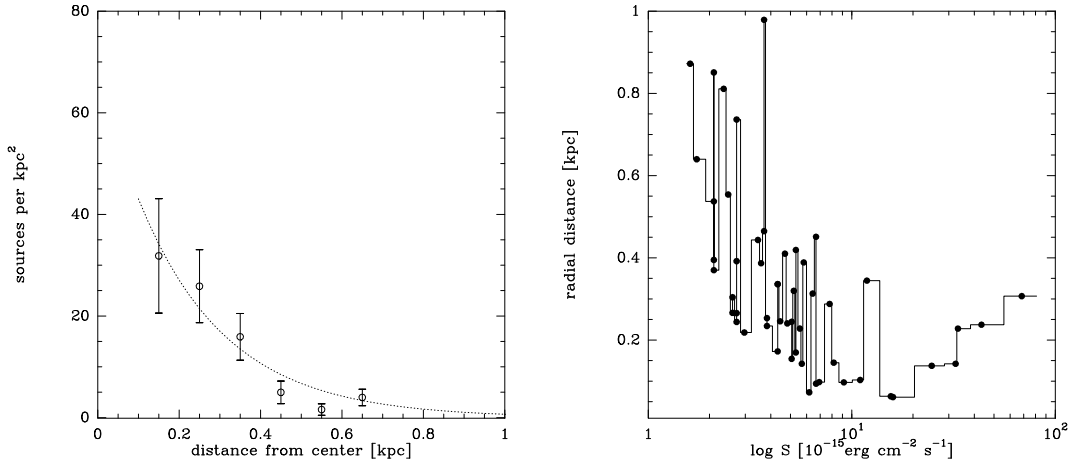

Fig. 90: **Left**: *The radial distribution of CHANDRA point sources detected in NGC 5253. The dotted line shows an exponential fit to the data.* **Right**: *Radial distances as a function of source flux.*

effect where filaments of the hot gas are seen in projection.

One of the plasma sources is outstanding: source ID 3. According to Strickland & Stevens (1999) this source is a SSC embedded in an HII region containing ≈ 1000 OB stars (Turner et al., 1998). This superbubble, as it is called by Strickland & Stevens (1999), in the young star burst region is thus responsible for the hot gas seen in the X–ray data. The luminosity of the source derived from the CHANDRA data is in agreement with the luminosity derived by Strickland & Stevens (1999) from the ROSAT data.

The diffuse hot gas of the galaxy as a whole will be investigated in the next section. Having the classification of the point sources, one now can look for the spatial arrangement of the point sources.

At first, the radial dependence of the fluxes is investigated. Note that an inclination angle of $i = 67^{\rm o}$ is assumed (Summers et al., 2004). In Fig.90(right) the dependence of the fluxes with regard to the radial distance is shown for the morphological center as the reference position. It seems as if the sources with low flux are farther away from the center than the high flux sources. This argues for the picture where the old sources (and therefore low flux) dispersed through the galaxy whereas the young (high flux) sources are still located at their "birth places" in the center, where the SSCs are situated.

The number density of the sources as a function of radius is shown in Fig.90(left). The dotted line is an exponential fit to the data, yielding a characteristic scale length of $r_{\rm o} = 0.22 \pm 0.04$ kpc. Although there is a dip between r=0.45 kpc and r=0.55 kpc the general exponential behavior is clear. This is in agreement with the exponential disk described in Sersic & Donzelli (1992)

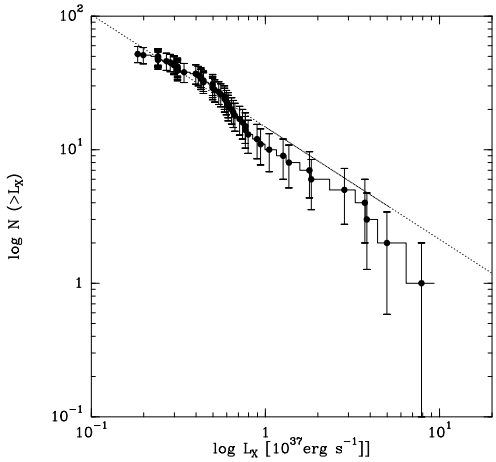

Fig. 91: *The XLF of NGC 5253 CHANDRA sources shows no breaks. The dotted line is a power–law fit with* $\beta = -0.84 \pm 0.03$. *Since the X–ray sources represent old objects (*10^7 *yr or older) these diagram shows that there was no pronounced star burst before that time. Recent star burst do contribute only slightly giving the wavy pattern.*

Having the distance of 3.1 Mpc one can calculate the luminosities from the fluxes. From these the XLF is derived and shown in Fig.91. It turns out that the XLF is unbroken within the uncertainties. As pointed out before, the star burst in NGC 5253 is very young and apparently did not enter in the XLF yet. This supports the assumption made in the case of NGC 4449. The XLF of NGC 5253 only shows a slight wavy pattern which might be a contribution of a star burst but within the uncertainties this pattern is not significant. This pattern is not seen in the work of Summers et al. (2004) since they only incorporate their 17 brightest sources in the XLF.

The slope of the XLF derived in the present work is $\beta = -0.84 \pm 0.03$. According to Summers et al. (2004) this slope is quite steep. They fitted $\beta = -0.54 \pm^{0.21}_{0.16}$ which is still steeper than the slopes for larger star burst galaxies like M 82 or the Antennae (Zezas et al., 2001). On the other hand, the slope derived in the present work is flatter than the value given by Colbert et al. (2004) which is $\beta = -0.92$. Summers et al. (2004) claim that the steeper slope of Colbert et al. (2004) stems from the different derivation of the luminosity of the sources. While Summers et al. (2004) derive the luminosity from the source spectra, Colbert et al. (2004) assume a fixed model for all sources. The latter is also carried out in this work, hence $\beta = -0.84 \pm 0.3$ is in better agreement with Colbert et al. (2004).

5.1.8.1 Diffuse emission In order to reveal the physical properties of the diffuse hot gas of NGC 5253 a spectrum is extracted from the CHANDRA event list. The point sources found are subtracted from the region of interest, encircling the emission shown in Fig.89. The background is not subtracted due to the issues of Poisson statistics.

It turns out that the ungrouped spectrum has an insufficient signal–to–noise. The data,

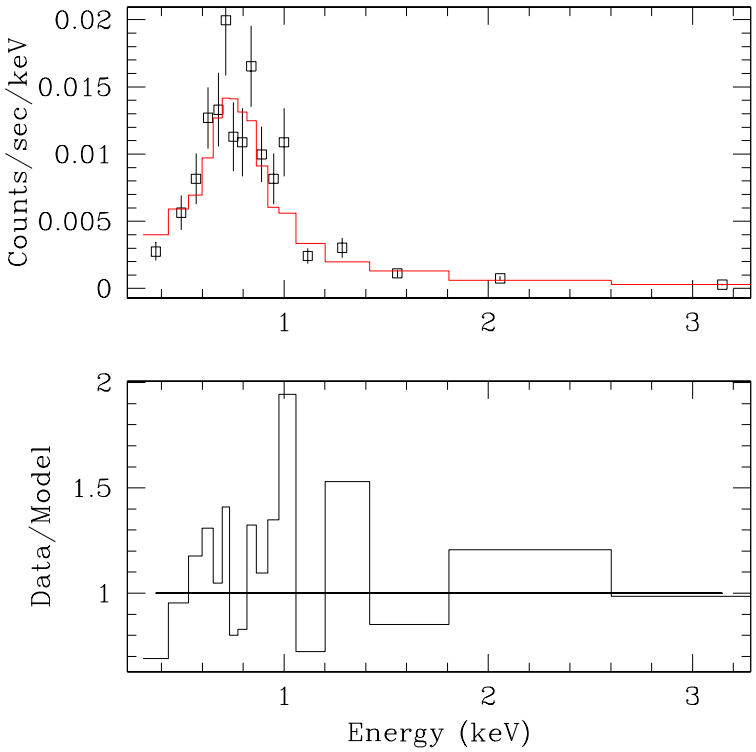

Fig. 92: *The diffuse emission CHANDRA spectrum of NGC 5253 (data points in the upper panel) together with the fitted model (solid line in the upper panel). The lower panel shows the ratio of data/model.*

thus, is grouped so that at least 25 photons per bin are reached. This spectral data is then fitted with a simple model. The model consists of one plasma component and a power–law component. The latter is intrinsically absorbed by the mean column density at the plasma position ($N_{HI} \approx 2.0 \times 10^{21}$ cm^{-2}). Both components then are absorbed by the Galactic foreground. Hence the model yields $\mathrm{abs_{gal}} \cdot (\mathrm{plasma} + (\mathrm{abs_{int}} \cdot \mathrm{powerlaw}))$. The galactic foreground column is fixed to the value given by Summers et al. (2004) of $N_{HI} = 3.87 \times 10^{20}$ cm^{-2} and the power–law index is fixed at $\Gamma = 1.5$.

The spectrum is displayed in Fig.92 together with the fitted model and the data/model ratio. The fit yields a χ^2 of 1.6 and an intrinsic column density of $N_{HI,int.} = 3.8 \times 10^{21}$ cm^{-2}. Again, more physical parameters can be derived from the fit parameters using equations 10 to 14 and assuming spherical symmetry for the emitting volume ($V = 4.1 \times 10^{64}$ cm^3):

- $T = 10^{6.6}$ K
- $n_e \cdot f^{1/2} = 1.12 \times 10^{-2}$ cm^{-3}

- $P \cdot f^{-1/2} = 1.23 \times 10^{-11}\,\mathrm{dyn\,cm^{-2}}$
- $M \cdot f^{-1/2} = 0.4 \times 10^{6} M_{\odot}$
- $E_{th} = 7.00 \times 10^{53}\,\mathrm{erg}$
- $t_{\mathrm{cool}} = 230\,\mathrm{Myr}$
- $v_{\mathrm{sound}} = 230\,\mathrm{km\,s^{-1}}$

The fitted and derived values have to be compared to the findings of Summers et al. (2004). They assume a different model which is justified by studies of the galaxies NGC 4449 (Summers et al., 2003) and NGC 1569 (Martin et al., 2002) where they claim that at least two plasma components are necessary to fit the data. Their model yields $\mathrm{abs_{gal}} \cdot ((\mathrm{abs_{int1}} \cdot \mathrm{plasma1}) + (\mathrm{abs_{int2}} \cdot \mathrm{plasma2}) + (\mathrm{abs_{int3}} \cdot \mathrm{powerlaw}))$. Their results for NGC 5253 give temperatures for the two plasma components of $T_1 = 10^{6.4}$ K and $T_2 = 10^{6.9}$ K. Their power–law index amounts to $\Gamma = 1.43$. Unfortunately they do not provide a χ^2 of their fit.

As shown in the present work the diffuse emission can be fitted with a model which has less plasma components than the model assumed by Summers et al. (2004). The single plasma component here has an HI mass of $0.4 \times 10^{6} M_{\odot}$ which is lower than the one given by Summers et al. (2004). The temperature derived from my spectral data is between the temperatures of the two plasma components given by Summers et al. (2004). The thermal energy is lower than the one derived by Summers et al. (2004) by a factor of 10. But, again, as with the mass this figure depends highly on the assumed geometry and filling factors and hence, the values are only conditionally comparable. Another reason for the different values arises from the background treatment. Summers et al. (2004) subtracted a background from the spectral data while I account for it with the power–law component. A subtraction of the background, again, is not advisable due to the Poisson statistics, as pointed out before.

However, taking the time scale of 230 Myr and sound velocity into account, the plasma can reach sufficiently large distances from the galaxy of 55 kpc (upper limit). This is in agreement with the investigation performed by Summers et al. (2004) where they also claim that the stellar ejecta can escape the gravitational well of the galaxy.

Although the XMM–Newton data is not adapted for the point sources it is used for the diffuse emission study. Summers et al. (2003) used the XMM–Newton spectral data only for a total emission spectrum and not for the diffuse emission associated with the galaxy center. Here, the XMM–Newton data is used to compare it to the CHANDRA data. Therefore, a spectrum is taken from the same region than the CHANDRA spectrum. The same model is fitted to the XMM–Newton data, not subtracting a background or point sources. The spectrum is shown in Fig.93. The fixed parameters of the CHANDRA fit are adopted, thus the fit of the XMM–Newton data yields the following plasma parameters:

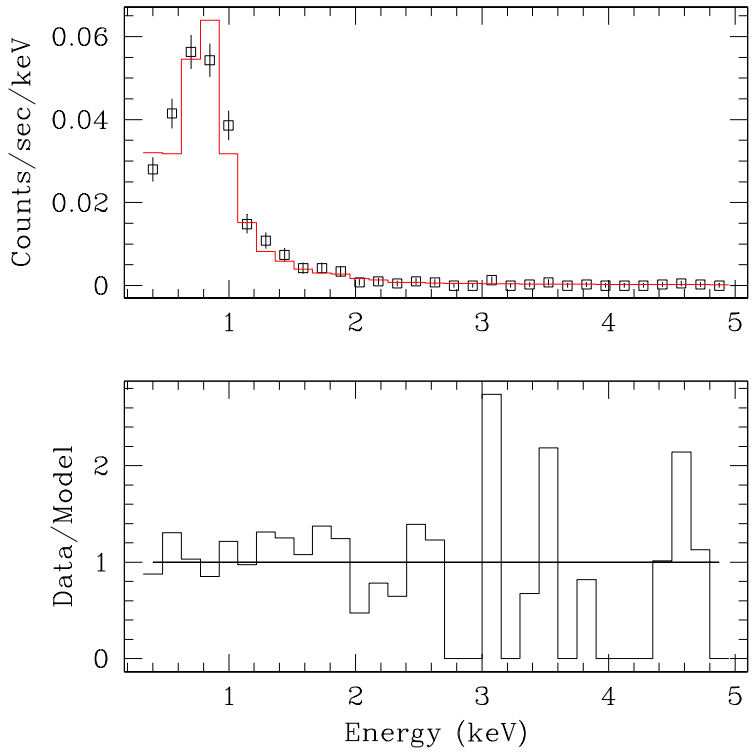

Fig. 93: *The diffuse emission XMM–Newton spectrum of NGC 5253 (data points in the upper panel) together with the fitted model (solid line in the upper panel). The lower panel shows the ratio of data/model.*

- $T = 10^{6.8}\,\mathrm{K}$
- $n_e \cdot f^{1/2} = 3.39 \times 10^{-3}\,\mathrm{cm}^{-3}$
- $P \cdot f^{-1/2} = 5.60 \times 10^{-12}\,\mathrm{dyn\,cm}^{-2}$
- $M \cdot f^{-1/2} = 0.12 \times 10^{6}\,M_{\odot}$
- $E_{th} = 3.44 \times 10^{53}\,\mathrm{erg}$
- $t_{\mathrm{cool}} = 1.1\,\mathrm{Gyr}$
- $v_{\mathrm{sound}} = 290\,\mathrm{km\,s}^{-1}$

The goodness of fit turns out to be better for the XMM–Newton data with $\chi^2 = 1.14$. However, the temperature is higher while the electron density, pressure, mass and energy is lower here. The discrepancy is attributed to the calibration uncertainties (RMF

and ARF), different spectral binning and also to the point sources which are not subtracted in contrast to the CHANDRA data. Subtracting the point sources from the XMM–Newton data leads to an insufficient signal–to–noise and hence they cannot be subtracted. Due to the different model the values also differ from the ones given by Summers et al. (2004). On the other hand, the χ^2 shows that the data can be explained by a single plasma component model, which is in qualitative agreement with the CHANDRA data presented here. Moreover, the cooling time and sound velocity derived from the XMM–Newton data support the picture of escaping gas from the galaxy. However, the discrepancies found in the two data sets show that the diffuse emission is not easy to constrain although they might be attributed to the different treatment of point sources in both data sets.

5.1.8.2 Summary Taking the XMM–Newton data from the archive only one point source is spotted in NGC 5253. The situation changes when the CHANDRA data is investigated: the smoothed M1M2 image, clipped to 4-σ above background reveals 52 point sources within the HI distribution of the galaxy. The log(N)-log(S) relation shows that the contamination by unrelated background sources is negligible.

With the help of the X–ray colors the point sources can be decomposed into plasma and power–law sources. This decomposition is more reliable than the one presented by Summers et al. (2004) because the choice of the X–ray bands here provides a clearer separation of the tow model curves. It turns out that 35 of the 52 sources are plasma sources while the remaining are power–law sources. One of the power–law sources (ID 52) is most likely a foreground star which is seen in the DSS2 red and blue data.

The large number of plasma sources might stem from a blending of hot clumps in the diffuse X–ray emission or they arise from line–of–sight effects in the diffuse gas phase. This is motivated by the patchy morphology of the emission in the center of the galaxy. Almost all of them are confined to the area where diffuse emission is found. However, one plasma source (ID 3) is located in an HI shell and is likely responsible for the formation of the shell. This is in agreement with the ROSAT studies performed by Strickland & Stevens (1999).

Two of three supernova remnants are identified with X–ray point sources. The third supernova remnant does not show up in the CHANDRA data. Here, the interpretation is that it is an old remnant which has cooled down so that it does not emit X–rays anymore.

The spatial distribution of the X–ray point sources is analyzed. The radial distance from the morphological center as a function of source flux shows a decline towards higher fluxes. This means that statistically low flux sources are distributed across a larger volume than the high flux sources. Hence, the picture of old sources (which means low flux) dissipating through the galaxy and young sources (here, high flux) confined more to the inner star burst region, is likely.

The surface density of the point sources as a function of distance to the center declines exponentially with a characteristic scale length of $r_o = 0.22 \pm 0.04$ kpc. This is in agreement with the exponential disk described in Sersic & Donzelli (1992). Converting the fluxes to luminosities the XLF is evaluated. Here, the XLF is better constrained than the one derived by Summers et al. (2004) because of the higher number of X–ray point sources. As in the case of NGC 4449 the XLF shows no breaks. The young star burst, hence, has not entered into the XLF and therefore it is almost flat besides a small undulation within the uncertainties.

The diffuse X–ray emission of NGC 5253 is seen in the adaptively smoothed image. Spectral data is extracted from the CHANDRA event list. The point sources are subtracted and then the spectrum is fitted. It turns out that the spectral significance is not high enough so that the spectrum has to be regrouped. The grouped spectrum is then fitted with an absorbed two component model, having one plasma term and one power–law term which is absorbed intrinsically by the galaxy, to account for the XRB. The plasma component (T=$10^{6.6}$ K) can escape the galaxy provided the cooling time scale and the sound velocity of that component. The mass estimate of the coronal gas is slightly lower than in the work of Summers et al. (2004). This, however, is attributed to differences in the assumed emission geometry and especially in the background treatment of the spectral data.

In addition to Summers et al. (2004) the XMM–Newton data is evaluated with respect to the spectral information. It turns out that the same model used for the CHANDRA data can be applied to the XMM–Newton data yielding a better goodness–of–fit. The parameters, however, deviate from the parameters derived from the CHANDRA data which is attributed to the different treatment of the point sources as well as to the uncertainties in the calibration and different spectral binning of both data sets. Qualitatively the XMM–Newton data is in agreement with the CHANDRA data yielding an escape of coronal gas from NGC 5253.

5.2 An important Note on the Milky Way X–ray emission

The analysis performed reveals diffuse emission of coronal gas in the dIrr galaxies, except for Sextans A and Holmberg II. The emission is attributed to the coronal gas. The underlying emission from the XRB is taken into account by introducing an absorbed power–law component. However, the observations are contaminated also by a foreground component. This component is caused by the emission of the local hot bubble (LHB) (McCammon & Sanders, 1990) and also by the X–ray halo of the Milky Way (Kerp et al., 1996; Kuntz & Snowden, 2000). This is referred to as the soft X–ray background (SXRB)

These foreground components were studied by Kappes et al. (2003); Pradas et al. (2003); Pradas (2004). The flux of the LHB and halo component in the ROSAT all–sky

survey (Snowden et al., 1995, 1997) is about 60×10^{-6} cts arcmin^{-2} s^{-1} in the ROSAT M–band(0.44-1.21 keV) (values taken from Pradas, priv. comm.). Now, one can estimate the contribution of the foreground emission of the LHB and the Galactic halo to the diffuse emission found in the dIrr galaxies.

The ROSAT flux can be converted into XMM–Newton flux using the mission calculator PIMMS[16], which is a very powerful and commonly used tool to calculate X–ray astronomy related values for a lot of different telescopes. For this aim, one has to assume a model for the foreground emission. Referring to Kappes et al. (2003); Pradas et al. (2003); Pradas (2004), the temperature is about $10^{6.2}$ K and the mean absorption column of the ISM of the Milky Way is $N_{\rm HI} \approx 1.0 \times 10^{21}$ cm^{-2}. Here, the column density of the neutral hydrogen is the tracer for the photoelectric absorption cross section of the ISM. The ROSAT M–band flux yields $1.2 \pm 0.4 \times 10^{-3}$ cts arcmin^{-2} s^{-1} in the XMM–Newton B3 band of the EPIC–*pn* camera.

This is compared to the total emission in the XMM–Newton B3 band EPIC–*pn* data of the diffuse coronal gas found in the dIrr observations. Taking Holmberg I as an example, the total XMM–Newton flux in the B3 band of the diffuse emission is $2.0 \pm 0.1 \times 10^{-3}$ cts arcmin^{-2} s^{-1}. Hence, the soft X–ray foreground originating from the LHB and Milky Way halo makes about 60 % of the total emission observed in the diffuse emission of Holmberg I. This is approved by the ratio of on–source counts to background counts in Holmberg I: The background makes about 70 % of the total emission observed on–source (i.e. on the diffuse emission). The discrepancy of 10 % arises from the circumstance that the ROSAT flux given above does not include the XRB, but only the LHB and Milky Way halo components.

An interesting question arises from the discussion of the SXRB: How is the emission measure of the spectrum, taken from the diffuse emission, affected by the SXRB? An answer is given by the following considerations.

I take a spectrum of a background region of the Holmberg I XMM–Newton observation. This background then is fitted with a model, according to Kappes et al. (2003); Pradas et al. (2003). In a more formal way, the model yields $AG \cdot (MP_1 + MP_2 + PL)$, where AG is set to $N_{\rm HI} = 2.5 \times 10^{20}$ cm^{-2}, MP_1 is set to T$= 10^{5.9}$ (LHB), MP_2 is set to T$= 10^{6.15}$ (halo) and finally PL is set to $\Gamma = 1.5$ (XRB). These values are fixed and the only free parameters are the emission measures of the plasma components and the normalization of the power–law.

The extracted spectrum together with the fitted spectrum is displayed in Fig.94. The model yields a χ^2 of 0.95 and the following emission measures: $\mathrm{EM_{LHB}} = 2.7 \times 10^{-4}$ pc cm^{-6} and $\mathrm{EM_{HALO}} = 7.2 \times 10^{-6}$ pc cm^{-6}. These are lower than the emission measure derived for the diffuse emission of Holmberg I (see Tab.8).

Since this model describes all backgrounds completely, all parameters are freezed now and the emission spectrum of the diffuse component in Holmberg I is fitted with an

[16] http://cxc.harvard.edu/toolkit/pimms.jsp

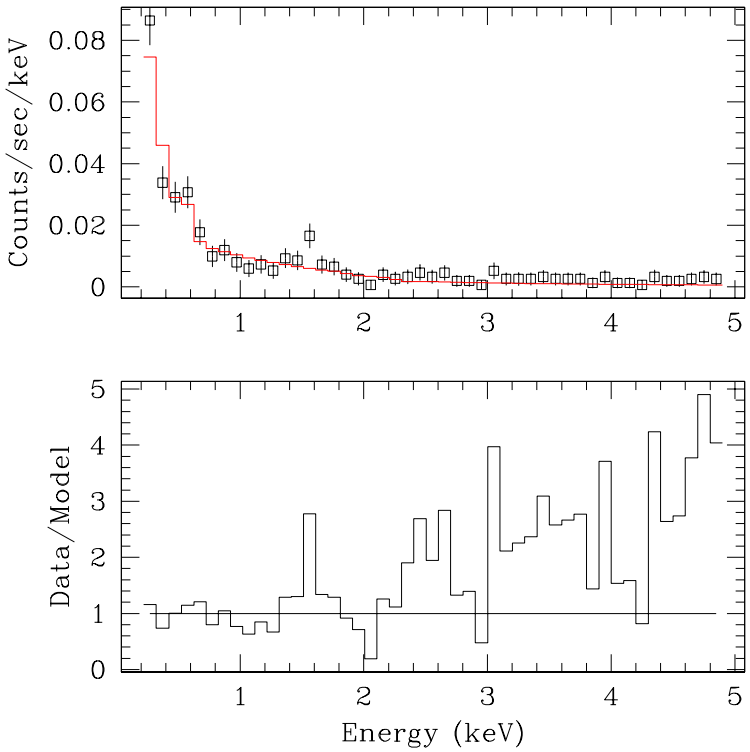

Fig. 94: *The XMM–Newton spectrum of a background field in Holmberg I is given by the data points in the upper panel. The solid line is the model for the SXRB as reported by Kappes et al. (2003); Pradas et al. (2003). The χ^2 is 0.95. The lower panel gives the ration of data/model.*

additional plasma component, accounting for the diffuse emission of Holmberg I. This is feasible, since the XRB component needs no additional absorption for the power–law component and the diffuse emission is hardly attenuated by the disk of Holmberg I. Hence the complete model yields $AG \cdot (MP_1 + MP_2 + PL + MP_{\text{Holmberg I}})$. The fit gives a temperature for the diffuse emission of T= $10^{6.3}$ K and an electron density of $n_e = 2.74 \times 10^{-3}\,\text{cm}^{-3}$.

These values are compared to the values derived from the original spectral fit of the Holmberg I data. It turns out that the new fit gives a higher temperature and a lower electron density. This is clear since the soft emission is now distributed among three plasma components. The plasma parameters from the new fit yield:

- $T = 10^{6.3}\,\text{K}$
- $n_e \cdot f^{1/2} = 2.74 \times 10^{-3}\,\text{cm}^{-3}$
- $P \cdot f^{-1/2} = 1.51 \times 10^{-12}\,\text{dyn}\,\text{cm}^{-2}$
- $M \cdot f^{-1/2} = 1.5 \times 10^{6}\,M_{\odot}$
- $E_{th} = 1.48 \times 10^{54}\,\text{erg}$
- $t_{\text{cool}} = 480\,\text{Myr}$
- $v_{\text{sound}} = 166\,\text{km}\,\text{s}^{-1}$
- $d = 80\,kpc$

According to the blow–out scenario claimed by Ott et al. (2001); Vorobyov et al. (2004) these values agree better. Based on the enhanced model, including the SXRB, the coronal gas can reach distances of up to 80 kpc above the plane of Holmberg I. However, the general conclusion remains qualitatively the same as with the simpler model.

Interestingly, most authors do not account for the SXRB at all. Some account for it by subtracting a background spectrum from the source spectrum in order to minimize the contributions of the foreground and background (i.e. SXRB and XRB). But as stated before, this subtraction is *not* feasible due to the Poisson statistic of the data. As demonstrated here for the case of Holmberg I it is a better choice to treat the background independently from the source emission. This can be improved by using the exact SXRB parameters derived by Pradas (2004), in contrast to the mean values used here.

Tab. 39: *Intermediate results from the galaxy sample. The abbreviations are 'SB" for star burst galaxies, 'D' is the distance, 'r' is the radius in terms of the outermost X–ray point source, 'N_{tot}', 'N_{pl}', N_{HMXB} and '$N_{plas.}$' are the total number of X–ray point sources, number of power–law sources, number of HMXB and number of plasma sources, respectively. The letters 'E' and 'P' in the profile shape column denote an exponential law or peculiar behavior of the area density profile, whereas the letters 'F' and 'B' denote a flat or a broken shape of the XLF. The figures for the SFR are explained in the text.*

ID	Object name	SB	HI mass 10^6 $M_\odot$	D Mpc	r kpc	N_{tot}	N_{pl}	N_{HMXB}	$N_{plas.}$ emission	diffuse shape	profile shape	XLF $M_\odot$ yr^{-1}	SFR
1	Holmberg I	—	110	3.8	2.8	14	13	2	1	√	E	F	0.7
2	IC 2574	—	600	4.0	9.5	36	33	7	1	√	P	B	5.2
3	Sextans A	—	58	1.4	1.4	9	7	0	1	—	P	F	5.1
4	Holmberg II	—	640	3.1	6.7	62	45	6	10	—	E	B	2.8
5	NGC 1569	√	130	2.2	1.4	62	45	4	1	√	E	F	8.4
6	NGC 4214	√	550	2.7	5.0	71	27	5	7	√	E	B	57
7	NGC 4449	√	300	4.2	5.6	20	17	7	2	√	E	F	72
8	NGC 5253	√	140	3.1	1.0	52	17	1	2	√	E	F	38

5.3 X–ray Point Source Content of the whole Sample

The investigation performed reveals a number of X–ray properties of irregular dwarf galaxies. At this point I like to compile shortly some figures derived above. These parameters are given in Tab.39 together with other parameters taken from the literature.

The type of galaxy (star burst or not) is taken from the literature as well as the HI mass of the galaxy. In the case of NGC 4449, which has a very disturbed HI distribution, only the inner disk–like part is assumed for the HI mass. In the other cases, the HI mass is the one found in the related papers as given in the overview of this chapter.

The distances given are the ones quoted in the overview of this chapter, too. The radius of the galaxy is given by the (deprojected) distance of the outermost X–ray point source found with respect to the morphological center. Since in every case there is at least one X–ray source at the very edge of a galaxy this radius assumption is good, although the HI radius depends on how deep the radio observation is.

The "profile shape" column denotes whether the radial dependency of the X–ray source area density follows an exponential or not, in which case it is denoted "peculiar". Similar, the XLF is "flat" in the case where it is fitted by one power–law function whereas it is "broken" in the case where a broken power–law function has to be assumed.

A new parameter introduced here is the star formation rate (SFR) of the galaxy in question. This issue is not unambiguous. Different ways can be followed to derive the SFR of a galaxy. Conventional indicators need some assumptions like the dust content, initial mass function, etc.

Moreover there are SFR estimates based on empiric equations. Having the flux of a galaxy in a certain band of the EM spectrum one can calculate the SFR (Rosa-González

et al., 2002). With canonical formulae by Kennicutt (1998) one obtains the following relations:

$$\mathrm{SFR_{H\alpha}} = 1.1 \times 10^{-41} \mathrm{L_{H\alpha}(erg\,s^{-1})} \quad (25)$$

$$\mathrm{SFR_{UV}} = 6.4 \times 10^{-28} \mathrm{L_{UV,\nu}(erg\,s^{-1}Hz^{-1})} \quad (26)$$

$$\mathrm{SFR_{FIR}} = 4.5 \times 10^{-44} \mathrm{L_{FIR}(erg\,s^{-1})} \quad (27)$$

Here, the last relation only applies for infrared selected starburst galaxies. There is also a relation between the radio emission and the SFR given by Condon (1992) which reads:

$$\mathrm{SFR_{radio}} = 1.82 \times 10^{-28} \nu_{\mathrm{GHz}}^{0.1} \mathrm{L_\nu(erg\,s^{-1}Hz^{-1})} \quad (28)$$

which only applies for thermal emission, e.g. in HII regions. However, the luminosities are not found in the literature for all the galaxies. Moreover, the SFRs calculated from the different luminosities vary substantially which makes a comparison very uncertain. Hence, it is a better choice to calculate SFR for each galaxy in the sample from a luminosity which is available for all the galaxies even when this SFR is not the best value. At least this value provides an identical basis for the SFR value.

Fortunately, there is such a relation between SFR and the B–band luminosity L_B derived by Thronson et al. (1987) yielding:

$$\mathrm{SFR_B} = 6.5 \times 10^{-9} \mathrm{L_B[L_\odot]} \quad (29)$$

This, however, assumes a constant SFR over a timescale of 10^9 yr, a Salpeter–IMF and a mass range of formed stars from 0.1 to $100\,\mathrm{M_\odot}$. With this and the B–band luminosities the SFR can be calculated for each galaxy. The figures are in units of solar masses per year and appear very high, at least in some cases. This shows, on the one hand, that the SFR derived is a *mean* rate over the last 10 billion years and on the other hand this enables one to have SFR for each galaxy which are comparable.

Thus, in the next chapter I will analyze different correlations of the parameters derived.

6 Point Source Correlations and the Standard Model

With the data derived in the previous chapter, one can study correlations between the different quantities. Grimm et al. (2003) suggested a correlation between the number of HMXB and the SFR of a galaxy. They carried out this correlation on a sample of starburst galaxies (up to z≈1.2). Here, they used the SFR based on the FIR flux. Hence, it is expected to find a deviation from the results of Grimm et al. (2003) because in the present work the SFR values are based on the B–band luminosities. Although the SFR based on the FIR luminosity of a galaxy might be the better choice (think of extinction etc.) I used the SFR based on B–band luminosities because FIR data is not available for all the galaxies in the sample. Thus, the data is consistent using B–band luminosities.

Furthermore Grimm et al. (2003) limited their sample to galaxies which are known to have a high SFR, which is not the case for the dIrr sample presented here. Also their sample consists of late–type galaxies (Hubble–type Sa, Sb or Sc), which are not comparable with the sample at hand. However, the correlation for the dIrr sample might give insight into the relation between X–ray point sources and the SFR of dIrrs.

6.1 Point Source Correlations

Before the correlation suggested by Grimm et al. (2003) is discussed, I will show other correlations concerning the HMXB in the galaxy sample. Following Grimm et al. (2003) the HMXB are the type of X–ray point sources which seem to be correlated to other measurable quantities.

First, the number of HMXB is correlated with the galactocentric distance of the outermost X–ray point source found in the HI distribution. This correlation is show in Fig.95.

The lines are regression lines representing the correlation degree which turns out to be 85%. The uncertainty for the number of HMXB is assumed to be Poissonian, thus the square root of the number value. Taking other X–ray point sources than only the HMXB, the correlation breaks down. This suggests that the number of HMXB is a characteristic quantity for the distribution of X–ray point sources.

Since the outermost sources have a galactocentric distance which is comparable to the HI extend of their host galaxy, it is suggested that the number of HMXB increases with the size of the galaxy. However, the size of a galaxy observed in HI emission is not a good measure for the size of the galaxy. Interestingly the sample shows the following correlation (see Fig.96). It is suggested that the number of HMXB depends on the amount of (neutral) gas in a galaxy.

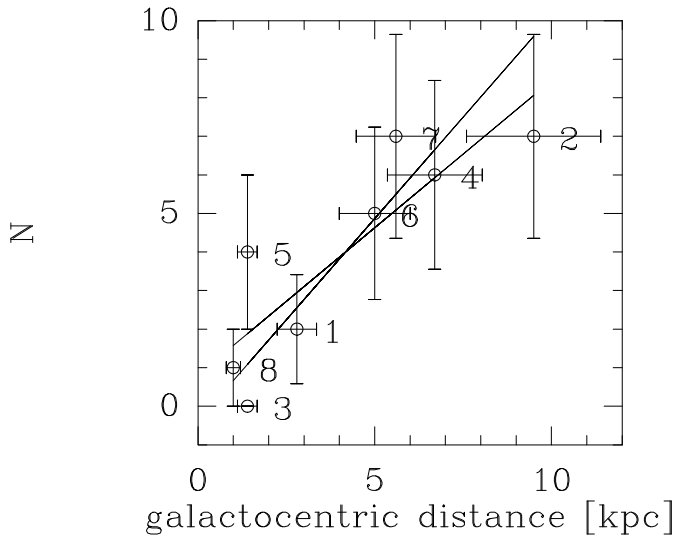

Fig. 95: *Linear correlation between the number of HMXB and the galactocentric distance of the outermost X–ray point source. The solid lines are linear regressions to the data which show the correlation degree of 70%. Numbers correspond to the IDs given in Tab.39.*

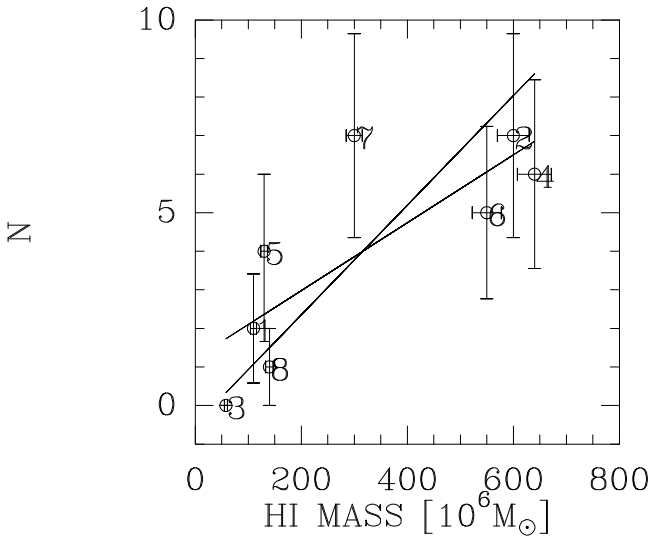

Fig. 96: *Linear correlation between the number of HMXB and the* HI *mass of the host galaxy. Numbers correspond to the IDs given in Tab.39. The lines represent the correlation degree of 78%.*

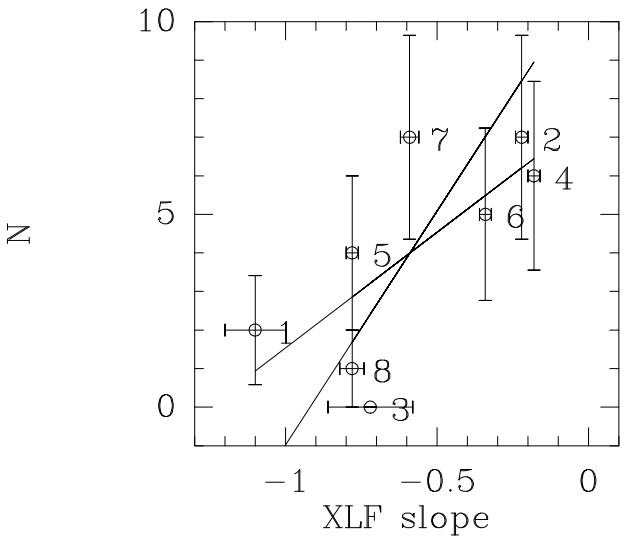

Fig. 97: *Linear correlation between the number of HMXB and the XLF slope of the host galaxy. The three galaxies having broken power–law XLFs are evaluated by taking only the slope below the break luminosity. Numbers correspond to the IDs given in Tab.39. The lines represent the correlation degree of 70%.*

Also the HI mass of a galaxy from the sample is correlated with the number of HMXB. Of course, the HI mass is not easy to determine especially for galaxies like NGC 4449, which show a complex morphology of the neutral gas distribution. However, the HI mass is only taken from that part of the galaxy where the X–ray point sources are detected. Again, the number of HMXB appears as a characteristic quantity for the HI mass. The uncertainties here are of course dependent on the mass estimation. If all other X–ray point sources are included the correlation breaks down.

Furthermore, the XLFs were calculated from the X–ray point sources detected in all eight galaxies. It turned out that three galaxies have a broken XLF which means that they can not be fitted with a single power–law function. For these galaxies only the slopes below the break are regarded together with the slopes of the other galaxy XLFs.

Plotting the number of HMXB versus the XLF slopes another correlation is seen. In Fig.97 this 70% correlation is displayed. Taking the slopes above the break luminosities gives no correlation as well as taking other X–ray point sources than HMXB. Taking only the three galaxies with the broken XLF and here the slope above the break luminosity, the correlation is still there. However, three data points are not yielding a trustworthy correlation.

In the context of broken XLFs another correlation turns out to be interesting, that is the connection between SFR and HI mass. Figure 98 shows that the SFR increases with increasing HI mass. Here, only the galaxies without a broken XLF are displayed in Fig.98. With these five galaxies the correlation degree is 92%. Including the broken XLF galaxies yields a correlation degree of 10% which is virtually no correlation.

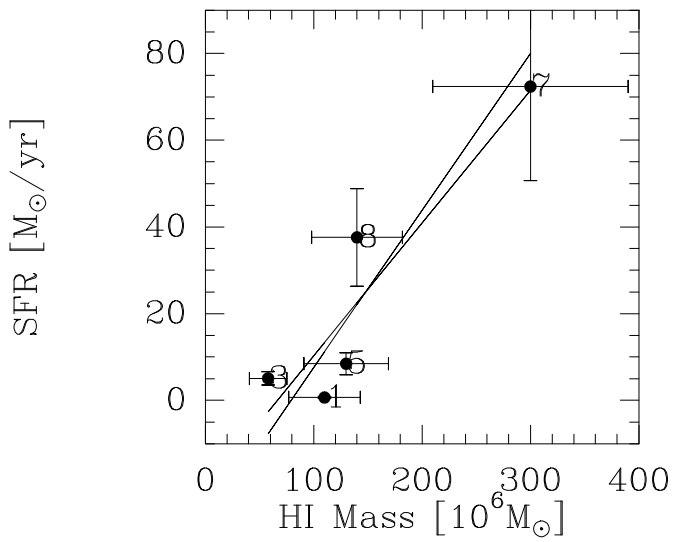

Fig. 98: *Galaxies with ID 2, 4 and 6 (the galaxies with broken XLFs) are skipped which leads to a correlation degree of 92 %. Numbers correspond to the IDs given in Tab.39.*

The aforementioned correlations suggest two different results. First, the number of HMXB correlates with the X–ray binary spacial distribution and with the HI mass associated with the extend defined by the outermost X–ray source. The number of HMXB correlates also with the XLF slopes when the slope below the break luminosity is taken into account for galaxies with broken XLFs.

This first result suggests that the HMXB are candidate X–ray point sources which can be used as an indicator for properties of dIrrs rather than all the different types of X–ray sources found in these galaxies. Finding the HMXB as "indicator sources" is in agreement with the findings of Grimm et al. (2003) although they restrict the "indicator sources" even more by a luminosity limit of $2.0\times10^{38}\,\mathrm{erg\,s^{-1}}$. This luminosity limit will be discussed further below.

The second result is the correlation of the SFR rate (derived from the B–band luminosity) with the HI mass (derived from the extend defined by the outermost X–ray point source). This suggests a dependence of the SFR on the HI mass. The idea here is, that a larger gas supply can produce a larger number of stars and hence a higher SFR. This dependence is there although the estimates of the SFR based on the B–band luminosity as well as the HI mass are not the best quantities one can think of to characterize these dIrrs. More precise, the SFR in general depend more likely on the surface mass density of the *molecular* hydrogen (H_2). Also the SFR is assumed to be constant over the last 10^9 yr which might give deviations of the correlation found.

However, the SFR rate presented here is proportional to L_B and thus one can regard the SFR-HI correlation as a correlation of HI mass and L_B.

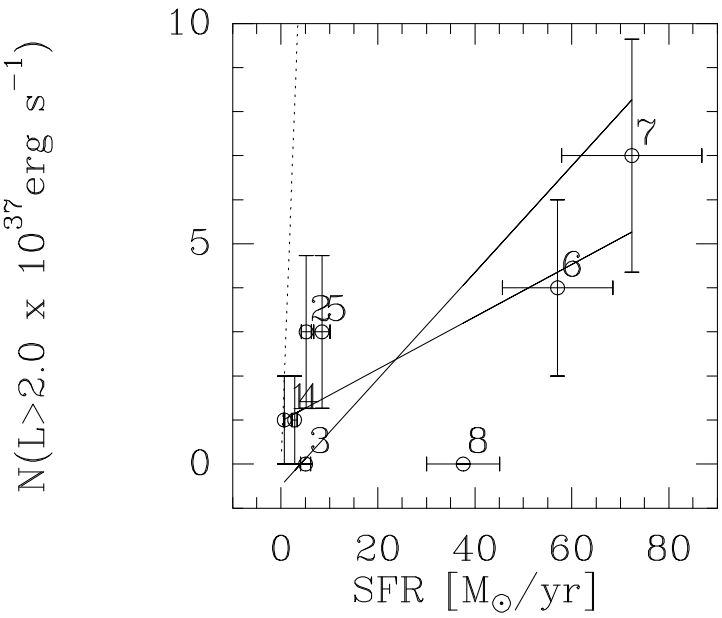

Fig. 99: *Linear correlation between SFR and the luminosity limited number of HMXB of the dIrr sample. The lower luminosity limit for HMXB is 2.0×10^{37} erg s^{-1}. For comparison the dotted line refers to the correlation found by Grimm et al. (2003). The solid lines are linear regressions to the data, yielding a correlation degree of 70 %. Numbers correspond to the IDs given in Tab.39.*

6.1.1 Star Formation Rate

With the number of HMXB and the SFR the results obtained by Grimm et al. (2003) can now be discussed. They claim a correlation of the number of HMXB exceeding a luminosity of 2.0×10^{38} erg s^{-1} with the SFR derived from UV, Hα and FIR luminosities.

The question here is whether or not the HMXB–SFR correlation of Grimm et al. (2003) still holds for the present sample with a different derivation of SFRs and another luminosity limit. This question is not answered in the literature up to now.

It turns out that a luminosity limit of 2.0×10^{37} erg s^{-1} helps to minimize residual contributions of bright LMXB and still it gives at least one HMXB per galaxy so that more data points are available. For this limit the SFR based on L_B shows a correlation with the number of HMXB . The correlation degree is here 70% (see Fig.99).

The slope of the correlation given by Grimm et al. (2003) is shown as a dotted line in Fig.99 which is much steeper than the slope of the present sample.Since the SFR yield higher values when derived from the B–band luminosity, it is clear that the slope is flatter in this case. The difference in the values for SFR occurs because the B–band and FIR band trace different stellar components, i.e. L_B traces primarily the past star formation rate of high mass stars younger than 10^9 yr on the main sequence.

On the other hand the FIR traces the "recent" star formation over the last 10^6 yr. Referring to Kohle (1999) the different luminosities yield different SFR, as already said. For example, for NGC 4449 he derives $\mathrm{SFR}_{\mathrm{L_B}} = 2\,\mathrm{M}_\odot\,\mathrm{yr}^{-1}$ and $\mathrm{SFR}_{\mathrm{L_{FIR}}} = 0.9\,\mathrm{M}_\odot\,\mathrm{yr}^{-1}$ which is more than a factor of two off. Hence the expected deviation between this investigation here and the results of Grimm et al. (2003) can be attributed to the different derivations of the recent and past SFR.

The general trend that higher star formation yields higher number of HMXB is still present. But to claim that this is an independent indicator for the SFR of a galaxy in general is questionable. However, one can test this by fitting the slope in the form $\mathrm{N} = \alpha \cdot SFR + \beta$. This gives a slope of $\alpha = 0.06 \pm 0.02$ and a linear off–set of $\beta = 0.97 \pm 0.87$. Inserting the SFR of the Milky Way of $0.25\,\mathrm{M}_\odot\,\mathrm{yr}^{-1}$ yields ≈ 1 HMXB which is in agreement with the findings of Grimm et al. (2002) within the uncertainties who also perform this test.

The correlation also depends on the limiting luminosity. Taking a lower luminosity threshold of $1.0 \times 10^{37}\,\mathrm{erg\,s}^{-1}$ yields a different correlation of only 59 %. This is the limit where the correlation breaks down. This also shows that the luminous HMXBs are dominating the dIrr galaxies. This was also pointed out by Colbert et al. (2004) who investigated a much larger sample of spiral and elliptical galaxies, which also includes some dIrr galaxies, namely NGC 1569, NGC 4449 and NGC 5253. Moreover, they claim that there might be different star formation modes for different galaxy morphologies, which also corroborates the results found in the present work.

6.1.2 X–ray Luminosity Function

The XLFs for all galaxies derived in the last chapter are examined now. Since the XLF of each galaxy in the sample is at hand, one can study the connection between XLF and SFR. The XLFs as derived in chapter 5 are different for each galaxy. However, now at this point there is evidence that the number of X–ray point sources respectively the number of HMXB is proportional to the SFR of a galaxy.

Following Grimm et al. (2003) the XLFs can be scaled with the SFR so that they are equal within a certain range. The goal here is to find out whether or not there exists a universal XLF (which implies a universal initial mass function). The individual XLFs are consistent in the sense that all the luminosities are derived in the same energy band. However, there might be a spread in luminosities due to the two different instruments used but as pointed out by Grimm et al. (2003) these uncertainties are negligible.

The XLFs of all eight dIrrs are given in Fig.100 (left). Following Grimm et al. (2003) the XLFs can be scaled in N by the ratio of their individual SFR to the SFR of Holmberg II. This ratio is the scaling factor. Why Holmberg II is chosen as the reference galaxy will be clear later. This scaling of the XLFs leads to a narrower distribution of the XLFs in the log(N)-log(L) plane as one can see in Fig.100 (right).

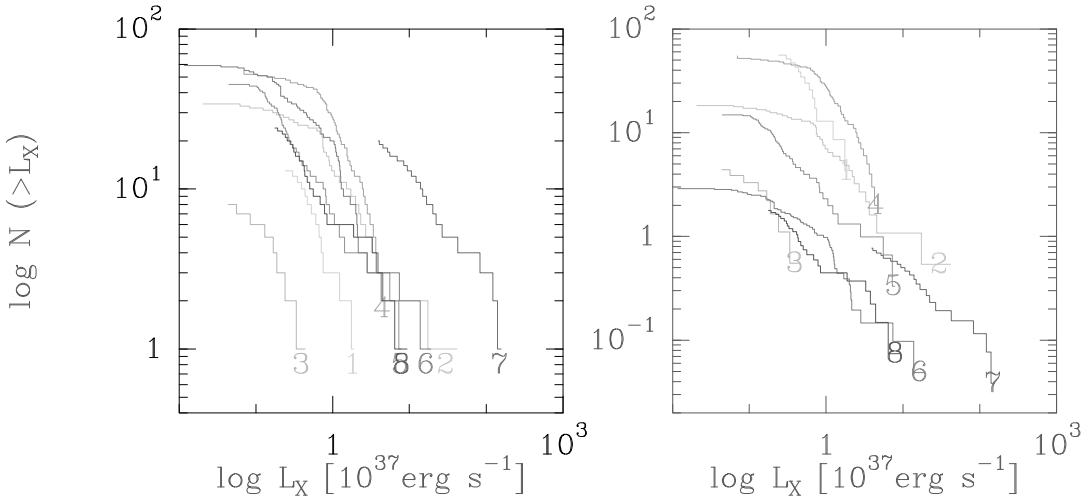

Fig. 100: *The XLFs of the dIrr sample.* **left***: XLFs for the eight galaxies of the dIrr sample as derived in the last chapter.* **right***: XLFs of the same galaxies scaled in N by the ratio of their SFR to the SFR of Holmberg II (ID 4). The distribution is narrower compared to a). Numbers correspond to the IDs given in Tab.39.*

After rescaling the XLFs, they seem to be consistent within a factor of ≈ 15 in the log(N)-log(L) plane. In first place this is not very satisfying but in relation to the spread in SFR (a factor of ≈ 110) the spread in the log(N)-log(L) plane is small. This would imply a universal XLF if the spread was zero within the uncertainties.

One can put this now the other way around in the following way. For each XLF the normalization factor (i.e. the scaling factor) is calculated with respect to the XLF of Holmberg II. For this aim, the XLF is shifted by a scaling factor which leads to an agreement of the XLF to the one of Holmberg II within the uncertainties. These scaling factors can be different from the ones derived from the ratios of corresponding SFRs.

The new scaled XLFs are displayed in Fig.101. It shows that the *shapes* of the XLFs are very similar within a narrow band and the scatter is considerably smaller than for the case where the normalization is computed from the SFR. The interesting question now is: What is the difference between the scaling factors derived from the SFR ratios on the one hand, and the scaling factors derived from the shifted XLFs on the other hand?

The answer to this question is given in Fig.102. Both normalizations differ significantly by two orders of magnitude. Figure 102 now gives the justification for choosing Holmberg II as the reference for the normalization: It simply provides the minimal difference between both normalizations. However, the differences are still crucial and give raise for the conclusion that a universal XLF is unlikely at least for the dIrr sample presented here. Owing to the number of uncertainties in the XLF investigation (especially the SFR issues), the accuracy is difficult to judge. However, even if there is

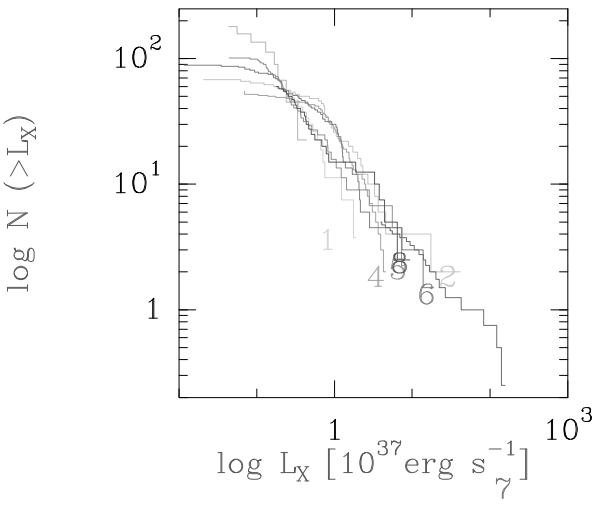

Fig. 101: *The XLFs scaled by shifting all XLFs to the XLF of Holmberg II. Basically this is the same as in Fig.100 (right) but the normalization is somewhat arbitrary since it is not based on the SFR but on a shift in N. Even so, it shows that the shapes of the XLFs are very similar within a narrow band and the scatter is considerably smaller than in Fig.100 (right). Numbers correspond to the IDs given in Tab.39.*

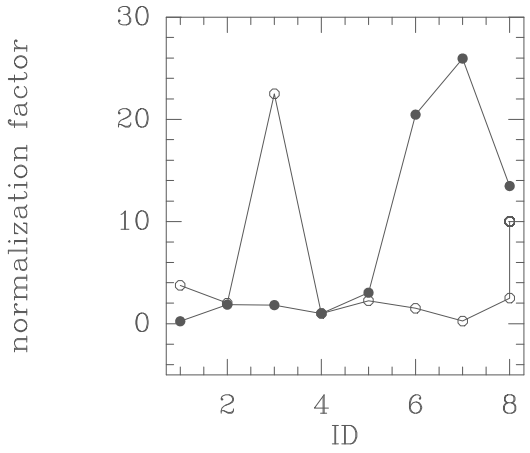

Fig. 102: *Comparison of the normalizations given by the SFR (filled circles) and the one derived by shifting the XLFs (open circles). Apart from the reference galaxy (ID 4) and ID 2 and 5, the normalizations are different. IDs are given in Tab.39.*

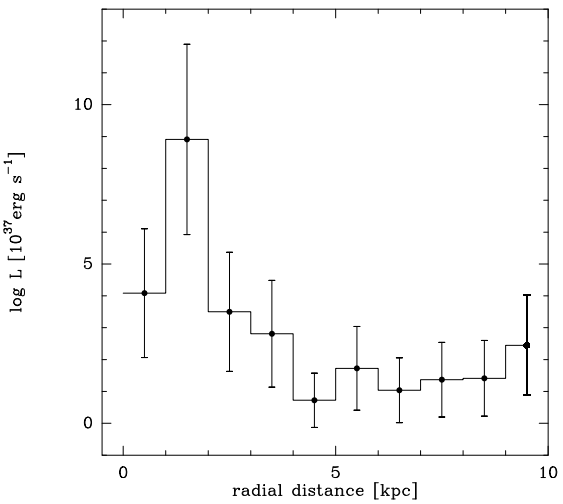

Fig. 103: *The combined luminosity/galactocentric distance data of all dIrr galaxies in the sample. High–luminosity sources are concentrated at a galactocentric distance of 1.5 kpc. The center is populated with intermediate luminous sources. Outside a galactocentric distance of 1.5 kpc this drops and remains constant outside 5 kpc.*

no universal XLF for dIrr galaxies, which is implied here, the results of Grimm et al. (2003) might still be valid for spiral galaxies.

6.1.3 Spatial Distribution of X–ray Point Sources

In chapter 5 I derived the radial distribution of X–ray point sources in an individual galaxy as a function of source flux. Since the fluxes depend on the distance, they are converted into luminosities taking the distances quoted in chapter 5. This data can now be regarded for all galaxies together. Since the number of point sources per galaxy provides no good significance for an individual galaxy, now the significance can be gained by putting all point sources together.

The data is binned into galactocentric distance bins of 1 kpc width and for each bin the luminosities are averaged. It is to note, that the most luminous source in the sample (source ID 4 of Holmberg II) is skipped since it outshines all other sources by two orders of magnitude and thus it dominates the complete sample. The skipped source is in the 2.5 kpc bin. The luminosity versus galactocentric distance of the sources is show in Fig.103.

The mean galactocentric distance of all outermost point sources is 4.2 kpc, with four galaxies bigger than the mean and four smaller than the mean. With respect to this mean galactocentric distance, the sample is split into a “small” (i.e. small extent) and a “large” (i.e. large extent) part. Moreover, the bin size for the small sample is decreased (0.3 kpc) and the result is displayed in Fig.104.

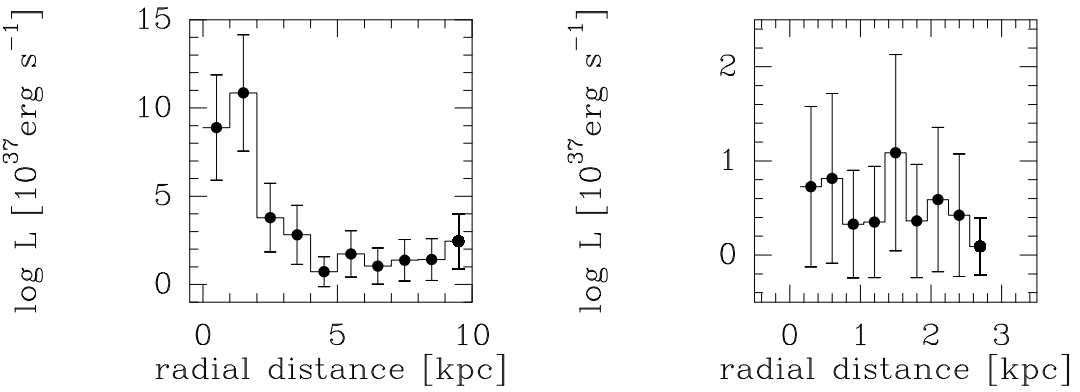

Fig. 104: *The same as in Fig.103 except that the sample is now split into a "large" (left) and a "small" (right) subsample. The small sample has galactocentric distances below the mean radius of 4.2 kpc and vice versa. In contrast to the luminosity peak for the large sample, the small sample shows constant luminosity within the uncertainties.*

It turns out that the small sample has a constant luminosity within the uncertainties. In contrast, the large sample still shows the luminosity peak at the same radius (1.5 kpc) as in the full sample of Fig.103. The difference is that due to the missing low luminosities of the small sample, the mean luminosities in the large sample is higher for the inner part. Since there are 318 X–ray point sources in total in the sample and 137 point sources (43%) in the small subsample this finding is significant. This, again, suggests a different star formation process for the small and large dIrrs.

6.2 The Standard Model

Extended diffuse soft X–ray emission is detected in the galaxies Holmberg I, IC 2574, NGC 1569, NGC 4449 and NGC 5253. Sextans A does not show any extended diffuse emission. For Holmberg II and NGC 4214 some X–ray point sources are associated with soft X–ray emission which is also extended but in contrast to the first mentioned five galaxies the extend is much less.

In this chapter I like to discuss whether or not the extended diffuse emission is related to other parameters of the host galaxy. A characteristic parameter for the diffuse emission is the temperature of the coronal gas.

It turns out that the temperature correlates with the total number of X–ray point sources when, for coronal gas with two plasma components, only the cooler component is regarded. This correlation is given in Fig.105. The correlation degree is 96%. If the hotter component for two component plasma phases is regarded, the correlation degree drops to 73% which still is a good correlation. The correlation breaks down when only the HMXB or only the plasma sources are regarded. Hence, a higher number of X–ray point sources provides a higher energetic input to the ISM in general.

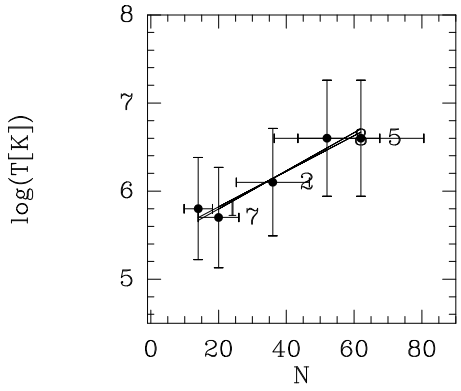

Fig. 105: *Correlation of total number of X–ray point sources with the temperature of the diffuse emission. For coronal gas with two plasma components only the cooler component is regarded. The lines are linear regression lines which represent a correlation degree of 96%. Numbers correspond to the IDs given in Tab.39.*

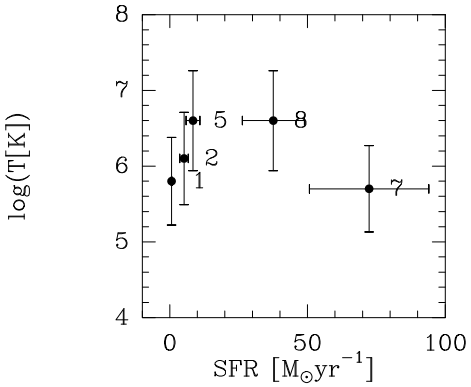

Fig. 106: *Correlation of SFR with the temperature of the diffuse emission. For coronal gas with two plasma components only the cooler component is regarded. Numbers correspond to the IDs given in Tab.39.*

According to the SFRs of the galaxies, one might expect also a correlation of the extended diffuse gas and the SFR. For the five galaxies with coronal gas in the disk/halo interface this correlation, however, is simply not there as one can see in Fig.106. This shows that the existence of extended coronal gas is not dependant on the average (or past) SFR over the 10^9 yr. It is more likely that it depends on the existence of high energetic stellar events in the host galaxy which might not contribute significantly to the past SFR.

This argues for the standard model in general. However, the extended diffuse coronal gas cannot be attributed to specific shells found in the HI distribution. This is, because the gas is expelled out of a shell and then it is delocalized due to its movement away from the disk. This is supported by the fact that the diffuse gas detected in the dIrrs most likely escapes from the disk, as pointed out in chapter 5.

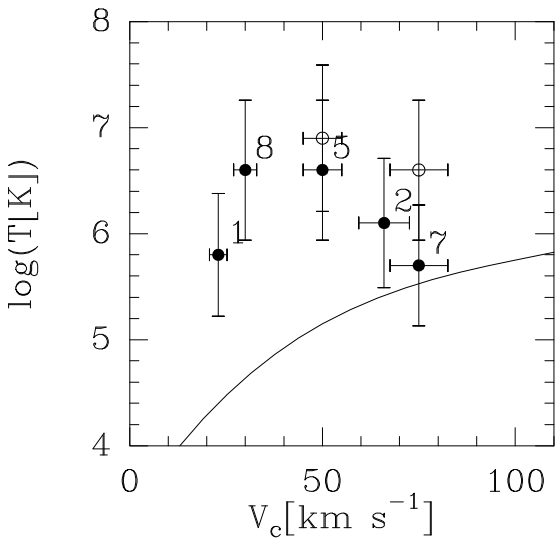

Fig. 107: *Temperature of extended thermal X–ray emission vs. maximum* HI *rotation velocity. The curve for* $v_{\rm esc} = 1.414 V_c$ *is taken from Martin (1999). The numbers correspond to the IDs of Tab.39. For galaxies with two plasma components the higher temperature is represented by the open circle. Uncertainties are assumed to be 10%.*

Of course, in the cases where two plasma components are needed to fit the spectral data at least one component can escape the galaxy. However, the escape scenario is based only on the time scales and velocity scales given by the cooling time and the sound speed of the plasma. In order to decide whether a blow–out or a blow–away is observed in a galaxy, the escape velocity has to be compared to the sound speed in the coronal gas.

The issues of blow–out and blow–away scenarios from a theoretical viewpoint are discussed in Mac Low & Ferrara (1998, 1999); Strickland & Stevens (2000). However, the escape velocity is proportional to the total mass of the galaxy which is very uncertain and in most cases it is unknown. Moreover, the escape velocity is inverse proportional to the radius at which the gas starts to escape from the galaxy. This is in general also unknown.

Fortunately there is another way to derive whether or not the gas is only blown–out or blown–away from the galaxy. As pointed out by Martin (1999) the gas can escape the galaxy if its temperature is above a certain escape temperature $T_{\rm esc}$ which is proportional to the escape velocity $v_{\rm esc}$. For a measured rotation speed V_c of the HI disk the escape velocity at $R(\max V_c)$ is at least $1.414 V_c$. Hence, if the temperature of the X–ray emitting gas is above $T_{\rm esc} = 1.5 \times 10^5 (v_{\rm esc}/100\,{\rm km\,s^{-1}})^2$ the gas can escape the gravitational potential of the host galaxy. This is displayed in Fig.107 where the curve for $v_{\rm esc} = 1.414 V_c$ is taken from Martin (1999). The data points correspond to the lowest temperatures provided by the spectral fit of the XMM–Newton and CHANDRA data.

Every data point which is above the solid line in Fig.107 corresponds to gas which

can escape the galaxy. The maximum rotation velocities for the galaxies are adopted from Ott et al. (Holmberg I 2001), Martimbeau et al. (IC 2574 1994), Stil & Israel (NGC 1569 2002), Hunter et al. (NGC 4449 1998), Kobulnicky & Skillman (NHG 5253 1995).

In addition to what was found in chapter 5 the diffuse coronal gas phases can escape the host galaxy, except for the cold component detected in NGC 4449. This is in agreement with the findings based on the cooling time and sound speed estimation. In this sense the standard model fits nicely into what is observed. Hot coronal gas probably originates from high energetic stellar events and is vented into the halo of the host galaxy. However, the origin of the coronal gas is uncertain because the extended emission is hardly identified with single shells in the HI distribution. IC 2574 is a good example for coronal gas in the halo of the galaxy which cannot be attributed precisely to a shell but as pointed out in chapter 5 the gas probably stems from the Walter & Brinks (1999) shells number 22 and/or 26.

Having now the estimation for the extended diffuse emission one can evaluate the standard model on smaller scales. This means that there might be soft X–ray emission associated with individual shells in the HI distribution of a galaxy. In the following I give an overview about the X–ray sources probably associated with shells.

For Holmberg I one source is in agreement with a shell and it also shows some Hα emission. However, the luminosity is very low and the interpretation of the source being a supernova remnant is uncertain. In IC 2574 there are 14 X–ray point sources associated with HI shells where 4 of them are in the very centers of the shells. Only one of the four sources, namely the brightest source ID 9, is very likely a supernova remnant (Brinks et al., 2003).

Sextans A only shows a low number of X–ray sources and none of them is associated with any shell. This is in agreement with the fact that no diffuse soft X–ray emission is found down to the detection limit. Hence, the standard model is likely not applicable here. This is also supported by the shallow star formation of the galaxy in the past.

Also Holmberg II shows some evidence for the standard model. Here, ID 56 is likely related to hot gas filling an HI cavity and on the rim of the cavity new stars show up in an HII region, where also the DSS2 maps show their peak intensity. However, according to Bureau & Carignan (2002) most of the shells observed in Holmberg II especially in the outer parts of the HI distribution are probably produced by ram–pressure effects.

NGC 1569 exhibits one plasma source associated with a shell structure in the neutral ISM (Mühle et al., 2005). This source (ID 53) may be hot gas filling this cavity but on the other hand the DSS2 images show a bright star at this position. Hence, the object is more likely a foreground star. Moreover, the plasma sources ID 15 and 18 are located in the HI funnel (Mühle et al., 2005) together with the SSCs and the X–ray power–law sources ID 21, 27, 30 and 33. Here, the HI funnel may stem from the winds produced

in the SSCs together with the X–ray sources in agreement with the findings of Mühle et al. (2005).

NGC 4214 shows some diffuse emission which is also in positional agreement with a low column density region in the HI. However, this is not a shell but a low density region in the spiral–like appearance of the HI distribution. The central source, which also shows plasma emission is located at a rim of a shell which is open towards the southwest. The diffuse emission associated with sources ID 13 and 15 is not connected to a shell but rather located at high column densities.

In NGC 4449 the most interesting X–ray sources are probably the three super soft sources. However, they are not associated with shells. The only source which is located towards the center of a shell is ID 14. According to the HR of this source it is most likely a LMXB. Hence, it is not a candidate for the standard model.

The only plasma source in NGC 5253 located in an HI shell is source ID 3. According to Strickland & Stevens (1999) this source is a SSC embedded in an HII region containing ≈ 1000 OB stars (Turner et al., 1998). This shell associated with the young star burst region is likely filled with the hot gas seen in the X–ray data. Accordingly, this shell is very likely explained by the standard model.

For the standard model it turns out that only a few X–ray plasma sources are located within shells or shell–like structures showing up in the HI distribution. The presence of hot gas in the interior of shells, e.g., in the LMC (Bomans et al., 1994) suggests that other HI shells are also filled with hot X–ray emitting gas. But as with other observations performed until now (e.g., Walter et al. (1998); Zezas et al. (1999); Kerp et al. (2002)), also the present work failed to detect this coronal gas in a large number of shells. This situation might reflect that the sensitivity even of the modern X–ray telescopes is too low, or more likely that the coronal gas inside the shells has already cooled down and the emission is not detectable in X–rays anymore.

7 Summary and Future Prospects

Using state–of–the–art X–ray telescopes, providing a sufficient angular and spectral resolution, an investigation of local dwarf irregular galaxies (dIrr) is performed. Dwarf galaxies in general are most numerous in the universe. In that sense, they are frequently called the building blocks of the universe, since they are thought to build up structures on larger scales by mergers.

In particular, the dIrrs exhibit shells in their HI distribution. The standard model describes the origin of these shells, assuming that they are generated by stellar activity. The implications of this model are tested in this thesis at hand, as well as the properties of X–ray point sources found in each galaxy. Moreover, a statistical analysis is performed with respect to the detected X–ray point sources.

The standard model is tested by observing extended diffuse X–ray emission in the soft energy regime (0.2-1.0 keV) while the statistical analysis for point sources is taken out in a broader (0.2-5.0 keV) energy band. Both issues are summarized separately.

7.1 The Standard model

For the test of the standard model, the data is regarded with respect to diffuse emission. Thus, the X–ray data has to be treated differently to X–ray point sources. While the latter have sufficient high count rates in a small area, the former shows low count rates in a much larger region.

Therefore, the issues of filtering the light curves and vignetting have to be accounted for very carefully. A new software tool provides filtered light curves on an user adjustable significance threshold. The light curves are filtered with respect to the full spectral band, as well as for individual bands. This is because, in contrast to what was known before, the flares are also detected in soft bands. With this, the light curves are filtered reliable, keeping as much photon events as possible. This filtering is applied to all XMM–Newton data.

After the filtering, the data is splitted into energy bands which provide spectral information. Since the signal–to–noise is expected to be low in the case of diffuse soft emission, the issue of vignetting has to be treated carefully, too.

For this aim, new exposure maps for all different energy bands are calculated, because it is shown that the dedicated exposure maps, provided by the XMM–Newton software are virtually incorrect.

The new, enhanced exposure maps are calculated by adding source free images of deep observations and smoothing them with a broad Gaussian filter. The enhanced exposure maps are shown to be more reliable than the dedicated ones. However, the outer FOV

beyond 20′.0 from the optical axis are still not matching the observations. On the other hand, the galaxies observed here fit well into the inner 20′.0 where the exposure map correction works well.

The vignetting (or exposure) corrected maps are examined for diffuse emission making use of the adaptive smoothing algorithm. This ensures that at least a certain signal–to–noise is achieved (here 4-σ above background). For the data analysis only photon images are used.

The individual galaxies have different properties concerning their diffuse emission in the X–rays. **Holmberg I** exhibits a faint diffuse emission component in the northwest of the central HI depletion. The spectral data is fitted with different model spectra yielding a best–fit model with a temperature of $T = 10^{5.8}$ K. The cooling time and sound speed considerations provide distances the plasma can reach from the disk. These are in agreement with the blow–out scenario suggested by Ott et al. (2001); Vorobyov et al. (2004) from the central shell, if one regards the foreground X–ray emission of the Milky Way. This is also in agreement with the escape temperature considerations based on the work of Martin (1999).

With the enhanced procedures for XMM–Newton soft diffuse X–ray emission is also found in **IC 2574**. The spectral data is compatible with a model temperature of $T = 10^{6.0}$ K and the plasma can in general reach the galaxy halo. The thermal energy of the plasma leads to the picture that multiple supernovae produced the hot gas. The mass is about 1 % of the HI mass of IC 2574. As in contrast to Holmberg I the origin of the plasma (i.e. from which shell it stems) is uncertain because the galaxy is inclined. However, good candidate shells for the plasma origin are Walter & Brinks (1999) shells number 22 and/or 26. Only the brightest source ID 9, is very likely a supernova remnant (Brinks et al., 2003) filling an HI shell.

The third galaxy observed is **Sextans A**. Here, no diffuse emission is found down to the detection limit. The limiting luminosity however is lower than in the first two cases and hence the interpretation is that there is no diffuse component. This is also supported by the shallow star formation of the galaxy in the past.

In the case of **Holmberg II** diffuse emission is not detected on large angular scales which is due to the short exposure time and hence a relatively high luminosity limit. However, plasma emission is found in some HI shells which are most likely due to supernovae. In addition there are also shells (especially in the outer parts of the HI disk) which are not filled with hot plasma. These are unlikely produced in the picture of the standard model, but rather by ram–pressure effects due to the motion of the galaxy through an ambient medium (Bureau & Carignan, 2002).

For **NGC 1569** the XMM–Newton data is only used for the spectral information. The CHANDRA data is used for both point sources and diffuse emission. The bipolar outflow of coronal gas as reported by Martin et al. (2002) is confirmed qualitatively by CHANDRA and XMM–Newton. The spectral investigation of the CHANDRA data

yields a two–component model with temperatures $T_1 = 10^{6.97}$ K and $T_2 = 10^{6.68}$ K both of which can escape the galaxy. The temperatures derived from the XMM–Newton data are slightly higher ($T_1 = 10^{7.0}$ K and $T_2 = 10^{6.8}$) which does not change the result of the outflow of coronal gas. This is also supported by the considerations about the escape temperature (Martin, 1999).

As in the Holmberg II case, the galaxy **NGC 4214** shows more empty shells than plasma filled shells. Since the three candidates of filled shells turn out to be one supernova remnant and two HII regions, the standard model is not the main process triggering the shell formation. NGC 4214 also shows no high stellar activity outside the central star clusters and hence coronal gas is not expected to show up. In that sense NGC 4214 is comparable to Holmberg II where the standard model can be quoted only for a small number of individual shells.

The peculiar HI distribution of **NGC 4449** is well known to be quite turbulent in the outer parts of the galaxy. Thus, only the inner part where ordered rotation is present is investigated with respect to the X–ray emission. In concordance with previous work diffuse X–ray emission is found around the center of the galaxy. Also two components are needed to fit the spectral data but the model used here is simpler than in previous studies yielding comparable goodness–of–fit estimates (i.e. χ^2). The cold component ($T_1 = 10^{5.60}$ K) is confined to the galaxy potential while the hot component ($T_2 = 10^{6.58}$ K) can escape the galaxy. In addition to previous studies the XMM–Newton data is taken into account for the diffuse emission. The qualitative result is in agreement to what I found from the CHANDRA data. However, the temperatures derived from the XMM–Newton data are again slightly higher for T_1 ($T_1 = 10^{6.1}$ K and $T_2 = 10^{6.8}$).

Finally, **NGC 5253** is found to have a diffuse X–ray component as well. A simple one–component model is sufficient to fit the spectral data with plasma temperatures of $T = 10^{6.6}$ K. However, the figures for the plasma (here, HI mass, density, pressure) are lower compared to the findings of Summers et al. (2004). The gas is not confined to the gravitational potential of the galaxy. It is likely attributed to the young stellar activity while the cold component might stem from old stellar activity in the past. These findings are compared to the spectral data of XMM–Newton. The temperature is slightly higher yielding $T = 10^{6.8}$ K while the other parameters are lower than for the CHANDRA spectrum. Nevertheless, the gas can escape the galaxy.

The analysis of the diffuse soft X–ray emission shows that the standard model applies not for all cases of shells in the neutral gas. It is, nevertheless, the appropriate description for shell creation in a number of cases. Especially, the cases of Holmberg II and NGC 4214 exemplify that the shells can also stem from interaction with an ambient medium. Accordingly, the standard model is far from being ruled out but it surely provides not the only mechanism to create shells in the neutral gas of a galaxy. The findings for the blow–out/blow–away scenario based on the cooling time and sound speed of the plasmas is nicely supported by the escape temperature considerations following Martin (1999).

Since the Galaxy exhibits foreground components of X–ray emitting gas (the LHB and the halo), Holmberg I is taken as an example of how to account for these foregrounds. It turns out that the physical parameters of the coronal gas are in better agreement with the findings in the literature when the SXRB model (Pradas, 2004; Pradas et al., 2003; Kappes et al., 2003) is included in the investigation of the spectral data.

7.2 X–ray Point Sources

One must account for a number of issues when X–ray point sources are in the focus of interest. Of course, the light curve filtering is the first crucial point, whereas the vignetting is not so important since the background is subtracted for each point source.

The point sources have to be detected first in the image data. The standard procedure here is to make use of certain dedicated tools or algorithms which find point sources automatically. Here, however, another approach is followed which detects point sources more reliably.

The idea is to smooth the photon image with a Gaussian filter which results in a Gaussian noise distribution. Then the background level can be estimated and the image is clipped to $4-\sigma$ above the background. everything which is above the lower clipping threshold is concerned as a detection.

The advantage of this approach is the higher number of detections (up to $\approx$30 % more than with an automatic task). On the other hand, the disadvantage is that it is not an automated method and thus it is time consuming. Therefore, the source detection for the exposure map derivation is done with the automatic tasks because of the large number of data which have to be evaluated.

Of importance is also the interpretation of the HR of the individual sources, which is nearly unfeasible without additional data in other wavelengths. Only power–law and plasma sources can be separated roughly. The discrimination of black body model is not feasible at all since for low temperatures they are indistinguishable from the plasma models and for high temperatures they occupy the same range as the power–law models in the HR diagram.

Hence, if no additional information is at hand, one can only discriminate between accreting systems and plasma sources. A further distinction of HMXB and LMXB is more reliable with additional data like UV images. If no additional data is at hand, the luminosity is the only indication for the HMXB/LMXB distinction. Supernova remnants and HI regions can be separated with radio continuum data in at least two bands, which provide a spectral index.

With the help of HR diagrams and additional data, the source properties and hence the source type can be pinned down. From the classification different spacial and statistical tests are performed. This is summarized in the following.

The X–ray point source content of all sample galaxies is qualitatively similar. Supernova remnants, HII regions, as well as accreting sources like HMXB and LMXB are found and also three super soft sources are identified. The quantitative analysis demands the study of the log(N)-log(S) diagram in comparison to the cosmic X–ray background to make sure that only point sources related to the galaxy of interest are regarded.

For each galaxy, the radial distribution of the point sources is evaluated, taking the inclination into account. This deprojection allows to compare the different galaxies since the radial distance of the point sources from the center is then given in kpc, rather than in angular distance units.

In conclusion, the HMXB are the most characteristic point sources in a galaxy. The connection of the HMXB number with several other parameters correlates most significantly. So with the galactocentric distance of the outermost X–ray point source or HI mass, the number of HMXB increases as well. Moreover, the XLF is calculated for all galaxies. The slope of the XLF flattens for increasing number of HMXB.

In addition, the SFR of a galaxy is adopted from the B-band luminosity. Plotting the HI mass versus the SFR gives a nice correlation, but only for the case that the XLF is not a broken power–law. Thus, a broken power–law points to a non–uniform star formation history of the host galaxy.

Furthermore, there seems to be a correlation between the number of HMXB and the SFR of a galaxy. So, the dIrr sample is tested against a different sample of late–type galaxies, studied by Grimm et al. (2003). My results here show that the correlation between the number of HMXB and the SFR is best for a luminosity limited sample of HMXB, in concordance with the late–type galaxy sample. But in contrast to the late-tape galaxy sample here the slope is much flatter. This is most likely caused by the fact, that the SFR of both samples is derived differently (FIR luminosity vs. B–band luminosity).

A further test is performed for this correlation, namely the scaling of the XLF with the SFR. It turns out that the XLF of all galaxies can be scaled in the number of X–ray point sources so that the range covered in the log(N)-log(L) by the XLFs is minimal. But still the offset between the different XLFs is not negligible. Therefore, the XLFs are scaled individually by a scaling factor for each galaxy. A comparison of both scaling factors shows a discrepancy of about two orders of magnitude. Hence, it is argued that an universal XLF does not exist for dIrrs. This includes also the nonexistence of an universal initial mass function.

This means that the stellar content of dIrrs stems not from a universal process. This is supported by the investigation of the spatial distribution of X–ray point sources in the dIrr sample. It turns out that for galaxies larger than 4 kpc the most luminous sources are concentrated towards the center. In contrast to that, the smaller dIrrs show a constant luminosity of X–ray point sources for all radii. Here, the interpretation

is that the star formation history must be different at least in these two subsamples. Hence, it is not surprising that the work of Grimm et al. (2003) gives quantitatively different results.

7.3 Future Prospects

Although this study of irregular dwarf galaxies gives new insights in the evolution of these objects, as with most of the scientific investigations, this cannot be considered fully completed. There are at least two issues — the diffuse soft emission and the classification of X–ray point sources — which can be improved further.

The studies for diffuse emission can be improved in different ways. Since the signal of diffuse soft emission in the X–rays is very faint, an increased exposure time will lead to a higher signal–to–noise. However, the exposure map correction is the crucial point. Therefore, the enhanced exposure maps presented in this work can be improved further. Especially the outer FOV correction is still not perfect and taking more deep fields into account the outer FOV correction can be pushed to the limit (see also Pradas, in prep.).

Since future missions in X–ray astronomy are going to have larger collecting areas, it should improve the signal–to–noise of these faint emissions. On the other hand, the FOV of the planned missions are smaller than the XMM–Newton FOV and probably even smaller than the CHANDRA FOV. This makes it very difficult to observe objects such as the dIrr galaxies with an angular size of about 20 arcmin. Here, a further step can be achieved by mosaic pointings. But this in turn raises difficulties in the exposure map correction again. Hence, the improvement of the exposure maps and an adequate exposure time will give better detection limits.

The note on the Galactic X–ray emission exemplifies the need for a good model of the SXRB. If the photon statistic is good enough, the SXRB model by Pradas (2004); Pradas et al. (2003); Kappes et al. (2003) can be applied to the background of an XMM–Newton observation and thus, the parameters for a possible diffuse emission component is much more reliable.

The classification of X–ray point sources depends strongly on observations in other wavelengths. Only the X–ray band provides no good discriminators between LMXB and HMXB. This discrimination, however, is recommended as seen in chapter 6. Therefore, a dedicated survey of dIrrs in specific wavelength should be performed to minimize the uncertainties of point source classification.

Especially the XMM–Newton optical monitor should be used in every observation. This is feasible since the OM is independent from the other imaging devices aboard XMM–Newton. Here, I am somewhat surprised why observers do not make use of the OM in some of the observations.

Also the radio continuum bands have to be incorporated to discriminate between super nova remnants and HII regions. In addition Hα images can help to disentangle the different X–ray point source types reliable.

In summary, a dedicated observation of dIrr galaxies in the wavelength proposed above would give a homogeneous picture of the evolution and properties of these "building blocks" of the universe. Hence, the uncertainties of this heterogeneous sample can be minimized, also with the incorporation of more nearby dwarf galaxies. This then will give a deeper answer to the standard model and also to the issues of universal XLFs and universal SFRs and structure formation in the universe as a whole.

8 Acknowledgements

Writing a thesis without the support of many people is virtually not feasible. Thus, I take the opportunity to thank all of them.

First of all, I would like to thank my advisor Jürgen Kerp for giving me the opportunity to work on the XMM–Newton data and giving me all the support I needed to finish this work at hand. I always found an open door and even in the moments of my frustration, Jürgen found the right words to prod me to keep working on my thesis.

My thanks go also to Uli Klein who agreed spontaneously to inherit the task of the co-advisor. Also his help on the radio continuum data and the discussions about dwarf galaxies gave me valuable hints for this thesis.

Furthermore, I wish to thank all staff members of the Radio Astronomical Institut. Especially, I like to thank my office mate Juan Enrique Pradas Simón for all the fruitful discussions, computer code design for the pipeline, coffee and cigarettes. I also like to thank my former office mate Stephan Stanko who always had an answer to my *awk*-problems. Moreover, a lot of other colleagues gave me support. In the order of appearance, starting from the northwest corner of the institute building, these are Gyula István Géza "Josh" Józsa, Franz Kenn, Frank Bensch, $\Lambda\varepsilon\omega\nu\grave{\iota}\delta\alpha\varsigma\ \Delta\grave{\varepsilon}\delta\varepsilon\varsigma$, Jorge Luis Pineda Gálvez, Marek Jamrozy, Tobias Westmeier, Christian Brüns, Peter Kalberla, all the people from the lab, Philipp Richter, Michael Hilker, Matthias Kadler, Iván Cámara Mayorga, Enrique Ripoll Segovia and all other members and former members of the institute. Further, I am much obliged to our adept and precious secretary Christina Stein–Schmitz who kept me on the right track on my way through the bureaucratic jungle.

Then I would like to thank Fabian Walter for providing the HI data and also Elias Brinks for the hints and discussions about the first three galaxies of the sample.

There is also private life and special thanks go out to my friends Thilo, Kinne, Pütz, Chiwa, Hardeep, Olley, Bine, Bixi, Zet, Marco, Bob, Thomas, Günter, Anna, Svenja, Rolf, Gine, Steff, Marion, Zliq, Tatjana, Caro, Lukas, Andy & Andi, Crea, Harald and Florian. Heartfelt thanks go to Carla Berkenhoff who endured my bad temper.

Mein größter Dank gilt meiner Familie: meiner Mutter, meinem Vater sowie meiner Oma. Eure Unterstützung und eure Verbundenheit, auch wenn es mal wieder drunter und drüber lief, werde ich niemals vergessen!

Many thanks to all of you!

This work would not have been possible without the financial support of the Deutsches Zentrum für Luft- und Raumfahrt (DLR) in the framework of the project *Untersuchungen der heißen Phase des interstellaren Mediums von Zwerggalaxien und der Milchstraße mit XMM–Newton* under Grant No. 50 OR 0103.

9 Lebenslauf

Persönliche Daten:

Name	Michael Kappes
Geburtsdatum,-ort	1971, Köln
Eltern	Helmut Kappes, Doris Kappes geb. Berres
Staatsangehörigkeit	Deutsch
Familienstand	ledig
Adresse	

Schulbildung:

1977	Einschulung in die Städtische Grundschule Schulstr. in Köln Vingst
1981	Schulwechsel an das Johann–Gottfried Herder Gymnasium in Köln Buchheim
29.05.1990	Schulabschluß mit Abitur

Zivildienst:

1.10.1990 – 31.11.1991	Ableistung des Zivildienstes beim Deutschen Roten Kreuz in Köln

Studium:

WS 92/93	Beginn des Studiums der Physik an der Universität zu Köln
WS 96/97	Bestehen der Diplom–Vorprüfung in Physik
SS 97	Wechsel an die Universität Bonn zum Studium der Physik und Astronomie
Juli 2002	Erlangung des Diploms in Physik Titel der Diplomarbeit: “Korrelation der Röntgenstrahlung mit der galaktischen HI–Verteilung im Bereich des Lockman–Fensters” Angefertigt am Radioastronomischen Institut der Universität Bonn
seit Januar 2002	Angestellt als Wissenschaftlicher Mitarbeiter am Radioastronomischen Institut der Universität Bonn

References

Alexanian, M. 1968, Physical Review, 165, 253

Anders, P., de Grijs, R., Fritze-v. Alvensleben, U., & Bissantz, N. 2004, MNRAS, 347, 17

Antonucci, R. R. J. & Miller, J. S. 1985, ApJ, 297, 621

Bajaja, E., Huchtmeier, W. K., & Klein, U. 1994, A&A, 285, 385

Barnes, D. G. & de Blok, W. J. G. 2004, MNRAS, 351, 333

Barthel, P. 1989, Scientific American, 260, 20

Begeman, K. G. 1989, A&A, 223, 47

Belczynski, K., Kalogera, V., Zezas, A., & Fabbiano, G. 2004, ApJ, 601, L147

Blondiau, M. J., Kerp, J., Mebold, U., & Klein, U. 1997, A&A, 323, 585

Bomans, D. J., Dennerl, K., & Kurster, M. 1994, A&A, 283, L21+

Bondi, H. & Hoyle, F. 1944, MNRAS, 104, 273

Bosma, A. 1981, AJ, 86, 1825

Bowyer, C. S., Field, G. B., & Mack, J. E. 1968, Nature, 217, 32

Bregman, J. N., Schulman, E., & Tomisaka, K. 1995, ApJ, 439, 155

Breitschwerdt, D. & Schmutzler, T. 1999, A&A, 347, 650

Brinks, E. & Bajaja, E. 1986, A&A, 169, 14

Brinks, E., Walter, F., & Kerp, J. 2003, Ap&SS, 284, 627

Bureau, M. & Carignan, C. 2002, AJ, 123, 1316

Burton, W. B. 1985, A&AS, 62, 365

Calzetti, D., Conselice, C. J., Gallagher, J. S., & Kinney, A. L. 1999, AJ, 118, 797

Campbell, A. W. & Terlevich, R. 1984, MNRAS, 211, 15

Charles, P. A. & Seward, F. D. 1995, Exploring the X–ray Universe (Cambridge University Press), 398

Chu, Y., Chang, H., Su, Y., & Mac Low, M. 1995, ApJ, 450, 157

Chu, Y. & Mac Low, M. 1990, ApJ, 365, 510

Colbert, E. J. M., Heckman, T. M., Ptak, A. F., Strickland, D. K., & Weaver, K. A. 2004, ApJ, 602, 231

Condon, J. J. 1992, ARA&A, 30, 575

de Avillez, M. A. & Breitschwerdt, D. 2004, A&A, 425, 899

della Ceca, R., Griffiths, R. E., & Heckman, T. M. 1997, ApJ, 485, 581

Dewangan, G. C., Miyaji, T., Griffiths, R. E., & Lehmann, I. 2004, ApJ, 608, L57

Dohm-Palmer, R. C., Skillman, E. D., Mateo, M., et al. 2002, AJ, 123, 813

Dohm-Palmer, R. C., Skillman, E. D., Saha, A., et al. 1997a, AJ, 114, 2514

Dohm-Palmer, R. C., Skillman, E. D., Saha, A., et al. 1997b, AJ, 114, 2527

Dolphin, A. E., Saha, A., Skillman, E. D., et al. 2003, AJ, 125, 1261

Dopita, M. 1997, Publications of the Astronomical Society of Australia, 14, 230

Drozdovsky, I. O., Schulte-Ladbeck, R. E., Hopp, U., Greggio, L., & Crone, M. M. 2002, AJ, 124, 811

Efremov, Y. N., Elmegreen, B. G., & Hodge, P. W. 1998, ApJ, 501, L163+

Fabbiano, G. 1996, X–ray emission of Galaxies (Zimmermann, U. et al.), 347

Fabbiano, G. & White, N. E. 2003, astro-ph, 0307077

Fanelli, M. N., Waller, W. W., Smith, D. A., et al. 1997, ApJ, 481, 735

Ferrando, P., Abbey, A. F., Altieri, B., et al. 2003, in X-Ray and Gamma-Ray Telescopes and Instruments for Astronomy. Edited by Joachim E. Trümper, Harvey D. Tananbaum. Proceedings of the SPIE, Volume 4851, pp. 232-242 (2003)., 232–242

Freedman, W. L., Madore, B. F., Gibson, B. K., et al. 2001, ApJ, 553, 47

Freeman, P., Doe, S., & Siemiginowska, A. 2001, in Proc. SPIE Vol. 4477, p. 76-87, Astronomical Data Analysis, Jean-Luc Starck; Fionn D. Murtagh; Eds., 76–87

Friedman, H. & Byram, E. T. 1967, Science, 158, 257

Gendreau, K. C., Mushotzky, R., Fabian, A. C., et al. 1995, PASJ, 47, L5

Giacconi, R., Branduardi, G., Briel, U., et al. 1979, ApJ, 230, 540

Gondoin, P., Aschenbach, B., Erd, C., et al. 2000, in Proc. SPIE Vol. 4140, p. 1-12, X-Ray and Gamma-Ray Instrumentation for Astronomy XI, Kathryn A. Flanagan; Oswald H. Siegmund; Eds., 1–12

Grebel, E. K., Gallagher, J. S., & Harbeck, D. 2003, AJ, 125, 1926

Greve, A., Tarchi, A., Hüttemeister, S., et al. 2002, A&A, 381, 825

Grimm, H.-J., Gilfanov, M., & Sunyaev, R. 2002, A&A, 391, 923

Grimm, H.-J., Gilfanov, M., & Sunyaev, R. 2003, MNRAS, 339, 793

Gursky, H., Giacconi, R., Gorenstein, P., et al. 1966, ApJ, 146, 310

Hartmann, D. & Burton, W. 1997, Atlas of Galactic Neutral Hydrogen (Cambridge University Press, Cambridge)

Hartwell, J. M., Stevens, I. R., Strickland, D. K., Heckman, T. M., & Summers, L. K. 2004, MNRAS, 348, 406

Hasinger, G., Altieri, B., Arnaud, M., et al. 2001, A&A, 365, L45

Heike, K., Awaki, H., Misao, Y., Hayashida, K., & Weaver, K. A. 2003, ApJ, 591, L99

Heiles, C. 1979, ApJ, 229, 533

Heiles, C. 1984, ApJS, 55, 585

Hensler, G., Dickow, R., Junkes, N., & Gallagher, J. S. 1998, ApJ, 502, L17+

Hodge, P., Kennicutt, R. C., & Strobel, N. 1994, PASP, 106, 765

Humphrey, P. J. & Buote, D. A. 2004, ApJ, 612, 848

Hunter, D. A., van Woerden, H., & Gallagher, J. S. 1999, AJ, 118, 2184

Hunter, D. A., Wilcots, E. M., van Woerden, H., Gallagher, J. S., & Kohle, S. 1998, ApJ, 495, L47+

Israel, F. P. 1988, A&A, 194, 24

Jacobs, V. L., Davis, J., Kepple, P. C., & Blaha, M. 1977, ApJ, 211, 605

Kaaret, P., Alonso-Herrero, A., Gallagher, J. S., et al. 2004a, MNRAS, 348, L28

Kaaret, P., Ward, M. J., & Zezas, A. 2004b, MNRAS, 351, L83

Kappes, M., Kerp, J., & Richter, P. 2003, A&A, 405, 607

Karachentsev, I. D., Dolphin, A. E., Geisler, D., et al. 2002, A&A, 383, 125

Karachentsev, I. D., Sharina, M. E., Dolphin, A. E., et al. 2003, A&A, 398, 467

Kellogg, E., Murray, S., Giacconi, R., Tananbaum, T., & Gursky, H. 1973, ApJ, 185, L13+

Kennicutt, R. C. 1998, ARA&A, 36, 189

Kernighan, B. W. & Ritchie, D. M. 1988, The C Programming Language (second edition) (Prentice-Hall, Englewood Cliffs, NJ)

Kerp, J., Mack, K.-H., Egger, R., et al. 1996, A&A, 312, 67

Kerp, J., Walter, F., & Brinks, E. 2002, ApJ, 571, 809

Kim, S., Staveley-Smith, L., & Dopita, M. A. 1998, in The Magellanic Clouds and Other Dwarf Galaxies, Proceedings of the Bonn/Bochum-Graduiertenkolleg Workshop, held at the Physikzentrum Bad Honnef, Germany, January 19-22, 1998, Eds.: T. Richtler and J.M. Braun, Shaker Verlag, Aachen, ISBN 3-8265-4457-9, p. 169-172,, 169–172

Kobulnicky, H. A. & Skillman, E. D. 1995, ApJ, 454, L121+

Kobulnicky, H. A. & Skillman, E. D. 1997, ApJ, 489, 636

Kohle, S. 1999, NGC 4449, Clues to the Evolution of a Magellanic Galaxy (Ph.D. thesis, University of Bonn)

Ku, W. H.-M., Helfand, D. J., & Lucy, L. B. 1980, Nature, 288, 323

Kuntz, K. D. & Snowden, S. L. 2000, ApJ, 543, 195

Lee, H., McCall, M. L., & Richer, M. G. 2003, AJ, 125, 2975

Lisenfeld, U., Wilding, T. W., Pooley, G. G., & Alexander, P. 2004, MNRAS, 349, 1335

Lockman, F. J., Jahoda, K., & McCammon, D. 1985, NASA STI/Recon Technical Report N, 85, 27785

Lumb, D. H., Finoguenov, A., Saxton, R., et al. 2003, Experimental Astronomy, 15, 89

Lumb, D. H., Warwick, R. S., Page, M., & De Luca, A. 2002, A&A, 389, 93

Mac Low, M. & Ferrara, A. 1999, ApJ, 513, 142

Mac Low, M.-M. & Ferrara, A. 1998, Lecture Notes in Physics, v.506, Berlin Springer Verlag, 506, 559

MacKenty, J. W., Maíz-Apellániz, J., Pickens, C. E., Norman, C. A., & Walborn, N. R. 2000, AJ, 120, 3007

Maíz-Apellániz, J., Muñoz-Tuñón, C., Tenorio-Tagle, G., & Mas-Hesse, J. M. 1999, A&A, 343, 64

Makarova, L. N. & Karachentsev, I. D. 2003, Astrophysics, 46, 144

Martimbeau, N., Carignan, C., & Roy, J.-R. 1994, AJ, 107, 543

Martin, C. L. 1999, ApJ, 513, 156

Martin, C. L. 2003, in Revista Mexicana de Astronomia y Astrofisica Conference Series, 56–59

Martin, C. L. & Kennicutt, R. C. 1997, ApJ, 483, 698

Martin, C. L., Kobulnicky, H. A., & Heckman, T. M. 2002, ApJ, 574, 663

Marty, P. B., Kneib, J., Sadat, R., Ebeling, H., & Smail, I. 2003, in X-Ray and Gamma-Ray Telescopes and Instruments for Astronomy. Edited by Joachim E. Trümper, Harvey D. Tananbaum. Proceedings of the SPIE, Volume 4851, pp. 208-222 (2003)., 208–222

Mateo, M. L. 1998, ARA&A, 36, 435

McCammon, D. & Sanders, W. T. 1990, ARA&A, 28, 657

Miyawaki, R., Sugiho, M., Kokubun, M., & Makishima, K. 2004, PASJ, 56, 591

Morrison, R. & McCammon, D. 1983, ApJ, 270, 119

Mühle, S., Klein, U., Wilcots, E., & Hüttemeister, S. 2005, AJ, in press

Ott, J. 2003, PASP, 115, 141

Ott, J., Martin, C. L., & Walter, F. 2003, ApJ, 594, 776

Ott, J., Walter, F., Brinks, E., et al. 2001, AJ, 122, 3070

Pasetto, S., Chiosi, C., & Carraro, G. 2003, A&A, 405, 931

Pradas, J. 2004, The hot phase of the ISM, Investigation of the soft X–ray background (Ph.D. thesis, University of Bonn)

Pradas, J., Kerp, J., & Kalberla, P. M. W. 2003, Astronomische Nachrichten, 324, 150

Pringle, J. E. & Rees, M. J. 1972, A&A, 21, 1

Puche, D., Westpfahl, D., Brinks, E., & Roy, J. 1992, AJ, 103, 1841

Radice, L. A., Salzer, J. J., & Westpfahl, D. J. 1995, Bulletin of the American Astronomical Society, 27, 882

Read, A. M. & Ponman, T. J. 2003, astroph/0304147

Rhode, K. L., Salzer, J. J., Westpfahl, D. J., & Radice, L. A. 1999, AJ, 118, 323

Rosa-González, D., Terlevich, E., & Terlevich, R. 2002, MNRAS, 332, 283

Sánchez-Salcedo, F. J. 2002, Revista Mexicana de Astronomia y Astrofisica, 38, 39

Scheuer, P. A. G. 1974, MNRAS, 166, 513

Schild, R. 1984, Astrophys. Lett., 24, 85

Schwartz, C. M. & Martin, C. L. 2004, ApJ, 610, 201

Sersic, J. L. & Donzelli, C. J. 1992, Ap&SS, 193, 87

Shopbell, P. L. & Bland-Hawthorn, J. 1998, ApJ, 493, 129

Skillman, E. D., Terlevich, R., Teuben, P. J., & van Woerden, H. 1988, A&A, 198, 33

Snowden, S. L., Egger, R., Freyberg, M. J., et al. 1997, ApJ, 485, 125

Snowden, S. L., Freyberg, M. J., Plucinsky, P. P., et al. 1995, ApJ, 454, 643

Staveley-Smith, L., Sault, R. J., Hatzidimitriou, D., Kesteven, M. J., & McConnell, D. 1997, VizieR Online Data Catalog, 728, 90225

Stewart, S. G., Fanelli, M. N., Byrd, G. G., et al. 2000, ApJ, 529, 201

Stil, J. M. & Israel, F. P. 2002, A&A, 392, 473

Strickland, D. K., Heckman, T. M., Weaver, K. A., Hoopes, C. G., & Dahlem, M. 2002, ApJ, 568, 689

Strickland, D. K., Ponman, T. J., & Stevens, I. R. 1997, A&A, 320, 378

Strickland, D. K. & Stevens, I. R. 1999, MNRAS, 306, 43

Strickland, D. K. & Stevens, I. R. 2000, MNRAS, 314, 511

Summers, L. K., Stevens, I. R., Strickland, D. K., & Heckman, T. M. 2003, MNRAS, 342, 690

Summers, L. K., Stevens, I. R., Strickland, D. K., & Heckman, T. M. 2004, MNRAS, 351, 1

Sutherland, R. S. & Dopita, M. A. 1993, ApJS, 88, 253

Tenorio-Tagle, G., Franco, J., Bodenheimer, P., & Rozyczka, M. 1987, A&A, 179, 219

Theis, C. & Kohle, S. 2001, A&A, 370, 365

Thronson, H. A., Hunter, D. A., Telesco, C. M., Decher, R., & Harper, D. A. 1987, ApJ, 317, 180

Tongue, T. D. & Westpfahl, D. J. 1995, AJ, 109, 2462

Trümper, J. 1982, Advances in Space Research, 2, 241

Turner, J. L., Beck, S. C., & Ho, P. T. P. 2000, ApJ, 532, L109

Turner, J. L., Beck, S. C., & Hurt, R. L. 1997, ApJ, 474, L11+

Turner, J. L., Ho, P. T. P., & Beck, S. C. 1998, AJ, 116, 1212

Uyanıker, B., Reich, W., Yar, A., & Fürst, E. 2004, A&A, 426, 909

Valdez-Gutiérrez, M., Rosado, M., Puerari, I., et al. 2002, AJ, 124, 3157

van der Hulst, T. & Sancisi, R. 1988, AJ, 95, 1354

van Dyk, S. D., Puche, D., & Wong, T. 1998, AJ, 116, 2341

Vorobyov, E. I., Klein, U., Shchekinov, Y. A., & Ott, J. 2004, A&A, 413, 939

Walter, F. 2001, Astrophysics and Space Science Supplement, 277, 91

Walter, F. & Brinks, E. 1999, AJ, 118, 273

Walter, F. & Kerp, J. 2002, Bulletin of the American Astronomical Society, 34, 718

Walter, F., Kerp, J., Duric, N., Brinks, E., & Klein, U. 1998, ApJ, 502, L143+

Walter, F., Taylor, C. L., Hüttemeister, S., Scoville, N., & McIntyre, V. 2001, AJ, 121, 727

Wilcots, E. M. & Hunter, D. A. 2002, AJ, 123, 1476

Wilcots, E. M. & Thurow, J. C. 2001, ApJ, 555, 758

Wu, K. 2001, Publications of the Astronomical Society of Australia, 18, 443

Zezas, A., Fabbiano, G., Prestwich, A., Murray, S., & Ward, M. 2001, in Astronomical Society of the Pacific Conference Series, 425–+

Zezas, A. L., Georgantopoulos, I., & Ward, M. J. 1999, MNRAS, 308, 302

List of Figures

1 The Virgo cluster 4
2 Opacity of the earth atmosphere 8
3 Sketch of the XMM–Newton general layout 11
4 Effective area of the mirror assembly 12
5 Technical layout of the EPIC–MOS camera 13
6 Technical layout of the EPIC–*pn* camera 13
7 Quantum efficiency of the XMM–Newton cameras 14
8 Total effective area of the imaging instruments for different filters . . 15
9 Spectrum of a black body at different temperatures 17
10 Spectrum of bremsstrahlung 18
11 Sketch of X–ray binaries 23
12 Sketch of the unified model of AGN 23
13 Unfiltered EPIC–MOS and EPIC–*pn* images right after calibration . . 27
14 Raw and filtered light curve of the EPIC–MOS1 28
15 Radial plot showing the vignetting effect 30
16 Comparison of the SAS exposure map and the improved exposure map to the observational data 32
17 Flow chart for exposure map calculation 33
18 Cross section for photoelectric absorption in the ISM 36
19 Calculated HR for different source properties 37
20 M1M2 X–ray map of Holmberg I together with HI map. 45
21 log(N)–log(S) relation for Holmberg I (XMM–Newtondata) 49
22 XMM–Newton HR for X–ray point sources in Holmberg I. 49
23 OM image of Holmberg I 51
24 Spacial distribution of X–ray point sources in Holmberg I 52
25 XLF of Holmberg I 53
26 Image of diffuse emission in Holmberg I 55

27 The diffuse emission spectrum of Holmberg I 58
28 M1M2 maps and HI map of IC 2574 63
29 log(N)–log(S) relation for IC 2574 66
30 HR for the point sources found in IC 2574. 66
31 OM image of IC 2574 69
32 Spatial distribution of IC 2574 71
33 4-5 kpc ring of LMXB 72
34 XLF of IC 2574 72
35 Image of diffuse emission in IC 2574 74
36 Diffuse X–ray emission spectrum of IC 2574 75
37 M1M2 map and HI image of Sextans A 78
38 log(N)–log(S) relation for Sextans A 80
39 HR diagram of Sextans A 81
40 Spatial distribution of X–ray point sources in Sextans A 82
41 XLF of Sextans A 83
42 M1M2 map and HI map of Holmberg II 86
43 Comparison of XMM–Newton and CHANDRA image of the brightest X–ray source in Holmberg II 87
44 log(N)–log(S) relation for Holmberg II 87
45 HR of CHANDRA point sources in Holmberg II 90
46 Holmberg II XMM–Newton OM image 92
47 DSS2 blue image of Holmberg II 92
48 DSS2 red image of Holmberg II 93
49 Hα emission of Holmberg II 93
50 C band (6 cm) radio continuum map of Holmberg II 94
51 L band (21 cm) radio continuum map of Holmberg II 94
52 Blowup of X–ray source ID 56 in Holmberg II 96
53 Spacial distribution of X–ray point sources in Holmberg II 100
54 XLF of Holmberg II 101

55 HI map of NGC 1569 105
56 M1M2 X–ray map in the PS band of NGC 1569 106
57 Patchy X–ray emission in the center of NGC 1569 107
58 log(N)-log(S) relation of NGC 1569 108
59 HR of X–ray point sources in NGC 1569 111
60 HR diagram with black body models for NGC 1569 113
61 Adaptively smoothed CHANDRA image with UV contours and positions of super star cluster 115
62 Spacial distribution of X–ray point sources i NGC 1569 116
63 XLF of NGC 1569 117
64 Diffuse X–rays from NGC 1569 in B2, B3 and B4 bands 118
65 Spectrum of the diffuse emission in NGC 1569 121
66 XMM–Newton spectrum of the diffuse emission in NGC 1569 122
67 M1M2 map and HI map of NGC 4214 126
68 log(N)-log(S) relation for NGC 4214 126
69 HR for the point sources found in NGC 4214 127
70 CHANDRA PS band map of NFC 4214 131
71 X–ray spectrum of the SNR candidate in NGC 4214 132
72 Hardness ratio of the central CHANDRA sources in NGC 1569 133
73 Spatial distribution of NGC 4214 X–ray point sources 134
74 XLF of NGC 4214 135
75 Spectral extraction regions of CHANDRA data in the central region of NGC 4214 137
76 X–ray spectrum of the emission around ID 10 in NGC 4214 138
77 X–ray spectrum of the emission around ID 13 in NGC 4214 139
78 Adaptively smoothed image of NGC 4449 in the CHANDRA PS band 144
79 log(N)-log(S) relation for NGC 4449 X–ray point sources 145
80 HR for the point sources found in NGC 4449 147
81 OM image of NGC 4449 in the UV regime 148

82 Spacial distribution of X–ray point sources in NGC 4449 150
83 XLF of NGC 4449 150
84 Diffuse X–ray emission spectrum of NGC 4449 151
85 Diffuse X–ray emission spectrum of NGC 4449 (XMM–Newton data) 153
86 Adaptively smoothed image of the CHANDRA data in the PS band showing NGC 5253 158
87 log(N)-log(S) relation of NGC 5253 159
88 HR for the point sources found in NGC 5253 162
89 Adaptively smoothed CHANDRA image of NGC 5253 163
90 Spacial distribution of X–ray point sources detected in NGC 5253 . . 164
91 XLF of NGC 5253 165
92 Diffuse X–ray emission spectrum of NGC 5253 (CHANDRA data) . . 166
93 Diffuse X–ray emission spectrum of NGC 5253 (XMM–Newton data) 168
94 SXRB spectrum from a background region in Holmberg I 172
95 Linear correlation between the number of HMXB and the galactocentric distance of the outermost X–ray point source 178
96 Linear correlation between the number of HMXB and the HI mass of the host galaxy 178
97 Linear correlation between the number of HMXB and the XLF slope of the host galaxy 179
98 Correlation of HI mass and SFR for the galaxies with an unbroken XLF 180
99 Linear correlation between SFR and the luminosity limited number of HMXB of the dIrr sample 181
100 The XLFs of the dIrr sample 183
101 The XLFs scaled by shifting the XLF to the XLF of Holmberg II . . . 184
102 Comparison of the normalizations for the XLF 184
103 The combined luminosity/galactocentric distance data of all dIrr galaxies in the sample 185
104 The combined luminosity/galactocentric distance data of the splitted sample 186
105 Correlation of total number of X–ray point sources with the temperature of the diffuse emission 187

106 Correlation of SFR with the temperature of the diffuse emission . . . 187

107 Temperature of extended thermal X–ray emission vs. maximum HI rotation velocity, taken from Martin (1999) 188

List of Tables

1 Comparison of different X–ray telescope missions 10

2 Exposure times of the deep observations obtained for the calculation of exposure maps 31

3 X–ray band definitions and energy boundaries 35

4 Observational key data of the dIrr sample 44

5 Basic parameters of Holmberg I 44

6 Holmberg I XMM–Newton X–ray point source list 47

7 Holmberg I flux limits for individual XMM–Newton bands 48

8 Spectral models for diffuse X–ray emission 57

9 Basic parameters of IC 2574 63

10 IC 2574 flux limits for individual XMM–Newton bands 64

11 IC 2574 X–ray point source list 65

12 IC 2574 X–ray to optical correlation. 68

13 Spectral models for IC 2574 75

14 Basic parameters of Sextans A 78

15 Sextans A X–ray point source list 79

16 Sextans A flux limits for individual bands 79

17 Basic parameters of Holmberg II 85

18 Holmberg II X–ray point source list 88

19 Table.18—continued 89

20 Holmberg II flux limits for individual bands 90

21 Holmberg II X–ray to optical/radio correlation and X–ray luminosities. 98

22 Table.21—continued 99

23 Basic parameters of NGC 1569 104

24 NGC 1569 flux limits for individual bands 105

25 NGC 1569 X–ray point source list 109

26 Table.25—continued 110

27 Basic parameters of NGC 4214 125
28 NGC 4214 flux limits for individual bands 127
29 NGC 4214 X–ray point source list 128
30 Table.29—continued 129
31 Basic parameters of NGC 4449 143
32 NGC 4449 flux limits for individual bands 145
33 NGC 4449 X–ray point source list 146
34 NGC 4449 X–ray point source types 149
35 Basic parameters of NGC 5253 157
36 NGC 5253 flux limits for individual bands 157
37 NGC 5253 X–ray point source list 160
38 Table.37—continued 161
39 Intermediate results from the galaxy sample 174

Ich versichere, daß ich diese Arbeit selbständig verfaßt und keine anderen als die angegebenen Quellen und Hilfsmittel benutzt, sowie Zitate kenntlich gemacht habe.